LONG TERM RESPONSE OF MULTI-BARRIER SCHEMES FOR UNDERGROUND RADIOACTIVE WASTE DISPOSAL

Erdem Toprak

Doctoral Thesis

Civil and Environmental Engineering Department

Universitat Politècnica de Catalunya

Thesis Advisors:
Prof. Sebastià Olivella
Dr. Xavier Pintado

Barcelona, May, 2018

Abstract

The safest long-term management solution for high-activity radioactive waste is known as geological disposal. Many countries (e.g. Canada, Finland, France, Switzerland, Sweden, UK and USA) have chosen to dispose of all or part of their spent nuclear fuel in facilities constructed at an appropriate depth in stable geological formations. POSIVA Oy has been granted by the Finnish Government the contract to construct the final disposal facility of spent nuclear fuel and the operational license application will be submitted in forthcoming years.

This thesis contains the material characterization using laboratory tests and the description of 2D and 3D sensitivity studies carried out for the disposal method considered by POSIVA Oy. A series of cases have been considered to investigate the effect of various aspects related to the design of the vertical disposal method (KBS-3V, Juvankoski, 2010).

In this thesis, to perform THM calculations, the vertical scheme is approximated with a 2D axisymmetric and also 3D domain. The deposition hole, where the metal canister containing the spent nuclear fuel is emplaced, has the domain divided in the canister itself, the buffer blocks, the air gap between the blocks and the canister and the pillow pellets filling the gaps between the blocks and the rock. The backfilled drift is considered with a domain divided into several subdomains in order to take into account not only the compacted blocks but also the presence of the granules at the bottom of the drift and rod pellets filling the gap between the blocks and the walls. Previous models (Toprak et al., 2013 and 2016) considered a homogenous backfill for the drift. Beside this, rod pellets, pillow pellets and granules are simulated using the Barcelona Expansive Model (BExM, Gens et al., 1992) while Friedland clay backfill blocks and MX-80 buffer blocks are simulated with the standard Barcelona Basic Model for unsaturated soils (BBM, Alonso et al., 1990). The two models are implemented in CODE_BRIGHT (Olivella et al., 1994, 1996) which is able to use materials with several constitutive models. In this work, simultaneous use of Linear Elasticity for rock, BBM and BExM are considered.

Sensitivity analyses on fracture properties, saline water, properties and initial conditions of materials, meshing methods and geometrical challenges are some of the important issues that have been taken into account in this thesis.

This thesis ends with a comparison of the results and a brief description of the forthcoming work.

Acknowledgements

I wish to thank, first and foremost, my Professor Sebastian Olivella and Dr. Xavier Pintado. This thesis would not have been possible without their guidance and persistent help.

Also, I would like to thank the Finnish companies of Posiva Oy and Saanio&Riekkola Oy (formerly B+TECH) for providing funding for the thesis.

In addition, thanks to Prof. Enrique Romero for help during the performance of the oedometer tests at the UPC laboratory and Femi Adesola and Noora Kanarva for helping during the tests carried out at the Saanio&Riekkola Oy laboratory.

I also would like to mention the collaboration with colleagues and professors at Department of Civil and Environmental Department and Escola de Camins at UPC.

I would like to thank my parents who have given me the opportunity of an education from the best institutions and support throughout my life.

Contents

1. INTRODUCTION

Many countries are planning to dispose of all or part of their spent nuclear fuel in facilities constructed in stable geological formations. It is internationally accepted that geological disposal is a safe solution for the long-term management of spent nuclear fuel. The development of a geological disposal facility on a specific site requires a systematic and integrated approach. The characteristics of the spent nuclear fuel to be emplaced, the engineered barriers and the host rock (the three together being called the 'geological disposal system') and the geological setting of the host rock must be taken into account in order to construct a geological disposal facility.

The current situation and progress of the main disposal facilities for spent nuclear fuel around the world can be summarized as follows:

- United States of America: Disposal facility was proposed. Host rock was salt (Yucca Mountain).
- Hungary: Disposal facility is proposed. Host rock is claystone.
- Finland: Approved of disposal facility construction license. It is under construction. Host rock is crystalline rock (metamorphic rock) in Olkiluoto.
- Canada: License applications have been submitted for disposal facility construction. Host rock is limestone overlain by clay.
- Sweden: License applications have been submitted for disposal facility construction. Host rock is crystalline rock (metamorphic rock) in Forsmark.
- Germany: Selected host rock is limestone.
- France: Selected host rock is clay (Callovo-Oxfordian).
- Switzerland: Selected host rock is clay (Opalinus clay).
- Belgium: Selected host rock is clay (Boom clay or Ypresian clays).

This thesis is devoted to the project in Finland. The Government of Finland were the first to approve construction of a disposal facility in the world. Therefore, Finland now leads the world in spent nuclear fuel storage. A brief summary and background of the Finnish project, the subject of the thesis is given in the next Chapter.

1.1 Project

Posiva Oy has been preparing a project for final disposal of spent nuclear fuel in crystalline bedrock. Preparations for spent nuclear fuel management were already started in the 1970s, when the first power plants were still under construction. The site for the repository has been chosen on the basis of site investigations. In 1999, preliminary investigations were finished for four sites. Olkiluoto island in Eurajoki municipality, close to the Olkiluoto nuclear power plant, was proposed as the primary site for the repository.

Olkiluoto is an island (about 10 km^2) in the Baltic Sea coast and separated from the mainland by a narrow strait. There is a nuclear power plant with two reactors in operation and a third one under construction and a forth in planning stage as well VLJ repository for low and intermediate spent fuel is located in the western part of island. The final repository for the spent nuclear fuel is under construction and located in the central and eastern part of the island. The project name for the final repository is ONKALO that is an acronym based on the Finnish language expression for Olkiluoto Rock Characterization for the Final Disposal. The word “Onkalo” also means cave in Finnish.

The final repository is planned to be consisted of a system of exploratory tunnels that can extend to a depth of 460 m. The infrastructure of the site is almost completed. The concrete walls of the tunnel entrance, the washing hall, the fuel distribution station and the asphalting of the machine field and roads are completed. The site office has been built, the site perimeter has been fenced and site surveillance has been organized (Posiva, 2012)

The repository will consist of a series of deposition holes in the bedrock. In order to protect and insulate the disposed materials, compacted blocks and pellets manufactured with MX-80 bentonite (Kiviranta et al., 2016 and Karnland et al., 2006 among others) will be used as buffer material (Juvankoski et al., 2012). Friedland clay is considered one of the candidate porous materials to be used as drift backfill material to meet the long-term performance requirements set for backfilling of a disposal tunnel in the repository (Keto et al., 2013 and Börgesson et al., 2014). *Figure 1-1* shows site location (A), schematic description of project (B and C) interim storage in water pools (D) (a few years after removal from the reactor, spent fuel is transferred to interim storage. In there, it is stored in water pools) and finally, the schedule for project (E). The final disposal is scheduled to start in 2020's.

Excavation of tunnels is under progress. It is planned that in one panel, there will be 30 tunnel pairs and each tunnel pair, 50 canisters. Totally, there will be 1500 canisters. Disposing rate is 45 canisters per year. It takes 34 years to dispose all the canisters to one panel.

Totally, there will be 4500 canisters including the estimated spent nuclear fuel from the fourth reactor in Olkiluoto which has not been decided yet (Posiva, 2012).

There are two alternative disposal conditions of the spent fuel. The first alternative envisages the vertical emplacement of the canisters in vertical boreholes excavated in horizontal tunnels (KBS-3V disposal method). The second alternative envisages that the canisters will be disposed horizontally in the horizontal tunnels (KBS-3H alternative). In this thesis, KBS-3V concept is considered and the considered in license application. The KBS-3H is considered just as an alternative to KBS-3V.

Preliminary studies have been carried out based on the KBS-3V disposal method (Pintado and Rautioaho, 2013; Toprak et al., 2013 and Åkesson, et al., 2010 among others).

In some studies, dealing with the behaviour of a spent nuclear fuel repository, the aim is to understand full-scale in situ tests. Full-scale tests have been performed in the last decades for improving the knowledge of the thermo-hydro-mechanical processes which will take place in spent nuclear fuel repositories. Tests performed in Äspö HRL related with KBS-3 design are Canister Retrieval Test (Kristensson and Börgesson, 2015; Zandarín, et al., 2011), where a single canister was emplaced, and Prototype Repository Test (Johannesson et al., 2006; Chen et al., 2009), where six canisters were emplaced in six deposition holes. Backfill tunnel was also tested. In KBS-3H alternative, the MPT test has been performed in isothermal conditions (Pintado et al., 2017). Other “in situ” tests performed in Äspö HRL related with buffer behaviour assessment are TBT (Åkesson et al., 2009; Åkesson, 2010) and BRIE (Fransson, et al., 2011) among others. Another full-scale test is FEBEX (Enresa. 2000, 2006; Gens et al., 2009), where the Spanish concept was tested in Grimsel Test Site laboratory (GTS). This concept is similar to KBS-3H due to the canisters are emplaced in horizontal position. The Swiss concept has also been tested in Mont Terri laboratory (Bossart et al., 2017). In this concept, the canisters are also emplaced in horizontal position although surrounded partially with bentonite blocks and partially with pellets and host rock is a shale and not a crystalline rock like in KBS-3 concept. Finally, it is important to mention that the “in situ” tests are not reduced to test full-scale concepts, it is also possible to test in bench-scale (HE-E test, Bossart et al., 2017) or testing special phenomena, like the ones related with the operational period (drying the tunnel drift, Mayor, et al., 2007) or the gas generation due to corrosion (Olivella and Alonso, 2008). CODE_BRIGHT has been designed,

developed and used to model the disposal scenarios (Olivella, et al., 1994, 1996 and 2000), among other engineering problems like CO_2 storage (Vilarrasa, et al., 2013) or earth dams design (Pinyol, et al., 2008).

This thesis contains a work performed by CIMNE under the supervision of Saanio & Riekkola Oy in order to study the thermo-hydro-mechanical (THM) behaviour in a spent nuclear fuel repository. The disposal scheme is based on a crystalline host rock containing a clay buffer and a backfill among other elements. The time scale starts at the emplacement of the canisters till the performance target state is achieved following the KBS-3V disposal method for the buffer (Juvankoski et al., 2012) and for the backfill (Keto et al., 2013).

This thesis presents a wide range of possible combinations. It supports the task of defining the essential steps involved in designing a clay barrier that will safely isolate the canisters containing the spent fuel elements. Both boundary and initial conditions as well as the repository geometry must be established before modelling can proceed. The concept for storage adopted in this thesis is based on vertical boreholes excavated from horizontal tunnels and the reference geometry selected is that of the Olkiluoto 1 and 2 canisters (OL-1 and OL-2 in the KBS-3V disposal method, BWR canisters, (Raiko, et al., 2012). Thermal analyses for the entire repository were carried out using an analytical solution (Ikonen, 2003, Ikonen and Raiko, 2012 and Raiko, 2013) and were then used for defining the boundary conditions of the geometries analysed in this thesis. Version 7 of the FE (Finite Element)-solver CODE_BRIGHT, was used for the thermo-hydraulic (TH) and thermo-hydro-mechanical (THM) calculations.

As indicated, the concept for storage considered in this thesis is based on parallel vertical deposition holes excavated in horizontal tunnels (KBS-3V concept, see ***Figure 1-2*** for the deposition holes 1-2 from Loviisa (LO 1-2) and deposition holes 1-2 and 3 from Olkiluoto (OL 1-2 and OL 3, Saanio et al., 2012).

A gap between the canister and the ring blocks is considered to be 10 mm thick and the gap between the blocks and the rock is considered to be 50 mm thick (Juvankoski et al., 2012).

The buffer material will surround the canister placed in each deposition hole. The buffer is going to be fabricated with MX-80 bentonite. Bentonite disk blocks will be emplaced both on top and under the canister. The canister will be surrounded by the so called ring blocks. The gap between the bentonite blocks (rings and disks) and the host rock will be filled with MX-80 pillow pellets. More details about the buffer design can be found in Juvankoski et al., 2012. According to the current reference design, a 10 mm air-filled gap exists between the canister and the buffer rings.

Filling this thin gap with other materials is not possible. The hydro-mechanical behaviour of the bentonite buffer is of great importance. In fact, the closure of the gap is controlled by the swelling strains developed as the bentonite buffer saturates. The THM behaviour of MX-80 bentonite has been extensively investigated (Kiviranta et al., 2016; Pintado, et al., 2013a; Karnland, et al., 2006; Tang, et al., 2005 and Villar, 2005 among others).

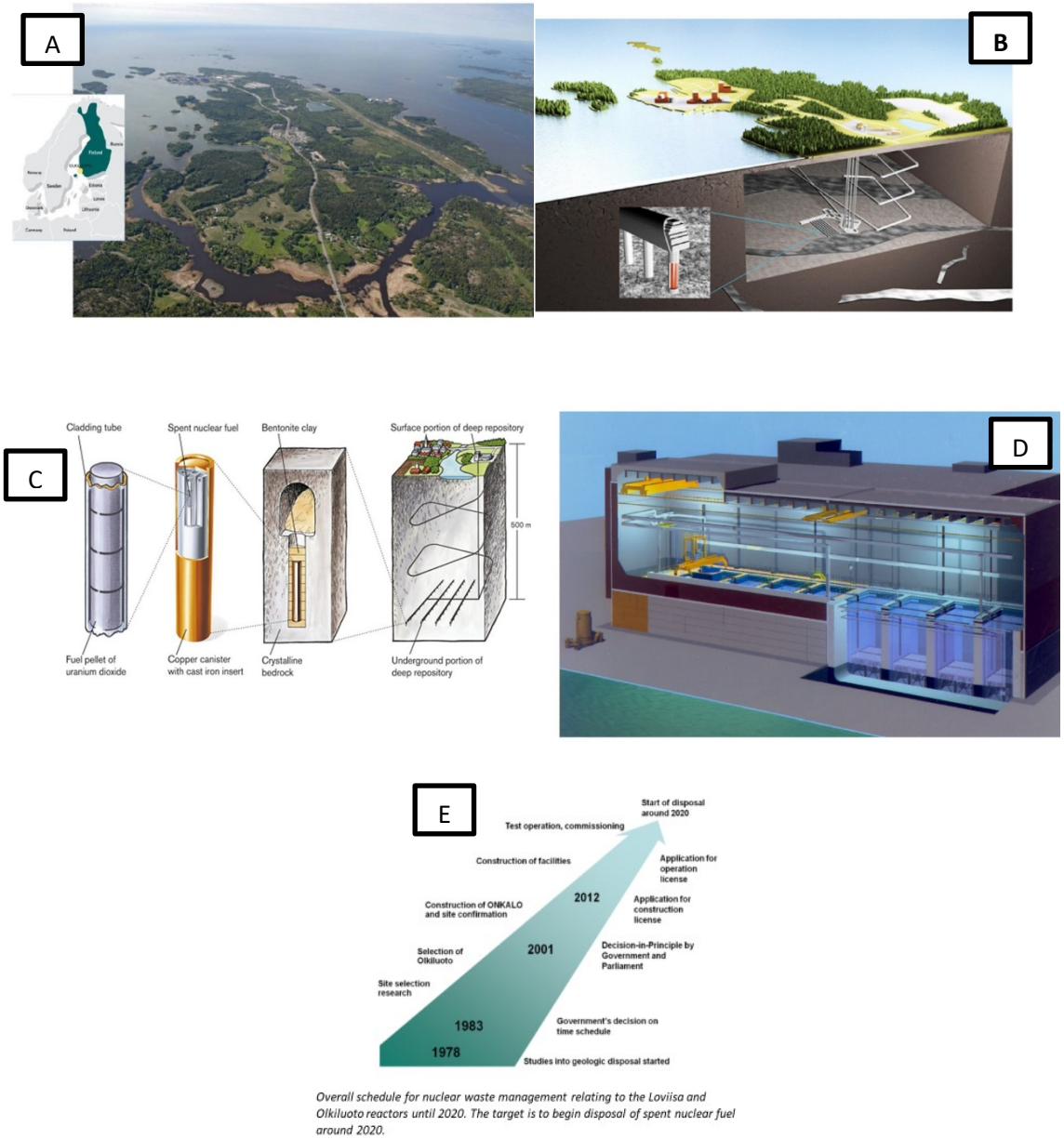

Figure 1-1. Site location (A), schematic description of project (B and C) *interim storage in water pools (D), schedule for project (E). (Posiva, 2012).*

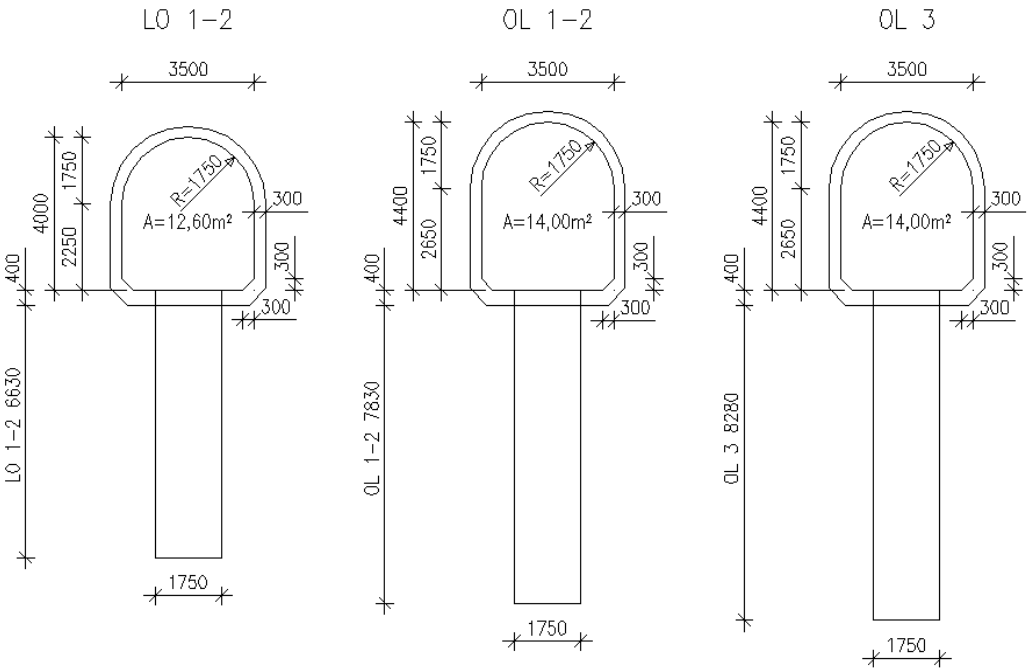

Figure 1-2. *Loviisa 1 and 2, Olkiluoto 1 and 2 and Olkiluoto 3 tunnel and deposition hole geometries. Dimensions in mm (Saanio et al., 2012).*

While an axisymmetric configuration (used here for the 2D sensitivity study) is very adequate for the representation and modelling of the borehole, it is less adequate to reproduce properly the backfilled drift. Therefore, a 3D geometry has also been considered.

1.2 Goals and objectives of the thesis

The construction, operation and emplacement of spent nuclear fuel in the repository will induce complex coupled thermo-hydro-mechanical processes within and around these repositories. All these THM processes are strongly coupled, interacting with each other in a complex manner in a spent nuclear fuel disposal system. In addition to in-situ and laboratory tests, numerical modelling is required to learn and understand more about such complex processes under long term conditions.

The main objective of the thesis is to obtain a better understanding of the thermo-hydro-mechanical processes and material properties that affect how the components of the spent nuclear fuel disposal system (buffer blocks, backfill blocks, pellets, rock, gaps and canister) behave during and after the installation in the repository.

Development, calibration and validation of numerical models (2D and 3D) and also laboratory tests to provide maximum reliability regarding the numerical responses of the repository is another important objective of the thesis.

This thesis aims to support the task of defining the essential steps involved in designing clay barriers (backfill and buffer) that will safely and securely isolate the canisters containing spent fuel elements.

The choice of material choice for the backfill and buffer is a fundamental task. Several clays are candidates for the backfill and buffer materials. There are many very well qualified sources of information regarding the thermo-hydro-mechanical properties of the reference buffer material MX-80 (see Åkesson et al., 2010, Pintado and Rautioaho, 2013, Toprak et al., 2013). However, there is a lack of information regarding the new reference material for the Friedland-Clay backfill. Laboratory and field tests are underway to decide the most efficient clays to be used as backfill material. The characterization of Friedland clay together with granules and pellet-based materials (rod and pillow) has been performed in this thesis. This thesis aims to demonstrate the performance of various clays over the long term that will be used as buffer or backfill. It will also help to select appropriate clays as backfill material (a mix of clay and pellets) by taking into account safety requirements.

Comparison of the experimental and modelling results for all components of the radioactive spent fuel disposal system to give support for the interpretation of the tests and modelling the THM response of the system by taking into account safety functions are considered as the objectives of the thesis.

1.3 Outline of thesis

Chapter 1: General information about the spent nuclear fuel repository concept. Background of the Finnish project “Onkalo”, site description, previous studies of characterization of materials and modelling work. Aim of the thesis.

Chapter 2: Explanation of thermo-hydro-mechanical processes in EBS (engineered barrier systems). General information about THM processes occurring in nuclear fuel repository.

Chapter 3: Theoretical basis and equations used to simulate THM processes. General information about mechanical models, for example, BBM Barcelona Basic Model (BBM) which is used to simulate MX-80 and Friedland Clay. Barcelona Expansive Model (BExM) is considered for pellet based materials (rod and pillow) and also granules. Elastic model for rock and canister; and bi-elastic model for gap element with two branches for considering the gap open and closed. Analysis of water retention curve depending on porosity and also the analysis of the water retention curve used for calcium-bentonite (FEBEX bentonite). Intrinsic permeability depending on porosity. Thermal conductivity depending on degree of saturation. Radiation effect on thermal analysis. Canister power decay calculations.

Chapter 4: Description of materials, laboratory test program and calibration of THM parameters for materials by means of conducted laboratory tests. There are five materials to characterize: MX-80, Friedland clay, pillow pellets, rod pellets and granules. Five different types of tests have been considered for the characterization of materials: water retention curve test, thermal conductivity test, infiltration test, oedometer test and tortuosity tests. For each material, the numerical simulation of the oedometer and infiltration tests is given.

Chapter 5: After the material characterization, 2D-sensitivity analysis is explained in this Chapter. This sensitivity analysis has been performed in accordance with the safety requirements of the project. Fracture position and permeability, groundwater salinity, initial conditions (water content), properties of materials (permeability, density, thermal expansion coefficient, thermal conductivity and porosity), filling material (slurry, water, pillow pellet or MX-80), geometrical issues (thickness of pillow pellets, bigger backfill tunnel and bigger volume of pillow pellets), and buffer material (sodium bentonite MX-80 or calcium bentonite FEBEX) are the main concepts for sensitivity analysis.

Chapter 6: Following the 2D-sensitivity analysis, a 3D domain is considered to validate the 2D calculations. A comparative study is given in this Chapter to check the effect of gas pressure over model results.

Chapter 7: A brief explanation of thesis, achieved objectives, methodology, limitations and results are discussed.

1.4 Methodology of the thesis

The thesis has been developed following a laboratory test program and data taken from the project site. To determine the THM parameters for each material, there has been considerable collaboration with the Saanio&Riekkola Oy laboratory.

Every new challenge emerging during the thesis, for example gap issues, salinity, double structure of pellets, 3D geometry or fractures in rock, has been handled as a continuous work which permits further advance. Most importantly, this thesis is a progressive study combining laboratory tests and modelling tasks.

1.5 Research dissemination

Journal Papers

Toprak E., Olivella S., Pintado X., (2016) Coupled THM modelling of engineered barriers for the final disposal of spent nuclear fuel isolation, Radioactive Waste Confinement: Clays in Natural and Engineered Barriers. Geological Society, London, Special Publications, 443, Published by The Geological Society of London. RWCClay-1558R1

Toprak E., Olivella S., Pintado X., (2018) Modelling Engineered Barriers for Spent Nuclear Fuel Repository using a Double Structure Approach for Pellet based Components. Environmental Geotecnics ENVGEO-D-17-00086 (accepted for publication)

Reports

Toprak E., Mokni N., Olivella S., Pintado X. (2013). Thermo-Hydro-Mechanical Modelling of Buffer. Synthesis Report, POSIVA 2012-47 (ISBN 987-951-652-229-9)

Toprak E., X. Pintado (2013). Modelling of Big Bertha test. B+TECH (Interim Posiva report)

Toprak E., Olivella S., Pintado X (2015). THM response of vertical schemes of radioactive waste disposal for various rock permeability conditions (Interim Posiva report)

Toprak E., Olivella S., Pintado X, (2016). Effect of air component on THM calculations for KBS-3V (Interim Posiva report)

Toprak E., Olivella S., Pintado X., (2017). KBS-3V Thermo-Hydro-Mechanical Sensitivity Analyses (Posiva working report – accepted for publication)

Conference abstracts and proceedings

Toprak E., Olivella S., X. Pintado (2015). THM response of vertical schemes of radioactive spent fuel disposal. 6th International Conference on Clays in Natural and Engineered Barriers for

Radioactive Waste Confinement. Brussels, Belgium.

Toprak E., Olivella S., X. Pintado (2015). Coupled THM modelling of Engineered Barriers for Waste Isolation. VI International Conference on Coupled Problems in Science and Engineering. Venice, Italy.

Toprak E., Olivella S., X. Pintado (2015). THM Modelling of Onkalo Project. SEG2015 Barcelona, Spain.

Toprak E., Olivella S., X. Pintado (2017). 2D sensitivity analysis for the final disposal of spent nuclear fuel isolation. 7th International Conference on Clays in Natural and Engineered Barriers for Radioactive Waste Confinement Davos, Switzerland. P143-P146.

Toprak E., Olivella S, X. Pintado (2017). Coupled THM modelling of engineered barriers for the final disposal of spent nuclear fuel isolation. V International Conference on Coupled Problems in Science and Engineering. Crete, Greece.

Workshops proceedings

Toprak E., Olivella S., X. Pintado (2013). THM modelling of final disposal repository including gap element. 5th Workshop of CODE_BRIGHT USERS. Barcelona, Spain.

Toprak E., Olivella S., X. Pintado (2014). THM modelling of final disposal repository in Onkalo project. 6th Workshop of CODE_BRIGHT USERS. Barcelona, Spain.

Toprak E., Olivella S., X. Pintado (2015). Long term response of multi-barrier schemes for underground radioactive waste disposal. 7th Workshop of CODE_BRIGHT USERS. Barcelona, Spain.

Toprak E., Olivella S., X. Pintado (2016). THM modelling of engineered barriers for spent fuel isolation. 8th Workshop of CODE_BRIGHT USERS. Barcelona, Spain.

Toprak E., Olivella S., X. Pintado (2017). Sensitivity study for a scheme of the disposal of spent nuclear fuel isolation 9th Workshop of CODE_BRIGHT USERS. Barcelona, Spain.

Training and seminars

The annual B+Tech – Clay Tech seminar (2013). Oral presentation. Modelling of Big Bertha Test (free swelling of bentonite and gap issues). Helsinki, Finland.

Training in B+Tech, (2016). Training in the B+Tech laboratory. Conducting water retention curve and infiltration tests. Three months of stay in Helsinki, Finland.

The annual B+Tech – Clay Tech summer seminar (2016). Oral presentation. THM modelling of pellets. Helsinki, Finland.

Onkalo work trip and seminar in Posiva Oy (2017). Oral Presentation. 2D sensitivity analysis for Onkalo project. Onkalo, Finland.

Training in B+Tech, (2017). Collaboration with scientist from B+Tech for 2D sensitivity analysis report. A month stay in Helsinki, Finland.

2 THM PROCESS DESCRIPTION

Numerical methods allow to simulate, to analyse and to understand the different coupled phenomena that take place in geo-materials. A spent nuclear fuel repository undergoes phenomena and processes that can be summarized as non-isothermal multiphase flow through deformable porous media. The multiphase flow includes heat transport, flows of vapour and water in liquid phase, dry air in gas phase and dissolved in liquid and, finally, the stresses and strains development as result of the multiphase flow. An assumption that allows to reduce the number of equations to be solved is that gas pressure remains constant and equal to the atmospheric pressure.

The functionality of the KBS-3 repository concept depends on the swelling and sealing capacity of the bentonite clay when it is emplaced in a host rock that provides water. When the bentonite clay buffer, with its main component being montmorillonite mineral, is subjected to wetting, water will be transported into the layered mineral structure. The water intake by the layered mineral structure is due to hydration and osmosis in the same way as this mechanism governs transport of water in a salt solution (e.g. see Norrish et al., 1954; Fritz 1986; Farnland et al., 2006 and Börgesson et al., 2014). The distance between the mineral layers will thereby increase and this results in a swelling of the clay structure. When the expansive material is confined, it cannot increase its volume and consequently pressure develops. If not new material constituents are introduced and considering simple load-paths, the hydraulic tightness and pressure at full saturation mainly depend on the mass of the montmorillonite per unit of material volume (i.e. more or less dry density). The concept is equally safe or even safer when in dry conditions since water is the main transport media for radionuclides from the canister to biosphere and for constituents modifying the system properties (like clay swelling pressure, clay's hydraulic conductivity and reducing canister thickness by copper corrosion).

2.1 Thermal process

As a general statement, it can be said that the magnitude of applied heating power will govern the level of temperatures in the repository. In the present analyses, however, this is a given input that will not be altered for the study (Chapter 3.4, thermal analysis).

The thermal problem may be considered as being determined by processes acting on a global and local scale. As for the global scale, the tunnel wall temperature for a certain deposition hole will be controlled by the position within the repository. The local scale processes determine the temperature difference between the deposition hole wall and points within the buffer. At the

local scale, the state of the inner gap (i.e. open/closed gap and degree of saturation) and the buffer adjacent to the canister (i.e. dry or fully saturated, contracted or swollen) is expected to be an important factor controlling the maximum temperature of the buffer and canister.

Heat transport takes place mainly by conduction. Heat dispersion is considered negligible as the fluid fluxes are small due to the low hydraulic conductivity of all the elements. The advective/convective heat transport is relatively low because the amount of mass moving through the buffer and rock is small (their hydraulic conductivities are quite low). The radiation heat transport is limited only to the gap between the canister and ring blocks and is active only during the time that the gap remains open (Chapter 3.3.).

An important process under thermal point of view is the inner gap closure. When the inner gap is open and dry, it has the maximum insulation capacity and therefore, the canister will increase its temperature as compared with other situations. Buffer temperature in contact with canister is higher when the gap is open than if it is closed because its thermal conductivity is lower when the gap is open than when the gap is closed. Closure of the gap is relatively fast (a few years) if the host rock supplies enough water. If the gap closes before the temperature in canister reaches the maximum, then two maximums in temperature can occur. The first one is caused by the closure and saturation of the gap, temperature increases somewhat more than in case of no gap (canister and buffer are in contact) and temperature drops due to thermal conductivity increase and the gap saturates and closes. A second maximum is due to the canister power decay.

Backfill temperature variations are moderate as compared with the ones taking place in the buffer. The maximum temperature expected in backfill is in the range of 50^{o}C. The mass of backfill is small compared with the rock mass, so the heat capacity and thermal conductivity of rock will be more important in heat dissipation than the backfill thermal properties.

2.2 Hydraulic process

During the early evolution of the repository, the hydraulic gradients induced by the open excavations and the thermal gradients due to the spent fuel heat decay are the main drivers for the transient flow and deformation phenomena. A few thousand years after the beginning of repository operations, anthropogenic gradients will disappear but not the natural ones. Geothermal gradients will remain as well as regional hydraulic gradients due to surface topography and hydrogeological zones. Natural gradients drive changes, albeit slow, thereafter.

The entire repository is expected to become fully saturated, although parts of it may reach saturation earlier, depending on the local conditions.

After the emplacement of the canister and buffer, water will flow through the rock to the pellet layer emplaced between buffer disks and rings and the host rock. The hydraulic conductivity of this material is quite large due to its open structure with large voids (Hoffmann, 2005; Hoffmann et al., 2007 and Kiviranta et al., 2016). The voids between pellets reduce quite quickly if there is enough water flowing from the rock to the deposition hole but the hydraulic conductivity of the pellets is still high compared to the hydraulic conductivity of blocks due their lower density. The inflows from the rock to the deposition holes are expected to be quite low and it is expected that the water inflows will be distributed in all surface of the deposition holes (Hjerne et al., 2016 and Pekkanen, 2016) without concentrated inflows in fractures. The deposition holes intersecting fractures with inflows larger than 0.1 L/min are not allowed according to design requirements (Posiva, 2012). This is an important issue and not all evidences show that the flow will be concentric and the deposition hole will be saturated in homogeneous way. Canister retrieval test (Kristensson et al., 2015) showed uniform saturation process due to artificial wetting but in Prototype repository (Olsson et al., 2013), the saturation process was not uniform, so in some cases, the saturation process could not be so uniform (Villar et al., 2007).

The buffer component in contact with the rock is a layer of pellets with 50 mm thickness (Juvankoski et al., 2012). The saturation process is strongly dependent on the amount of water flowing from the rock as it has been observed in pellet box tests, down-scaled tests (Pintado et al., 2013 and Pintado and Adesola, *publication pending*). Börgesson et al., 2015 have presented another interesting report about the early saturation process, where the water inflow and early water uptake in deposition holes are also analysed.

The wetting process of pellet layer and how the water is flowing from the rock to the buffer is an important issue which could have influence in the final state of the buffer after the hydration. If the saturation process is due to a few inflow points that supply water to the pellets and the inflows are low (less than 0.1 - 0.01 mL/min), the pellets could have a non-homogeneous saturation process and this will influence the saturation process of the blocks.

Different studies have been done in order to check the artificial wetting option (Marjavaara et al., 2011 and Holt et al., 2014). Artificial wetting or relatively large inflow rates from the rock will tend to fill large pores between pellets in a few hours. Pellet based materials are simulated with the BExM (Gens et al., 1992), which takes into account the presence of micro and macro

structure. The macro porosity does not necessarily correspond to the void space remaining between pellets.

It is assumed that there are no large voids due to the installation process, in other words, it is assumed that these will be occupied by expanded material during swelling. A few studies concerning the closure of these macro voids are available (Hoffmann, 2005 and Hoffmann et al., 2007). Other modelling works in bentonites under moist and erosion have been published using the BExM implemented in COMSOL Multiphysics (Navarro et al., 2014a) considering the free swelling of the bentonite (Navarro, et al., 2014b). The more detailed structure of pellets, with three levels of porosity is not taken into account in the current framework of the BExM (see e.g. Lloret et al., 2003 and Sánchez et al., 2005 among others).

There will also be water flow through the buffer from the canister outwards due to vapour flow which will produce an initial drying of the buffer close to the canister. The bentonite will also shrink due to this drying process and its hydraulic and thermal properties will change. This effect has been identified in laboratory tests (Pintado et al., 2002) and at in situ tests corresponding for instance to FEBEX project (Gens et al., 2009), in Prototype Repository test (Chen et al., 2009) and in Canister Retrieval Test (Kristensson et al., 2015). After a few years and, although the canister is still hot, the dried bentonite starts to hydrate back due to the dominant water flow from the rock (rates depend on rock hydraulic conductivity).

At the same time, water will flow to the backfill. The restrictions imposed to the inflows from the fractures intersecting the backfill are not as strong as the imposed restrictions in the case of deposition holes. Actually, backfilled drift can withstand localized flows up 0.1-0.5 L/min. Fractures with inflows larger than these values should be sealed according to the requirements (Posiva, 2012). The current backfill design has a bottom layer in contact with the buffer. The gap between the rock and the tunnel walls and roof will be filled with rod pellets (Keto et al., 2013). This means that the deposition tunnels will be backfilled with materials with relatively high hydraulic conductivity in contact with the rock, so the water can also reach the deposition holes through the backfill in sections intersected with fractures where high inflows appear through fractures with high transmissivity embedded in low hydraulic conductivity rock. The axisymmetric model does not allow to simulate fractures intersecting the backfill unless they are orthogonal to axisymmetric axis.

The models presented in this thesis only consider a fracture that intersects the deposition hole. The calculations are mainly done just for one deposition hole in 2-D with axisymmetric and a few models are done in 3-D but only with one deposition hole. The THM modelling of more than

one deposition hole and the backfill tunnel intersected by some fractures is defined as future work. These geometries (i.e. several deposition holes from a drift intersected by fractures) where modelled under thermo-hydraulic conditions by Pintado and Rautioaho, 2013.

2.3 Mechanical process

The changes in buffer components, once they are emplaced at the deposition holes, are due to the heat flow from the canister and the water flowing from the host rock. The heat flow will dry the bentonite and reduce its volume due to the drying induces shrinkage (inverse of swelling). This will affect the ring blocks and the disk blocks on top and at the bottom of the canister. It is a local effect and its effect finishes after a few years (if the host rock supplies enough water). The gap between canister and ring blocks will tend to close in a few years and the radial stress is expected to increase.

The water will flow from the host rock to the pellets first and from the pellets to the blocks and the clay minerals will hydrate and swell. This process in compacted bentonite such as MX-80 is well known and there is quite a lot of information available about it (see e.g. Karnland et al., 2006; Villar, 2005; Kiviranta et al., 2016; Sun, 2016 and Kiviranta and Kumpulainen, 2011 among others). There is also information about other clays which could be used as buffer materials, for instance FEBEX bentonite, the buffer material candidate for the Spanish design (Villar, 2002) or for Kunigel and Foca7 clays, from Japan and France, respectively (Delage et al., 2010).

The hydration and swelling process in pellets is a complex and probably not well-known understood yet. Only some works aforementioned before (Hoffmann, 2005 and Hoffmann et al., 2007) were found for studying the pellets behaviour during the hydration. If there is enough water, the large voids will reduce as the expansion of pellets takes place.

The difference in initial dry densities between pellets and blocks is large (1700 and 1752 kg/m^3 for discs and blocks and 919 kg/m^3 for pellets (Juvankoski et al., 2012). This means that pellets and blocks will undergo quite different swelling pressure and stiffness. In principle, it is expected that the blocks will expand and compress the pellets, so the density in blocks will decrease and the density in pellets will increase. This imply a tendency to evolve towards a more uniform distribution of densities.

There are some laboratory tests which investigate this process as reported in Dueck et al., 2016. It seems that the densities were not completely homogenised along the samples.

On the other hand, due to the different properties of buffer installed in the borehole and backfill installed in the drift, the contact surface between both components will not remain immobile during the saturation process.

It is expected that the buffer with a higher swelling capacity than the backfill. Therefore, buffer will tend to penetrate inside the backfill. Although some numerical analyses have been done (Leoni, 2013), there are still some uncertainties about this question. An in situ test was carried out in Äspö (ÅSKAR test by Sandén et al., 2016 modelled by Leoni, et al., 2015) and a specific mock-up test was done in VTT (BBI test, Rinta-Hiiro et al., 2017).

The interface shear behaviour of tunnel backfill materials has also been studied (Sinnathamby et al., 2014) but more information is needed for the proper understanding of this interaction. The density of the buffer should be between 1950 and 2050 kg/m^3 in saturated conditions (Juvankoski et al., 2012) and the penetration of the buffer inside the backfill should be limited.

3 THEORETICAL BASIS

The fundamental theoretical basis for this work comes from Olivella et al (1994, 1996). The description presented here of the thermal and hydraulic theory is a brief and less general version of what is given in Alcoverro and Alonso (2001).

The current simulations use a constant gas pore pressure (p_g = 0.1 MPa) and an assumption that air is not allowed to be dissolved into the liquid phase. Therefore, it is not necessary to solve the air balance equation. However, in Chapter 6 there is a 3D THM model that takes into account air in the gas phase air dissolved into the liquid phase. Air balance equations are given separately in Chapter 6.

The following notation will be used in writing balance equations:

ϕ: porosity
ρ: density
$\mathbf{j}$: total mass flux
$\mathbf{i}$: non-advective mass flux
$\mathbf{q}$: advective flux
$\mathbf{u}$: solid displacements
$\boldsymbol{\sigma}$: stress tensor
$\mathbf{b}$: body forces,
ω: mass fraction,
e: specific internal energy
$\mathbf{i}_c$: conductive heat flux
$\mathbf{j}_E$: energy fluxes due to mass motion
S_l, S_g: degree of saturation of liquid and gaseous phases i.e., fraction of pore volume occupied by each phase.
Superscripts w and a refer to water and air, respectively
Subscripts s, l and g refer to solid, liquid and gas phase, respectively.

The theory used in CODE_BRIGHT (DECA-UPC, 2017) is based on geomechanical porous media formulation, assuming that the material is a mixture of several components:

- minerals,
- liquid water,
- water vapour,
- dry air (if the air balance equation is solved),
- dissolved air (if the air balance equation is solved).

The constituents are divided in three *components* (i): minerals (m), water (w), and air (a) (the component is indicated by a superscript) and an assumption of three *phases* (α): solid (s), liquid (l), and gas (g) (the phase is indicated by a subscript) are made. The solid phase only consists of the mineral component, so the component superscript index (m) will not be written in the following. The water that remains in soil after drying at 110^{o}C following the ASTM D2216-10, could be considered part of the solid phase as it cannot be removed from it.

Here, for the mixture, the following basic variables can be defined:

- mixture volume element (v),
- solid phase volume (v_s),
- liquid phase volume (v_l),
- gas phase volume ($v_g = v - v_s - v_l$), and
- pore volume ($v_p = v - v_s$).

Further variables, regarding mass and energy are introduced for the constituents:

- solid mass (m_s),
- water mass in liquid (m_l^w),
- air mass dissolved in liquid (m_l^a), which is prescribed to zero in this work,
- water mass in gas (i.e. water vapour mass) (m_g^w),
- dry air mass in gas (m_g^a),
- specific internal energy for minerals in solid (e_s),
- specific internal energy for water in liquid (e_l^w),
- specific internal energy for air in liquid (e_l^a),
- specific internal energy for water in gas (e_g^w), and
- specific internal energy for air in gas (e_g^a).

With use of the definitions above, it is possible to formulate:

- porosity ($\phi = \frac{v_p}{v}$),
- solid density ($\rho_s = \frac{m_s}{v_s}$),
- liquid water mass per liquid phase volume ($\rho_l^w = \frac{m_l^w}{v_l}$),
- dissolved air mass per liquid phase volume ($\rho_l^a = \frac{m_l^a}{v_l}$), which becomes zero in this work,
- water vapour mass per gas phase volume ($\rho_g^w = \frac{m_g^w}{v_g}$),
- dry air mass per gas phase volume ($\rho_g^a = \frac{m_g^a}{v_g}$),
- liquid degree of saturation ($S_l = \frac{v_l}{v_p}$), and
- gas degree of saturation ($S_g = \frac{v_g}{v_p}$).

Below, when describing commonly used constitutive laws, functions that give values of variables are indicated with "~"above the variable name.

3.1 Balance relations

The solid mass per unit volume can be expressed as:

$$\frac{m_s}{v} = \frac{m_s}{v_s}\frac{v_s}{v} = \rho_s(1-\phi) \tag{3.1-1}$$

which is used in the balance equation:

$$\frac{\partial}{\partial t}\left(\rho_s(1-\phi)\right) + \nabla\cdot\left(\rho_s(1-\phi)\frac{d\mathbf{u}}{dt}\right) = 0 \tag{3.1-2}$$

If this equation is reorganized an equation for the porosity is obtained,

$$\frac{D\phi}{dt} = \rho_s(1-\phi)\frac{D\rho_s}{dt} + (1-\phi)\nabla\cdot\left(\frac{d\mathbf{u}}{dt}\right) = 0 \tag{3.1-3}$$

where $\frac{D(\ \ )}{dt} = \frac{\partial(\ \ )}{\partial t} + \frac{d\mathbf{u}}{dt}\cdot\nabla(\ \ )$ is the material derivative.

The water mass per unit volume of mixture can be expressed as,

$$\frac{m^w}{v} = m_l^w + m_g^w = \rho_l^w S_l\phi + \rho_g^w S_g\phi \tag{3.1-4}$$

If introducing a source term f^w and fluxes of water in the liquid and gas phase, $\mathbf{j}_l^w$ and $\mathbf{j}_g^w$, the mass conservation of water equation reads,

$$\frac{\partial}{\partial t}\left(\rho_l^w S_l\phi + \rho_g^w S_g\phi\right) + \nabla\cdot\left(\mathbf{j}_l^w + \mathbf{j}_g^w\right) = f^w \tag{3.1-5}$$

The balance of momentum for the porous media reads,

$$\nabla\cdot\boldsymbol{\sigma} + \mathbf{b} = \mathbf{0} \tag{3.1-6}$$

where the mechanical equilibrium condition has been used (inertia effects have been disregarded).

A continuity equation for energy can be formulated using the specific internal energies per volume element:

$$\sum e_p^e\frac{m_p^e}{v} = e_s\rho_s(1-\phi) + e_l^w\rho_l^w S_l\phi + e_l^a\rho_l^a S_l\phi + e_g^w\rho_g^w S_g\phi + e_g^a\rho_g S_g\phi \tag{3.1-7}$$

A source term, f^e, and fluxes $\left[\mathbf{h},\ e_l^w\mathbf{j}_l^w,\ e_l^a\mathbf{j}_l^a,\ e_g^w\mathbf{j}_g^w, e_g^a\mathbf{j}_g\right]$ will be considered for the energy conservation equation. The first element, **h**, in the given set of fluxes is the conductive heat flux of the mixture as a whole and the following energy fluxes are due to mass transport of the constituents with respect to the immobile solid (as here assumed). The obtained expression reads:

$$\frac{\partial}{\partial t}\left(e_s\rho_s(1-\phi) + e_l^w\rho_l^w S_l\phi + e_l^a\rho_l^a S_l\phi + e_g^w\rho_g^w S_g\phi + e_g^a\rho_g^a S_g\phi\right) + \tag{3.1-1}$$

$$+\nabla\cdot\left(\mathbf{h}+e_l^w\mathbf{j}_l^w+e_l^a\mathbf{j}_l^a+e_g^w\mathbf{j}_g^w+e_g^a\mathbf{j}_g^a\right)=f^e$$

To close the formulation, variables are selected as independent or dependent and material specific constitutive relations are specified where dependent variables are given by expressions of independent variables. The independent variables are T, p_l and **u**, the temperature, liquid pore pressure and displacement vector. The liquid pore pressure loses its ordinary physical meaning for the bentonite type of material and should for such materials only be considered an entity describing the material's water absorption potential.

3.2 Equilibrium restrictions

As a basic formulation is that all constituents have a common locally temperature, T. This comes from considering thermal equilibrium condition between phases.

For the present systems, accelerations are assumed insignificant. This mechanical equilibrium condition makes its appearance in the used quasi-static form of the balance of momentum.

The phase change equilibrium may be taken as manifested through the equality between chemical potentials of a constituent in different phases. Assuming phase change equilibrium for water and that the gas phase is a mixture of two ideal gases (air and water vapour) give the phase change equilibrium for water (Edelfsen et al., 1943),

$$\tilde{\rho}_g^w(p_l,T)=\frac{\tilde{p}_g^w(T)M_w}{R(273.15+T)}\exp\left(\frac{-(p_g-p_l)M_w}{R(273.15+T)\tilde{\rho}_l(p_l,T)}\right) \tag{3.2-1}$$

In the expression above, the physical parameters molar mass of water, M_w, and the constant of gases, R, appear.

For clarity, it could be mentioned that due to the assumption made regarding absence of air in the liquid phase, air conservation equation is not solved and gas pressure is considered constant, so Henry's law (Henry, 1803) the equilibrium restriction of phase change implemented in CODE_BRIGHT, is not considered in most of models presented in this work (air is only taken into account in a specific 3D calculations in Chapter 6).

3.3 Constitutive models

As mentioned, to close the formulation, variables are selected as independent or dependent. Material specific constitutive relations are designed to calculate dependent variables as a function of the independent variables. Independent variables are temperature, liquid pore

pressure and displacement vector. Below it follows a brief general overview of the constitutive relations needed for completion of the problem formulation.

a) Porous medium relations

These constitutive relations describe interactions between constituents in various phases.

The liquid degree of saturation (shortened to degree of saturation in the following) of the porous medium is related to the liquid pore pressure by use of a *retention law*, here exemplified by van Genuchten's retention law (van Genuchten, 1980):

$$\widetilde{S}_l(p_l) = \left(1 + \left(\frac{p_g - p_l}{P}\right)^{\frac{1}{1-\lambda}}\right)^{-\lambda} \tag{3.3-1}$$

with $P = P_0 \frac{\sigma}{\sigma_0}$, P_0 is the air entry value at certain temperature, σ_0 the water surface tension at that temperature and σ the surface tension as function of the temperature,

The parameters *P* and λ were measured for different porosities following the relations:

$$P_0(\phi) = P_0 \exp\big(a(\phi_0 - \phi)\big) \tag{3.3-2}$$

$$\lambda(\phi) = \lambda \exp\big(b(\phi_0 - \phi)\big) \tag{3.3-3}$$

These relations work well when the porosity does not change too much, so it is possible to use the same water retention curve for discs and rings and it is expected that the porosity changes will not be so large but for the pellets, with lower density and different structure, the relation is not valid and *P* and *l* parameters must be used without following the previous relations for such high porosity.

And an extended version of van Genuchten (Gens et al., 2009),

$$\widetilde{S'}_l(p_l) = \widetilde{S}_l(p_l)\widetilde{f}_d(p_l) \tag{3.3-4}$$

where,

$$\widetilde{f}_d(p_l) = \left(1 - \frac{p_g - p_l}{P_d}\right)^{\lambda_d} \tag{3.3-5}$$

The latter version, considered more capable of representing both wetting and extensive drying for bentonites (it was formulated for FEBEX bentonite) and is obtained by multiplying the original expression by a function f_d containing two additional parameters P_d and λ_d. For the reference case, the classical Van Genuchten equation has been used because the parameters

have a clearer physical meaning. The gas phase degree of saturation is given by $\widetilde{S_g}(p_l) = 1 - \widetilde{S_l}(p_l)$.

The mass fluxes are additively decomposed in terms of a non-advective (diffusive), $\mathbf{i}_\alpha^i$, and an advective, $\theta_\alpha{}^i\,\mathbf{q}_\alpha$, contribution, according to,

$$\mathbf{j}_\alpha^i = \mathbf{i}_\alpha^i + \rho_\alpha^i \mathbf{q}_\alpha\,, \qquad \alpha = l, g;\ i = w, a \tag{3.3-6}$$

The *advective* mass fluxes include the phase velocity, $\mathbf{q}_\alpha$, typically given by Darcy's law (Brown, 2002), which reads, for CODE_BRIGHT's formulation,

$$\mathbf{q}_l = -\frac{\mathbf{k} k_{rl}}{\mu_l}(\nabla p_l + \rho_l g \nabla z) \tag{3.3-7}$$

for the liquid and which for the gas phase becomes zero since the pressure is taken to be constant in the present work. Darcy's law is obtained from a combination of balance of momentum of the fluid phases together with constitutive assumptions of momentum exchange with other phases.

The relative permeability, k_{rl}, given by Gens et al., 2009; Åkesson et al., 2010 and Chen et al., 2009 is:

$$k_{rl} = A_l S_l^{\delta_l} \tag{3.3-8}$$

which is the relation presented by Brooks and Corey (1964). $\widetilde{S_l}(p_l) = S_l$

Diffusive (or non-advective) mass fluxes are usually described by Fick's law:

$$\begin{aligned} \mathbf{i}_g^w &= -\left(\tau\phi\rho_g S_g \mathbf{D}_m^w\right)\nabla\omega_g^w \\ \omega_g^w &= \frac{\rho_g^w}{\rho_g} \end{aligned} \tag{3.3-9}$$

for the water vapour and $\mathbf{i}_l^a = 0$ since in this study no air is dissolved in the liquid phase. Fick's law is obtained by consideration of: the constituent balance of momentum, the phase balance of momentum and the exchange of momentum with the other constituents. The diffusion coefficient, ($\mathbf{D}_m^w = \mathbf{I} D_m^w$) is given by:

$$\widetilde{D}_m^w(T) = \frac{D^w (273.15 + T)^n}{p_g} \tag{3.3-10}$$

The remaining diffusive (non-advective) mass fluxes are specified by the relations (for the case with air and vapour considered):

$$\sum_{i=w,a} \mathbf{i}_\alpha^i = \mathbf{0}, \quad \alpha = l, g \tag{3.3-11}$$

Additionally, hydro-dynamical dispersion can be considered as non-advective flow. Hydro-dynamical dispersion mass flux is computed by means Fick's law written as:

$$\mathbf{i}_\alpha^i = -(\rho_\alpha \mathbf{D}'_\alpha)\nabla\omega_\alpha^i \tag{3.3-12}$$

$$\mathbf{D}'_\alpha = d_t|\mathbf{q}_\alpha|\mathbf{I} + (d_l - d_t)\frac{\mathbf{q}_\alpha \mathbf{q}_\alpha^t}{|\mathbf{q}_\alpha|} \tag{3.3-13}$$

where d_l is longitudinal dispersivity and d_t is transversal dispersivity.

The *non-advective heat flux* is typically given by Fourier's law:

$$\mathbf{h} = -\lambda \boldsymbol{\nabla} T \tag{3.3-14}$$

where the thermal conductivity, λ, is often prescribed as a constant or dependent on water saturation. Some examples of expressions for the thermal conductivities are:

$$\tilde{\lambda}(S_l) = \lambda_{dry}(1 - f(S_l)) + \lambda_{sat} f(S_l), \tag{3.3-15}$$

where,

$$f(S_l) = S_l \text{ or } f(S_l) = \sin^2(S_l \pi/2), \tag{3.3-16}$$

(Chen, et al., 2009) and another example is (Villar, 2002)

$$\tilde{\lambda}(S_l) = \gamma_{dry}(1 - f(S_l)) + \gamma_{sat} f(S_l), \tag{3.3-17}$$

where

$$f(S_l) = A_{dry} + \frac{(A_{sat} - A_{dry})}{1 + \exp\left(\frac{S_l - S_l^*}{b}\right)} \tag{3.3-18}$$

S_l^* and b being parameters, and where A_{dry} and A_{sat} are given by solving,

$$\begin{bmatrix} \lambda_{dry} \\ \lambda_{sat} \end{bmatrix} = \begin{bmatrix} 1 - f(0) & f(0) \\ 1 - f(1) & f(1) \end{bmatrix} \begin{bmatrix} A_{dry} \\ A_{sat} \end{bmatrix}.$$

The radiation heat flow in gaps can be considered using the Fourier's law and a cubic polynomial thermal conductivity dependency of temperature if the difference between the temperatures in both faces of the gap is low (Ikonen and Raiko, 2015).

b) Solid phase relations

The *solid density* is given by

$$\tilde{\rho}_s(T) = \rho_{s0}\big(1 + \alpha_s(T - T_0)\big) \tag{3.3-19}$$

where α_s is the thermal expansion coefficient for solid and T_0 is a reference temperature are default values. The specific internal energy for the solid is given by $e_s = c_s T$. In a similar way, water and air energies are calculated. For the vapour, an additional term that corresponds to the evaporation latent heat is considered.

The mechanical constitutive relation for the soil skeleton is not explicitly given in terms of the solid phase stress. Instead, the mechanical relation incorporating the solid phase is formulated in terms of total stress, $\boldsymbol{\sigma}$, of the porous medium and the constitutive relations of the stress tensors of the fluid phases (pressures, p_α).

A rate form of the mechanical formulation for unsaturated conditions can be expressed, in a compact form, as:

$$\frac{d}{dt}(\boldsymbol{\sigma} - p_g \mathbf{I}) = \mathbf{D}\frac{d\boldsymbol{\varepsilon}}{dt} + \boldsymbol{\beta}\frac{dT}{dt} + \mathbf{h}\frac{d}{dt}(p_g - p_l) \tag{3.3-20}$$

where the following tensors need to be described:

$$\begin{aligned} \mathbf{D} &= \tilde{\mathbf{D}}(\boldsymbol{\sigma} - p_g \mathbf{I},\, p_g - p_l, T) \\ \boldsymbol{\beta} &= \tilde{\boldsymbol{\beta}}(\boldsymbol{\sigma} - p_g \mathbf{I},\, p_g - p_l, T) \\ \mathbf{h} &= \tilde{\mathbf{h}}(\boldsymbol{\sigma} - p_g \mathbf{I},\, p_g - p_l, T) \end{aligned} \tag{3.3-21}$$

The small strain tensor $\boldsymbol{\varepsilon}$ is given by the displacements according to,

$$\boldsymbol{\varepsilon} = -\frac{1}{2}\left(\frac{\partial \mathbf{u}}{\partial \mathbf{x}} + \left(\frac{\partial \mathbf{u}}{\partial \mathbf{x}}\right)^t\right) \tag{3.3-22}$$

With this definition, strains are positive in compression. It can be seen that the formulation for unsaturated states is given in terms of $\boldsymbol{\sigma}^* = \boldsymbol{\sigma} - p_g \mathbf{I}$ and$p_g - p_l$, usually denoted as net stress and suction, respectively. Note that the equation $\boldsymbol{\sigma}^* = \boldsymbol{\sigma} - p_g \mathbf{I}$ corresponds to stresses positive in compression. This is consistent with constitutive model equations.

When saturated states are considered, i.e. $p_g - p_l \leq 0$, the general mechanical formulation may be rewritten as,

$$\begin{aligned} &\frac{d}{dt}(\boldsymbol{\sigma} - p_l \mathbf{I}) = \mathbf{D}\frac{d\boldsymbol{\varepsilon}}{dt} + \boldsymbol{\beta}\frac{dT}{dt} \\ &\mathbf{D} = \tilde{\mathbf{D}}(\boldsymbol{\sigma} - p_l \mathbf{I}, T), \quad \boldsymbol{\beta} = \tilde{\boldsymbol{\beta}}(\boldsymbol{\sigma} - p_l \mathbf{I}, T) \end{aligned} \tag{3.3-23}$$

now given in terms of effective stress tensor.

A deviatoric stress tensor **s** can be defined as, $\mathbf{s} = \boldsymbol{\sigma} - p\mathbf{I}$**,** where *p* is the mean stress. The von Mises stress *q* can be expressed in terms of **s**. Often the *second invariant of the deviatoric stress tensor* $J_2 = \frac{1}{2}\mathbf{s}:\mathbf{s}$ is first introduced and then *q* is expressed as, $q = \sqrt{3J_2}$. A generalized effective stress tensor, applicable for unsaturated as well as saturated conditions, can be defined as $\sigma' = \sigma - \max(p_g, p_l)$ stresses are considered positive for compression as the BBM model uses this convention as logarithmic functions are used).

Finally, void ratio *e*, is a variable used in this thesis as some constitutive equations are expressed using this variable. It is defined by $e = v_p/v_s$ and can also be expressed in terms of the porosity$e = \frac{\phi}{1-\phi}$. Finally, dry density, ρ_d is also introduced as, $\rho_d = \frac{m_s}{v} = \frac{\rho_s}{1+e}$.

Mechanical bentonite material model for blocks

The Barcelona Basic Model (Alonso et al., 1990) has been used to model the thermo-hydro-mechanical (THM) behaviour of the buffer and backfill blocks. This model is implemented in CODE_BRIGHT (DECA-UPC, 2017) referred to as thermo-elasto-plastic (TEP) model. The model formulation has been described in this subsection.

The effective stress is defined as $\sigma' = \sigma - \max(p_g, p_l)$ (for positive compressions), which is a modification of the usual effective stress considered for saturated soils (Terzaghi, 1966). The effective mean stress *p'* or p_{eff} is defined as $p' = p - \max(P_g, P_l)$.The mechanical constitutive equation

$$d\boldsymbol{\sigma}' = \mathbf{D}d\boldsymbol{\varepsilon} + \mathbf{h}ds \tag{3.3-24}$$

is derived from $d\boldsymbol{\varepsilon} = d\boldsymbol{\varepsilon}^e + d\boldsymbol{\varepsilon}^p = (\mathbf{D}^e)^{-1}d\boldsymbol{\sigma}' + \alpha\mathbf{I}ds + \Lambda\frac{\partial G}{\partial \boldsymbol{\sigma}'}$ and the volumetric strain is defined as $\varepsilon_v = \varepsilon_x + \varepsilon_y + \varepsilon_z$.

Elastic, isotropic and non-isothermal volumetric strains are defined by:

$$d\varepsilon_v^e = \frac{k_i(s)}{1+e}\frac{dp'}{p'} + \frac{k_s(p',s)}{1+e}\frac{ds}{s+0.1} + (\alpha_o + 2\alpha_2\Delta T)dT \tag{3.3-25}$$

with parameter dependence on suction and stress as follows:

$$k_i(s) = k_{io}\left(1 + \alpha_i s\right) \tag{3.3-26}$$

$$k_s(p',s) = k_{so}\left(1 + \alpha_{sp}\ln p'/p_{ref}\right)\exp\left(\alpha_{ss}\, s\right) \tag{3.3-27}$$

where *e* is the void ratio, where p' is the mean effective stress, *s* is the suction, k_{io} and α_i are parameters for elastic volumetric compressibility against mean stress change, and k_{so}, α_{sp}, p_{ref} and α_{ss} are parameters for elastic volumetric compressibility against suction change. The parameters α_i, α_{sp} and α_{ss} do not belong to the original BBM model and were implemented later in order to be able to deal swelling clays with the BBM model. The model is quite sensitive to these parameters.

The elastic properties are defined using two constants κ and ν. The effective bulk modulus *K* depend on the mean effective stress p':

$$K = \frac{1+e}{\kappa} p' \tag{3.3-28}$$

The yield surface $F = F(\sigma', \varepsilon_v^p, s) = F(p', J, \theta, \varepsilon_v^p, s)$, where ε_v^p is the plastic volumetric strain, depends on stresses and suction and can be expressed using stress invariants:

Mean effective stress: $p' = \frac{1}{3}(\sigma'_x + \sigma'_x + \sigma'_x) = p - \max(P_g, P_l)$

Deviatoric stress: $J = \sqrt{\frac{1}{2}(\mathbf{s}:\mathbf{s})}$ $\mathbf{s} = \sigma' - p'\mathbf{I}$

Lode's Angle: $\theta = -\frac{1}{3}\sin^{-1}(1.5\sqrt{3}\det \mathbf{s}/J^3)$

For simplicity, a form of the classical Modified Cam-Clay model is taken as the reference isothermal saturated constitutive law, so the yield surface reads:

$$F = \frac{3J^2}{g_y^{\,2}} - L_y^{\,2}\left(p' + p_s\right)\left(p_o - p'\right) = 0 \tag{3.3-29}$$

where g_y is a function of the Lode angle and

$$L_y = M / g_y\Big|_{\theta=-\pi/6} \tag{3.3-30}$$

with *M* being a critical state line parameter, and p_o is considered to be dependent on suction:

$$p_o = p^c \left(\frac{p_o^*(T)}{p^c} \right)^{\frac{\lambda(o)-kio}{\lambda(s)-kio}} \tag{3.3-31}$$

$$p_o^*(T) = p_o^* + 2(\alpha_1 \Delta T + \alpha_3 \Delta T \left|\Delta T\right|)$$

$$\lambda(s) = \lambda(o)\left[(1-r)\exp\left(-\beta s\right) + r\right] \tag{3.3-32}$$

$$p_s = p_{s0} + ks\exp(-\rho \Delta T) \tag{3.3-33}$$

where p^c is the reference stress; p_o^* is the initial preconsolidation stress for saturated conditions; $\lambda(0)$ is the slope of void ratio in saturated conditions; r defines the maximum soil stiffness; β controls the rate of increase of soil stiffness with suction; α_1 and α_3 are parameters for elastic thermal strain, p_{s0} is the tensile strength in saturated conditions; k takes into account the increase of tensile strength due to suction; and ρ takes into account the decrease of tensile strength due to temperature.

Hardening depends on plastic volumetric strain according to:

$$dp_o^* = \frac{1+e}{\lambda(0)-k_{io}} p_o^* d\varepsilon_v^p \tag{3.3-34}$$

The plastic potential G is taken as

$$G = \alpha \frac{3J^2}{g_p^{\,2}} - L_p^2 \left(p' + p_s\right)\left(p_o - p'\right)$$
$$L_p = M / g_p\big|_{\theta=-\pi/6} \tag{3.3-35}$$

where g_p is a function of the Lode angle and α is a non-associativity parameter.

The BBM model was developed for studying unsaturated soils with moderate swelling capacity and is suitable for simulate swelling clays if several cycles of large swelling-shrinking are not expected.

Mechanical bentonite material model for pellets and granules

Since the original and important work of Collins et al. (1974, 1984) several researchers have observed the existence of two structural levels in compacted clays (Pusch, 1982; Romero et al., 1999; Pusch and Moreno , 2001; Lloret et al., 2003 and also Romero and Simms, 2008). Thus, the structure of the bentonites analysed. In this Section, it is idealized into two structural levels: macro and micro structures. The microstructural level is associated with both intersheet voids and intra-aggregate pores. See Figure 3-1 from Navarro (2014b), adapted from Pusch (1987). The pores between the aggregates, inter-aggregate or macropores, define the macrostructural level.

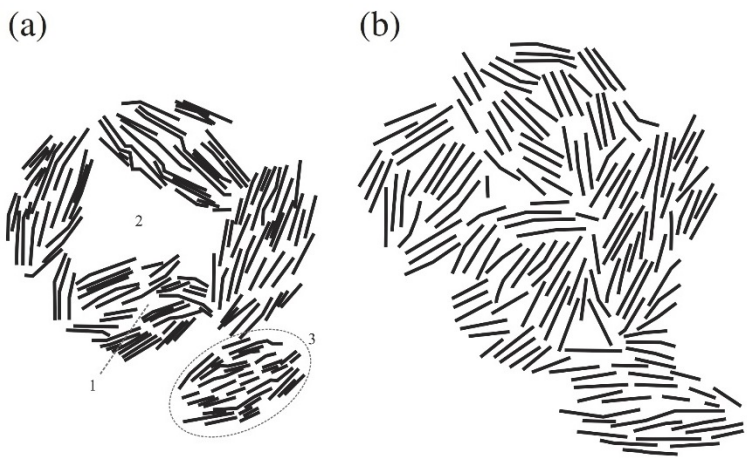

Figure 3-1. *Schematic particle arrangement in a highly compacted Na-bentonite; 1, intra-aggregate space; 2, interaggregate space; and 3, aggregate. (b) State after swelling and saturation from* (Navarro, et al., 2014b)*, adapted from* (Pusch, 1987).

Barcelona Expansive Model (Gens et al., 1992 and Alonso et al., 1999) was used to model the mechanical behaviour of the mechanical tests. Double porosity (Micro and Macro) concept is illustrated briefly in Figure 3-2.

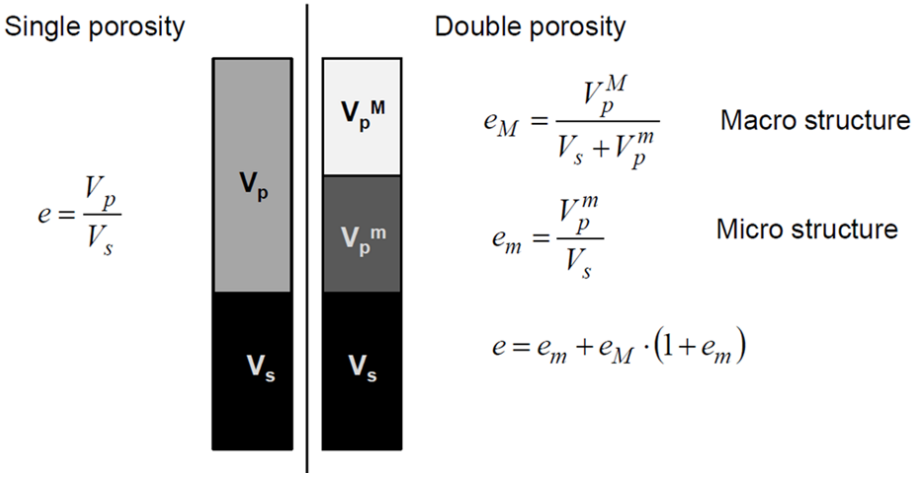

Figure 3-2 *Illustration of Micro and Macro voids.*

a) Elastic strain

Elastic volumetric strain of Micro voids and Macro Voids:

$$d\varepsilon_m^e = \frac{k_m}{1+e_m}\frac{d(p'+s)}{(p'+s)} \tag{3.3-36}$$

$$d\varepsilon_M^e = \frac{k_M}{1+e_M}\frac{dp'}{p'} + \frac{k_s}{1+e_M}\frac{ds}{s+p_{atm}} \tag{3.3-37}$$

b) Plastic strain

Plastic strain of Macro void

$$d\varepsilon_{vol}^{LC} + d\varepsilon_{vol}^{SD} + d\varepsilon_{vol}^{SI} = \frac{\lambda-\kappa}{(1+e_M)}\frac{dp_0^*}{p_0^*} \tag{3.3-38}$$

c) Yield function

$$F^{LC} = J^2 - \frac{M^2}{3}(p+p_t)(p_0-p) \tag{3.3-39}$$

where p_ts the clay tensile strength, p_0 the clay matrix isotropic yield locus and *M* the slope of the critical state line in the *p –q* diagram and J is the second invariant of the stress tensor. The following dependencies on suction are considered:

$$p_t = k_s s \tag{3.3-40}$$

$$p_0 = p^c\left(\frac{p_0^*}{p^c}\right)^{\frac{\lambda(0)-k^M}{\lambda(s)-k^M}} \tag{3.3-41}$$

$$\lambda(s) = \lambda(0)[(1-r)\exp(-\beta s) + r] \tag{3.3-42}$$

$$F^{SD} = \gamma^{SD} - p - s \tag{3.3-43}$$

$$F^{SI} = p + s - \gamma^{SI} \tag{3.3-44}$$

Figure 3-3 presents the Loading-Collapse (LC) curve, Suction decrease (SD) and Suction increase (SI) yield curve.

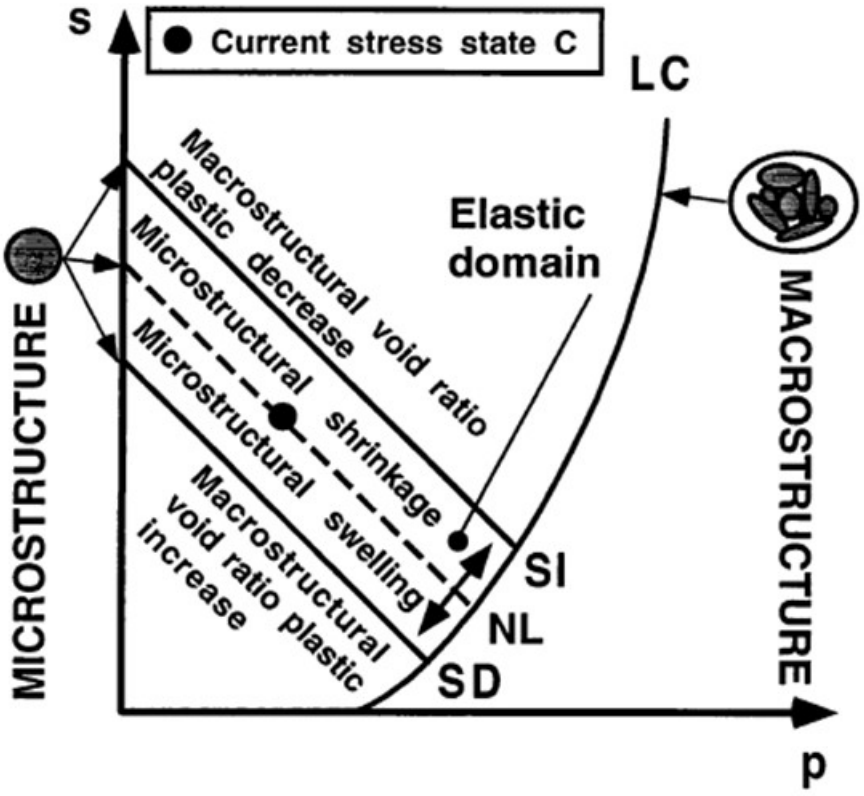

Figure 3-3. *Illustration of Loading-Collapse (LC), Suction Decrease (SD) and Suction Increase (SI) yield curve (Pinyol, 2014).*

d) Rate dependency

Rate dependency is introduced as a visco-plastic mechanism. Rate dependency is not considered in this study.

e) Plastic potential

$$G^p = J^2 - \omega \frac{M^2}{3}(p + p_t)(p - p_0) \tag{3.3-45}$$

ω is a parameter defining the non-associativity of the flow rule. It takes a value equal to 1 when associated and equal to 0 for null dilatancy. To respect the condition of null lateral strain during K_0 –loading, ω should be set to:

$$\omega = \frac{M\ (M-9)(M-3)}{9(6-M)} \frac{1}{1 - k/\lambda(0)} \tag{3.3-46}$$

f) Hardening law

The hardening/softening law is introduced through the following dependency of the saturated isotropic yield locus on the plastic strain:

$$\frac{dp_0^*}{p_0^*} = \frac{(1+e^M)}{\lambda-\kappa}\left(d\varepsilon_{vol}^{LC} + d\varepsilon_{vol}^{SD} + d\varepsilon_{vol}^{SI}\right) \tag{3.3-47}$$

Hardening of SD and SI is calculated as:

$$d\gamma^{SD} = \left(\frac{K^m}{f^{SD}} d\varepsilon_{vol}^{SD} + \frac{K^m}{f^{SI}} d\varepsilon_{vol}^{SI}\right) \tag{3.3-48}$$

$$d\gamma^{SI} = \left(\frac{K^m}{f^{SD}} d\varepsilon_{vol}^{SD} + \frac{K^m}{f^{SI}} d\varepsilon_{vol}^{SI}\right) \tag{3.3-49}$$

where f^{SD} and f^{SI} are the micro-macro interaction functions defined as follow:

$$f^{SD} = f_{SD0} + f_{SD1}\left(1 - \frac{p}{p_0}\right)^{n_{SD}} \tag{3.3-50}$$

$$f^{SI} = f_{SI0} + f_{SD1}\left(\frac{p}{p_0}\right)^{n_{SI}} \tag{3.3-51}$$

The Barcelona Expansive Model (BExM) can be used for describing the behaviour of a swelling clay in special conditions with a few modifications. Navarro et al. 2014b presented a small modification in BExM framework for the simulation of free swelling (UCLM-FS model).

Three different levels of porosity can be found in pellets structure (Hoffmann et al. 2007; Sánchez et al. 2015): The microstructure with the intra-aggregate pores and two levels of macrostructure, the first one with the inter-aggregate pores inside the pellets and a second level of macrostructure with the pores between the pellets. This second macrostructure is quite open. The pellets behaviour characterization is still open and a few works have been found for its characterization (Alonso et al., 2011). The EB test in Mont Terri is the only “in situ” test performed with pellets (García-Siñeriz et al., 2015).

The implementation of new capabilities in BExM in CODE_BRIGHT is out of the scope of this thesis, therefore the basic BExM is used.

c) Liquid phase relations

The liquid density, can be calculated:

$$\tilde{\rho}_l(p_l,T) = \rho_{l0} \exp\left(\beta(p_l - p_{l0}) - \alpha T\right), \quad (3.3\text{-}52)$$

where $p_{l0} = 0.1$ MPa is the default. The *liquid viscosity* is given by,

$$\tilde{\mu}_l(T) = 2.1 \times 10^{-12} \exp\left(\frac{1808.5}{273.15 + T}\right) \quad (3.3\text{-}53)$$

The specific internal energies are given by $e_l^{\,i} = c_l^{\,i} T, \quad i = w, a$.

d) Gas phase relations

As mentioned above, in the present simulations a constant gas pore pressure p_g = 0.1 MPa has been used. The gas phase is considered an ideal gas mixture, thus *Dalton's law* is adopted $p_g = p_g^{\,a} + p_g^{\,w}$. The *water gas pore pressure* and the *air gas pore pressure* (the latter recast in terms of gas air mass per gas phase volume) are given by,

$$\tilde{p}_g^{\,w}(T) = 136075 \exp\left(-5239.7/(273.15+T)\right) \quad (3.3\text{-}54)$$

and

$$\tilde{\rho}_g^{a}(T) = \left(p_g - \tilde{p}_g^{\,w}(T)\right) M_a / \left(R(273.15+T)\right), \quad (3.3\text{-}55)$$

respectively. The gas specific internal energies are given by $e_g^{\,i} = L_g^{\,i} + c_g^{\,i} T, \quad i = w, a$. Latent heat is only considered for vapour.

e) Air gap relations

With air being the only material in the gap between the canister and the buffer, the flow of radiant heat across the gap must be taken into account. Compared to solid materials, gases are significantly less conductive because of the relatively-large distances between atoms, and the significance of radiation as a process for heat transfer in gaseous materials is thereby increased. In the present case, the radiant flux in the air gap is determined following a formulation proposed by Hökmark et al. (2003).

Stefan-Boltzmann's law gives the radiant heat flux q_r from a non-reflecting, perfectly-absorbent surface with an absolute temperature T:

$$q_{radiation} = \sigma T^4 \quad (3.3\text{-}56)$$

where σ is the Stefan-Boltzmann constant 5.6697×10^{-8} W/m^{2}K^4).

This equation also applies to ideal blackbody radiation. For solid surfaces, heat output is also a factor of surface emissivity *e*:

$$q_{radiation} = e_{tot}\sigma T^4 \tag{3.3-57}$$

Total emissivity can be calculated (Ryti, 1973):

$$e_{tot} = \frac{e_1 e_2}{e_1 + e_2 - e_1 e_2} \tag{3.3-58}$$

For a gap that is small compared to the axial length and the radius, the net exchange of radiant heat between two grey surfaces (indicated here by the numbers 1 and 2) is given by (Ikonen, and Raiko, 2012):

$$q_{radiation} = \frac{e_1 e_2}{e_1 + e_2 - e_1 e_2}\sigma(T_1^4 - T_2^4) \tag{3.3-59}$$

If the temperature difference $\Delta T = T_1 - T_2$ between the two surfaces involved is small, the approximate heat flux is given by (the first term in the Taylor expansion):

$$q_{radiation} = \frac{e_1 e_2}{e_1 + e_2 - e_1 e_2}4\sigma T_2^3 \Delta T \tag{3.3-60}$$

The thermal conductivity equation in the Fourier's law form is:

$$q_r = -\lambda \nabla T \tag{3.3-61}$$

$|\nabla T|$ is equal to $\Delta T/\Delta l$, so the coefficient for modelling the transport of radiant heat as conductive heat transportation has to be multiplied by the gap width Δl. The thermal conductivity of hot air λ_{gas} connected with the conductive transfer of heat across the gap can be added to this effective conductivity in order to take both thermal radiation and heat conduction in the gas into account. Combining these factors, the effective thermal conductivity of the air gap can be expressed as:

$$\lambda_{gap} = \frac{e_1 e_2}{e_1 + e_2 - e_1 e_2}4\sigma(T + 273.15)^3 \Delta l + \lambda_{gas} \tag{3.3-62}$$

where the emissivities e_1 and e_2 now correspond to the emissivities of the canister and the buffer, and *T* is the average gap temperature in degrees Celsius. This expression is valid only if the absolute temperature *T*+273.15 K is large compared to the temperature drop across the gap.

This equation shows that the effective thermal conductivity increases linearly with gap width. Total emissivity expressed by the equation (3.3-58) is applied in a narrow cylindrical gap between the canister and bentonite (view factor = 1, see below). If the gap width increases, view factor is less than one and the total emissivity can be calculated from (Mills, 1999):

$$e_{tot} = \frac{1}{\frac{1-e_1}{e_1} + \frac{1}{F_{12}} + \frac{1-e_2}{e_2(r_2/r_1)}} \tag{3.3-63}$$

where r_1 and r_2 are the radii of the internal and external cylinders and the view factor F_{12}=1 (other view factors between internal and external cylinders 1 and 2 are F_{11}=0, F_{21}=r_1/r_2 and F_{22} = $1-r_1/r_2$). If for instance r_1=0.525 m, gap width is 10 mm, i.e. r_2 = 0.535 m, e_1 = 0.3 (emissivity of copper) and e_2 = 0.8 (emissivity of bentonite, Ikonen and Raiko, 2012), it follows from equation (3.3-63) that e_{tot} = 0.2794. From equation (3.3-58) it follows that e_{tot} = 0.2791. Thus so the equation (3.3-58) gives accurate enough results in case of gap widths in practice.

The emissivity of the copper surface depends strongly of the quality of the surface. Polished surface has an emissivity of about 0.02, clean machined surface about 0.3 and oxidized surface 0.6 (Ryti, 1973). In the analyses, the emissivity of the copper surface was assumed to be 0.3 (Ikonen and Raiko, 2012).

Since thermal conduction is not generally the primary mode of heat transfer in gases, the flow of radiant heat must be taken into account when considering air. The contribution from convection is expected to be small due to the narrow gap geometry and low levels of groundwater flow.

To treat radiation in a simple way is possible to modify the thermal conductivity of the gap under dry conditions by incorporating the radiation effect. This is done in the following simple way taking into account the equation given above. In this case the gap is considered with a high porosity and the thermal conductivity in its dry state is calculated. All other gap thermal and hydraulic properties are summarized in Chapter 4.4).

$$\lambda_{dry} = \frac{e_1 e_2}{e_1 + e_2 - e_1 e_2} 4\sigma(T + 273.15)^3 \Delta l + \lambda_{gas} \tag{3.3-64}$$
$$= 0.27 \times 4 \times 5.66 \times 10^{-8} \times (50 + 273)^3 \times 0.01 + 0.045$$
$$= 0.066\ \mathrm{W/m/k}$$

Since the gap thermal conductivity has been increased, the temperature results will have a slightly lower maximum.

3.4 Thermal analysis on canister power

There are two main parameters playing a fundamental role on thermal analyses of canister which are the residual power of canister at the time of deposition and the decay rate. The work by Hökmark et al. (2003) is taken into account as a reference for the calculation of the power and the decay heat rate. The power as a function of time for an individual canister can be expressed as:

$$P(t) = P(0)\sum_{i=1}^{7} a_i \exp\left(-t/t_i\right) \tag{3.4.1}$$

In this expression, $P(0)$ is the canister power at the time of deposition and a_i, t_i are parameters. The two parameter sets from SKB power data depending on the time of cooling previous to disposal are given in *Table 3-1*.

The coefficients given in *Table 3-1* are valid for an initial power of 1837.3 W (in the case of 30 year old fuel) and an initial power of 1545.3 W (in case of 40 year old fuel). The presently performed work is targeting a 1700 W of initial power at the time of deposition. The power function and prescribed temperature used in the models presented here is shown in *Figure 3-4*.

A 1700 W of canister power, 25 m of tunnel spacing and 11 m of canister spacing and variable temperature on the boundaries (*Figure 3-4*) are used to perform THM calculations (Toprak et al., 2013, for detailed information about thermal calculations under axisymmetric conditions).

Table 3-1. Parameters for the exponential equation for canister power calculations.

I	t_i (years)	a_i (30 years)	a_i (40 years)
1	20	0.070	0.049
2	50	0.713	0.696
3	200	-0.051	-0.059
4	500	0.231	0.271
5	2000	0.024	0.027
6	5000	-0.009	-0.010
7	20000	0.022	0.026

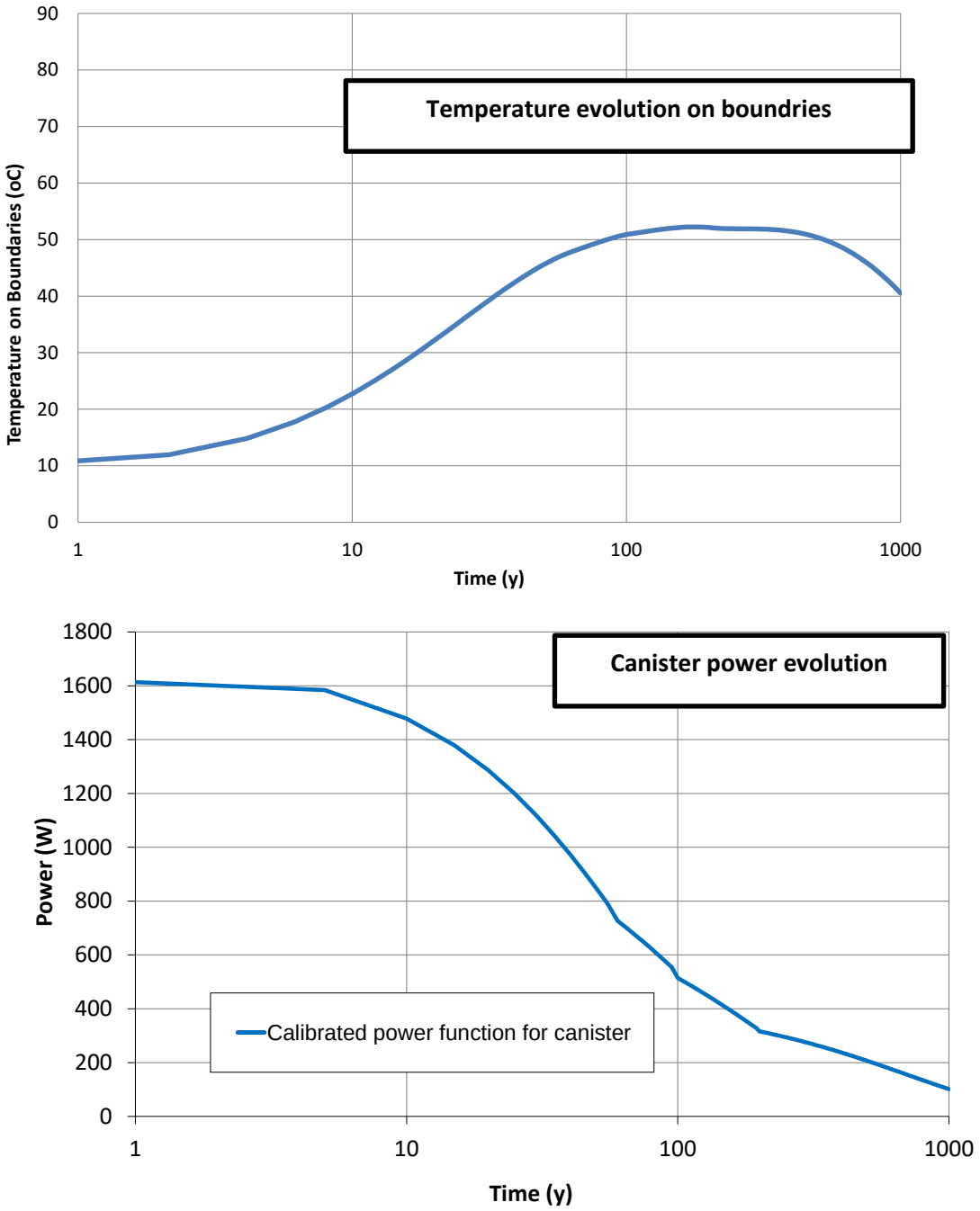

Figure 3-4.*Temperature calculated from an analytical model (Ikonen, 2003) prescribed on top and bottom boundaries and power decay of the canister considered.*

4 MATERIAL PROPERTIES AND EXPERIMENTAL PROGRAM

In this Section; material properties, safety requirements for materials and experimental program on materials have been discussed.

4.1 Materials in the project

As it can be seen from, Figure 4-1 and Figure 4-2 there are several materials in the KBS-3V design.

Backfill consists of three different components:

- Backfill blocks: Friedland clay has been chosen as the reference material for manufacturing the backfill blocks (Pastina and Hellä, 2010 and Keto et al., 2013). See Figure 4-2-A.
- Pellets**:** Rod pellets were manufactured from Milos bentonite. The characterization of the raw material is described in (Kiviranta et al., 2016 and Kiviranta and Kumpulainen, 2011). The ID (identification used by B+TECH) for the material is Be-Mi--NaA-BT0021-Pp-R. The pellets have a length of 9.4 mm and a diameter of 6.2 mm although the variation of these values is high. The pellets were manufactured by the extrusion method (Keto et al., 2013). The rod pellets component (Figure 4-2-B) is going to be used for filling the space between the backfill blocks and the tunnel wall (Keto et al., 2013). The rod pellet material is expected to represent a potentially significant proportion of the tunnel cross-section.
- Granules are going to be used as foundation bed, see Figure 4-2-C; (Hansen, 2010), (Posiva, 2012).

Buffer consists of three main components:

- Buffer blocks and rings: MX-80 bentonite has been chosen as main buffer material (see Figure 4-2-D, Kiviranta et al., 2011).
- Pillow pellets: Pillow pellets were manufactured with MX-80 bentonite. The characterization of the raw material is described in (Kiviranta et al., 2016). The ID material is Be-Wy--BT0027-Pp-R according to (Kiviranta et al., 2016), (Figure 4-2-E).
- Gap element: There is an air gap between canister and buffer blocks.

The canister consists of a copper shell and a nodular graphite cast iron insert (Figure 4-2-F) which holds the spent fuel elements (Raiko, 2013). Host rock (Posiva, 2009) and rock fracture network are the other components of the KBS-3V design. Geometry, meshing and detailed information about all components can be found in the chapter where the Base Case is described. As it has

been said before, only one fracture orthogonal to vertical axis will be taken into account. The axisymmetry does not allow any other orientation in fractures.

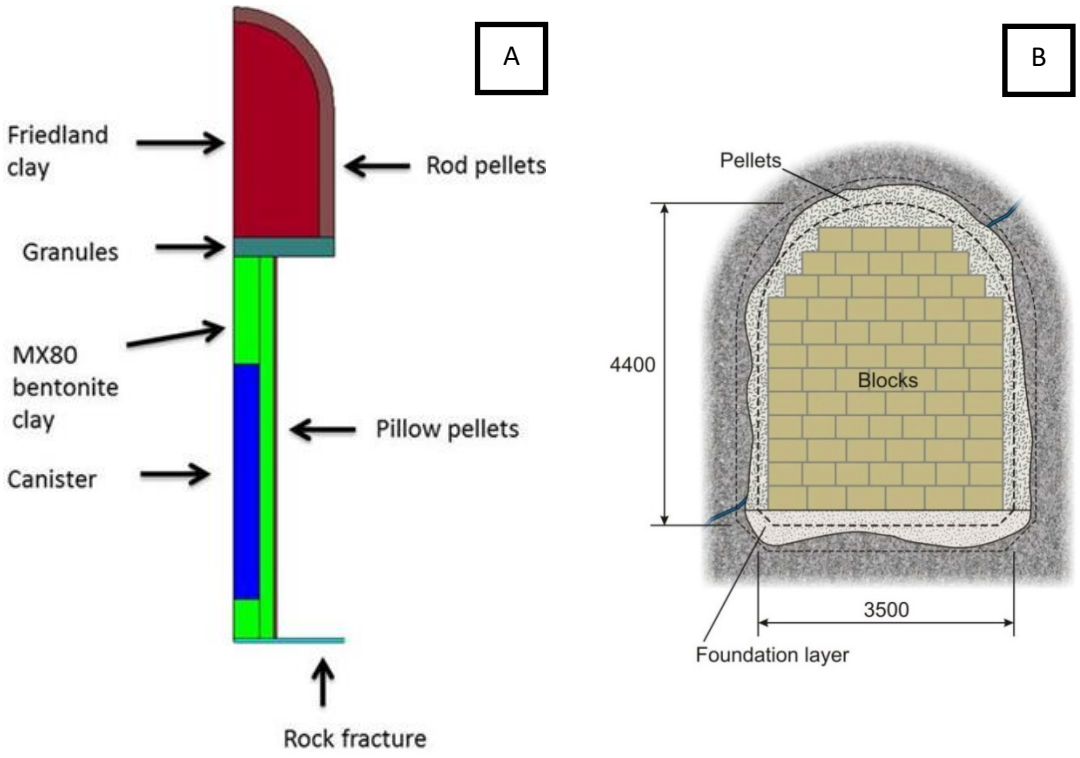

Figure 4-1. *Schematic figures showing the components of the whole system (A) and detailed backfill tunnel section (B).*

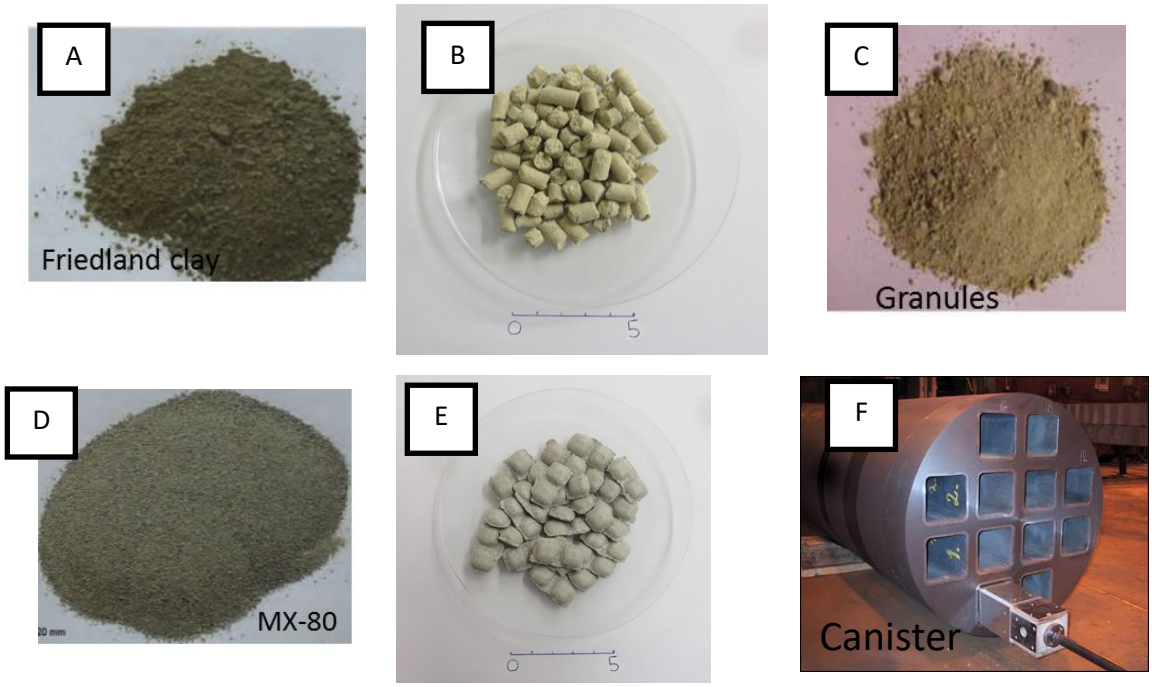

Figure 4-2. *Materials in the KBS-3V disposal method.*

The summary safety functions assigned to the EBS components in Posiva's repository concept are (Posiva, 2012 and SKB, 2010):

Canister:

- Ensure a prolonged period of containment of the spent nuclear fuel. This safety function rest first and foremost on the mechanical strength of the canister's cast iron insert and the corrosion resistance of the copper surrounding it.

Buffer:

- Contribute to mechanical, geochemical and hydrogeological conditions that are predictable and favourable to the canister.
- Protect canisters from external processes that could compromise the safety function of complete containment of the spent fuel and associated radionuclides.
- Limit and retard radionuclide releases in the event of canister failure.

Backfill:

- Contribute to favourable and predictable mechanical, geochemical and hydrogeological conditions for the buffer and canisters.
- Limit and retard radionuclide releases in the possible event of canister failure.
- Contribute to the mechanical stability of the rock adjacent to the deposition tunnels.

The material to be used as buffer material in ONKALO project is MX-80 bentonite. Several laboratory experiments have been performed to validate MX-80 performance as a buffer material. The performance targets for buffer material can be listed as:

- Bulk hydraulic conductivity: $k^{\text{Buffer}} < 10^{-12}$ m/s (Juvankoski et al., 2012),
- Swelling pressure> 2 MPa for avoiding microbiological activities (Miller, et al., 2007 and Juvankoski et al., 2012),
- Maximum temperature $T^{Buffer} < 100$°C for avoiding the mineral transformation of the buffer (Posiva, 2012)
- Minimum temperature $T^{Buffer} > -5$°C (Raiko, 2013)
- Minimum buffer saturated density at the deposition hole > 1,950 kg/m^3 (Posiva, 2012)
- Maximum buffer saturated density at the deposition hole < 2,050 kg/m^3 (Posiva, 2012)

The performance targets for the backfill are:

- Hydraulic conductivity of backfill should be < 10^{-10} m/s (Posiva, 2012).
- Backfill shall ensure a tight contact with the rock wall. So that swelling pressure of backfill should be > 200 kPa (Keto et al., 2013).

The performance targets of the canister for nuclear waste disposal can be listed as (Posiva, 2012):

- The surface temperature shall not be more than + 100 ºC to guarantee the mineralogical stability of the surrounding bentonite (Posiva, 2012).
- The canister must be designed to resist the loads caused by disposal at a depth of 400 - 450 m with a nominal depth of 420 m. The groundwater hydrostatic pressure expected is 4.1 MPa. The maximum ice layer during glaciation at Olkiluoto area is 2.5 km, which will create an additional pressure of about 25 MPa. The maximum swelling pressure expected from MX-80 bentonite is up 15 MPa, so the sum of isostatic pressure load for a canister at Olkilutos site is about 44 MPa (Raiko, 2013).

4.2 Description of Tests

For the material characterization, five different tests were proposed (Pintado et al., 2013a). These tests were carried out at SROY (www.sroy.fi) laboratory:

- Water retention curve tests
- Thermal conductivity tests
- Infiltration tests
- Oedometer tests
- Tortuosity tests

To determine the THM parameters of materials, data from these tests have been used. Calibrated parameters by means of laboratory tests have been listed in Chapter 4.4.

4.2.1 Water retention curve tests

The water retention curve test has been performed for MX-80, Posiva pillow pellets as buffer materials and for Friedland clay, Minelco granules and Cebogel (rod) pellets as backfill materials. Tests have been carried out in SROY (www.sroy.fi) laboratories. The calibrated test data are given in Table 4-21 and Table 4-22 in Chapter 4.4 and used for THM calculations (Chapter 5).

Figure 4-3 shows a schematic picture of measurement set-up (A) and a picture of test set up from SROY laboratory (B). The air with relative humidity controlled flows through upper and

bottom inlets of the measurement cell in Dueck's test set-up in order to impose the suction to the sample. However, the air flows only through the upper inlet in this work. In Dueck's cell, the RH is measured continuously with a capacitive hygrometer.

The suction was imposed assuming that the suction can be evaluated following the psychrometric law (Edelfsen et al., 1943). After the test, the suction was measured with a capacitive psychrometer (HMT337 from Vaisala, accuracy ± 1 % for RH 0-90 %, and accuracy ± 2 % for RH 90-100 %) while the sample was inside the test cell and with chilled mirror dewpoint psychrometer (Decagon WP4, accuracy ± 0.1 MPa in 0-10 MPa range, and ± 1 % in 10-300 MPa range) after the sample was removed from the test cell.

MX-80: The results obtained in the SROY laboratory for Volclay MX-80 and Cetco MX-80 bentonite are presented in ***Figure 4-4***. Equations 3.3.1 to 3.3.3 have been used to calibrate water retention curve parameters. The calibrated parameters are P_0= 27 MPa, λ=0.45, a=11 and b=4 λ_0 is 0.4245. The parameters are listed in Table 4-21. Calibrated water retention curve for MX-80 is shown in Figure 4-6 together with the other materials.

Friedland clay: The results of the WRC measurements are shown in ***Figure 4-4***. The WRC can be fitted with the Van Genuchten curve with the parameters P_0 and λ as a function of the porosity (equations 3.3.1 to 3.3.3). The relations are: The parameters for Friedland clay are: P_0= 4.5 MPa, λ=0.25, a=22 and b=8. λ_0 is 0.393. The parameters are listed in Table 4-21. Calibrated water retention curve for Friedland clay is shown in Figure 4-6 together with the other materials.

P*osiva pillow pellets:** The water retention curve in pellets is difficult to describe as it has been commented before and in Posiva pillow pellets, it is possible to have the same conclusions. The pellets are still independent units when the suction is high. For lower suctions, the pellets are jointed together but still maintain big porous (Figure 4-5***). The results of the WRC measurements are shown in ***Figure 4-5***. The parameters for Posiva pillow pellets are: P_0=5 MPa and λ=0.34. The parameters are listed in ***Table 4-26***. Calibrated water retention curve for pillow pellets is shown in Figure 4-6 together with the other materials.

Minelco granules: The samples were quite dry in high suctions and disaggregated easily but for lower suctions, presented a more consistent structure (***Figure 4-5***). The parameters for Minelco granules are: P_0=12 MPa and λ=0.4. The parameters are listed in ***Table 4-26***. Calibrated water retention curve for granules is shown in Figure 4-6 together with the other materials.

FEBEX bentonite: Equations 3.3.4 and 3.3.5 has been used to calibrate water retention curve parameters of FEBEX (Gens, et al. 2009). Calibrated parameters for FEBEX are P_0=7 MPa, λ=0.1, λ_d=2.1 and P_d=1100. These parameters are listed in ***Table 5-22***. Calibrated water retention curve for Febex bentonite is shown in Figure 4-6 together with the other materials**.**

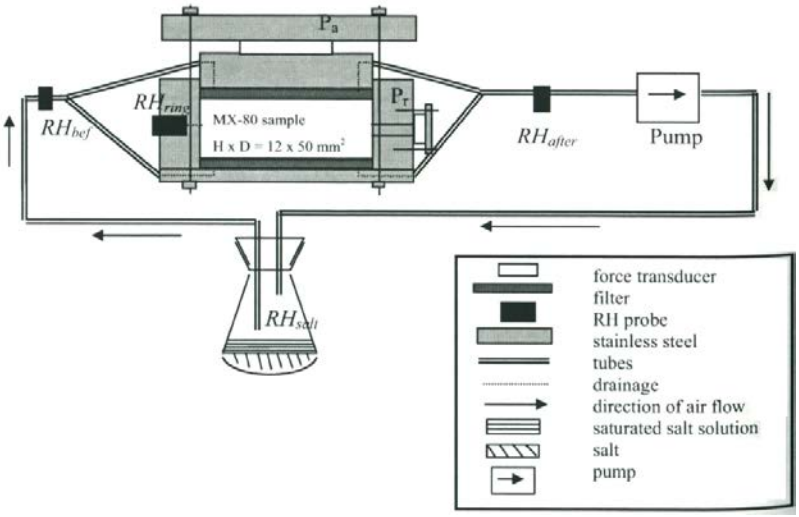

Figure 4-3*. Schematic picture of the measurement set-up* (Dueck, 2004) *(A) and picture of test set-up in the SROY laboratory (B)*

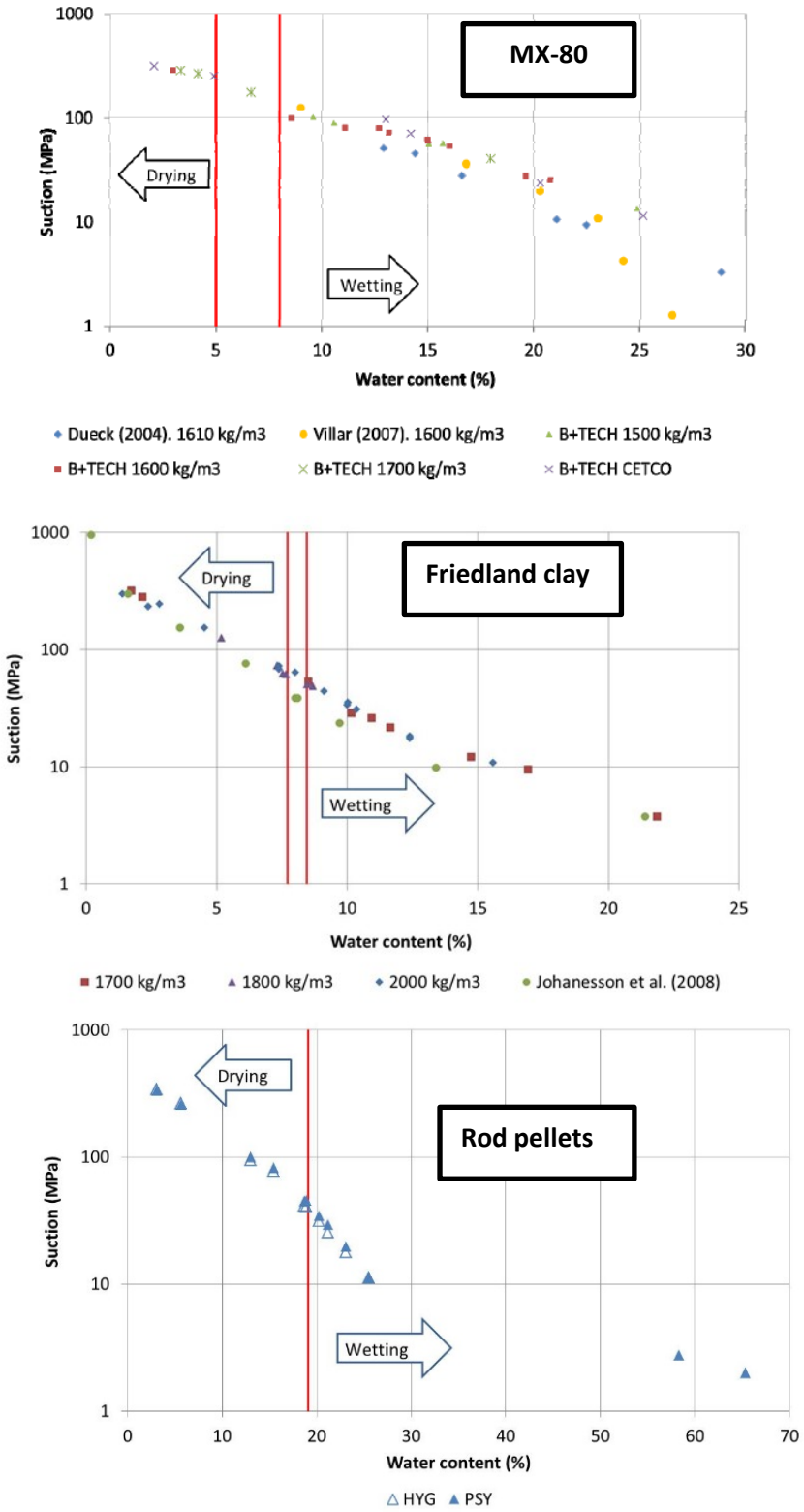

Figure 4-4*. Water retention curve test results in terms of water content vs suction of MX-80 (Pintado et al., 2013), Friedland clay and rod pellets.*

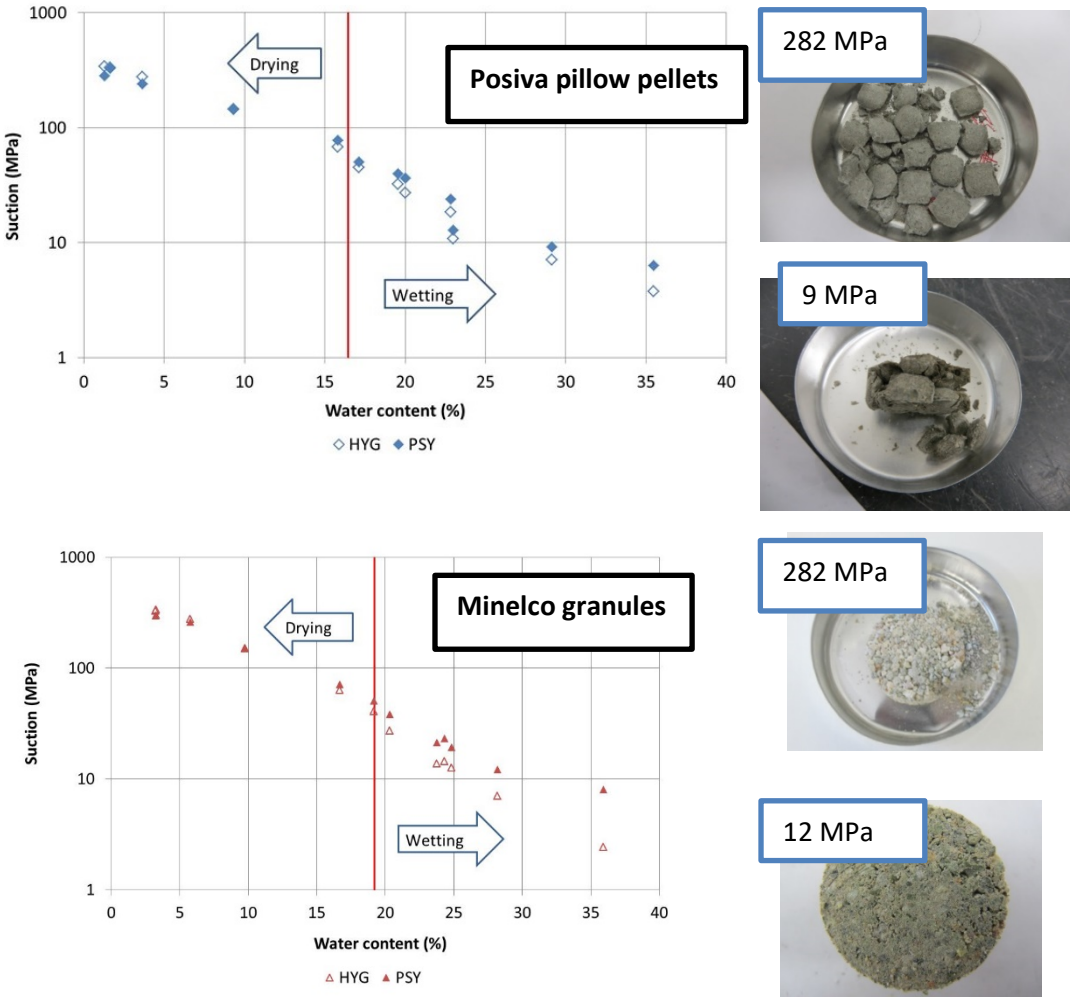

Figure 4-5 *Water retention curve test results in terms of water content vs suction for Posiva pillow pellets and Minelco granules together with sample pictures before and after the test.*

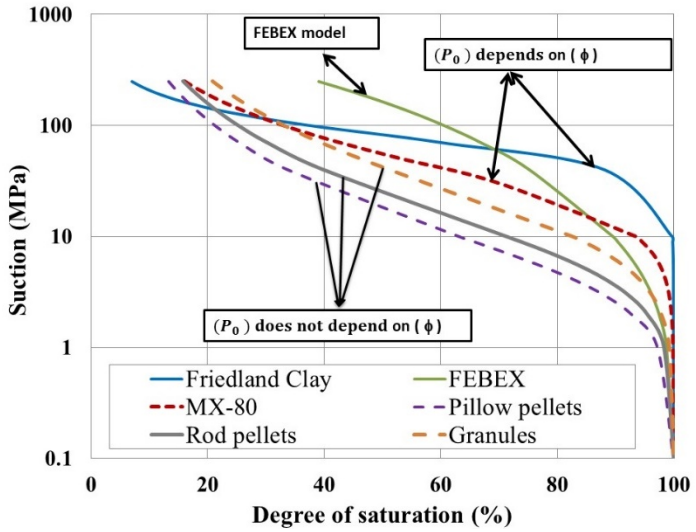

Figure 4-6 *Calibrated water retention curves for all materials.*

4.2.2 Thermal conductivity tests

The objective of this test is to study the thermal conductivity of a soil sample, by the thermal needle probe procedure (ASTM D5334-08). Tests have been carried out in SROY laboratories. The calibrated test data have been given in Table 4-23 and Table 4-27 in Chapter 4.4 and used for THM calculations (Chapter 5).

The thermal conductivity can be determined by using a variation of the line source test method and employing a needle probe consisting of a heating element and a temperature measuring element. *Figure 4-7* shows the experimental equipment used for the thermal conductivity test. Cylindrical samples have an approximate height of 160 mm and a 50 mm of diameter. A Manson EP-613 DC Regulated Power Supply provided a constant current and voltage to the needle probe. The HH506RA thermometer used to measure temperature was connected to a computer containing temperature measurement software. The sample was enclosed in thermally insulating material during the test procedure (Pintado et al., 2013).

Figure 4-7 *Thermal conductivity test experimental set-up. From left to right: power supply, the sample being tested with the needle probe placed in its centre, digital thermometer (yellow frame), and computer. (Pintado et al., 2013)*

Figure 4-8 shows thermal conductivity of materials used in the project as a function of degree of saturation. Thermal conductivity increases according to saturation degree of the materials. The thermal conductivity also increases with the porosity. Equations 3.3-17 and 3.3-18 have been considered to calibrate the thermal conductivity of materials used in the project.

The thermal conductivity in pellets was measured in dry conditions by Kivikoski, et al., 2015. When the pellets are saturated, the thermal conductivity assumed is the water thermal conductivity. The thermal conductivity of saturated pellets will be higher but due to the lack of data, it has been decided to use a low limit.

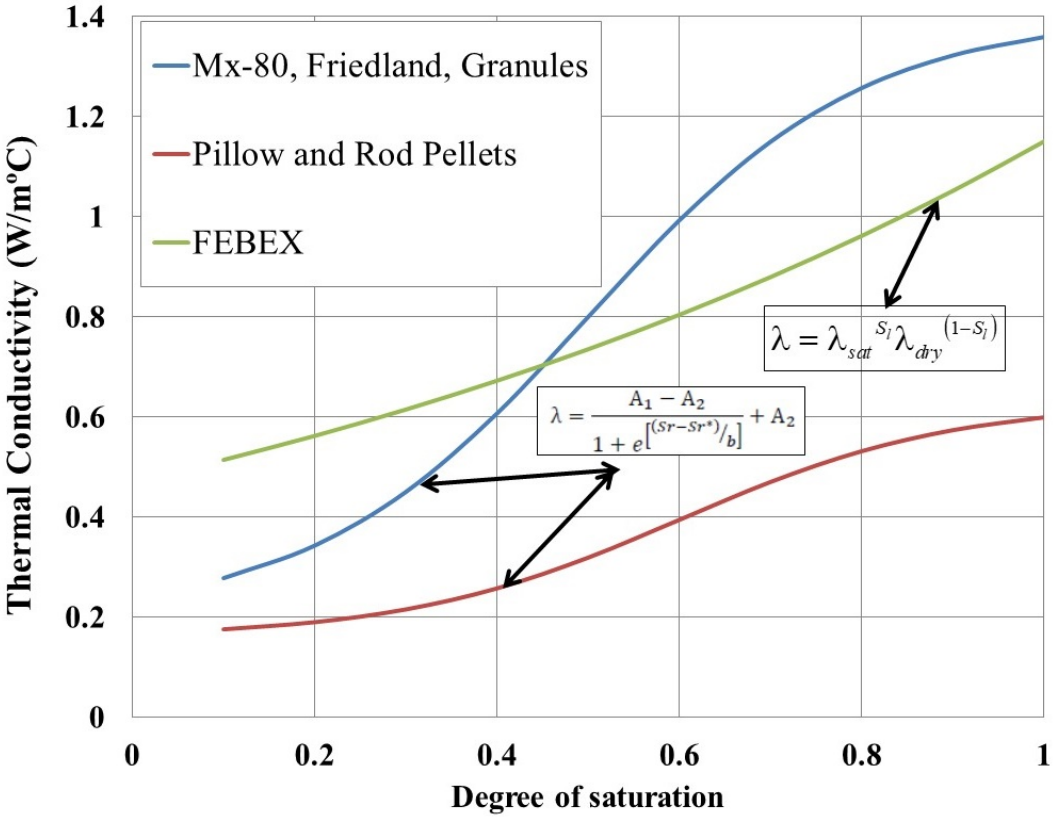

Figure 4-8 *Calibrated thermal conductivity curves for all materials.*

4.2.3 Infiltration tests

In KBS-3V concept, system components (buffer and backfill) are in unsaturated conditions when they are emplaced in the deposition holes. These components are saturated as the groundwater flows into the tunnels and deposition holes. The saturation process starts when the water flows in a natural way from the host rock.

The non-saturated hydraulic conductivity can be measured in porous materials by suction controlled oedometer tests (Romero et al., 1999) which impose the suction by the axis translation technique. However, these tests cannot be performed in bentonites due to their high suction taking into account that the axis translation cannot be used for suctions higher than 1500 kPa with high entry value porous stones. In this case, for measuring the non-saturated hydraulic conductivity, it is necessary to perform inverse analysis from infiltration tests (Pintado et al., 2002; Villar, 2005). Dueck et al. (2010) presented a test where the boundary condition on the inlet water side was high relative humidity control instead of constant water pressure control.

Hoffmann et al. (2007) and Alonso et al. (2011) have carried out investigation on pellets manufactured with FEBEX bentonite. Hoffmann (2005) also presents infiltration tests conducted on the same bentonite.

Villar et al., 2005 present an infiltration test heating the sample on the opposite side of the infiltration section.

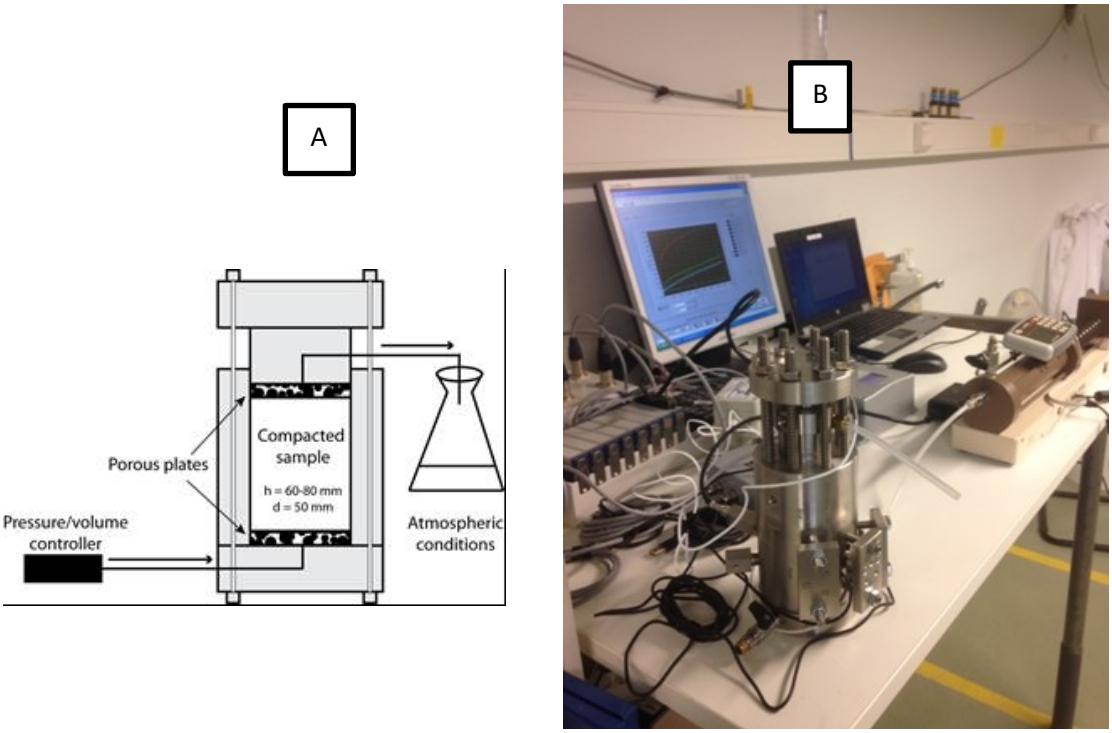

Figure 4-9. *Diagram (A) and B+Tech infiltration test setup (B).*

As shown in Figure 4-9-A and Figure 4-9-B, the infiltration tests involve a column of material. Performed tests for all materials is summarised in Table 4-1. In total seven infiltration tests have been calibrated. Numerical simulations of these tests is detailed in Chapter 4.3

The infiltration cell is made of stainless steel. The inner diameter of the infiltration cell is 50 mm, and the height of the sample was approximately 63 mm. There were two sintered porous frits made of stainless-steel balls with a diameter of 10 µm at the top and bottom of the sample. The materials were compacted directly inside the cells. During the tests, a target water pressure was applied at the bottom of the sample by a pressure/volume controller manufactured by GDS (www.gdsinstruments.com). On the other side, the boundary condition was seepage boundary condition, that is, when the sample is still unsaturated, the liquid flow is 0 but when the sample is saturated, the liquid pressure is fixed in 0.1 MPa (atmospheric pressure). Although the relative humidity is almost high, the evaporation is really avoided due to there is not air circulation around the sample. The tests have been performed at the laboratory room temperature (approximately 24 °C). The suction of the materials was measured before the tests with a chilled mirror psychrometer WP-4 (www.decagon.com). The sample volume was kept constant during the test, and the water inlet flow was measured continuously. At the end of the test, the sample was cut into slices with a saw. After cutting the sample, the water content and bulk density were measured. In addition, the suction was also measured with the psychrometer. In some tests, the axial pressure and radial swelling pressure in three positions at 30, 40 and 50 mm from the bottom of the sample were measured. The radial swelling pressure was measured with pistons of 10 mm diameter.

Table 4-1. *Infiltration tests performed.*

Material	Test ID		
MX-80	100108a	101027a	100623a
Friedland clay	120420c		
Posiva pillow pellets	1412191A		
Cebogel pellets	131030C		
Minelco granules	140508A		

After the tests, a lower dry density near the injection zone has been observed which indicates that swelling was taken place. The swelling near the injection zone was possible because other parts of the sample undergo compressed. Some level of suction was still measured at the end of the tests. This means that the sample was not fully saturated which could be motivated due to the process of sample dismantling. Dismantling has an associated unloading which may induce

some suction due to the swelling developed. It should be also mentioned that the sample may dry out during the dismantling and measuring operations. This is an important issue because the hydraulic analysis presents some limitations due to the change of density, which has direct impact in the hydraulic conductivity.

4.2.4 Oedometer tests

The oedometer cells are made of stainless steel. In case of pillow pellets tests, the diameter of the sample was 70 mm and the height 25 mm. The samples for rod pellet tests had a diameter of 50 mm and a height of 36 mm. There were two stainless-steel porous frits at the top and bottom of the sample to facilitate the hydration process. A linear variable differential transformer (LVDT) was used for measuring the axial displacements. In addition, a force transducer was placed on the radial direction of the samples for measuring the radial stresses.

Figure 4-10-A and Figure 4-10-B present the layout of the oedometer test and a picture of the setup in SROY laboratories. There were some cells with the hydration systems and the loading arm lever. Some weights were placed on the lever to exert the defined axial pressure on the samples.

The materials were placed directly into the cells. Performed tests for all materials is given in Table 4-2. In total seven oedometer tests have been calibrated. Numerical simulations of these tests are given in Chapter 4.3.

The radial swelling pressure was also measured at 20 mm from the bottom with a piston of 10 mm diameter.

Table 4-2. *Oedometer tests for materials*.

Material	Test ID		
MX-80	100212c	110222f	101222a
Friedland clay	111215a	111215d	
Posiva pillow pellets	131181a		
Cebogel pellets	140912		

There is a limitation when the tests are performed in pellets. In oedometer tests, the diameter and height of the sample should be at least 6 times greater than the largest particle size within

the specimen (ASTM D4546-08) and in triaxial tests (dimensions similar to the infiltration test), the limitation applies to the diameter (always lower than the height), which should be 6 times greater than the largest particle size within the specimen (ASTM D4767-11). The size of the pellets is larger than the size specified by ASTM. In long term, it does not have any influence due to the pellets structure disappears and the material becomes continuous but at the early stages, when the pellets structure still exist, it should be taken into account.

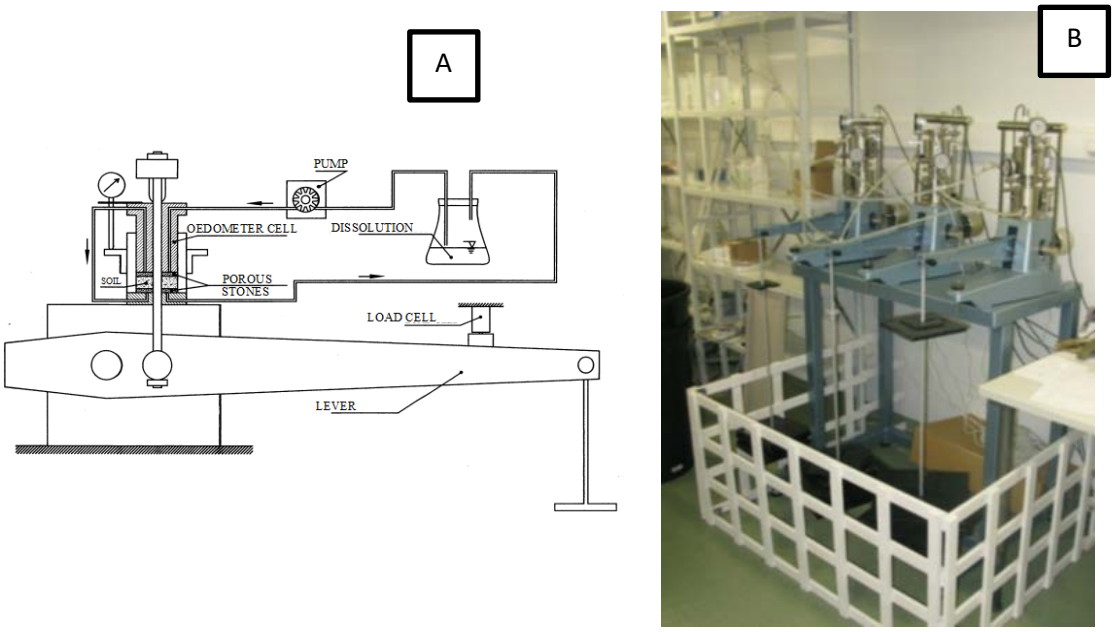

Figure 4-10. *Diagram (A) and SROY oedometer test setup (B).*

4.2.5 Tortuosity tests

Vapour transportation is an important process in KBS-3V concept because heat flow from canister may reduce the thermal conductivity of buffer, especially close to the canister. Tortuosity tests provide a measure of tortuosity or vapour transportation capacity (diffusion) in a porous medium. Tortuosity tests have been carried out and calibrated in SROY laboratories. The calibrated test data have been given in Chapter 4.4 (Table 4-21 and Table 4-26) and used for THM calculations (Chapter 5).

Figure 4-11 presents a schematic of the experimental equipment, and a brief description of the test follows (Pintado et al., 2002 and 2013). At the end of the test, the change in diameter of the specimens was measured with an accuracy of 0.01 mm at certain number of locations. Finally, the specimens were sliced laterally into six small cylinders, and the water content of each cylinder was determined (Pintado et al. 2013).

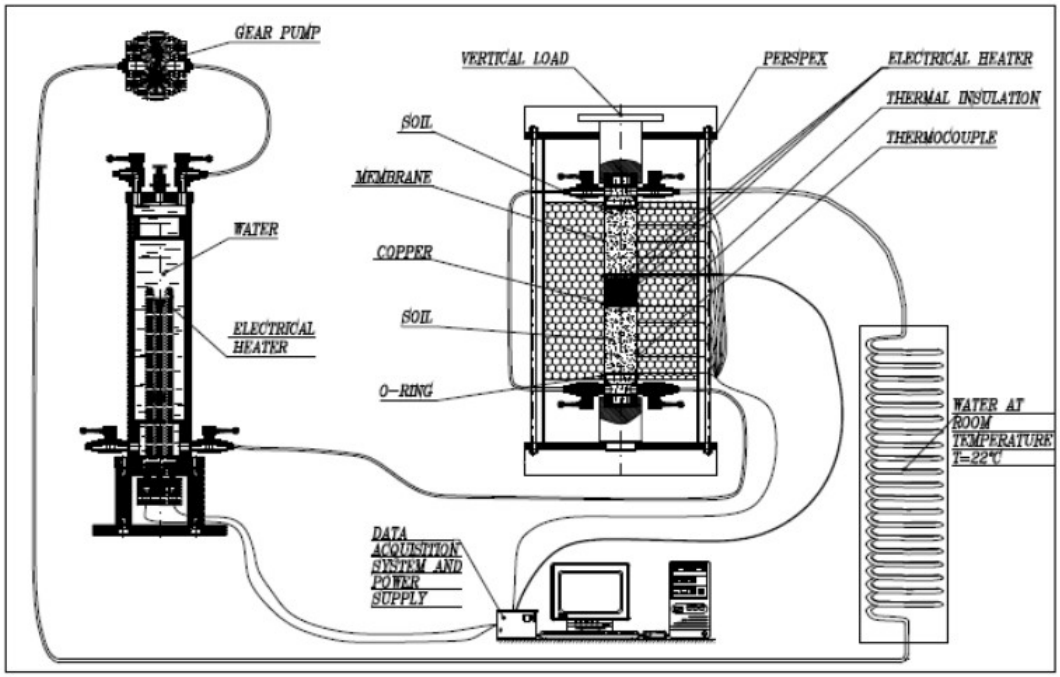

Figure 4-11. *Schematic of the tortuosity test set-up. Two soil samples with a heater located between them are surrounded by insulating material, and the other ends of the samples are cooled to a constant temperature by circulating water. Heating of the system is controlled by a constant power source (Pintado et al., 2002)*

4.3 Numerical simulation of infiltration and oedometer tests

The Barcelona Basic Model BBM (Alonso et al., 1990) has been used for performing the simulation of MX-80 and Friedland clay. However, this model presents limitations for modelling double structure (for example, pellet based materials) in clay materials. Therefore, the Barcelona Expansive Model BExM was developed (Gens et al., 1992; Alonso et al., 1999) and Sánchez et al., 2005) to represent better the expansive response of clay materials. The expansive model incorporates two porosities: macro and micro porosities. Originally, the microstructure was associated to clay particles and the macrostructure was associated to the macro pores and coarse aggregates. The microstructure behaviour has an impact on the macrostructure behaviour. Additional description of the model is included in Chapter 3.

In total, 14 tests have been simulated (*Table 4-1* and *Table 4-2*). For MX-80, the effect of the salinity has also been studied. For the rest of the materials, tests have been carried out only with deionized water (DI water).

In tests performed with saline water, the mixtures were:

- Total dissolved solids (TDS) content = 35 g/L: This solution was prepared by dissolving $CaCl_2$ and NaCl in an aqueous medium at a Ca^{2+}/Na^{+} mass ratio of 1:1. This means 16.7519 g NaCl and 18.2481 g $CaCl_2$ for each litre of desired solution.
- Total dissolved solids (TDS) content = 70 g/L: This solution is prepared by dissolving $CaCl_2$ and NaCl in an aqueous medium at a Ca^{2+}/Na^{+} mass ratio of 3:2. This means 26.5757 g NaCl and 43.4243 g $CaCl_2$ for each litre of desired solution.

4.3.1 Friedland clay

In order to determine hydro-mechanical parameters (BBM) of Friedland clay, an experimental program has been followed. *Table 4-3* and *Table 4-4* summarizes the initial properties and loading-unloading steps in oedometer tests for Friedland clay. Two oedometer and one infiltration test have been simulated for Friedland clay. Calibrated hydro-mechanical parameters for Friedland clay by means of oedometer and infiltration test results are listed in Chapter 4.4 (Table 4-20 and Table 4-21).

Oedometer Tests on Friedland Clay: Test 111215A and Test 111215D

This section is devoted to the simulation of two oedometer tests performed by SROY laboratory. Model geometry and initial condition are represented *Figure 4-12*. The clay sample has a diameter of 50 mm and a height of 21 mm (average of the different heights because it is not possible to fix an exact height of the samples). Numerical simulation of oedometer test is conducted using Barcelona Basic Model. Several simulations were carried out to show the reliability of the model. In these two tests, loading-unlading steps are different (*Table 4-4* and *Figure 4-13*).

Modelling of these tests was carried out by using 2D geometry. Oedometric boundary conditions have been applied as shown in *Figure 4-12*. Horizontal displacements were restricted.

Table 4-3 shows test data and initial conditions of the sample. The sample, initially unsaturated, reaches full saturation at the end of test. There is a period of impoundment of the sample before loading. The maximum loading is 6.92 MPa in Test 111215D and it is quite larger as compared to the Test 111215A.

Tests have a free swelling period (flooding) and afterwards it follows a loading-unloading stage as shown in *Figure 4-13*.

Figure 4-14 shows the void ratio versus axial stress for the simulation of two oedometer tests. Due to flooding, void ratio almost doubles in Test 111215A during the hydration phase. The results obtained by the numerical model show reasonably good correspondence with the experimental values.

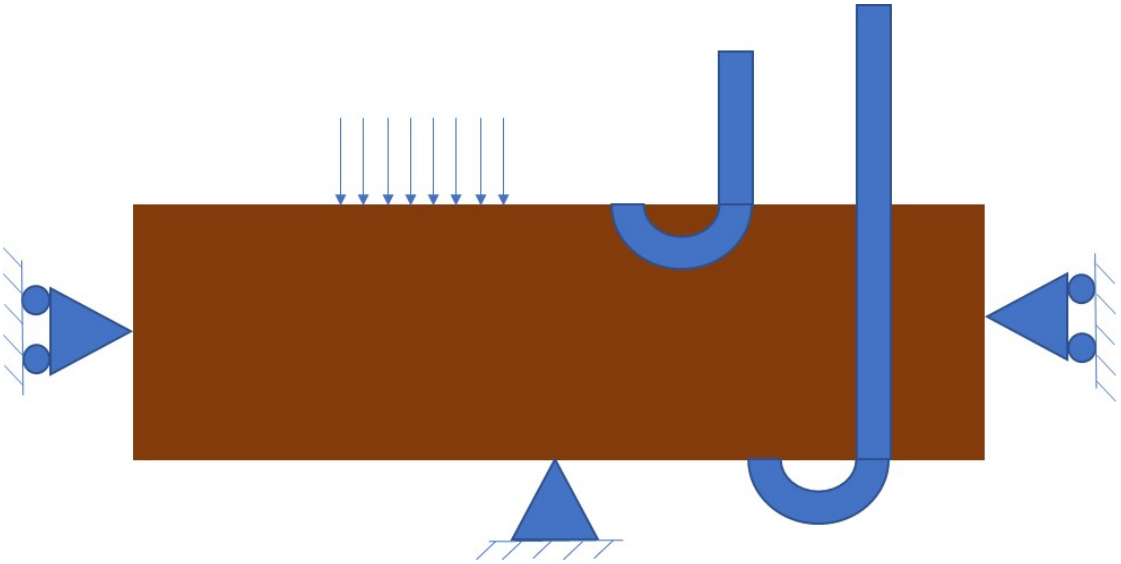

Figure 4-12 Geometry and initial conditions for oedomenter test for Friedland clay

Table 4-3 Oedometer test data for Friedland clay

	Test 111215A	**Test 111215D**
Water content (%) w_o	8.9	8.9
Void Ratio e_0	0.4	0.4
Degree of Saturation (%) S_{r0}	59	61
Dry Density (kg/m^3)	1950	1980
Initial height of sample (mm)	21	21
Diameter of sample (mm)	70	50

Figure 4-15 shows the evolution of the porosity for two tests. The initial porosity of the sample is 0.3 and at the end of the test, the value of the porosity is 0.42 for Test 111215A. Due to high suction at the beginning of the test and the process of wetting, there is a sharp increase of porosity because of the swelling capacity of this backfill material. It can be observed that in both tests, model reproduces quite well the experimental results in terms of porosity. During the free swelling phase, the sample shows a big swelling capacity, almost 50% in porosity variation (in Test 111215A). When loading takes place, sample compresses and porosity decreases. After the

loading phase, unloading is carried out and the sample almost recovers the volume lost occurred in the period of loading. During loading process, the sample compresses significantly due to high loading of 6.92 MPa in Test 111215D. It recovers a little bit during unloading period and gets back to the initial value of porosity (*Figure 4-15*).

Table 4-4 Loading-unloading oedometer test data for Friedland Clay

Test 111215A			**Test 111215D**		
σ_v (MPa)	s (MPa)	e	σ_v (MPa)	s (MPa)	e
0.100	40	0.42	0.196	40	0.40
0.100	0	0.78	0.196	0	0.62
0.529	0	0.76	0.476	0	0.61
1.386	0	0.69	1.036	0	0.57
2.244	0	0.64	2.157	0	0.52
2.959	0	0.61	4.4	0	0.45
1.529	0	0.63	6.92	0	0.41
0.815	0	0.66	3.53	0	0.41
0.386	0	0.70	1.569	0	0.44

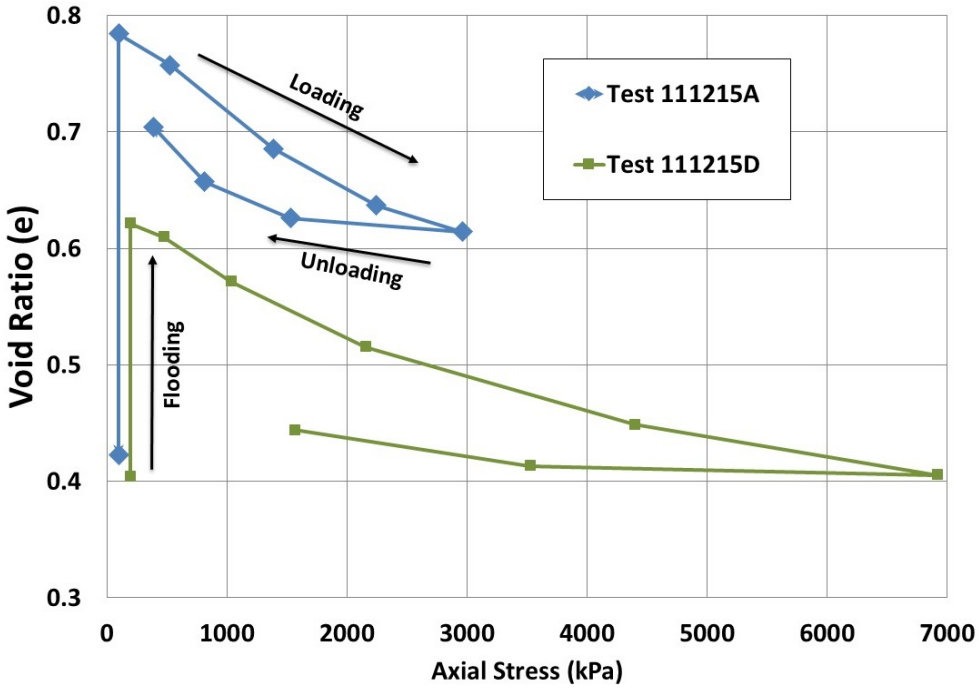

Figure 4-13 Flooding, loading and unloading process in oedometer tests for Friedland-clay.

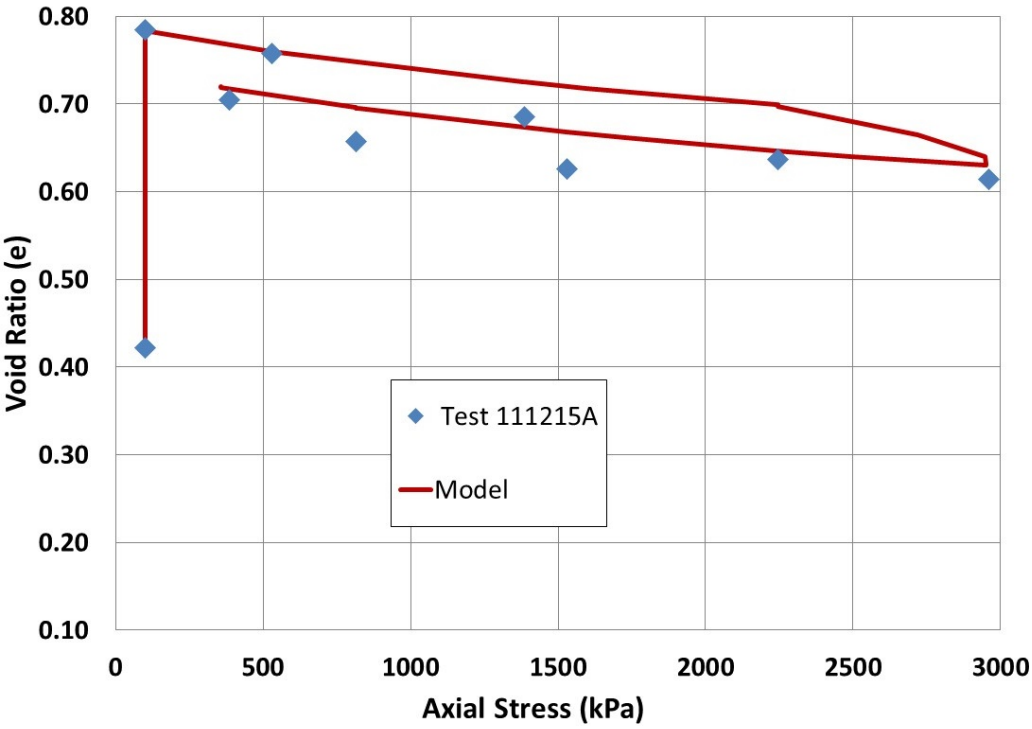

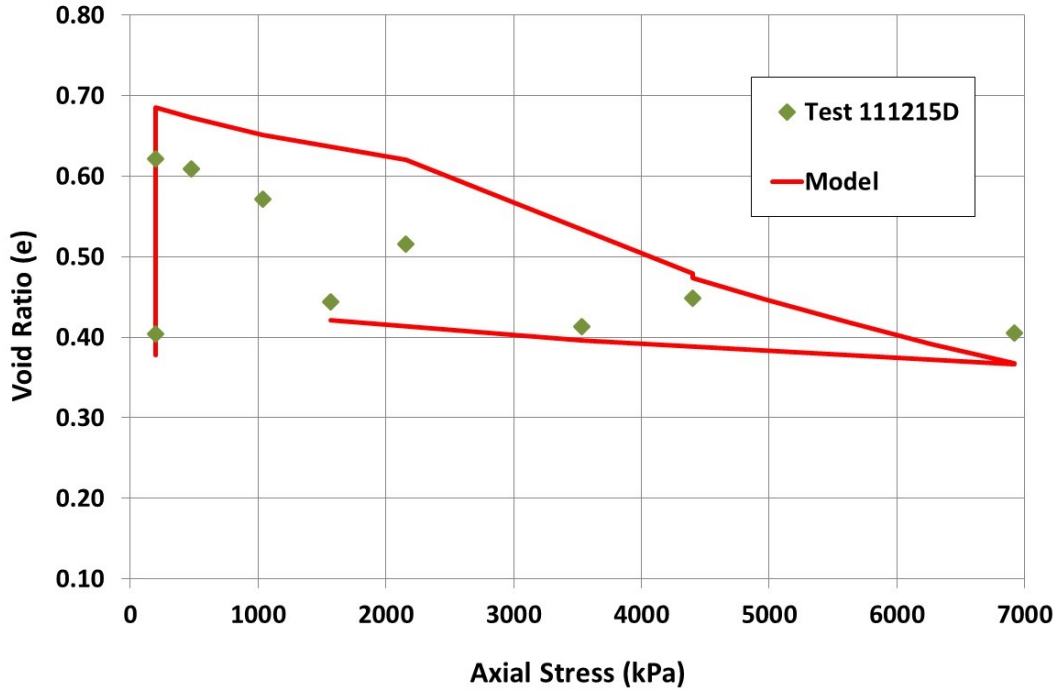

Figure 4-14 *Void ratio vs axial stress, test results over model results for two tests.*

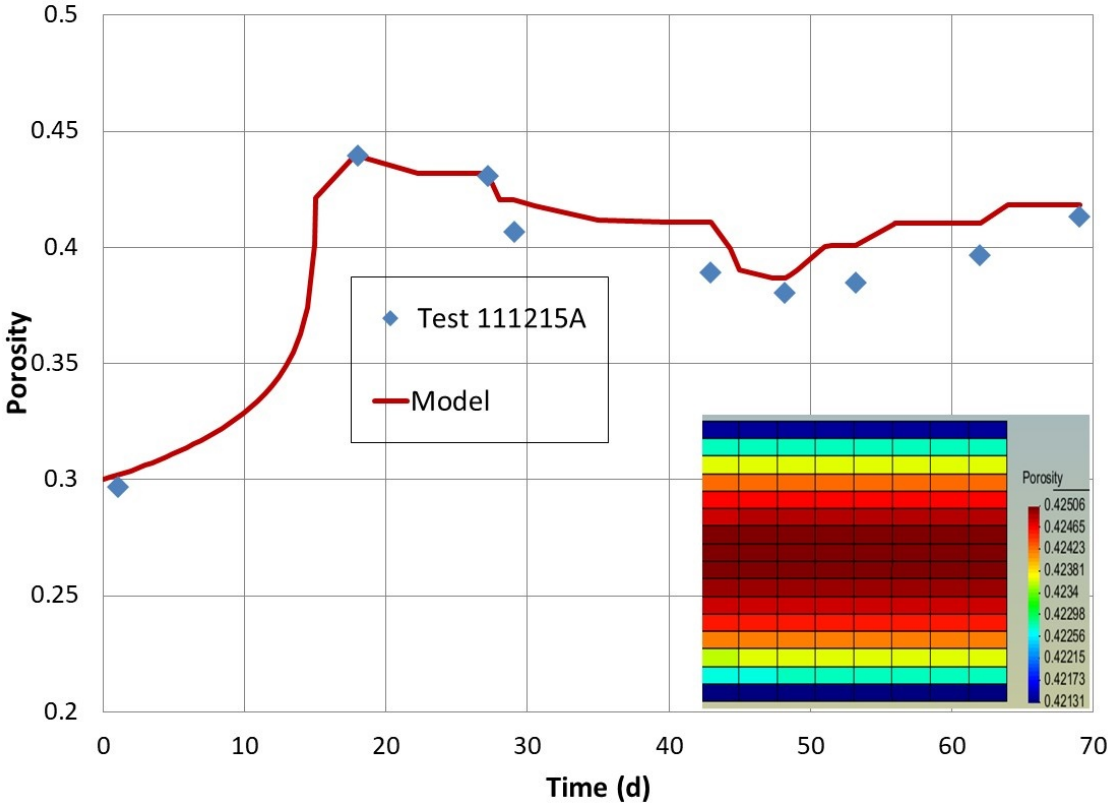

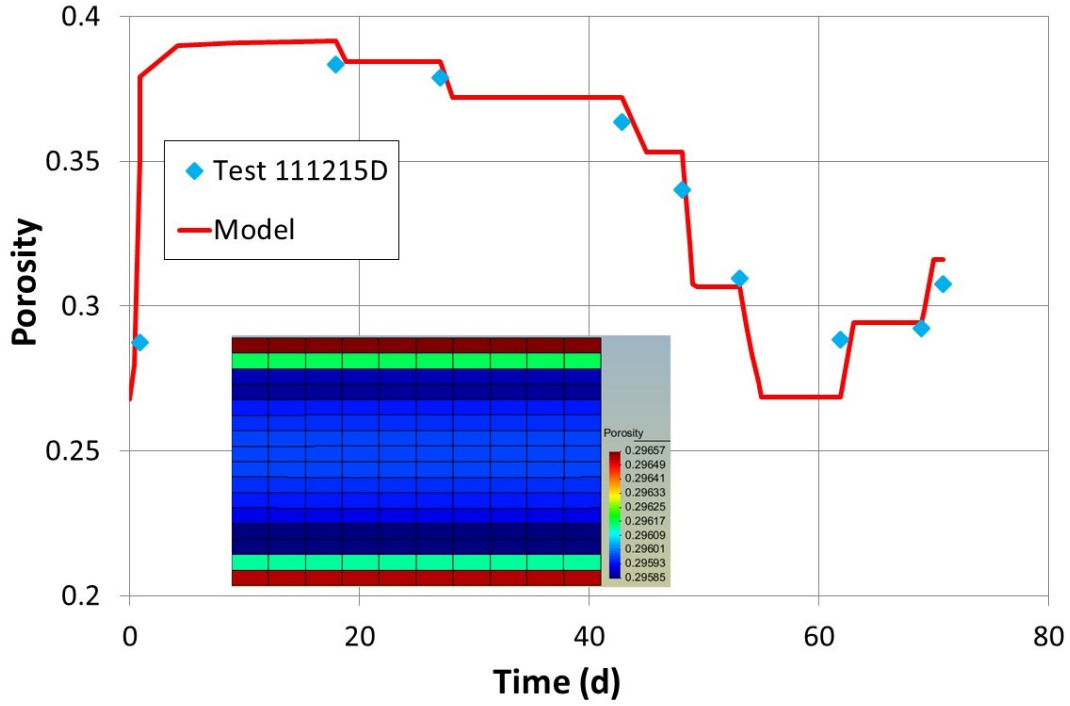

Figure 4-15 Evolution of the porosity in two tests.

Infiltration test for Friedland clay

Data for the infiltration test for Friedland clay is shown in *Table 4-5*. The sample has a 50 mm of diameter and a height of 62 mm. The test is performed under confined conditions. Along the vertical and horizontal boundaries of the domain, displacements are restricted. Water inflow is allowed at the lower boundary of the domain.

Table 4-5 Infiltration test data for Friedland-clay.

Volume (cm^3) V_0	121.74
Wet Sample (g)	229.62
Dry Sample (g)	213.12
Water (g)	16.50
Initial water content (%)	7.7
Initial porosity (%)	37
Initial void ratio	0.59
Initial degree of saturation (%)	37
Dry Density (kg/m^3)	1750
Specific Density (g/cm^3) (Kiviranta et al., 2016)	2.79

The sample was not saturated at the beginning of the test. The degree of saturation was low (37 %). Duration of the test was 13 days.

The same mechanical parameters as for the oedometer tests were used to the numerical simulation of infiltration test.

Figure 4-16 shows the changes of dry density along the vertical cross-section at the end of the 13 days. As the injection point was the lower boundary, dry density decreases more in this domain due to water flooding. Model results have a similar behaviour as compared with the test results.

At the end of the test, the sample is not fully saturated which could be motivated due to the process of sample dismantling. *Figure 4-17* shows how suction changes along the vertical cross-section at the end of 13 days. Results of the model are in accordance with the test results.

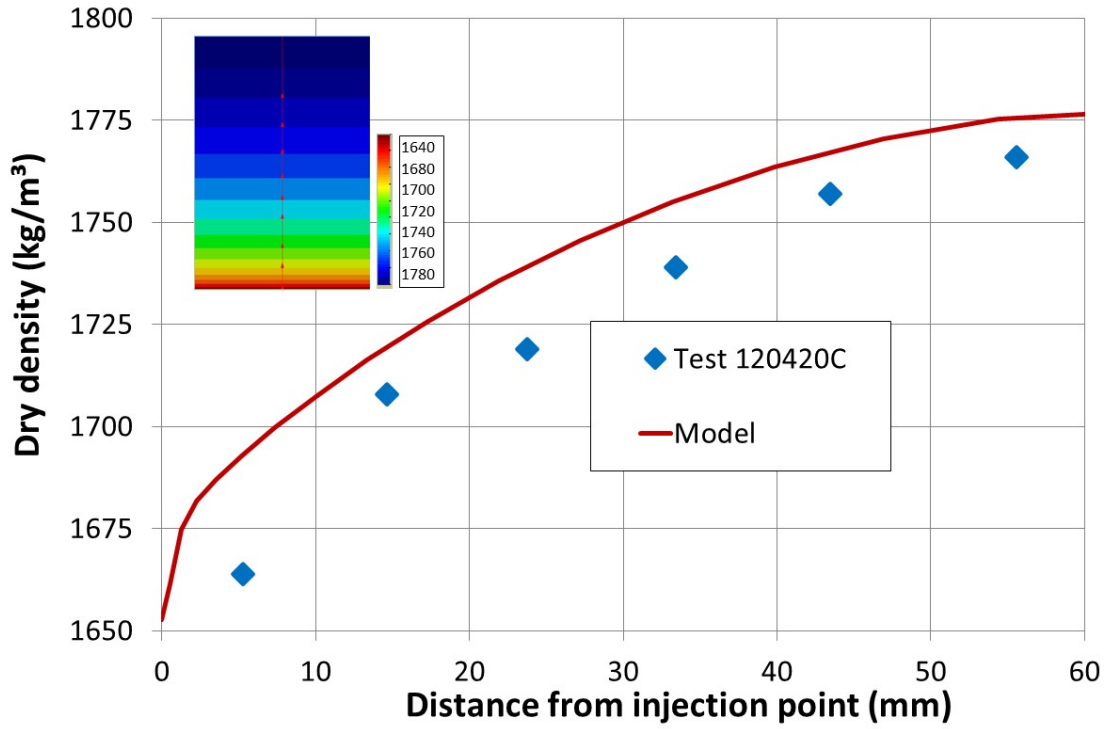

Figure 4-16 Dry density distribution at the end of test.

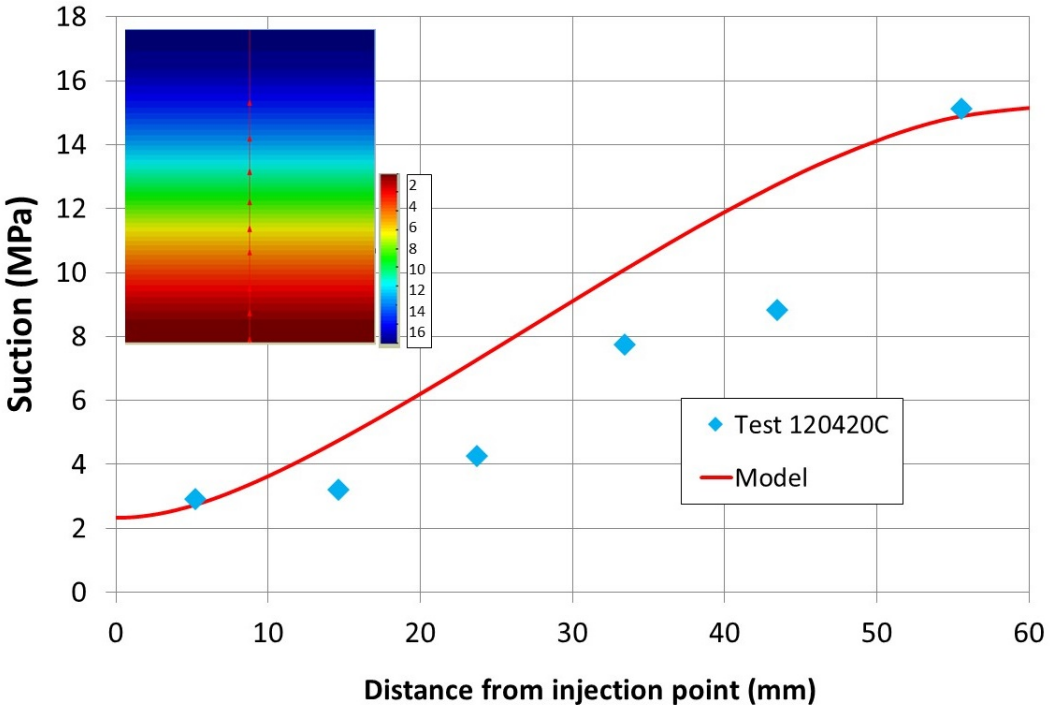

Figure 4-17 Suction distribution at the end of test.

The sample was not fully saturated at the end of the test. Water content changes were proportional to the distance from the injection point. Model results go well with the test results as can be seen in ***Figure 4-18***.

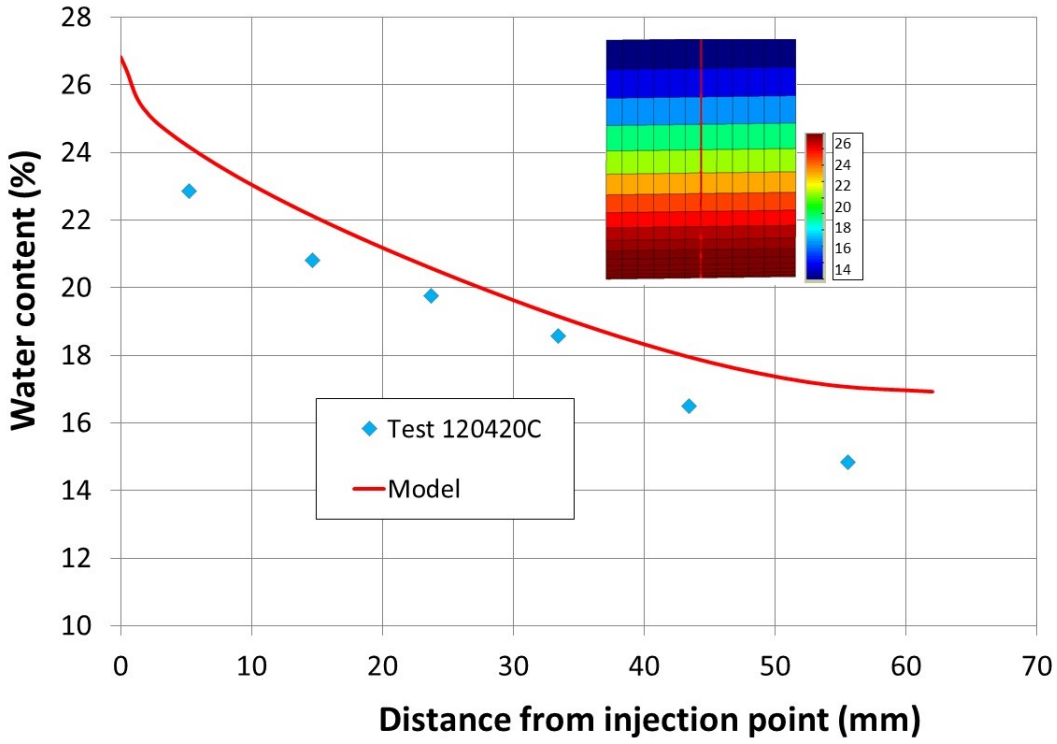

Figure 4-18 Water content distribution at the end of the test.

4.3.2 MX-80

Characterization of the MX-80 (Test 100212c) is detailed in Toprak et al., 2013 which was used to perform preliminary THM simulations. There are three oedometer and three infiltration tests available to investigate the effect of saline water on the hydro-mechanical behaviour of MX-80. Calibrated hydro-mechanical parameters for MX-80 by means of oedometer and infiltration test results are listed in Chapter 4.4 (Table 4-20 and Table 4-21).

The performance of MX-80 according to changes in groundwater salinity is important when the density is relatively low and when the density increases, the impact of the groundwater salinity is lower. Saline groundwater may decrease the swelling pressure and result in an increment in the hydraulic conductivity of buffer. It is fundamental that for the repository to be constructed at the depth of about 500 meters at Olkiluoto, all engineered barriers must be designed to perform properly at groundwater salinities ranging from DI water to 70 g/L. In this study, the salinities ranging 35 (3.5%) to 70 g/L (7%) are investigated. The change in properties in MX-80

due to the presence of salt was described by Karnland et al., 2006 and Martikainen and Schatz (2011) among others.

Oedometer Tests on MX-80: Test 100212c, Test 110222f and 101222a

Initial data for the tests is given in *Table 4-6* Oedometer test data for MX-80*Table 4-6*. Loading and unloading process is summarized in *Table 4-7*. Comparison of hydro-mechanical parameters according to rate of salinity is given *Table 4-8*. In Chapter 5.4, detailed information has been given for impact of rate of salinity for KBS – 3V design.

Figure 4-19 shows the suction-stress path for the three tests. In the Test 101222a (salinity: 7 %) and Test 101222f (salinity: 3.5 %), initial suction was 219 MPa. In the test 100212c, the water used was DI water and initial suction was 153 MPa. This suction was measured in powder before sample compaction.

The void ratio - vertical stress curves for three tests are shown in *Figure 4-19*. The main difference between the three curves is the rate of swelling at the beginning of the tests. It can be clearly observed that the test performed with DI water has a larger swelling capacity. Swelling capacity of the bentonite decreases with the salinity.

Figure 4-20 shows the numerical simulation of the oedometer test for MX-80 with different salinities. The changes in void ratio (*Figure 4-20* for DI water, salinity 3.5 % and salinity 7 %) during the loading-unloading steps have been well simulated.

Table 4-6 Oedometer test data for MX-80

	100212c (DI water)	110222f (Salinity: 3.5%)	101222a (Salinity: 7%)
Dry density (kg/m^3)	1600	1740	1600
Initial water content (%)	6.04	5.1	5.98
Initial suction (MPa)	153	219	219
Salinity (%)	0.0	3.5	7
Initial height (cm)	1.9	1.9	1.9
Initial diameter (cm)	5	5	5

Table 4-7 Loading-suction oedometer test data for MX-80.

100212c (DI water)			110222f (Salinity: 3.5%)			101222a (Salinity: 7%)		
σ_v (MPa)	s (MPa)	e	σ_v (MPa)	s (MPa)	e	σ_v (MPa)	s (MPa)	e
0.23	153	0.64	0.19	219	0.63	0.20	219	0.75
0.23	0	1.23	0.19	0	1.16	0.20	0	1.06
0.39	0	1.22	0.47	0	1.16	0.48	0	1.04
0.95	0	1.12	1.03	0	1.12	1.04	0	0.98
2.63	0	1.0	2.15	0	1.04	1.88	0	0.92
4.88	0	0.87	4.4	0	0.94	3.56	0	0.85
2.63	0	0.89	2.15	0	0.96	5.24	0	0.81
0.95	0	0.96	0.47	0	1.07	1.60	0	0.84
						1.04	0	0.86
						0.48	0	0.90
						0.20	0	0.95
						1.88	0	0.89
						4.12	0	0.83
						1.88	0	0.85

Table 4-8 BBM parameters for different salinities.

Parameters	Symbols	MX-80 DI water	MX-80 Salinity: 3.5%	MX-80 Salinity: 7%
Parameters for elastic volumetric compressibility against suction change	κ_{s0}	0.09	0.065	0.05
Intrinsic permeability (m^2)	k	$5.59x10^{-21}$	$1.6x10^{-20}$	$2x10^{-20}$

*For parameters κ_{s0} and k (m^2) a mean value has been adopted by calibration of several infiltration and oedometer tests.

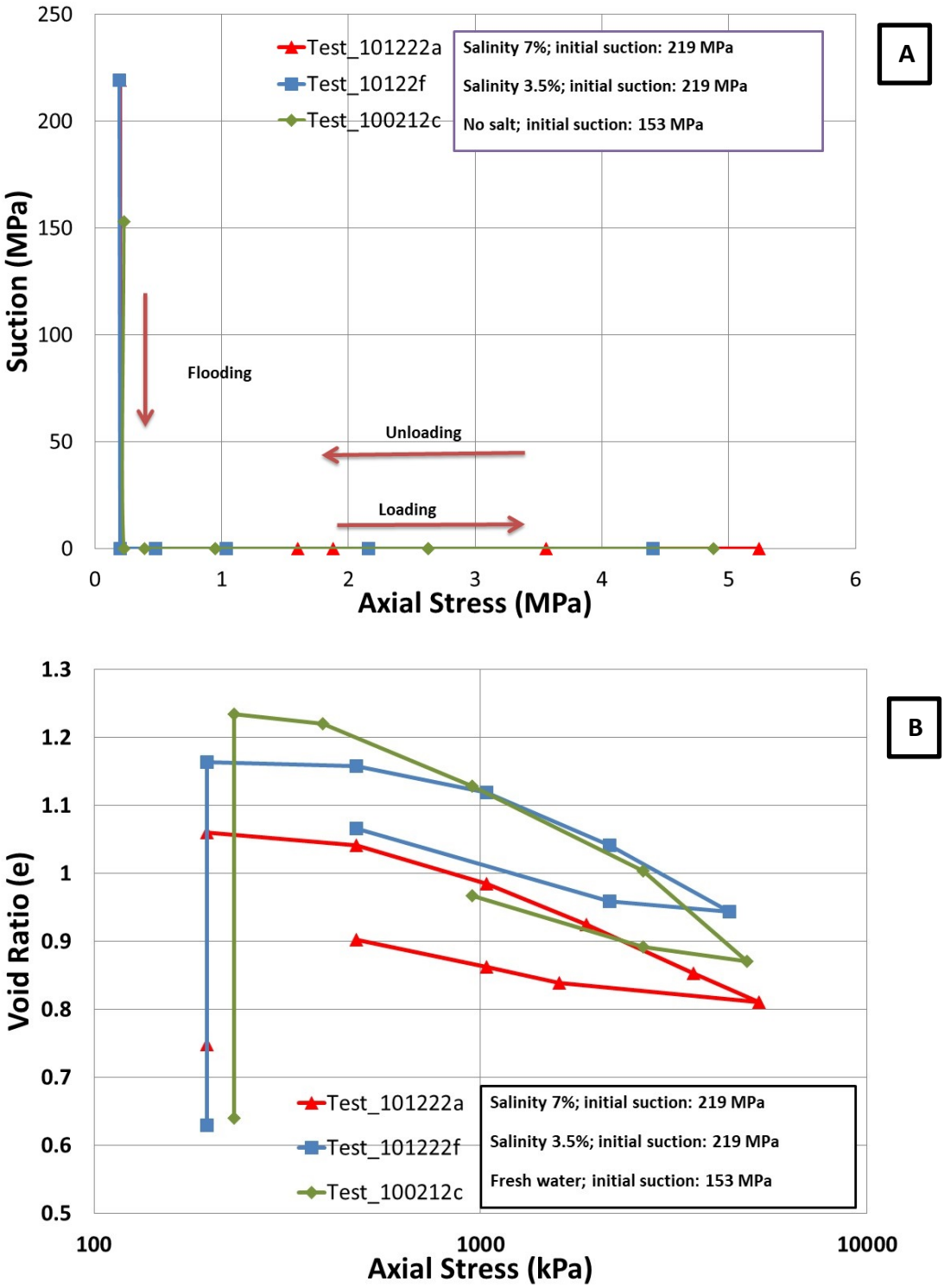

Figure 4-19 Suction-axial stress path (A) and void ratio versus axial stress (B) of the oedometer tests for DI water, 3.5% and 7% saline water.

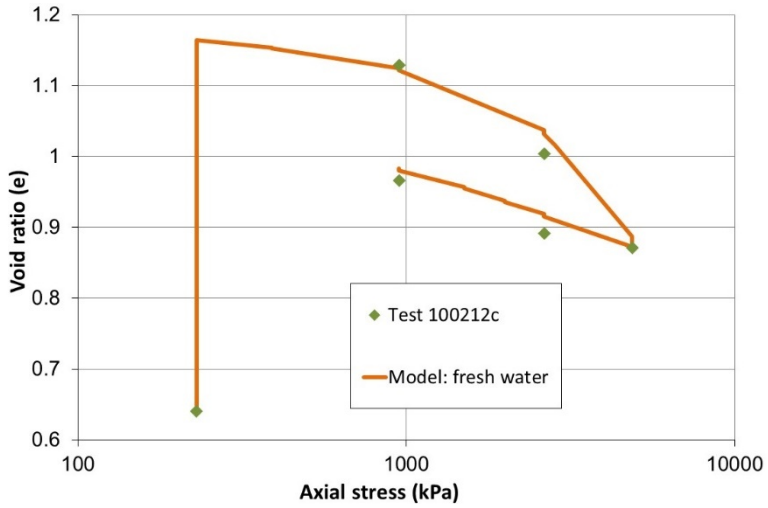

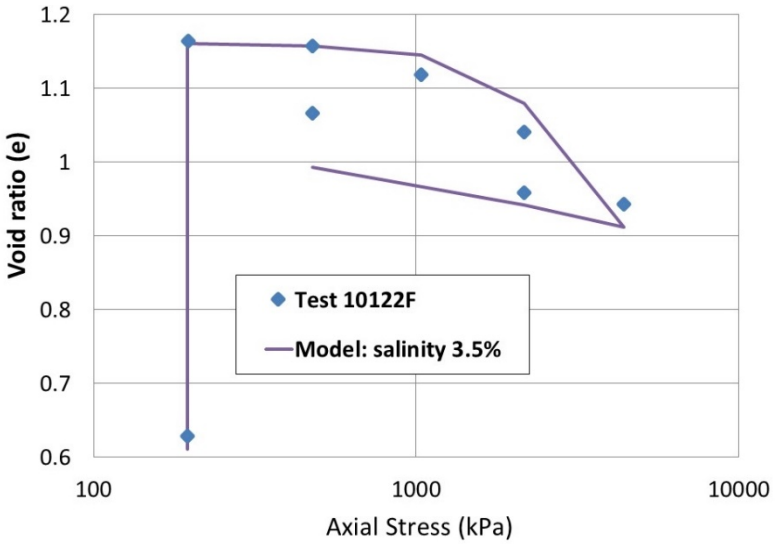

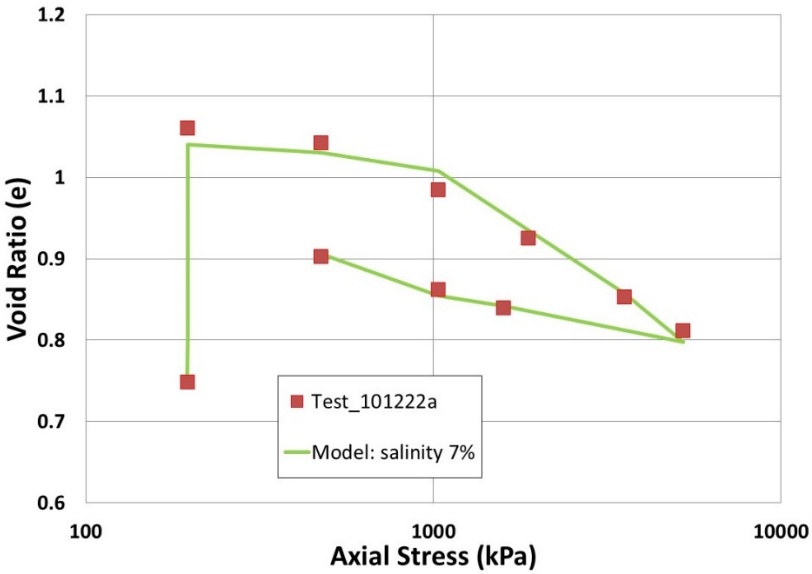

Figure 4-20 Void ratio versus axial stress tests and model. DI water (A), 3.5 % saline water (B) and 7 % saline water (C).

Infiltration tests for MX-80: Test 100108a, Test 101027a and 100623a

The initial properties, test ID and rate of salinity for MX-80 are summarized in Table 4-9. The initial suction was measured in powder, before the compaction of the samples. The salinity varies from 3.5% to 7%. The rest of the initial conditions in infiltration tests were similar. The material used was characterized by Kiviranta and Kumpulainen (2011). The material was named Volclay in that report.

The comparison of generated maximum swelling pressures in the infiltration tests with different salinities is shown in Figure 4-21. When the test was performed with DI water, the maximum swelling pressure succeeded was almost 10 MPa. When salinity was 3.5 %, the maximum swelling pressure of the sample had a value of 8 MPa. In a higher salinity (7 %), swelling pressure of MX-80 decreases to 7 MPa. It can be concluded that swelling pressures decreases with the salinity.

Figure 4-21 shows final water content according to distance from injection point. Although the initial water content and the duration of the tests were not the same in the samples, it can be seen that there are hydraulic behaviour changes according to salinity.

Figure 4-22 shows model performance over the test results. The salinity is 3.5 % in *Figure 4-22*. Reached maximum swelling pressure value is 8 to 9 MPa both in the model and test. The swelling pressure decreases where the salinity is 7% (*Figure 4-22*). Test results are correctly captured with the numerical simulation.

The detailed numerical simulation of infiltration test for DI water (Test 100108a) has been carried out by Toprak et al., 2013.

Table 4-9 *Initial conditions of infiltration tests for MX-80*

	Test 100108a (DI water)	Test 101027a (Salinity: 3.5%)	Test 100623a (Salinity: 7%)
Dry density (kg/m^3)	1700	1670	1670
Initial water content (%)	5.33	7.22	6.94
Initial Saturation degree	23.3	30.1	29.2
Salinity (%)	0.0	3.5	
Initial height (cm)	6.3	6.3	6.3
Initial diameter (cm)	5	5	5
Duration (days)	69	112	89

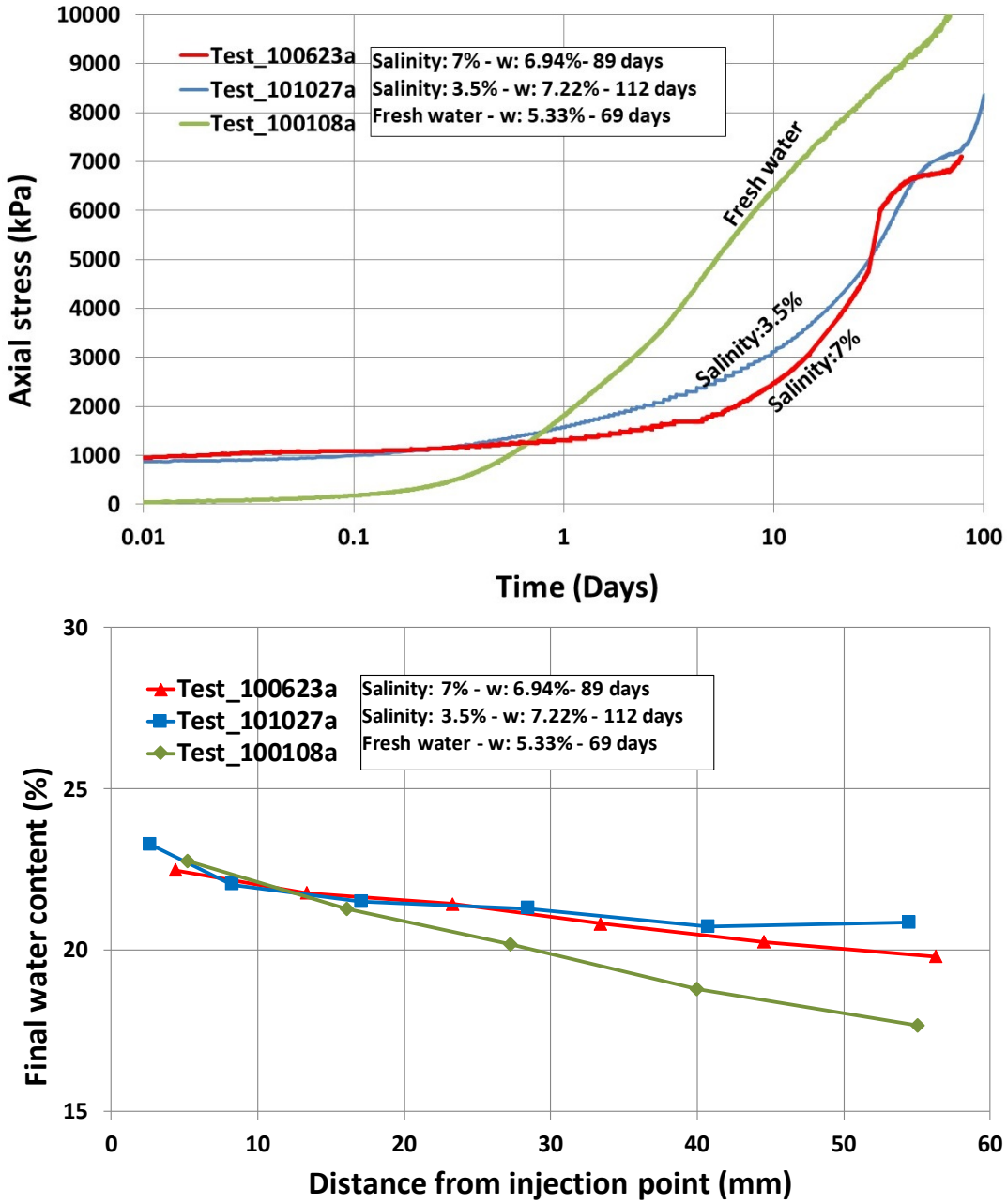

Figure 4-21 *Generated axial stresses during the tests and final water content according to the distance from injection point at the end of the tests.*

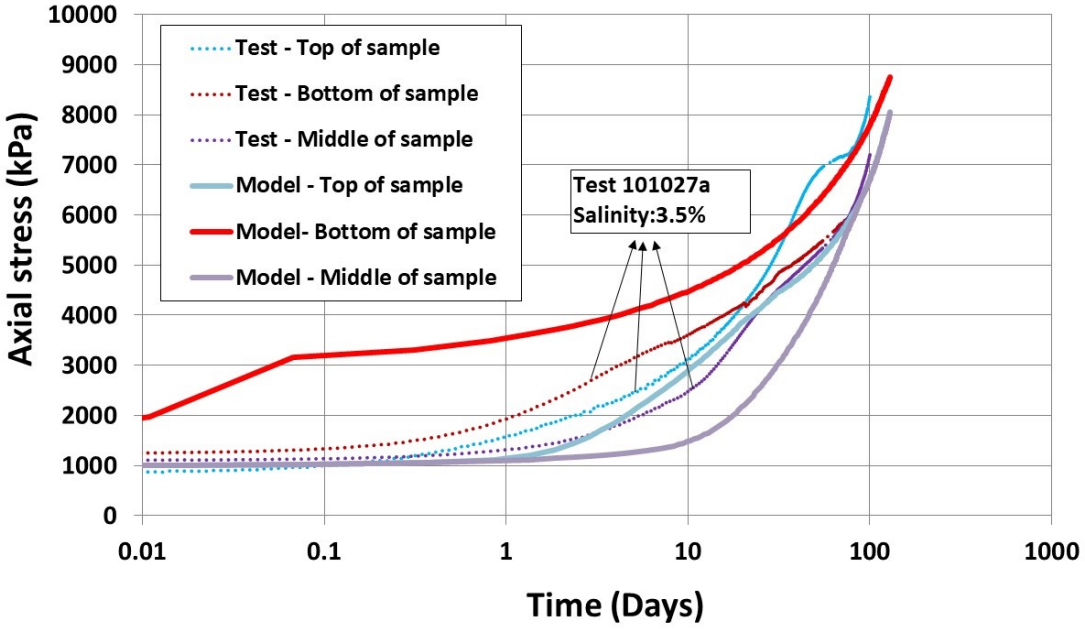

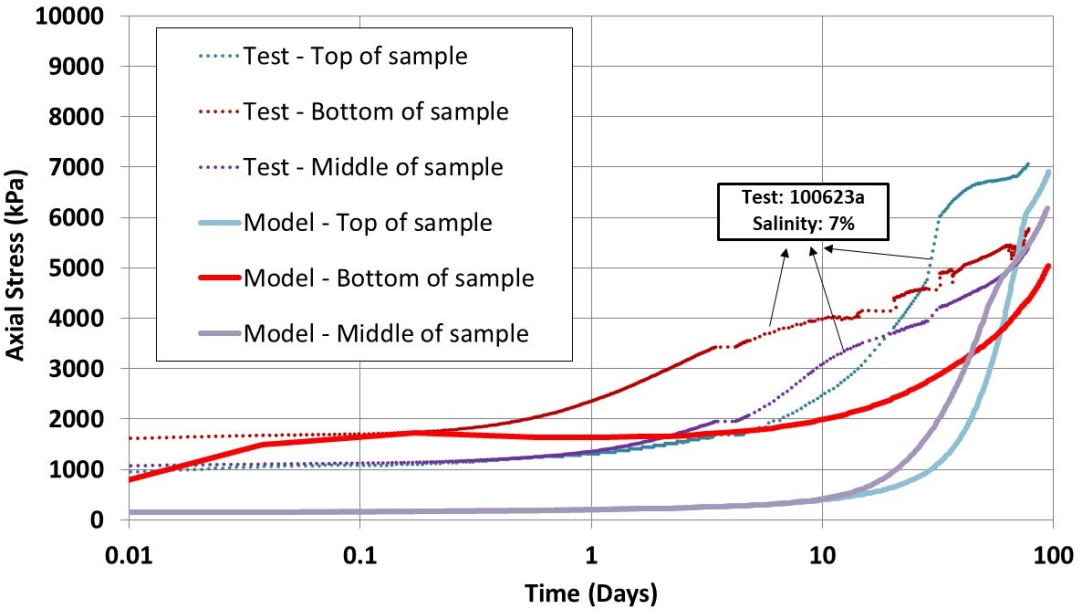

Figure 4-22 Swelling pressures reached in the tests and the models. 3.5 % saline water and 7 % saline water.

4.3.3 Pillow Pellets

An oedometer test and an infiltration test have been simulated to calibrate hydro-mechanical parameters of pillow pellets. Double structure of pellet based materials has been considered for numerical simulation. BexM (Barcelona Expansive Model) have been used to simulate hydro-mechanical response of pellets. Calibrated hydro-mechanical parameters for pillow pellets by

means of oedometer and infiltration test results are listed in Chapter 4.4 (Table 4-24, Table 4-25 and Table 4-26).

Oedometer test on Pillow pellets: Test 131118a

Test data and information for loading-unloading process is given in Table 4-10 and Table 4-11 respectively. The changes in void ratio during the loading-unloading step after the saturation of the sample in the oedometer test are well simulated. The results are presented in *Figure 4-23* for three set of parameters (κ^{micro}*=0.045;* κ^{micro}*=0.09 and* κ^{micro}*=0.135*). The evolution of porosity as a function of time is shown in *Figure 4-23*. The loading of the sample causes a decrease of both macro porosity and total porosity. During compression, microporosity increases somewhat according to model calculations. This is not surprising as it is defined with respect to the total volume of the sample. During unloading, macropores are elastically recovered.

Table 4-10 Oedometer test 131118a data for pillow pellets.

Initial water content (w)	16.05 %
Height:	25.6 mm
Diameter:	70 mm
Initial dry density:	947.66 kg/m^3
Initial weight:	108.29 g

Table 4-11 Oedometer Test 131118a loading-unloading data for pillow pellets after the saturation.

Loading steps (MPa)	Porosity changes
0.14	0.66
0.14	0.64
0.43	0.60
1.00	0.58
2.14	0.57
3.15	0.57
2.14	0.57
1.00	0.59
0.43	0.61

During the flooding of the sample, there was a small collapse of 0.7% in axial strains. This was due to the open structure of the pellets and the low density, so the swelling of the pellets could not compensate the collapse of the macroporosity related with the big voids between pellets.

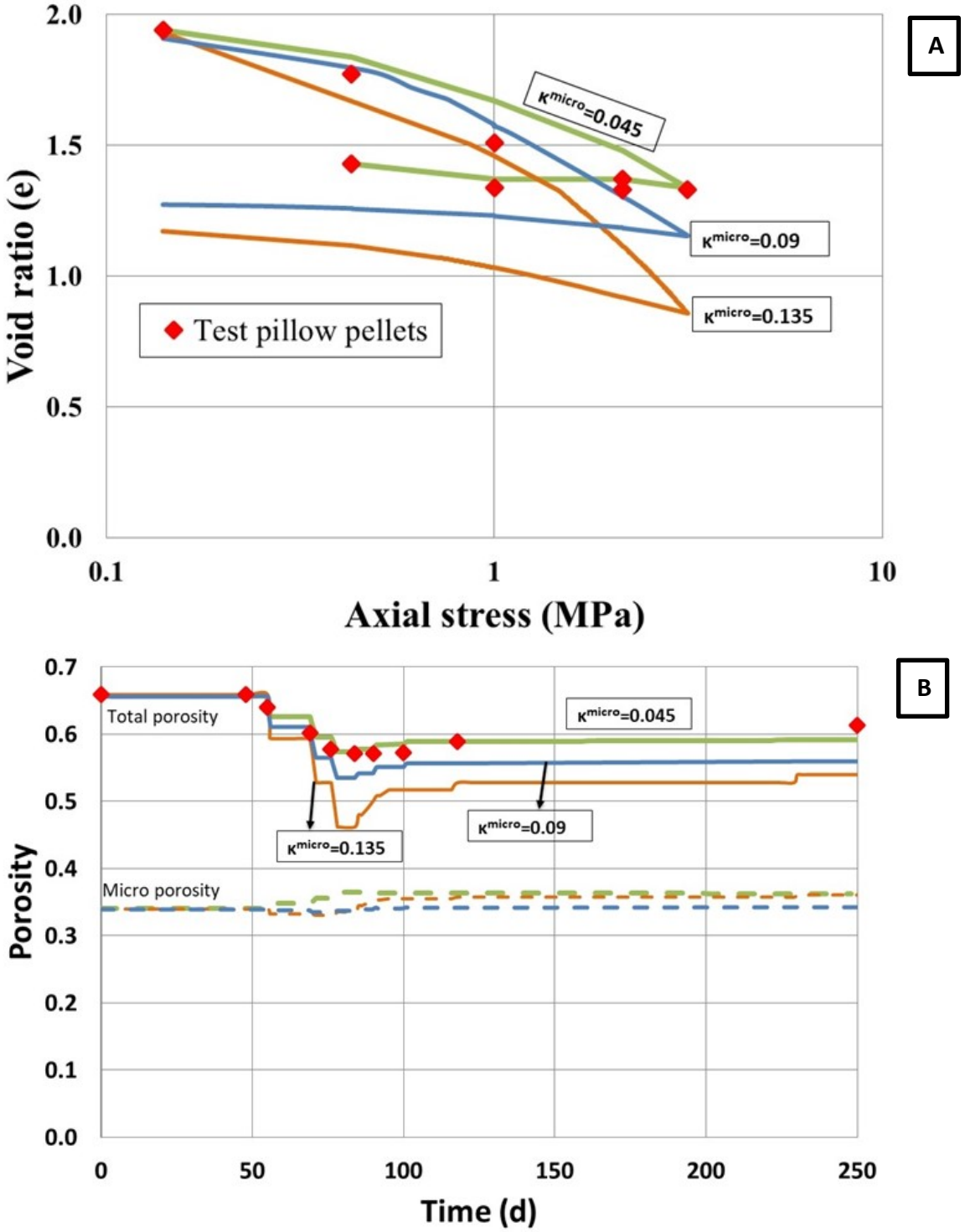

Figure 4-23. *Void ratio vs. axial stress (A) and porosity vs. time (B) in the oedometer test for pillow pellets, three set of parameters (κ^{micro}=0.045; κ^{micro}=0.09 and κ^{micro}=0.135) are subjected to sensitivity analysis (experimental and model results).*

Infiltration test on pillow pellet: Test 1412191A

An infiltration test has been simulated for pillow pellets. Test data is given in Table 4-12 and results are summarised in Table 4-13.

Table 4-12 Infiltration test 1412191a data for pillow pellets

Initial water content (%)	16.80
Height (mm):	80.4
Diameter (mm):	50
Initial dry density (kg/m^3):	891
Initial weight (g):	108.29
Initial degree of saturation (%)	22.0

Table 4-13 Infiltration test 1412191a results for pillow pellets

Height (mm)	w (%)	s (MPa)	T (ºC)
71.72	65.0	3.76	21.50
55.78	66.3	3.37	21.90
39.85	71.6	2.43	22.30
23.91	76.4	2.59	22.60
7.97	85.6	2.70	23.20

One of the objectives of this work is to apply a model for the hydration of pellets and contribute to demonstrate its interest. A relevant issue on the hydro-mechanical response of pellets is the intrinsic permeability. It is assumed here that intrinsic permeability is a function of macro porosity with the following form:

$$\mathbf{k} = \mathbf{k_0} \exp\left(b(\phi^{Macro} - \phi_0^{Macro})\right) \tag{4.3-1}$$

where $\mathbf{k}_0$ is a reference intrinsic permeability tensor, b is a parameter and ϕ_0^{Macro} is reference macro porosity. During the test, macro porosity decreases due to the swelling of the pellets, and this happens at all points of the sample which is subjected to hydration at constant volume. As intrinsic permeability is considered a function of macro porosity, intrinsic permeability reduces due to macro porosity reduction.

The MIP has been performed in a sample with a dry density of 1750 kg/m^3 and in a pillow pellet, which dry density was expected to be 1800 kg/m^3. The results can be seen in Figure 4-24-A. The first maximum is clear and it is the same for both materials. This maximum is associated with the microporosity. The second maximum, associated with the macroporosity, is clear in the

compacted sample and not as clear in pellet. The voids between pellets (3rd level of porosity) are not presented in this Figure.

Figure 4-24-B shows calculated variables for the infiltration test. It displays the evolution of macro, micro and total porosity close to the top of the sample.

The pillow pellets were subjected to 31 days of water infiltration. As can be seen in Figure 4-25, macro pores of the sample were almost invisible after hydration. The transition from a pellet discontinuous arrangement to a more homogeneous material, which is visible in Figure 4-25, is a feature that the BExM model can represent to some extend while BBM does not include.

Figure 4-25 also shows the final profile of dry density and of suction along the sample, as a function of the distance from the injection point. The numerical simulation reproduces well the measurements at the end of the test, except for the suction near the injection point. The sample was still not completely saturated when the test was dismantled. It has already been mentioned that it is possible that unloading may have induced a small suction increment or drying out has taken place during the test dismantling and measurement operations.

Two set of parameters ((κ^{micro}=0.045 and κ^{micro}=0.135) are considered for modelling the infiltration test. The total porosity of the sample remains constant during infiltration for both sets of parameters. However, microporosity increases because of the expansion of the pellets and there is a consequent reduction of macroporosity. At the end of the test, macropores have reduced, more significantly for the case that uses a larger parameter (i.e. κ^{micro}=0.135) for the microstructure swelling.

A larger κ^{micro} value seems essential for the infiltration test, it is necessary to obtain a significant increase of micro pores (swelling of pellets) and a corresponding reduction of macro pores (occupied by the swollen pellets). In contrast, for the case of the oedometer test simulation, a lower value is required in order to correctly capture the compression and expansion, respectively, during loading and unloading.

As it is not possible to model both tests with the same set of parameters, it seems that a modification of the BExM would be necessary in order to separate the elastic deformations of the micro structure by splitting the gradient of *p* and *s* into two contributions and hence, having two different values for (κ^{micro}), instead of one. This seems to indicate that the model BExM, in its current form is adequate for modelling double structure clays rather than for pellet-based

materials. In this context, it is likely that pellets would require a triple structure model. The new contribution to deformations can be referred to as deformation at the meso scale.

$$d\varepsilon_{kl} = d\varepsilon_{kl}^{Macro} + d\varepsilon_{kl}^{meso} + d\varepsilon_{kl}^{micro} \tag{4.3-2}$$

The idea is that deformation of the pellets is motivated by a combination of the meso structure and a micro structure. The micro structure can be a function of (*p*+*s*) because this is related to the deformation of the micro pores of the clay aggregates, which remain practically saturated even when suction develops. The meso structure can be represented by independent terms related to mean net stress and to suction. Finally, macro structure deformations correspond to the deformation associated with pellet reorganization. Development of this kind of model is not straightforward as it requires the incorporation of interaction functions and, at present, there is not enough experimental data. In addition, standard tests such as infiltration and oedometer tests might not be able to supply enough information for the calibration of the models. The triple structure in pellets has been identified by Hoffmann (2005), Hoffmann et al. (2007) and Alonso, et al. (2011) in FEBEX pillow pellets.

The evolution of intrinsic permeability and its product by relative permeability (total permeability is defined as the product of intrinsic and relative permeability =$\mathrm{k}k_{rl}$) is depicted in Figure 4-26. The intrinsic permeability is considered as a function of macro porosity as it was indicated above. It has a lower value at the end of the test because of the macro pores close (more significantly, when the microstructure swells more, i.e. when κ^{micro} for infiltration test is used). The model gives a small variation of the product of intrinsic permeability and relative permeability although each one undergoes large variations. Intrinsic permeability decreases because macro-pores tend to close while relative permeability increases because the material is in a process of saturation. An improved model would require a combination of fluxes through macro pores and micro pores (or even meso pores), at least for the conditions that pellets swell and macro porosity vanishes (Alonso and Navarro, 2005 and Navarro et al., 2014a).

The developed stresses during the infiltration tests are shown in Figure 4-26. The stresses developed range from 1.75 to 2.25 MPa depending on the κ^{micro} used.

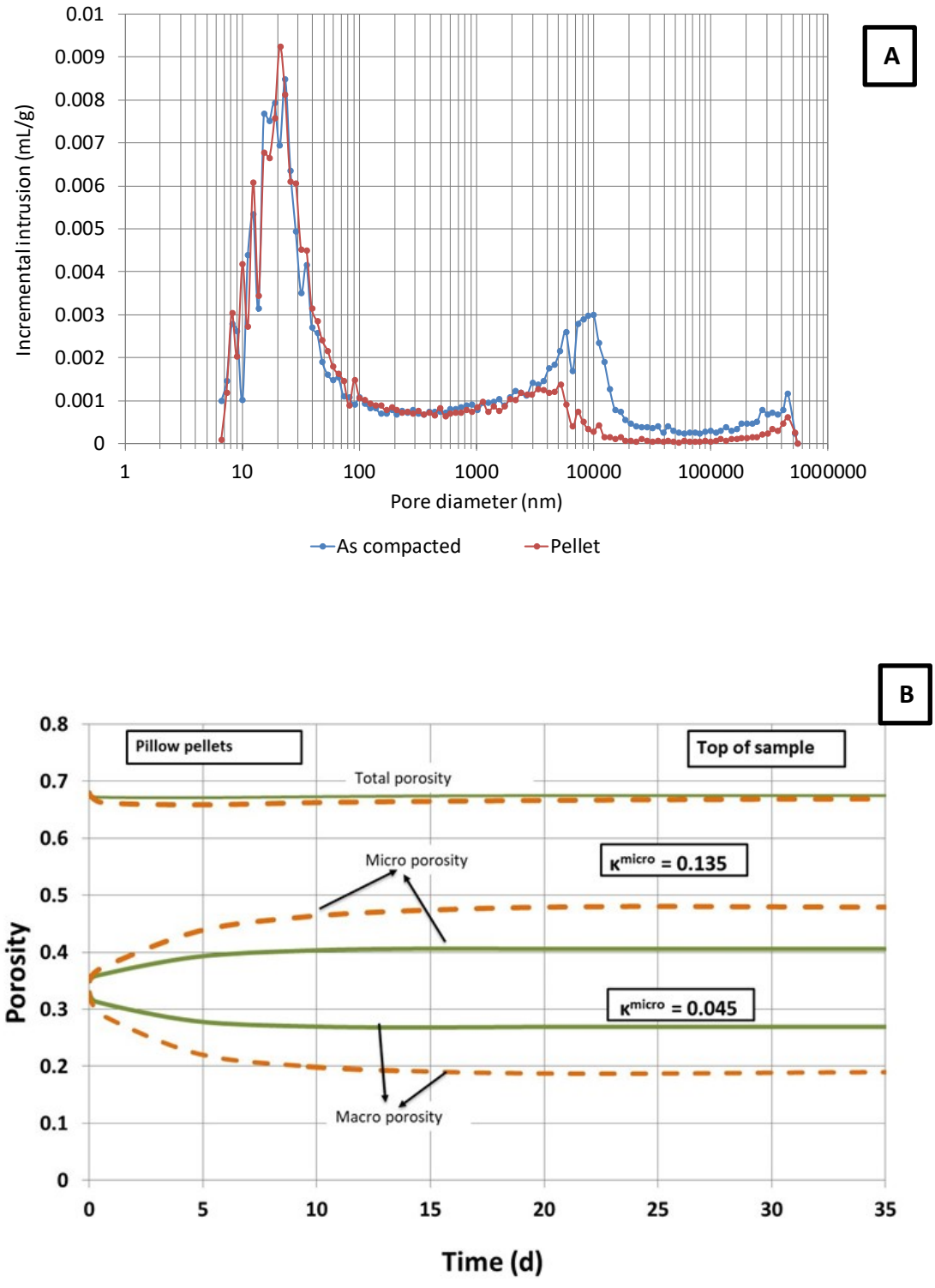

Figure 4-24. Mercury intrusion porosimetry in a compacted sample and in pellet *(A). Calculated evolution of porosity on the top of the sample for pillow pellets, (model results). Two set of parameters (κ^{micro}=0.045 and κ^{micro}=0.135) are subjected to sensitivity analysis (B).*

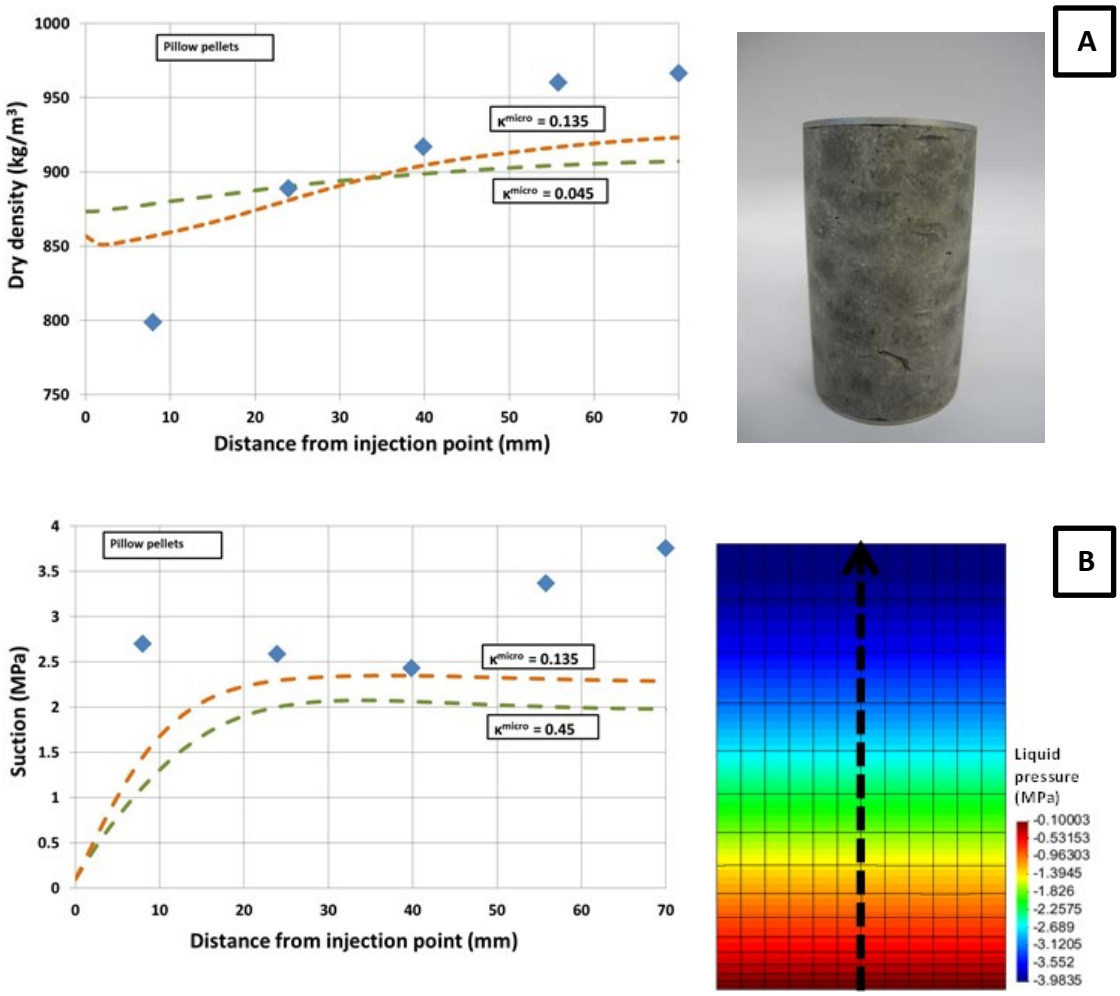

Figure 4-25.*Distribution of dry density (A) and suction (B) as a function of distance from injection point for pillow pellets at the end of the test: 31 days, Two set of parameters (κ^{micro}=0.045 and κ^{micro}=0.135) are subjected to sensitivity analysis (experimental and model results).*

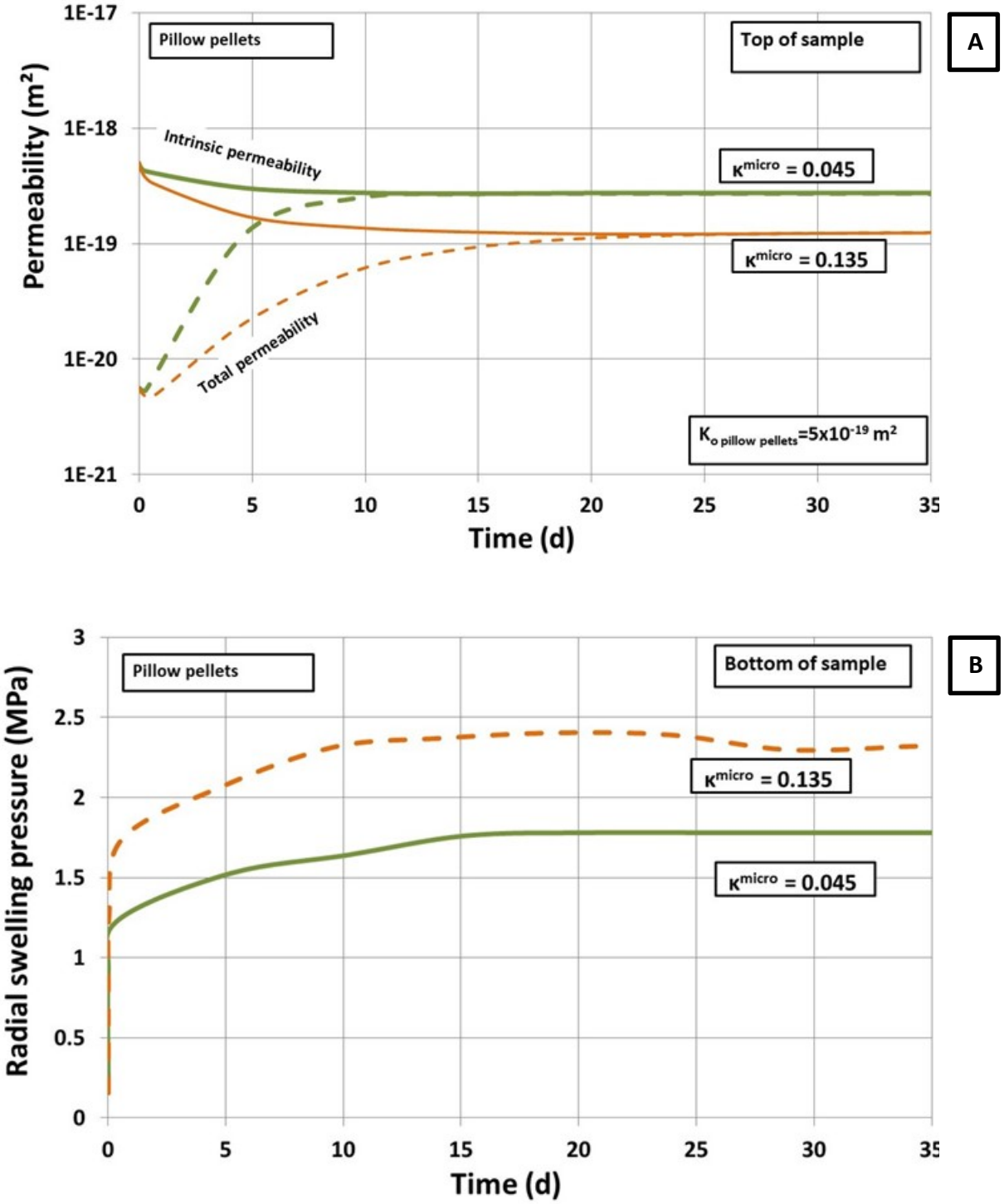

Figure 4-26 *Evolution of permeability (A) and radial stress (B) for infiltration tests on pillow pellets, (model results Two set of parameters (κ^{micro}=0.045 and κ^{micro}=0.135) are subjected to sensitivity analysis.*

4.3.4 Rod Pellets

Infiltration and oedometer tests carried out by SROY for rod pellets to examine the hydro-mechanical response of the material. Calibrated hydro-mechanical parameters for rod pellets by means of oedometer and infiltration test results are listed in Chapter 4.4 (Table 4-24, Table 4-25 and Table 4-26).

Oedometer test on rod pellets: Test 140912

Initial data-conditions of the sample and loading-unloading information of oedometer test for rod pellets are given in Table 4-14 and Table 4-15 respectively. The response of the material in the oedometer test for three sets of parameters (κ^{micro}=0.045; κ^{micro}=0.09 and κ^{micro}=0.135) are presented in Figure 4-27. This plot shows the void ratio versus vertical stress response showing the elastoplastic loading and the elastic unloading. The calculated evolution of total porosity is compared with the measurements (Figure 4-27), and this plot is completed with the predictions using the constitutive model of total porosity, micro porosity and macro porosity. It can be observed that the response of the numerical simulation is good. The model can successfully reproduce total porosity changes under loading and unloading cycles.

Table 4-14 *Oedometer* Test 140912 data for rod pellets

Total mass (g):	67.44
Diameter (mm)	50
Height (mm):	36.53
Initial water content (%):	14.4
Initial dry density (kg/m^3):	820
Density of solids (kg/m^3) (Kiviranta and Kumpulainen, 2011)	2837

Table 4-15 *Oedometer* Test 140912 loading-unloading information rod pellets

Loading - Axial stress (MPa)	Porosity	Unloading - Axial stress (MPa	Porosity
0.96	0.70	4.400	0.61
1.037	0.66	3.279	0.62
2.158	0.64	2.158	0.62
3.279	0.63	1.037	0.63
4.400	0.62	0.96	0.65
6.082	0.61		

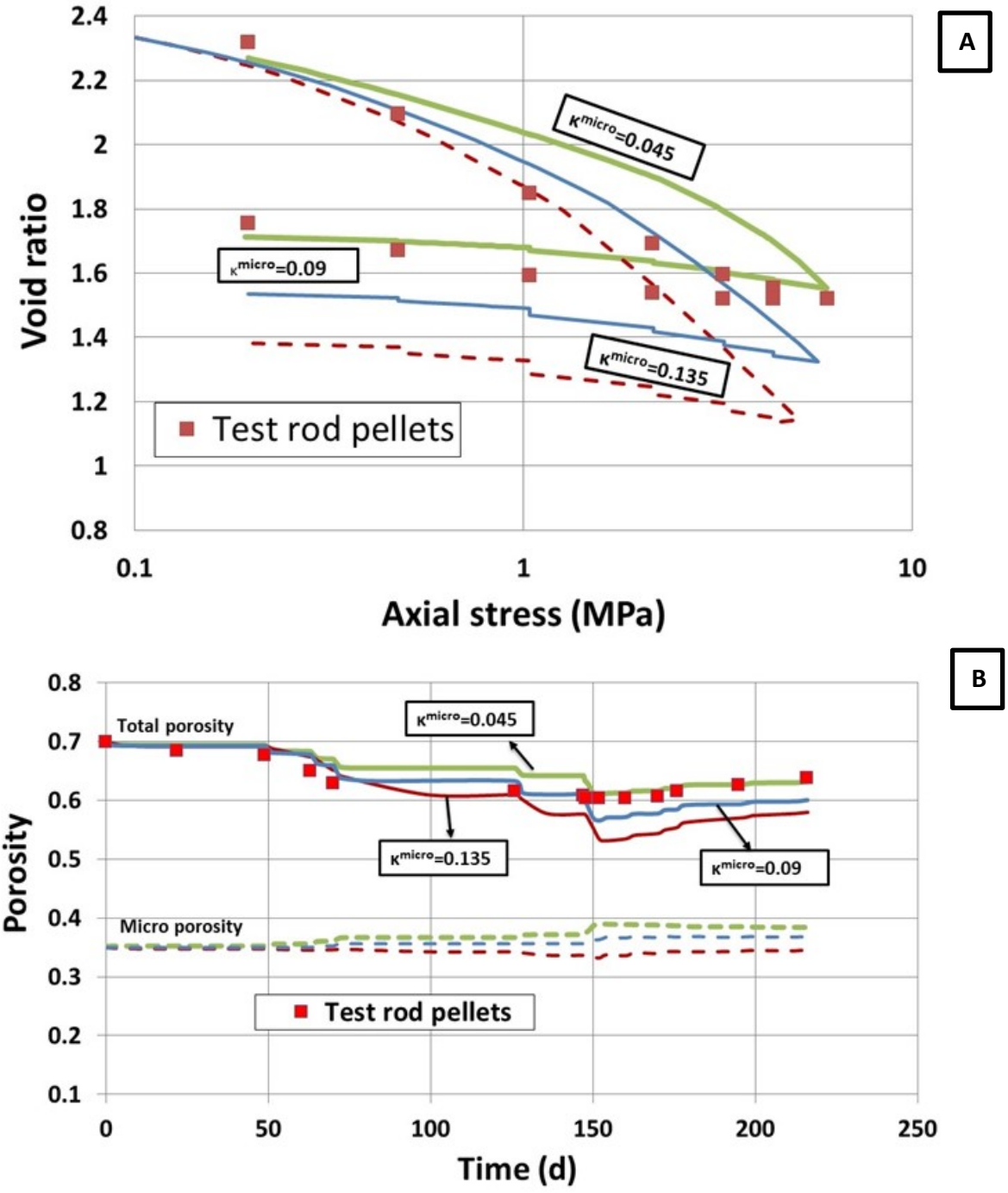

Figure 4-27. *Void ratio vs. axial stress (A) and evolution of total, macro and micro porosity (B) for rod pellets, three set of parameters (κ^{micro}=0.045; κ^{micro}=0.09 and κ^{micro}=0.135) are subjected to sensitivity analysis (experimental and model results).*

Infiltration test on rod pellets: Test 131030C

Initial conditions for the sample is given in Table 4-16. Infiltration test results are summarised in Table 4-17.

Table 4-16 *Infiltration* Test 131030C data for rod pellets

Total mass (g):	67.44
Diameter (mm)	50
Height (mm):	78.7
Initial water content (%):	18.5
Initial dry density (kg/cm^3):	867
Initial degree of saturation (%)	23

Table 4-17 *Infiltration* Test 131030C results for rod pellets

Height (mm)	w (%)	s (MPa)	T (ºC)
64.53	65.8	4.13	22.4
50.19	63.9	2.53	24
35.85	64.8	2.9	24.1
21.51	67.4	2.57	24.3
7.17	80.8	2.65	24.3

Figure 4-28 shows the evolution of macro, micro and total porosity at the top of the sample during the infiltration test. The total porosity of the sample remains nearly constant.

Figure 4-29 shows the final distribution of dry density (A) and suction (B) of the sample in the infiltration test as a function of distance from the injection point. The numerical simulation reproduces well the test results for the dry density distribution. At the end of the test, the sample seems to be still unsaturated, since some remaining suction values were measured. However, this may be caused by drying and uncompressing during test dismantling.

The evolution of intrinsic permeability and its product by relative permeability are depicted in Figure 4-30. Figure 4-30 displays curves for two sets of parameters which differ only in the value of κ^{micro} used. The reference value of intrinsic permeability for rod pellets in the infiltration tests is calibrated as 1.4x10^{-18} m^2. Macro porosity is set as 0.307 and total porosity is 0.657. The developed stresses during the infiltration tests are shown in Figure 4-30. The stress developed ranges from 2.75 to 3.5 MPa depending on the κ^{micro} used.

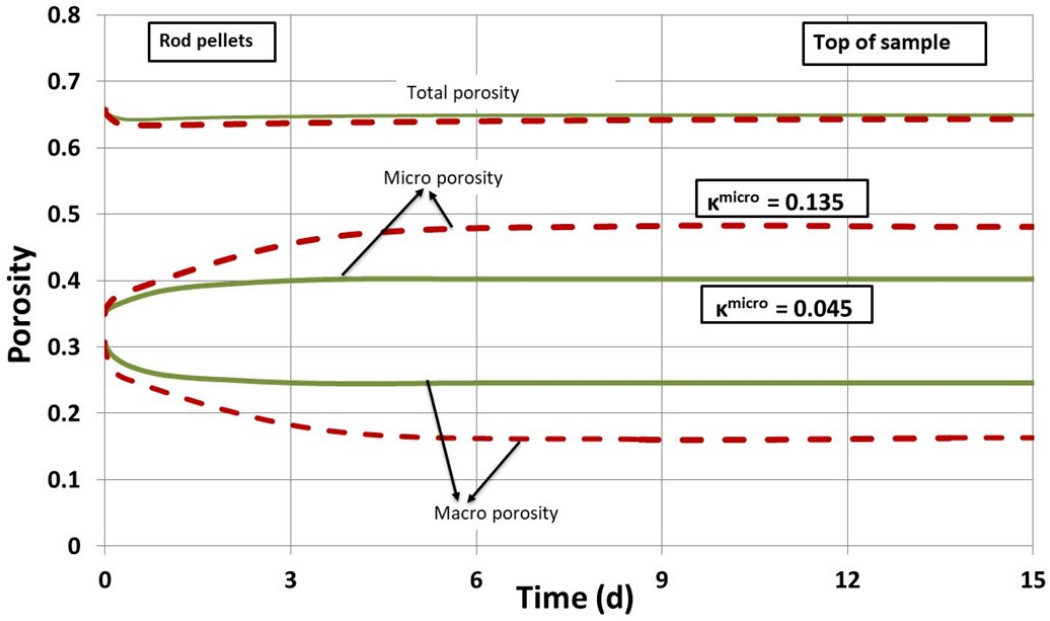

Figure 4-28. *Evolution of porosity at the top of the sample for rod pellets (model results). Two set of parameters (κ^{micro}=0.045 and κ^{micro}=0.135) are subjected to sensitivity analysis.*

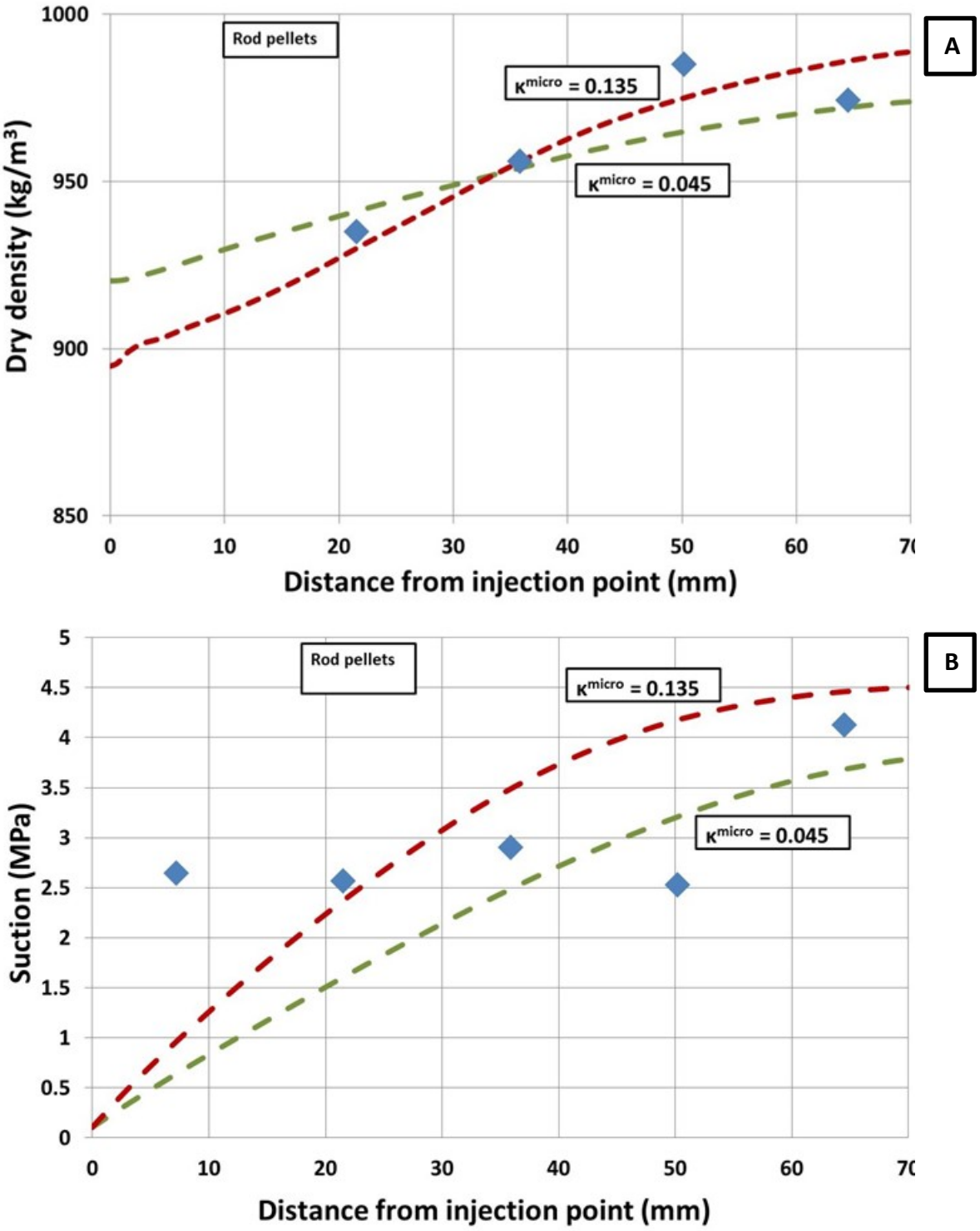

Figure 4-29. *Distribution of dry density (A) and suction (B) as a function of distance from injection point for rod pellets at the end of the test: 15 days, Two set of parameters (κ^{micro}=0.045 and κ^{micro}=0.135) are subjected to sensitivity analysis (experimental and model results).*

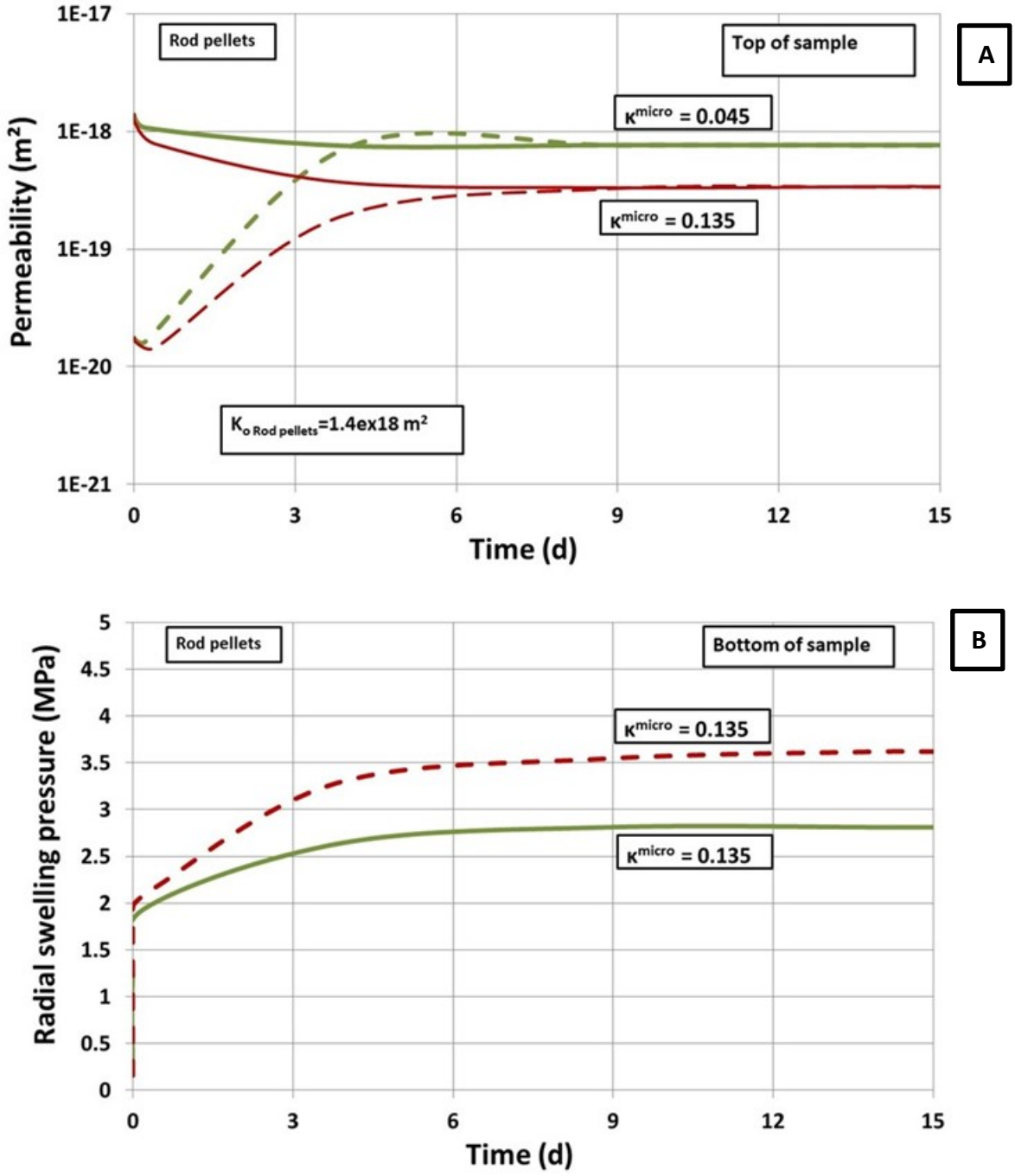

Figure 4-30. *Evolution of permeability (A) and radial stress (B) for infiltration tests on rod pellets, (model results). Two set of parameters (κ^{micro}=0.045 and κ^{micro}=0.135) are subjected to sensitivity analysis*

4.3.5 Minelco Granules

To examine HM behaviour of minelco granules, an infiltration test has been simulated. Initial conditions for sample and test results are given in Table 4-18 and Table 4-19 respectively. Calibrated hydro-mechanical parameters for minelco granules by means of infiltration test results are listed in Chapter 4.4 (Table 4-25 and Table 4-26).

Figure 4-31 shows the final distribution of dry density and suction of the sample in the infiltration test as a function of distance from the injection point. The numerical simulation reproduces well the test results for the dry density and suction distribution. At the end of the test, the sample seems to be still unsaturated, since some remaining suction values were measured.

Table 4-18 *Infiltration* Test 140508A data for Minelco granules

Porosity	0.55
Diameter (mm)	50
Height (mm):	7.84
Initial water content (%):	13.9
Initial dry density (kg/m^3):	1240
Initial degree of saturation	31

Table 4-19 *Infiltration test 140508A results for Minelco granules.*

Height (mm)	w (%)	s (MPa)	T (ºC)
71.23	32.7	6.90	25.3
55.40	32.1	4.09	25.8
39.57	39.1	3.44	25.4
23.74	43.9	2.27	25.4
7.91	49.9	1.99	25.3

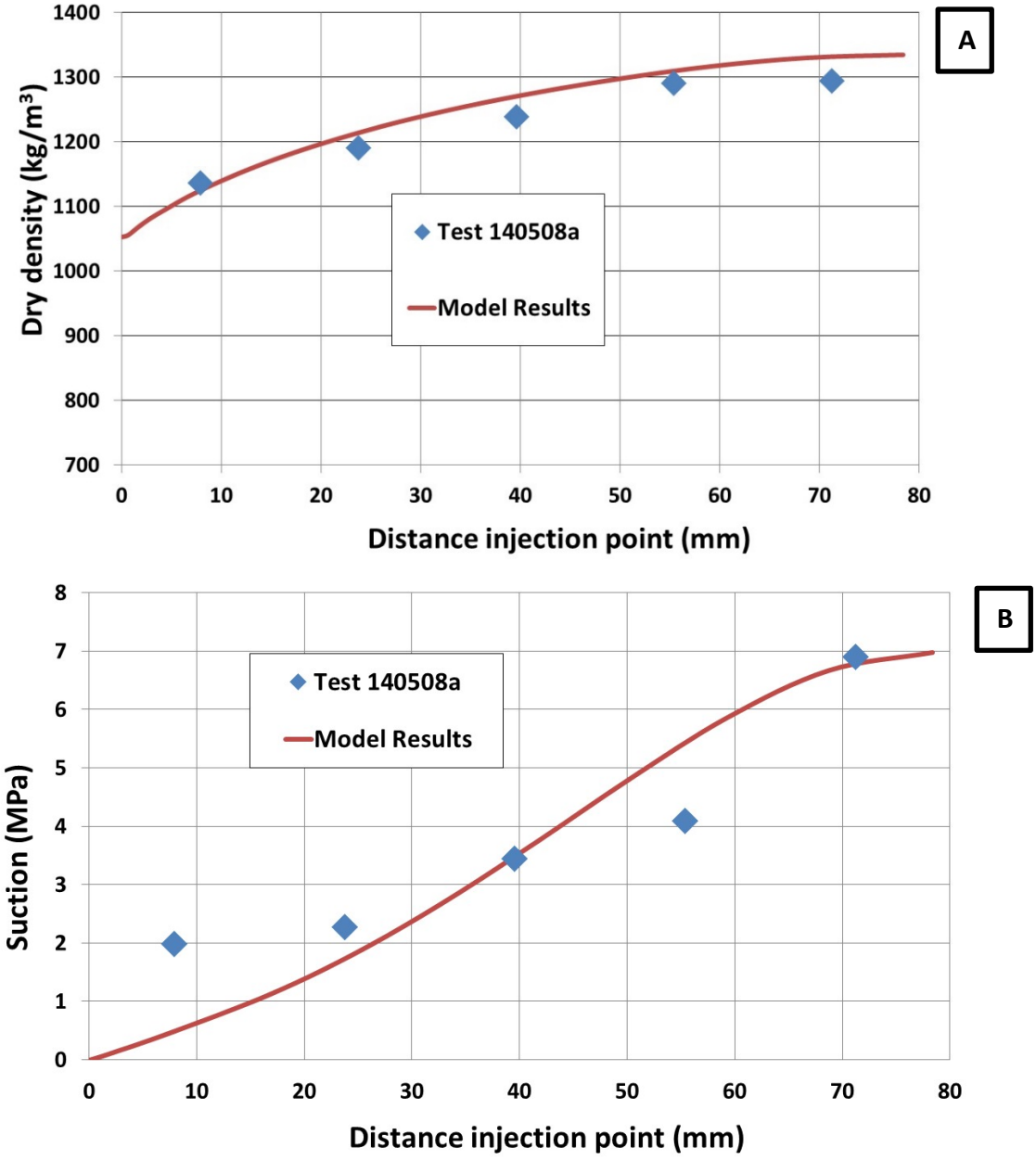

Figure 4-31. *Distribution of dry density (A) and suction (B) as a function of distance from injection point for minelco granules at the end of the test: 31 days, (experimental and model results).*

4.4 Thermo-hydro mechanical properties of materials

Characterization of MX-80, Friedland clay, pillow and rod pellets and granules have been carried out by laboratory tests (Chapter 4.2 and Chapter 4.3). Calibrated hydro-mechanical parameters for these materials are listed from Table 4-20 to Table 4-27.

Table 4-20. *BBM parameters for Buffer and Backfill blocks (Toprak et al., 2016).*

Parameter	Symbol	MX-80	Friedland Clay
Poisson ratio (-)	ν	0.3	0.3
Minimum bulk module (MPa)	K_{min}	10	10
Reference mean stress (MPa)	p_{ref}	0.01	0.01
Parameters for elastic volumetric compressibility against mean net stress change (-)	κ_{i0}	0.09	0.05
Parameters for elastic volumetric compressibility against suction change (-)	κ_{s0}	0.09	0.05
Parameter for elastic thermal strain ($^oC^{-1}$)	α	$9x10^{-4}$	$9x10^{-4}$
Slope of void ratio – mean net stress curve at zero suction (-)	$\lambda(0)$	0.25	0.18
Parameters for the slope void ratio – mean net stress at variable suction (-,MPa^{-1})	r	0.8	0.8
	β	0.02	0.02
Reference pressure for the P_0 function (MPa)	p^c	0.1	0.1
Pre-consolidation mean stress for saturated soil (MPa)	P_o*	2	2
Critical state line (-)	M	1.07	1.07

The host rock (Hagros et al., 2003) and the canister (Raiko, 2013) were considered linear elastic with parameters E, ν and α, respectively for Young modulus, Poisson ratio and coefficient of linear thermal expansion. Mechanical parameters for air gap have been proposed in Toprak et al. (2013). The 10 mm air gap (between canister and buffer) is modelled for simplicity using a bi-linear elastic model which uses two Young moduli, one for opened gap and the other for the closed gap. A large value of young modulus (E_c) is used for the closed gap (representing contact between gap surfaces) and a relatively low value (E_0) is used for the open gap. Compression strain is used to check whether the gap is open or closed. Thermo-hydro- mechanical properties of the host rock, canister and air gap element are given in Table 4-21, Table 4-22 and Table 4-23.

Table 4-21. *Hydraulic parameters for rock, MX-80, Friedland clay and gap element.*

Equation	Parameter	Rock	MX-80	Friedland clay	Gap element
Van Genuchten retention curve	P (MPa)	1.5 (1)	27 (2)	4.5 (3)	0.001
	λ (-)	0.3 (1)	0.45 (2)	0.25 (3)	0.5
	a (-) in $P(\phi)$	-	11 (2)	22 (3)	15
	b (-)in $\lambda(\phi)$	-	4 (2)	8 (3)	-
	ϕ_0	-	0.4245 (2)	0.393 (3)	0.8
Darcy flux	k (m^2)	$1.52x10^{-19}$ (1) (Fracture: $1.52x10^{-16}$)	$5.6x10^{-21}$ (1)	$7.6x10^{-20}$ (4)	10^{-16}
	b (-)in $k(\phi)$	-	15 (1)	16 (4)	15
	ϕ_0	-	0.438 (1)	0.36 (4)	0.8
	m (-)	3	3	3	1
Diffusive flux	τ (-)	0.4	0.4	0.4	0.4

1-Pintado et al., 2013; 2- Pintado et al., 2017; 3-Kiviranta et al., 2016

4-Calculated from oedometer test results for DI water presented (Kiviranta et al., 2016) and hydraulic conductivity tests presented in (Karnland et al., 2006), (Johannesson et al., 2006), (Sandén et al., 2008) and (Schatz et al., 2012)

Table 4-22. *Mechanical parameters for air gap element, rock and canister (Toprak et al., 2016).*

Parameter	Rock	Canister	Parameters	Gap Element
E (MPa)	63000	21000	E_c (MPa)	100
ν	0.25	0.3	ν	0.3
α ($^oC^{-1}$), linear	0.85 x10^{-5}	10^{-5}	α ($^oC^{-1}$), linear	-
			E_o (MPa)	1
			Strain limit	0.95

Table 4-23. *Thermal parameters for rock, MX-80 and gap element (Pintado et al., 2017). The thermal parameters of Friedland clay have not been measured. Due to the relatively large distance from the canister and its low mass compared with rock, it was not considered their measurement and taking into account that it is a clay, the same parameters used for MX-80 have been used for Friedland clay.*

Parameter	Rock	Canister	Buffer	Backfill	Gap element
ρ_s (kg/m^3)	2743	8930	2780	2780	-
c_s (J/kgK)	764	390	830	800	-
λ_{dry} (W/mK)	2.82	390	0.2	0.2	0.045
λ_{sat} (W/mK)	2.82	390	1.4	1.4	0.6
b in $\lambda(S)$	-	-	-0.15	-0.15	-
S_r* in $\lambda(S)$	-	-	0.5	0.5	-
$\phi_{initial}$	0.005	0.01	0.37/0.388	0.27	0.8

Table 4-24. Mechanical parameters used for pellet-based materials in the numerical simulations of tests.

Parameter	Pillow pellets	Rod Pellets
κ^{Macro} (-)	0.045	0.045
κ^{micro} (-)	0.045, 0.09, 0.135 (*)	0.045, 0.09, 0.135 (*)
κ_s^{Macro} (-)	0.01	0.01
ν^M (-)	0.3	0.3
f_{sd0} (-)	-0.1	-0.1
f_{sd1} (-)	1.1	1.1
n_{sd} (-)	2	2
f_{si0} (-)	-0.1	-0.1
f_{sd1} (-)	1.1	1.1
n_{si} (-)	0.5	0.5
M (-)	1	1
r (-)	0.8	0.8
β (MPa^{-1})	0.0001	0.0001
p_c (MPa)	0.1	0.1
P_{to} (MPa)	0.01	0.01
$\lambda(0)$ (-)	0.19	0.3
P_0^* (MPa)	2	4

(*) Three different values have been used to model the oedometric test and two different values to model the infiltration test

Table 4-25. *BExM Parameters for Pellet based materials (vertical disposal modelling).*

Parameter	Pellets buffer-rock gap (Pillow)	Pellets backfill-buffer transition (Granules)	Pellets backfill-rock transition (Rod)
κ^{Macro} (-)	0.045	0.045	0.045
κ^{micro} (-)	0.09	0.09	0.09
κ_s^{micro} (-)	0.01	0.01	0.01
$K_{\min}^{Macro}$ (MPa)	10	10	10
$K_{\min}^{micro}$ (MPa)	0.001	0.001	0.001
ν^M (-)	0.3	0.3	0.3
f_{sd0} (-)	-0.1	-0.1	-0.1
f_{sd1} (-)	1.1	1.1	1.1
n_{sd} (-)	2	2	2
f_{si0} (-)	-0.1	-0.1	-0.1
f_{sd1} (-)	1.1	1.1	1.1
n_{si} (-)	0.5	0.5	0.5
M (-)	1	1	1
r (-)	0.8	0.8	0.8
β (MPa^{-1})	0.0001	0.0001	0.0001
p_c (MPa)	0.1	0.1	0.1
P_{to} (MPa)	0.01	0.01	0.01
$\lambda(0)$ (-)	0.19	0.3	0.3

Table 4-26. *Hydraulic parameters for pellet-based materials (vertical disposal modelling).*

Equation	Parameter	**Pellets buffer-rock gap (Pillow)**	**Pellets backfill-buffer transition (Granules)**	**Pellets backfill-rock transition (Rod)**
Van Genuchten retention curve	P (MPa)	5 (1)	12 (1)	7 (3)
	λ (-)	0.34 (1)	0.4 (1)	0.4 (3)
	a (-) in $P(\phi)$	-	-	-
	b (-)in $\lambda(\phi)$	-	-	-
	ϕ_0	-	-	-
Darcy flux	k (m^2)	$5x10^{-19}$	$1.5\ x10^{-19}$ (2)	$1.4x10^{-18}$
	b (-)in $k(\phi)$	10	10 (2)	10
	ϕ_0	0.319	0.302	0.35
	m (-)	3	3	3
Diffusive flux	τ (-)	0.4	0.4	0.4

(1) (Kiviranta et al., 2016)

(2) Calculated from Karnland et al., 2006 and in Martikainen and Schatz, 2011

(3) Calculated from water retention curve tests presented in (Kiviranta et al., 2016)

Table 4-27. *Thermal parameters for pellet-based materials (vertical disposal modelling)*

Parameter	Pellets buffer-rock gap (Pillow)	Pellets backfill-buffer transition (Granules)	Pellets backfill-rock transition
ρ_s (kg/m^3)	2780	2780	2780
c_s (J/kgK)	830	830	830
λ_{dry} (W/mK)	0.16	0.2	0.16
λ_{sat} (W/mK)	0.63	0.63	0.63
b in $\lambda(S)$ (-)	-0.15	-0.15	-0.15
S_r* in $\lambda(S)$ (-)	0.6	0.5	0.6
$\phi_{initial}$ (-)	0.669	0.552	0.7

5 2D-SENSITIVITY ANALYSES

Sensitivity analyses represent alternate models or data to those of the Base Case, but remain within the scope of the base . Analyses of the sensitivity cases illustrate the effect of model and data uncertainties.

Sensitivity analysis in this thesis is a continuation of the modelling task performed by CIMNE and B+Tech reported in Toprak et al., 2013. The contribution of this thesis are:

- Buffer material, the water retention curve parameters of MX-80 buffer blocks have been updated (Kiviranta et al., 2016). In Chapter 4.2, calibrated water retention curves for all characterized materials are given.

- Modelling has been performed with the updated pellets parameters calculated in Kiviranta et al., 2016 (water retention curve) and Kivikoski et al., 2015 (thermal conductivity). Numerical simulation of tests for pellets is explained in Chapter 4.3.

- The different components of the backfill are considered, so the backfill geometry has been divided taking into account the three components: bottom layer (granules), backfill blocks and pellets (rod) following the design presented in Keto et al., 2013. Chapter 4 is devoted to characterization of these materials.

The main purpose of performing sensitivity analyses can be listed as:

- The consequences of future climate change might have an impact on groundwater properties due to the intrusion of fresh water in the repository after the glaciation (water from melted ice). The current groundwater has a salinity of 10 g/L with variations from minimum values of 5 g/L in some parts of the tunnel till a maximum calculated for the operational phase between 12 and 25 g/L although it may reach 50 g/L at the deepest part of the repository (Pastina and Hellä, 2010).
- Demonstrating the feasibility of candidate barriers under certain conditions (for example initial conditions of selected materials).
- To handle bedrock uncertainty (presence of fractures and fractures location).
- To evaluate alternative buffer or filling (between buffer and rock or between buffer and canister) materials in terms of long-term safety of the repository after closure.
- To evaluate the buffer-backfill interaction in order to check the evolution of the buffer density. This process is evaluated in Sandén et al., 2016 (experimental).
- To develop a better understanding of the modelled system and test robustness.

Sensitivity analyses have considered effects of:

Buffer and backfill design options:

- Pellet thickness: Case P1, Case P2;
- Initial w of buffer: Case W1, Case W2, Case W3, Case BM1
- Average saturated density of buffer: Case D1
- Filling material between rock and buffer: Case FM1, Case FM2
- Artificial wetting of pellets: Case PW1, Case PW2
- FISST gaps: Case GP1
- Filling material between buffer and canister: Case GP2, Case GP3
- Bigger backfill tunnel (equivalent to 3D geometry): Case GM1
- Buffer material: Case FE

Geological conditions:

- Fracture Position: Case F1, Case F2, Case F3
- Salinity: Case S1, Case S2. Case S3
- Rock permeability: Case R1, Case R2, Case R3
- Fracture permeability: FP1

Numerical simulation parameters

- Lagrangian method: Case L1
- Sensibility to pellet parameters: Case M1
- Thermal expansion coefficient of buffer: Case TE1
- Radiation effect in gap element: Case RD1
- Thermal expansion coefficient for rock: Case RTE1
- 3D TH calculations: Case 3D1

There are 34 cases in total. These cases can be summarised as below (order in the thesis):

- Base Case General description in section below
- Case F1 : Fracture at bottom of canister
- Case F2 : Fracture at mid-height of canister
- Case F3 : Fracture at upper of canister
- Case P1 : Pellet thickness: 35 mm
- Case P2 : Pellet thickness: 60 mm
- Case S1 : Salinity: 3.5%
- Case S2 : Salinity:7 %
- Case S3 : Salinity 7%; w_{buffer}: 19.7%
- Case W1 : w_{buffer}:11%
- Case W2 : w_{buffer}:21.7%
- Case D1 : Average saturated density buffer 2100 kg/m^3
- Case L1 : Lagrangian method
- Case M1 : K^{Micro} for pellets is 0.145
- Case FM1 : Between rock and buffer: slurry
- Case R1 : No fracture, k_{rock}:1.52x10^{-19} m^2
- Case R2 : No fracture; k_{rock}:3x10^{-19} m^2
- Case R3 : No fracture; k_{rock}:3x10^{-21} m^2
- Case TE1 : α_{buffer} (ºC^{-1}) is 9x10^{-4}
- Case TC1 : λ_{sat} for buffer is 1 W/m·K
- Case PW1 Initial Sr for pellets: 80%; water injection to pellets
- Case GP1 : FISST gaps, air gap between canister and buffer
- Case GP2 : FISST gaps, pellets between canister and buffer
- Case GP3 : FISST gaps, MX-80 between canister and buffer
- Case PW2 : Current geometry; initially saturated (96%) pellets
- Case GM1 : Bigger backfill tunnel
- Case FE : Buffer material is FEBEX
- Case FM2 : Between rock and buffer is water gap
- Case W3 : Current geometry, w_{buffer}:11%
- Case RD1 : Gap has radiation parameters
- Case BM1 : w_{buffer}:14%, ρ_d: 1600 kg/m^3
- Case RTE1 α_{rock} (ºC^{-1}) is 8x10^{-6}
- Case FP1 : $k_{fracture}$:1.5x10^{-15} m^2
- Case 3D1 : 3D TH calculations

Detailed information for each case is explained in the corresponding section.

5.1 Base Case

In Base Case, backfill has three components: Friedland clay blocks, rod pellets and granules (foundation layer). The buffer has also three components: MX-80 bentonite blocks (buffer ring and buffer disc), air gap element between buffer ring and pillow pellets. The thickness of the air gap element is 10 mm. The rock fracture is considered at the bottom of the buffer. The materials are shown in Figure 5-1-A. The representative points for buffer ring, buffer disc, backfill blocks, rod pellets, pillow pellets, granules, the air gap element and buffer backfill intersection are indicated in Figure 5-1-B. The mesh and geometry are presented in Figure 5-2. Equations are solved with finite element method (FEM).

The buffer geometry is derived from Juvankoski et al. 2012.

Figure 5-2 shows the geometry for backfill tunnel which is derived from Keto et al. (2013). The foundation layer has 0.4 m of thickness and the rod pellets made layer has a thickness of 0.3 m. The fracture has a thickness of 0.08 m. The reason for the relatively large thickness is just to avoid too small elements that may affect the development of the mesh in the vicinity of the fracture. Under hydraulic point of view, the thickness is small enough.

The assumed initial pressures and initial stresses are shown in Figure 5-3-A and Figure 5-3-B, respectively. Figure 5-4-A shows total porosity for all components. The micro-porosity for pellets (rod and pillow pellets) and granules are presented in Figure 5-4-B.

The initial pressures in filling components have been calculated from the water content and dry density prescribed for the filling components in buffer (Juvankoski et al., 2012) and in backfill (Keto et al., 2013). The degree of saturation is directly related with water content and dry density and with the water retention curve, it is possible to calculate the suction. The porosity is related directly with the dry density.

Hydraulic boundary conditions are shown in Figure 5-5-A. In a short-term first interval, excavation process is simulated and the boundary condition in rock walls is atmospheric pressure for liquid (P_l=0.1 MPa). On the upper and lower boundaries, hydro-static water pressure is imposed. There is also water supply from the rock fracture. Figure 5-5-B shows mechanical boundary conditions. The system is confined. Regarding thermal conditions; the upper and lower boundaries have prescribed temperature (not constant) calculated from the analytical solution of the entire repository and heat flow from the canister is modelled as volumetric power considering a decay function as it is explained in Chapter 3.4.

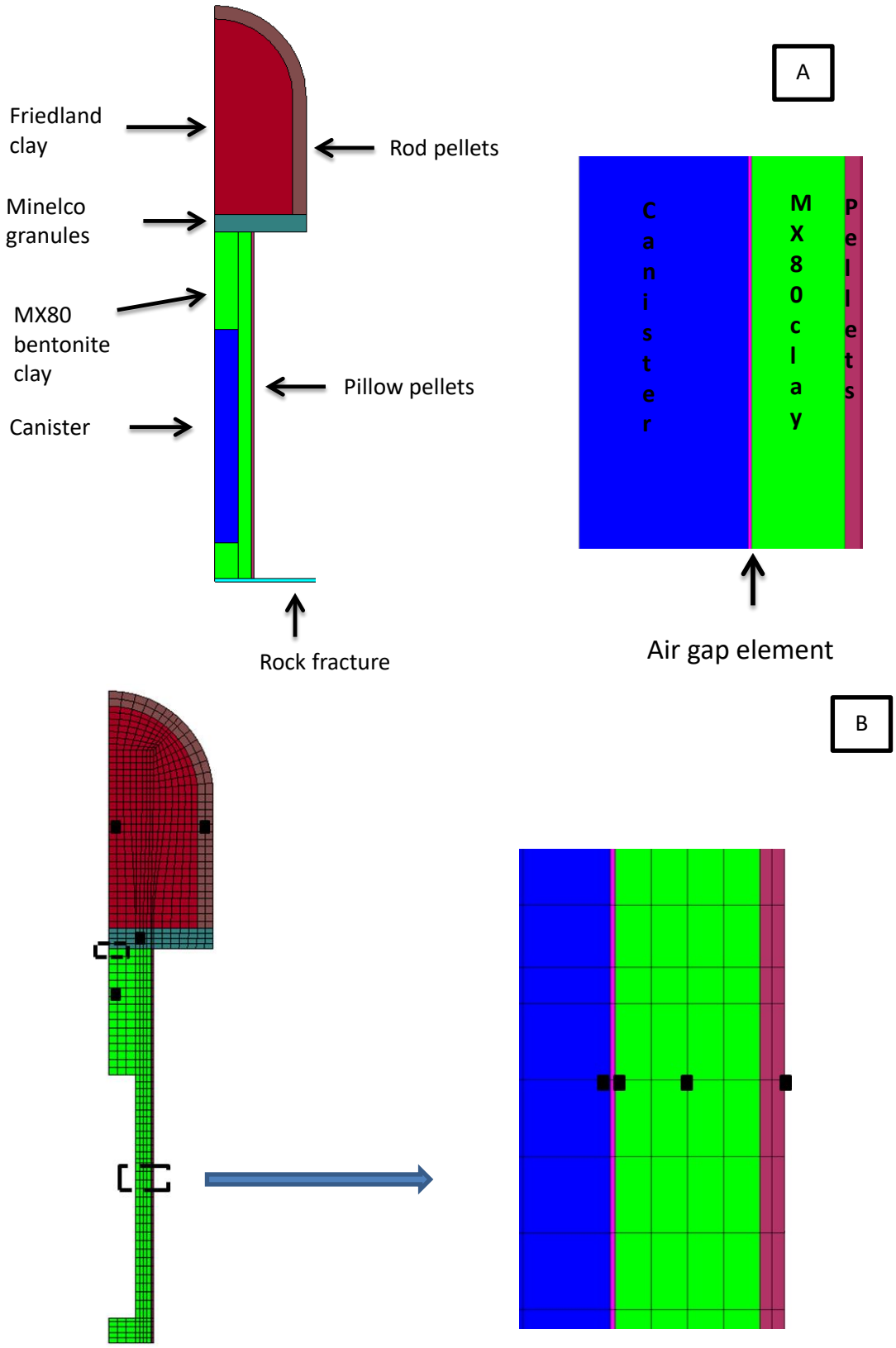

Figure 5-1. *Materials in base case model (A) and representative points of materials for calculations (B).*

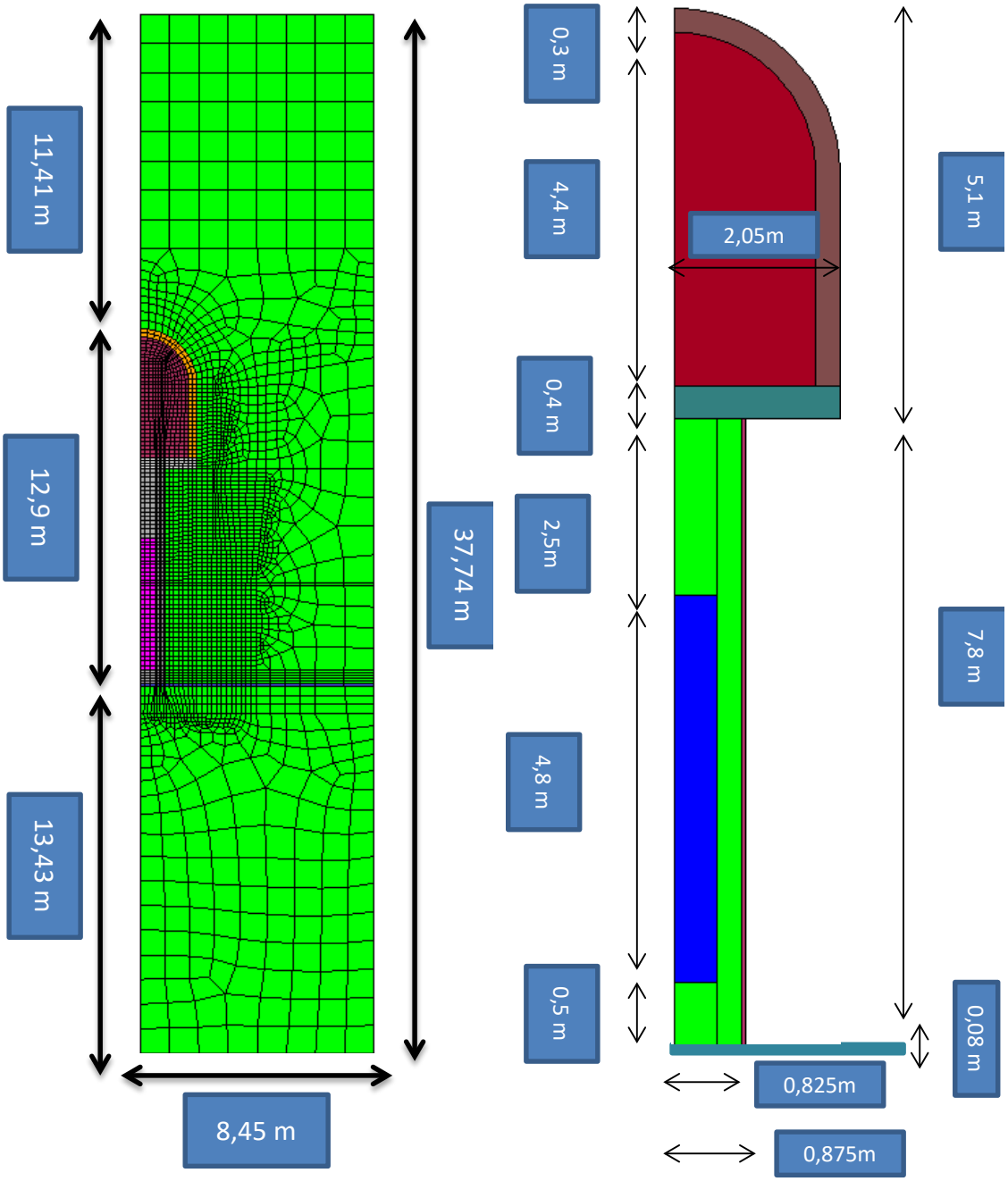

Figure 5-2. *Geometry and mesh for base case model.*

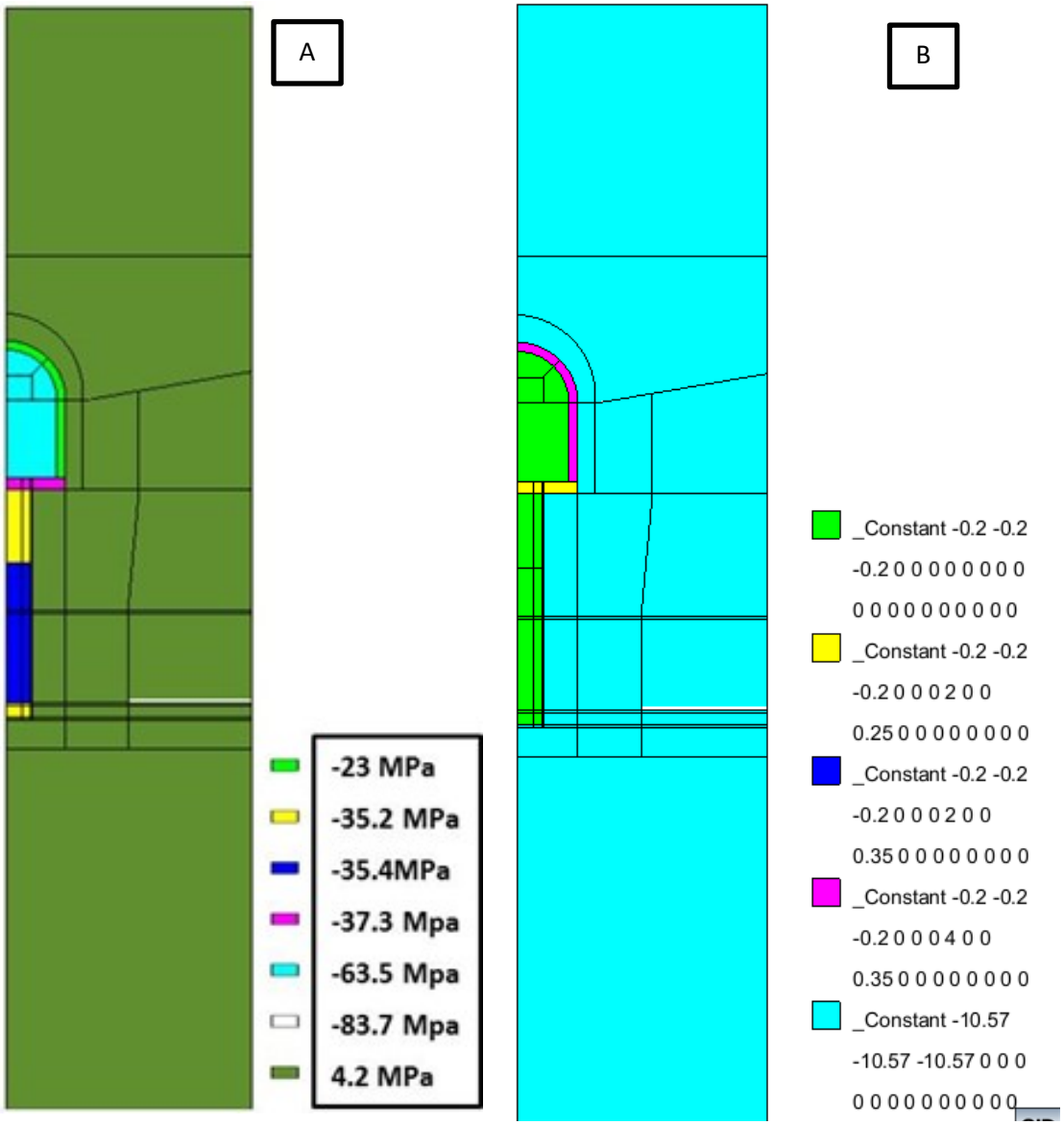

Figure 5-3. *Initial suction (A) and initial stress (B) for base case model.*

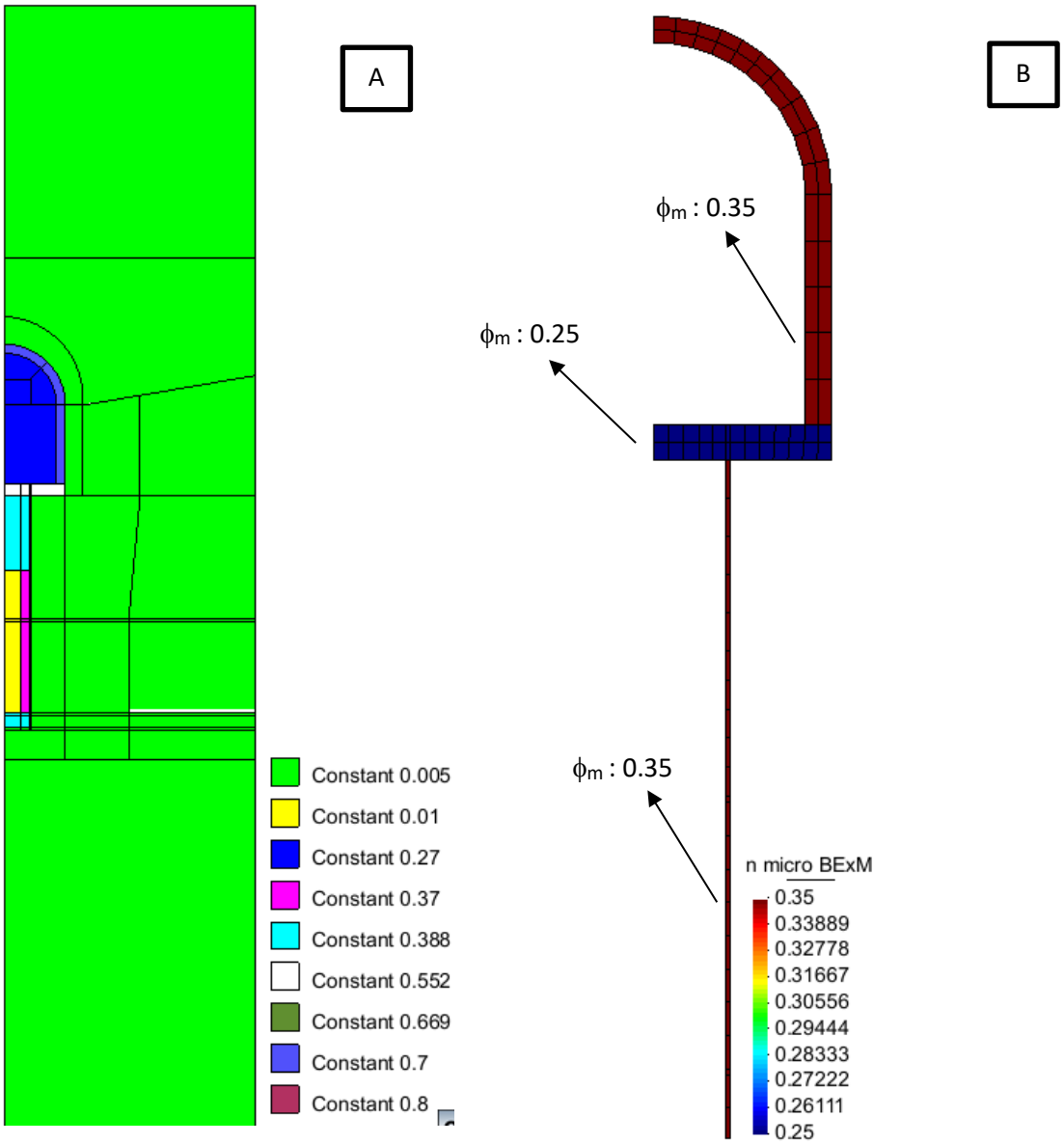

Figure 5-4. *Initial total porosity (A) and micro porosity (B).*

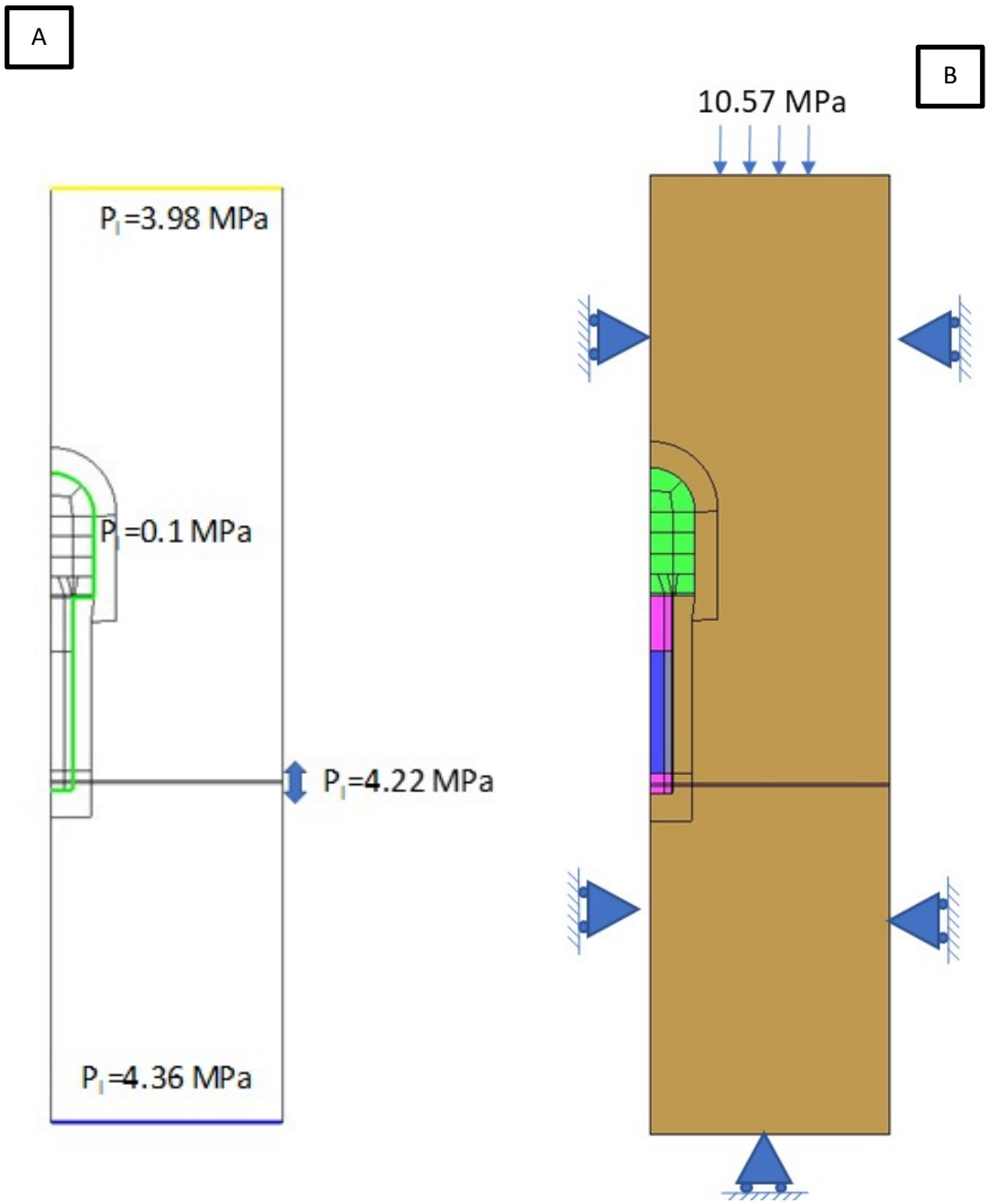

Figure 5-5. *Hydraulic (A) and mechanical (B) boundary conditions for Base Case.*

In Base Case, MX-80 and Friedland clay are modelled with BBM and pellet based materials with BExM (Barcelona Expansive Model). Their parameters are given in Chapter 4.4.

In order to ensure that buffer will retain its properties in long term, the maximum temperature on the canister - bentonite interface is limited to the design temperature of +100°C. Due to uncertainties in thermal analysis parameters (like scattering in rock conductivity or in predicted decay power), the nominal calculated maximum canister temperature is set to 95°C. The nominal temperature is controlled by adjusting the space between adjacent canisters, adjacent tunnels and the precooling time of the spent fuel affecting on the decay power of the canisters (Ikonen, 2003). Figure 5-6 shows the temperature evolution on the considered nodes and the distribution of temperature in the system after 30 years of deposition. The maximum temperature is fairly below 90^{o}C. The effect of air gap can be observed. This is evident as the temperature at both sides of the gap is different by nearly 10^{o}C during the 2 first years after the emplacement of the canister but reduces significantly afterwards. The imposed variable temperature on boundaries is also depicted in the plot, this is necessary to account for the relatively close boundaries.

Figure 5-7-A shows the evolution of the degree of saturation and Figure 5-7-B shows the evolution of liquid pressure. It can be seen the de-saturation of the area adjacent to the canister in both figures. The saturation of the system takes around 10 years, according to the represented points.

One essential functional requirement for the deposition tunnel is that the backfill as a whole has a sufficient rigidity in unsaturated state to ensure that, even if the buffer is swelling and compressing the backfill, the buffer saturated density does not decrease below a critical value estimated in 1950 kg/m^3 (Hansen *et al.,* 2010). The evolution of dry density and saturated density for buffer disc, buffer ring and backfill blocks is presented in Figure 5-8-A. The total and micro porosity for rod pellets, pillow pellets and granules are presented in Figure 5-8-B. Due to the hydration and the corresponding swelling, micro porosity increases. Since total porosity changes only slightly, the increase in micro-porosity induces a reduction of the macro-porosity.

Keeping the buffer in place can be considered as one of the main design requirement for backfill. Buffer should not reduce its density too much. Some upwards swelling of buffer discs is expected since the backfill has a lower swelling pressure and compressibility than the buffer.

Figure 5-9-A shows the generation of stresses in buffer and backfill due to swelling. Swelling pressure should not exceed 15 MPa in order to avoid excessive isotropic stresses on the canister

during the glaciation period, when the ice sheet can reach 2.5 km (Raiko, 2013). In the buffer, it reaches the value of 7 MPa. The vertical displacements at the intersection of buffer and backfill are presented in *Figure 5-9*-B. It is observed that the tendency is that the buffer penetrates in the backfill, which is motivated by the relative higher swelling capacity of the buffer with respect to the backfill. Maximum vertical displacements reach a value of 10 cm.

Figure 5-10 shows stress-void ratio- suction path for buffer blocks adjacent to buffer-backfill interface (A) and granules (B). It can be seen that buffer disc first compresses due to backfill installation. Since the saturation develops, buffer disc starts swelling and compresses granules. After the saturation process stresses still decrease due to cooling. This point is important because the final state depends of the thermal expansion of the buffer and not only of the swelling pressure depending how fast is the saturation reached. The first reduction in mean effective stress is due to positive pore pressure (Toprak et al., 2016).

Figure 5-11-A shows p_{eff}-q-s (mean effective stress-deviatoric stress and suction) path for buffer disc under canister. Figure 5-11-B demonstrates the forces acting on the canister surface. There are four forces: F_{Top} (forces acting on top of the canister), F_{bottom} (forces acting on the bottom of the canister), T (shear force acting on lateral surface of the canister) and $W_{canister}$ (weight of canister). The canister movements caused by the weight of the canister is an important issue in terms of canister sinking. The magnitude of force on bottom is greater than the force on the top of canister. The reason is that the bottom of canister has a faster wetting due to the fracture. Figure 5-11-B also shows the distribution of the shear stress on the rock surface in contact with the buffer. As a results of stress development, the normal forces (F_{Top} and F_{bottom}) are significantly larger than the weight of the canister and the shear force. Canister sinking has been studied by Börgesson and Hernelind (2006).

Figure 5-12-A depicts the evolution of intrinsic permeability and Figure 5-12-B shows the evolution of total permeability, i.e. the product of intrinsic permeability and relative permeability. The first depends on porosity while the second on degree of saturation. There are not large changes in the intrinsic permeability of MX-80 and Friedland clay, which is not surprising as these clays are modelled with BBM and the porosity (only total porosity is calculated) changes moderately. In contrast, the intrinsic permeability of pillow pellets, granules and rod pellets decreases during saturation process. This is motivated due to the decrease of macro-porosity as the micro-porosity increases.

As indicated above, total permeability is the product of intrinsic permeability and relative permeability. Total permeability of all materials increases during saturation process and later, it reaches the steady-state conditions.

Figure *5-13*-A shows stress-void ratio- suction path for buffer ring adjacent to canister. Drying of buffer due to strong heating of canister can be seen from the figure. The closure of the air gap element between the canister and buffer is demonstrated in Figure *5-13*-B. It has 10 mm of thickness. It has a certain effect on the temperature evolution till it closes. In Base case, it closes in five years.

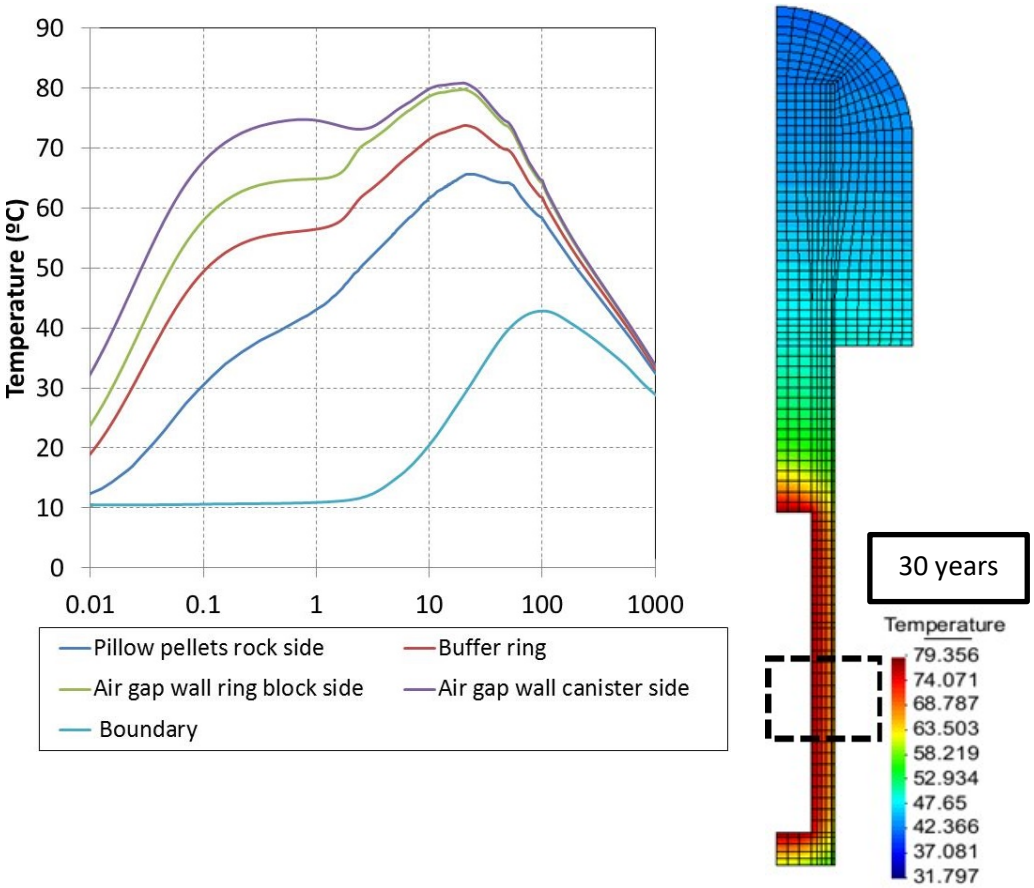

Figure 5-6. *Temperature evolution and distribution (30 years).*

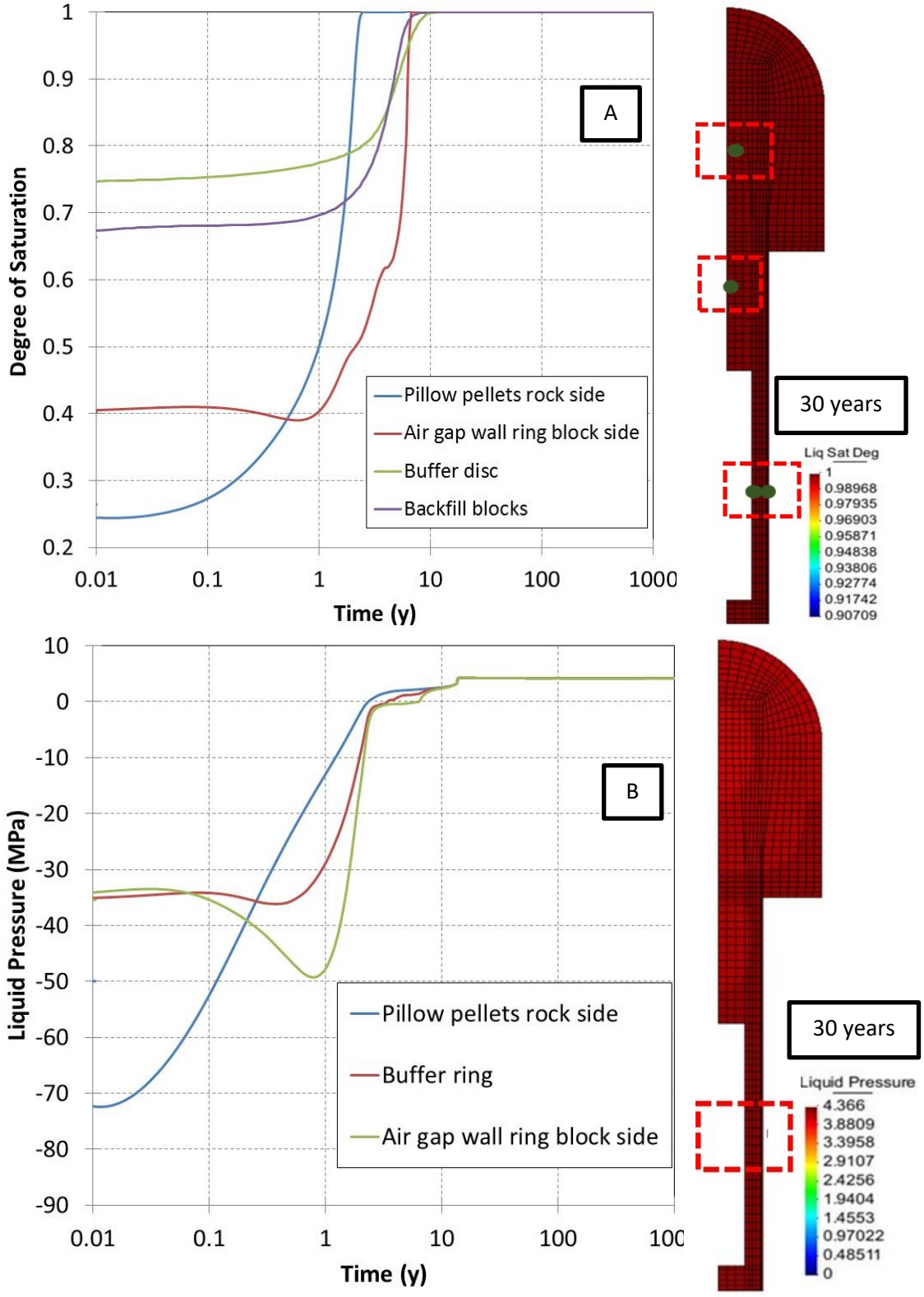

Figure 5-7. *Evolution of degree of saturation (A) and liquid pressure (B).*

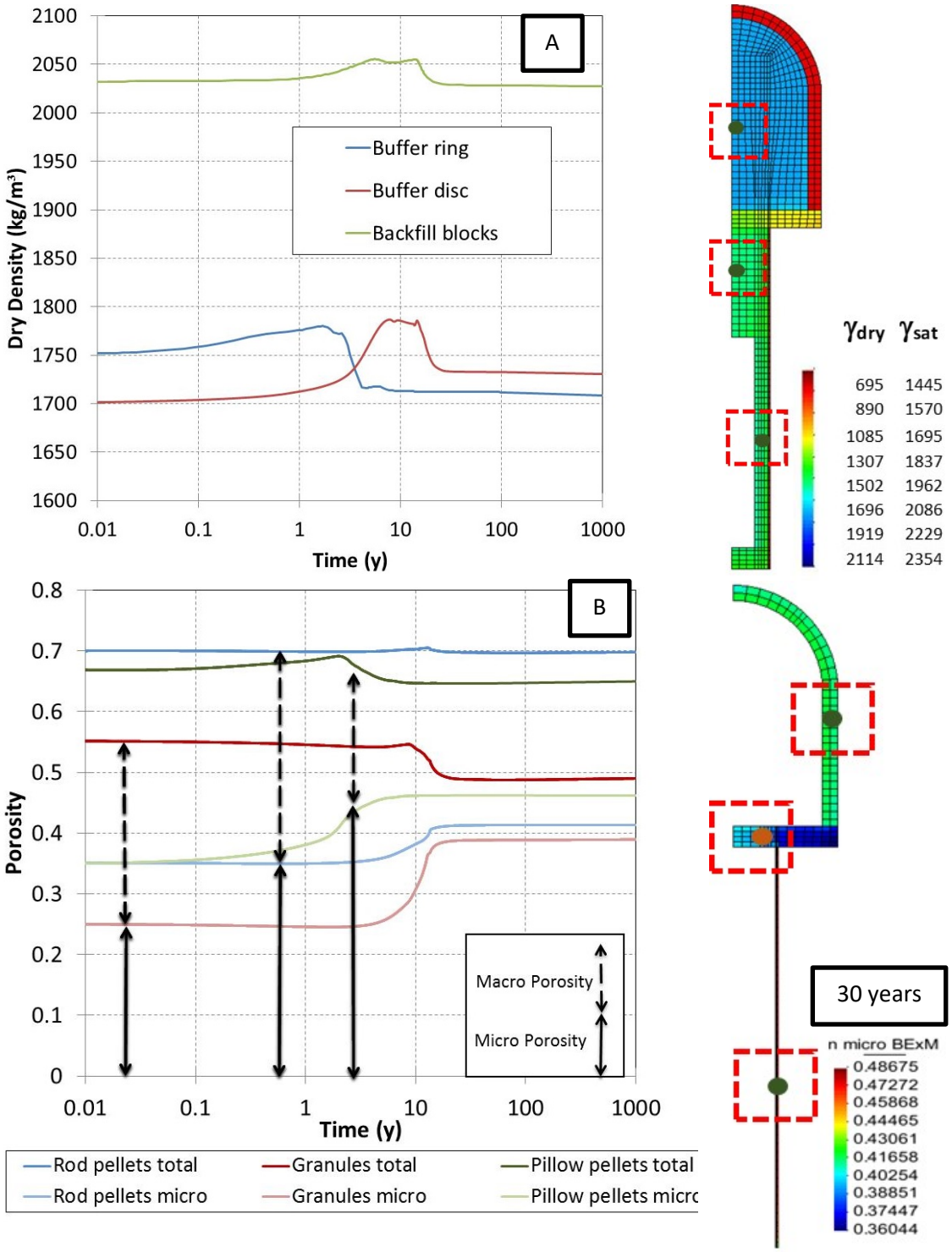

Figure 5-8. *Evolution of dry and saturated density (A) for buffer and backfill and micro-porosity for pellets (B).*

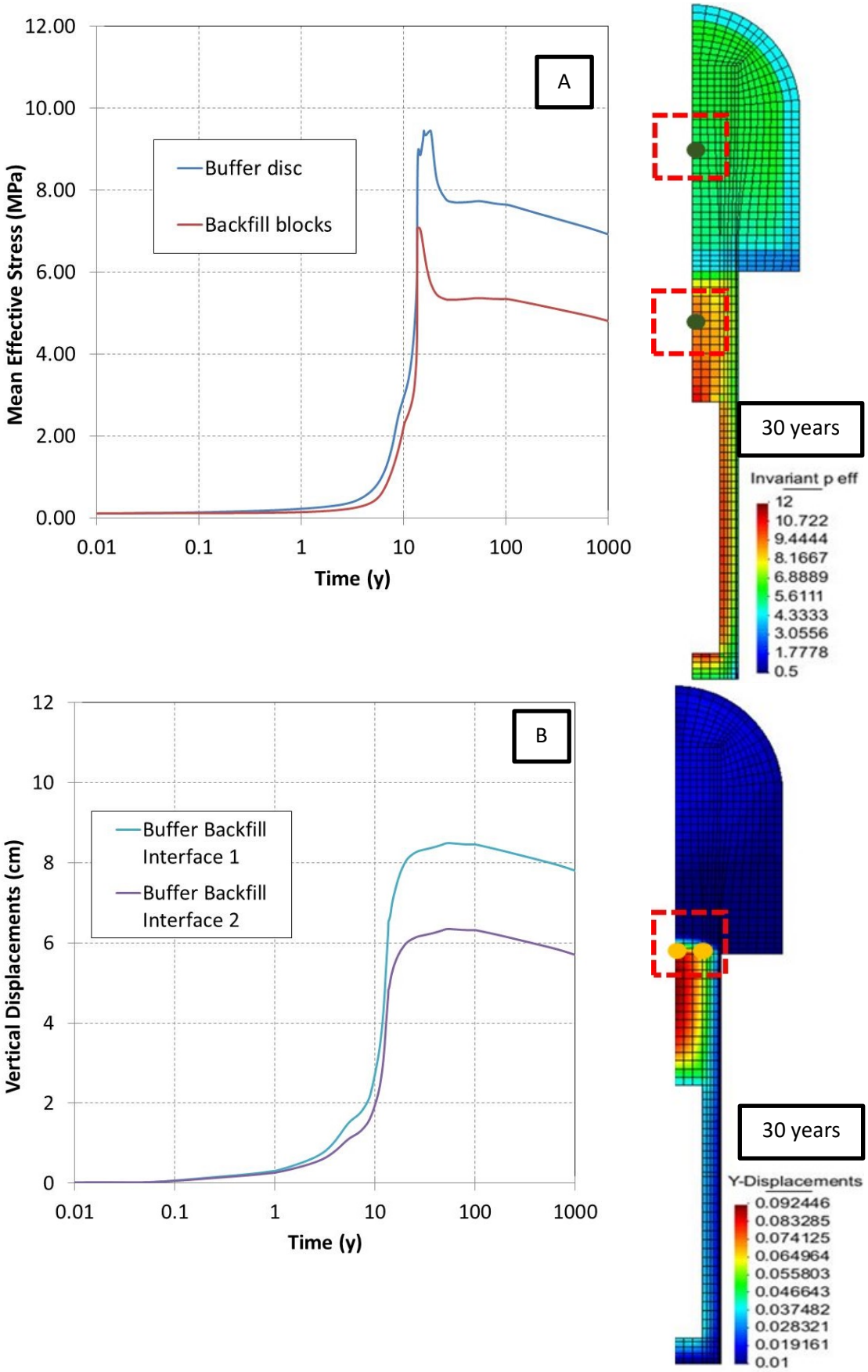

Figure 5-9. *Generated stresses (A) and vertical displacements (B) on the buffer-backfill intersection*.

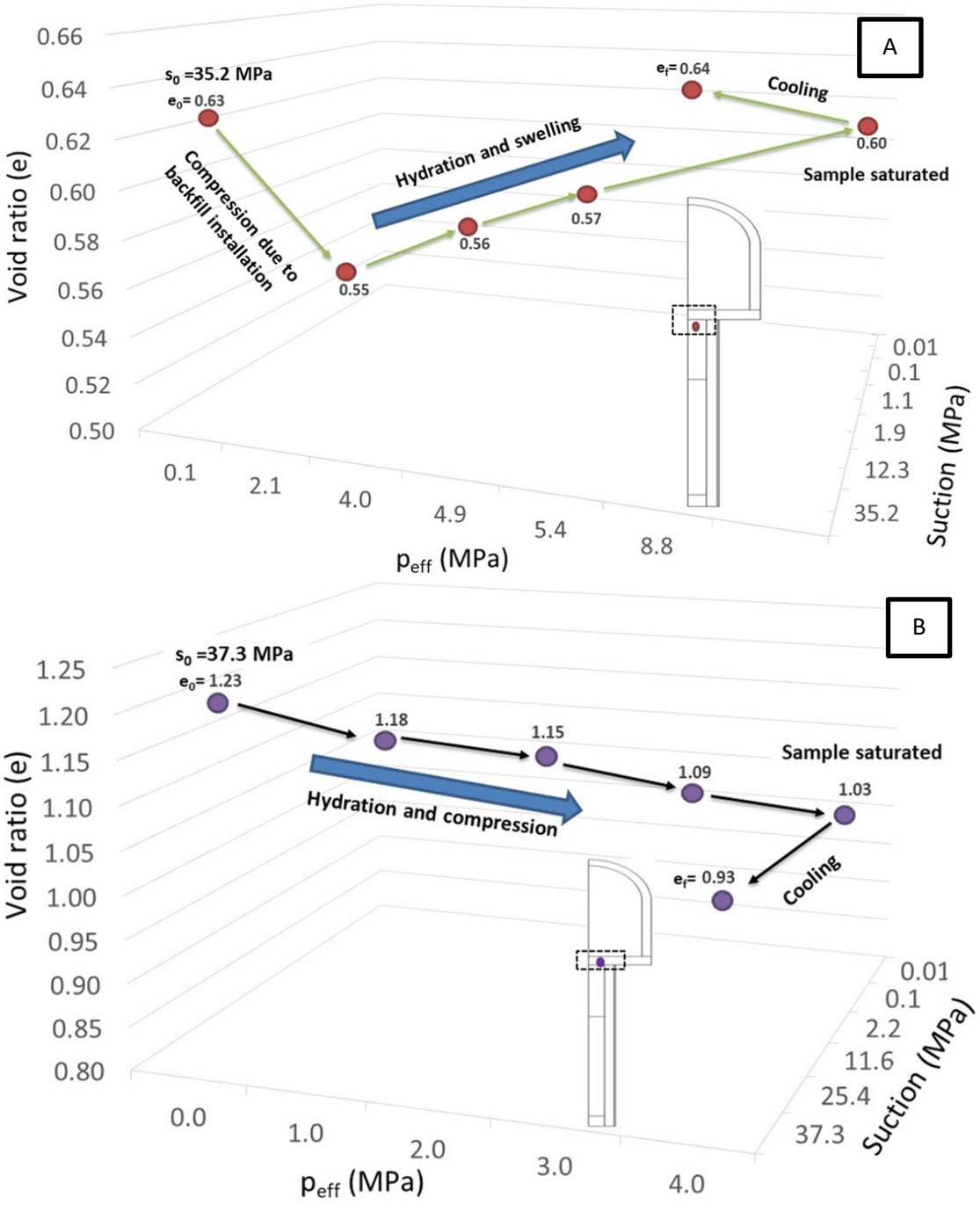

Figure 5-10 *Mean effective stress-suction-void ratio path for buffer disc (A) and granules (B)*

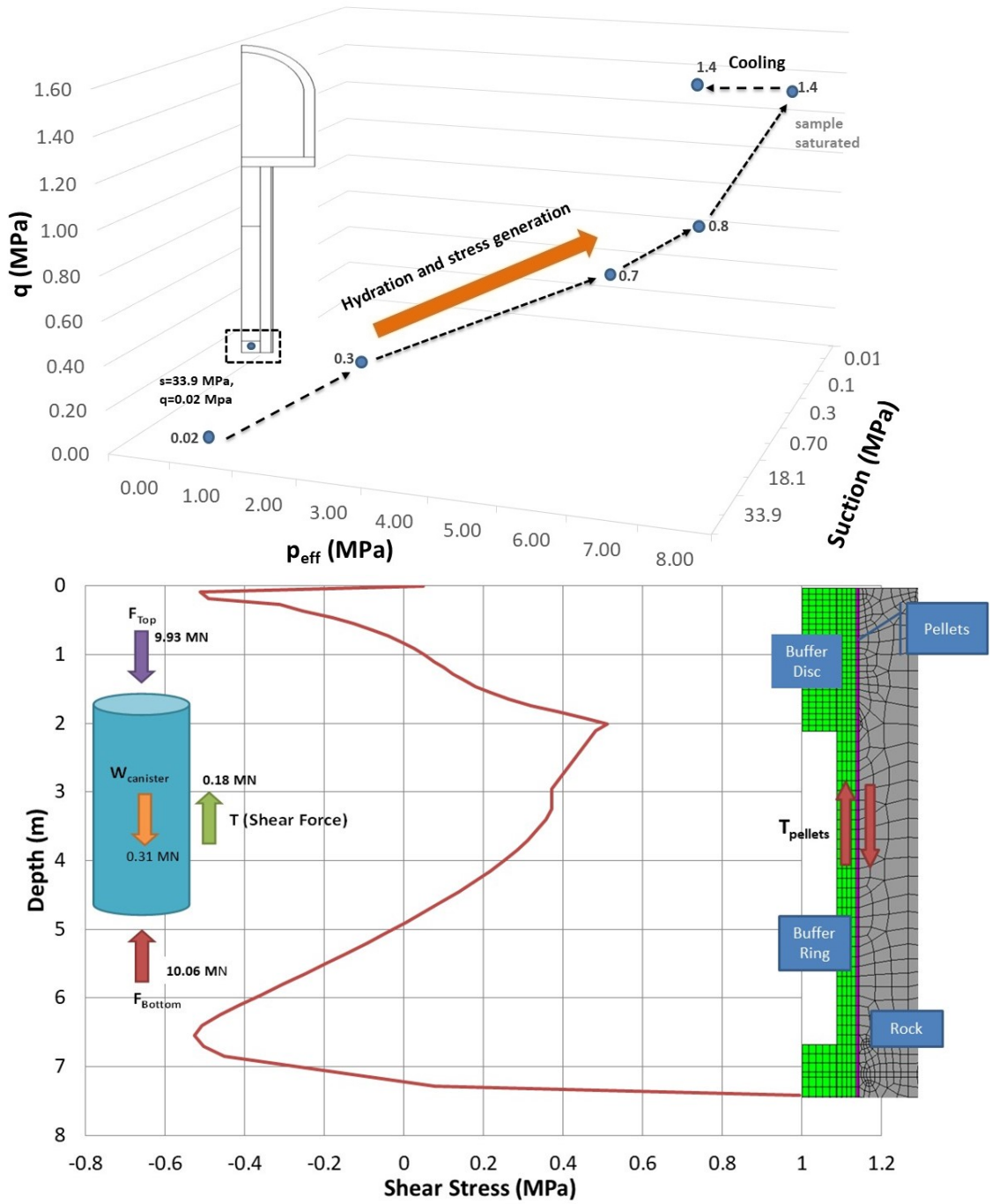

***Figure 5-11**. Mean effective stress –deviatoric stress – suction path for buffer disc under canister (A), acting forces on the canister and shear stress along pillow pellets profile.*

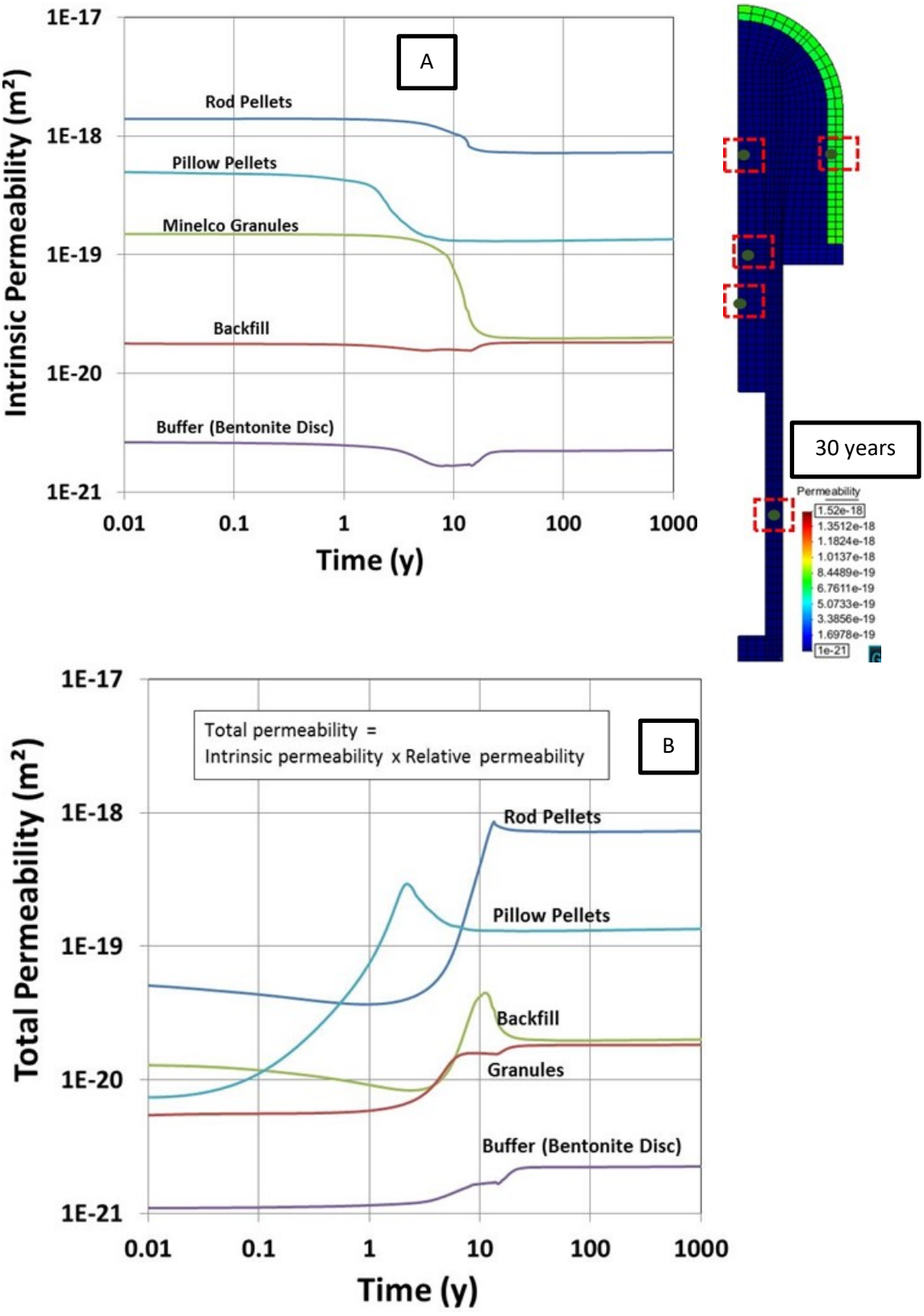

Figure 5-12. *Evolution of intrinsic permeability (A) and total permeability (B) for materials.*

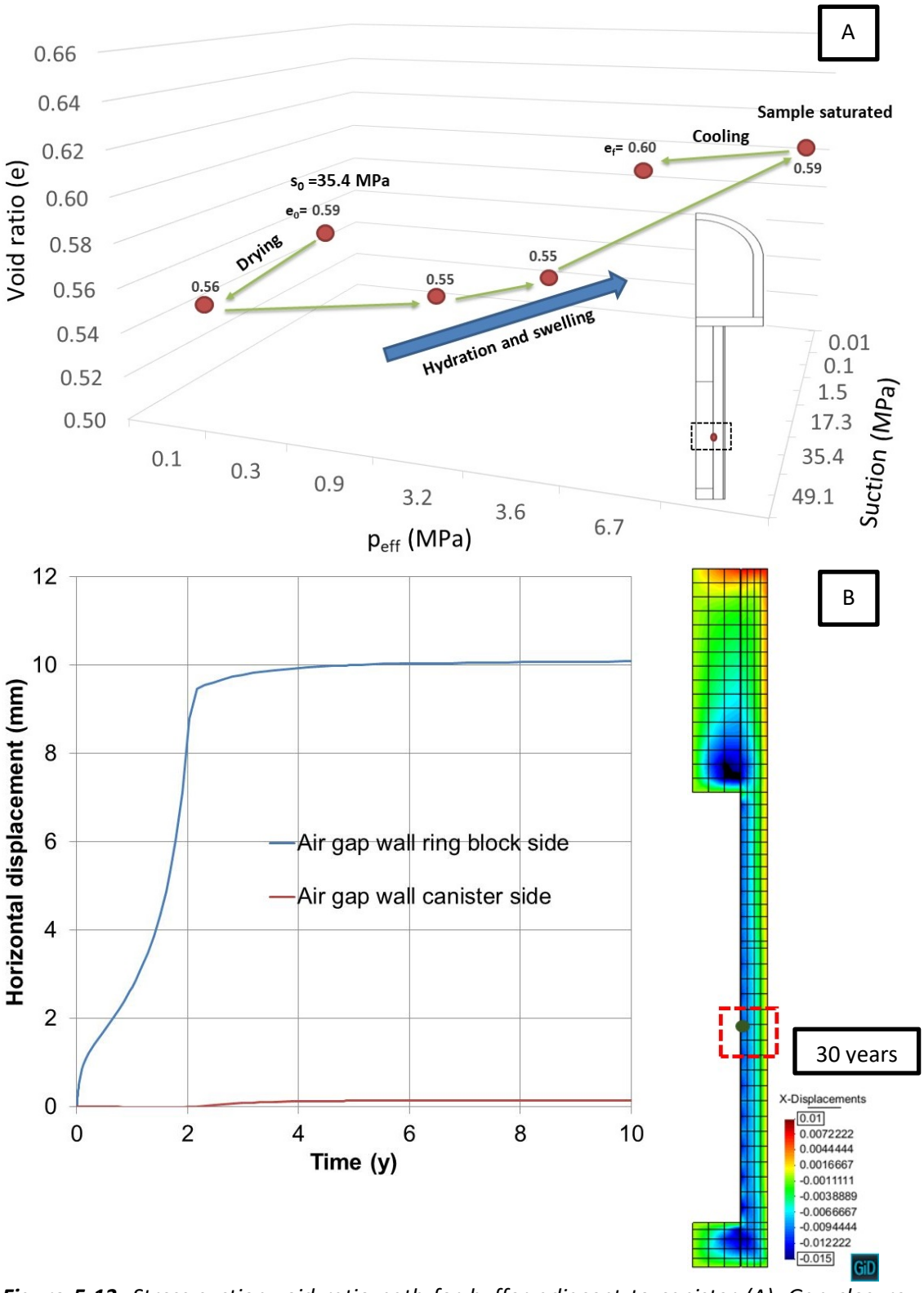

Figure 5-13. *Stress-suction-void ratio path for buffer adjacent to canister (A). Gap closure evolution.* In the picture of horizontal displacement distrubution, the units are in meter (B).

5.2 Effect of Fracture Position

In this Chapter, the effect of the fracture position on model results has been investigated. Most of the rock properties were selected from Löfman et al. (2010), but have been modified to take into account some considerations of the transmissivity of fractures. Thermo-hydraulic modelling of fractures has been partly discussed by Pintado et al. (2013). Fracture network in Olkiluoto and its effect has been partly studied in Poteri et al., 1997 and Rautakorpi et al., 2003.

Table 5-1 summarizes the differences between four cases. The intrinsic permeability of fracture has been set as 1.52×10^{-16} m^2. Comparative results for four cases are given in Table 5-1.

The transmissivity of the inflowing fracture is 1.2×10^{-9} m^2/s. These cases are the following:

- Base case: Fracture is at the bottom of buffer blocks.
- Case F1: Fracture is at the bottom of canister.
- Case F2: Fracture is at the mid-height of canister.
- Case F3: Fracture is at the upper canister.

Table 5-1. *Comparison of cases according to fracture position.*

Results	Cases			
	Base Case (Bottom Buffer)	Case F1 (Bottom Canister)	Case F2 (Mid-height of Canister)	Case F3 (Upper Canister)
T_{max} (°C) (air gap canister wall)	80.7	80.7	80.6	80.5
Time (years) for S_r = 99 % (Buffer disc)	8.4	8.2	6	4
Time (years) for S_r = 99 % (Backfill block)	6.7	6.7	5.5	3.2
Buffer density (kg/m^3) (Disc)	1729	1730	1734	1726
Backfill density (kg/m^3) (Bentonite disc)	2027	2027	2028	2035
Max. Effective Stress (MPa) (Backfill blocks)	9.4	9.4	9.5	8.8
Displacements at buffer-backfill intersection (cm)	8.4	8.7	10.2	16.4
Time (years) for closing air gap	4.9	3.2	1.2	5.1

Figure 5-14 shows fracture position in four models. As it is demonstrated in Figure 5-15, there is a considerable difference in terms of generated vertical displacements. In Case F3, where the fracture is located to above canister, generated displacements at the buffer-backfill intersection

are two times higher than the Base Case. Time to reach full saturation is also sensitive to fracture position. Maximum temperature and densities are not affected considerably.

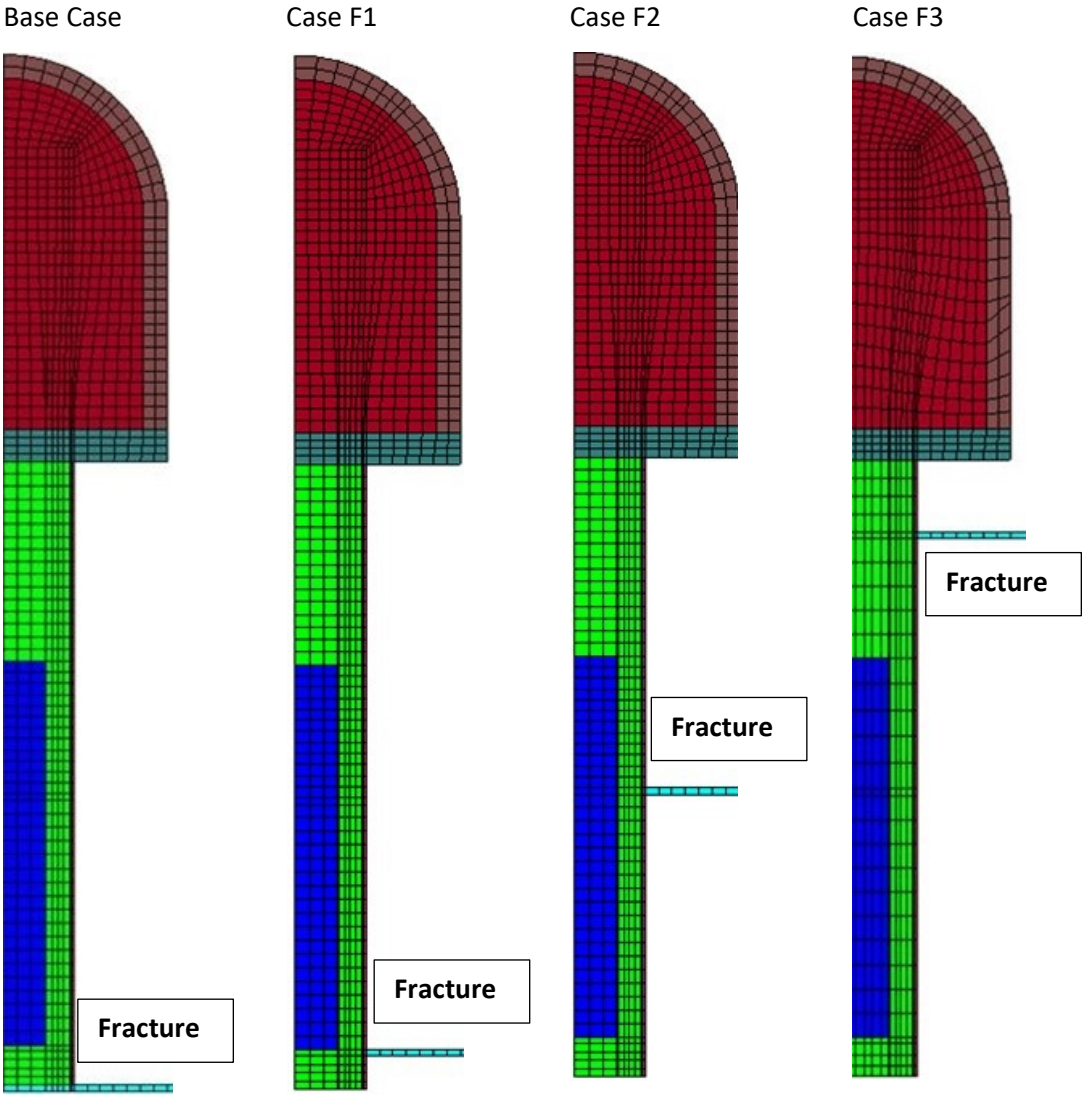

Figure 5-14. *Fracture position in Base Case, Case F1, Case F2 and Case F3*

In Case F1, the fracture is closer to central buffer position than in Base Case and it reaches full saturation slightly earlier than in Base Case. Accordingly, closing time for air gap decreases in Case F1. Although the position of fracture has been modified slightly, THM response of the model has not varied considerably.

In Case F2, the fracture is at the central buffer position. Hence, the central buffer reaches full saturation earlier than the Base Case. The drying of the central buffer is larger in Base Case. Time needed to close the air gap between buffer blocks and canister considerably decreases in Case F2 compare to Base Case.

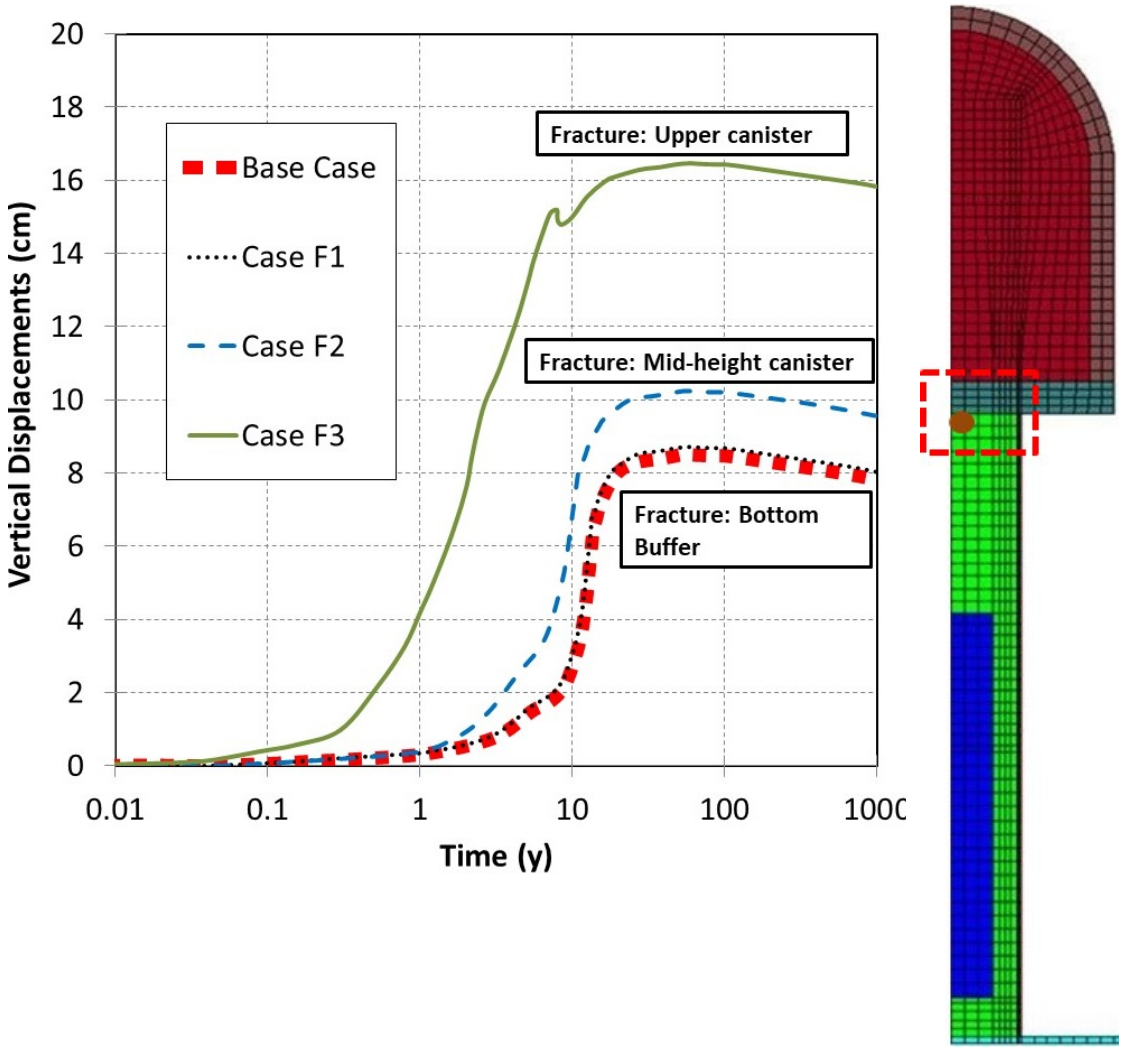

Figure 5-15 *Vertical displacement development in four cases*

In Case F3, the fracture is between the canister and buffer-backfill intersection. The main difference in these two cases is the developed displacements at the buffer-backfill intersection as it is depicted in Figure 5-15.

5.3 Effect of Pillow Pellet Thickness

In this Chapter, the effect of pellet thickness on model results has been investigated. The width of pellet slot between rock and buffer has been set as 50 mm (Posiva, 2012). Table 5-2 summarizes the differences between three cases. These cases are the following:

- Base case: Thickness of pillow pellets is 50 mm.
- Case P1: Thickness of pillow pellets is 35 mm.
- Case P2: Thickness of pillow pellets is 60 mm.

Table 5-2. *Comparison of cases according to pellet thickness.*

Results	Cases		
	Case P1 (t:35 mm)	Base Case (t=50 mm)	Case P2 (t:60 mm)
T_{max} (°C) (air gap wall)	80	80.7	81
Time (years) for S_r = 99 % (buffer disc)	8	8.4	9
Time (years) for S_r = 99 % (Backfill block)	6.5	6.7	7
Buffer Density (kg/m^3) (Disc)	1729	1729	1728
Backfill Density (kg/m^3) (Backfill blocks)	2017	2027	2027
Max. Effective Stress (Disc)	10.7	9.4	9.3
Displacements at buffer-backfill intersection (cm)	10	8.4	8.4
Time (years) for closing air gap	3.9	4.9	4.9

“t” refers to pellet thickness

It has been observed that there is no considerable difference in these three cases. Time to reach full saturation has been affected slightly. There are also slight differences in terms of vertical displacements and generated stresses. When the pillow pellets have a lower thickness, displacement at the buffer-backfill intersection and stresses increase slightly probably due to the lower density average of the buffer. Maximum temperature and densities are not affected considerably.

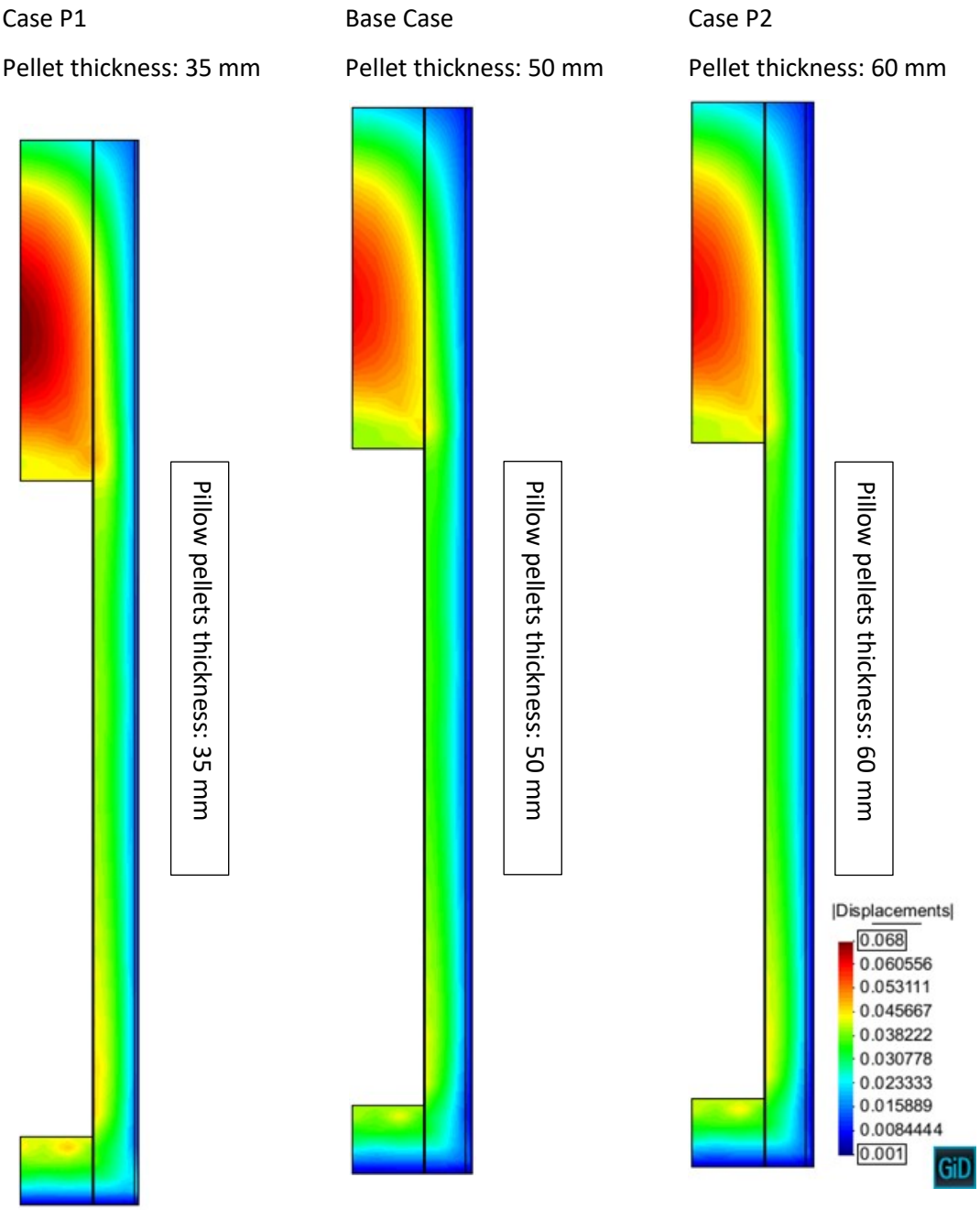

Figure 5-16. *Displacement distribution in three cases at the end of* five years.

The stress generation in Case P1 is stronger than the Base Case. Accordingly, vertical displacements at the buffer-backfill intersection are larger in Case P1 and it is depicted in ***Figure 5-16***. In general, THM response of these two cases is similar. There are no significant differences.

Time needed to full saturation of buffer and backfill is larger in P2 than in Base Case. In general, THM response of these two cases is similar.

5.4 Effect of Salinity

In this chapter, effect of salinity on model results has been investigated. The combined effect of salinity and initial water content has been explored in Case S3. Table 5-3 summarizes the differences between three cases. These cases are the following:

- Base case: Fresh water, equivalent to DI water.
- Case S1: Total dissolved solids (TDS) content is 35 g/L (salinity: 3.5%).
- Case S2: Total dissolved solids (TDS) content is 70 g/L (salinity: 7 %).
- Case S3: Total dissolved solids (TDS) content is 70 g/L; initial water content (w) of the buffer is 19.7%. In Base Case, Case S1 and Case S2; initial water content of the buffer is 17%.

Table 5-3. *Comparison of cases according to TDS.*

Results	Cases			
	Base Case (Fresh water)	Case S1 (TDS: 35 g/L)	Case S2 (TDS: 70 g/L)	Case S3 (TDS: 70 g/L; w_{buffer}: 19.7%)
T_{max} (°C) (air gap wall)	80.7	80.7	80.7	80.7
Time for S_r = 99 % (Buffer discs)	8.4	6.8	6.3	6.3
Time for S_r = 99 % (Backfill blocks)	6.7	6.8	6.3	6.3
Buffer Density (kg/m^3) (Disc)	1729	1717	1728	1728
Backfill Density (kg/m^3) (Backfill blocks)	2027	2042	2027	2027
Max. Effective Stress (MPa) (Buffer discs)	9.4	6.7	4.1	4.3
Displacements at buffer-backfill intersection (cm)	8.4	7.3	5.5	3.8
Time (years) for air gap closure	4.9	5.1	5.8	9.7

It has been observed that there is a considerable difference in terms of generated vertical displacements and stresses in these four cases. In Case S2, where the TDS is 70 g/L, generated displacements at the buffer-backfill intersection are considerably less than in the Base Case. Time to reach full saturation is also sensitive to rate of salinity because the materials have different hydraulic conductivities according to the rate of salinity of water. Maximum temperature and densities are not affected significantly.

Figure 5-17 shows the salinity of groundwater in deep boreholes (Ruotsalainen et al., 2000). A design basis TDS value for a repository excavated at the depth of about 400 meters at Olkiluoto could be, for example, 35 g/L. All the repository systems and engineered barriers should perform properly at least at groundwater salinities ranging from fresh water to 35 g/L. Today, the

considered salinity at the depth of the repository is 10 g/L. A design basis value of 35 g/L would allow intrusion of groundwater presently lying 100 to 200 meters below the 500-meters level. As 35 g/L is the salinity of Baltic sea water, it would also take into account the maximum possible salinity of water infiltrating at the surface. If the repository were planned to be constructed deeper in the bedrock, the design basis salinity value needs to be raised. For example, if the repository would be located at a depth of 700 meters, a possibility of intrusion of highly saline, brine-type groundwater (TDS nearing or exceeding 100 g/L) into the repository should be taken into consideration.

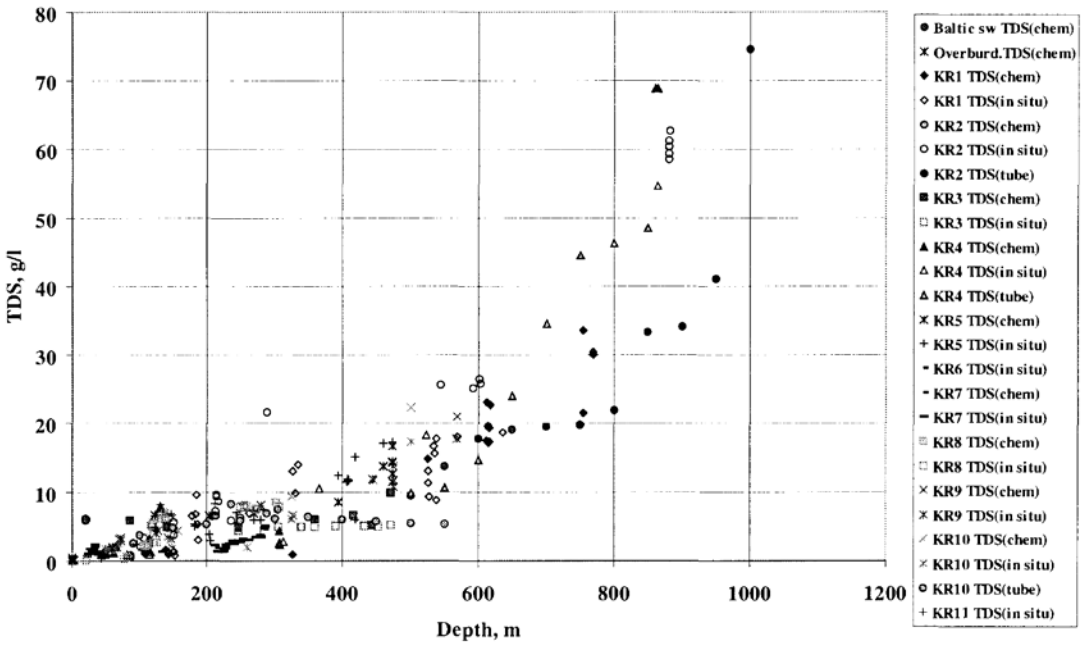

Figure 5-17. *Salinity of groundwater in deep boreholes. (Ruotsalainen et al., 2000).*

The studies of Dixon (2000) and Vieno (2000) are considered to investigate the impact of salinity on THM response of the system. As it is shown in Figure 5-18, when the dry density is higher than 900 kg/m^3, there is no consistent reduction of the swelling pressure of bentonite-based materials tested under highly saline conditions relative to those observed under fresh water percolation. Salinity becomes an important influence on swelling pressure developed once the dry density decreases below approximately 900 kg/m^3. Other authors show that the saline water reduces the swelling pressure at higher dry densities (Karnland et al., 2006) and (Martikainen and Schatz, 2011). It can be said that salinity has more impact on pellet based materials rather than in MX-80 and Friedland clay blocks.

It is understood that under fresh water conditions, there would be a certain proportion of the water that is tightly adsorbed to the clay particles and not available to participate in hydraulic

processes. Under saline or "brine" conditions, it might be expected that the quantity of adsorbed water would be lower and so the porosity available for participation in mass transport would be higher. The result would be a higher measured hydraulic conductivity. The data show that at dry densities exceeding approximately 900 kg/m^3 (MX-80 and Friedland clay blocks), the hydraulic conductivity of bentonite-based materials is not considerably affected by the presence of saline water. Swelling pressure relationship according to rate of salinity (Dixon, 2000) is presented in Table 5-4. According to this relationship, hydro-mechanical parameters of materials in this project (clay and pellet based materials) have been set for different rate of salinitys. Table 5-5 gives the parameters considered for different rate of salinitys. It is important to point out that the analysis presented in this Chapter does not include the reactive transport and any chemical analysis. The properties of the materials change with the salinity and it is considered that it is fixed during all analyses, this means that the repository is saturated with fresh water or water with TDS of 35 and 70 g/L. Hydro-mechanical-chemical (HMC) analysis can be found in Navarro et al., 2017 and Yustres et al., 2017.

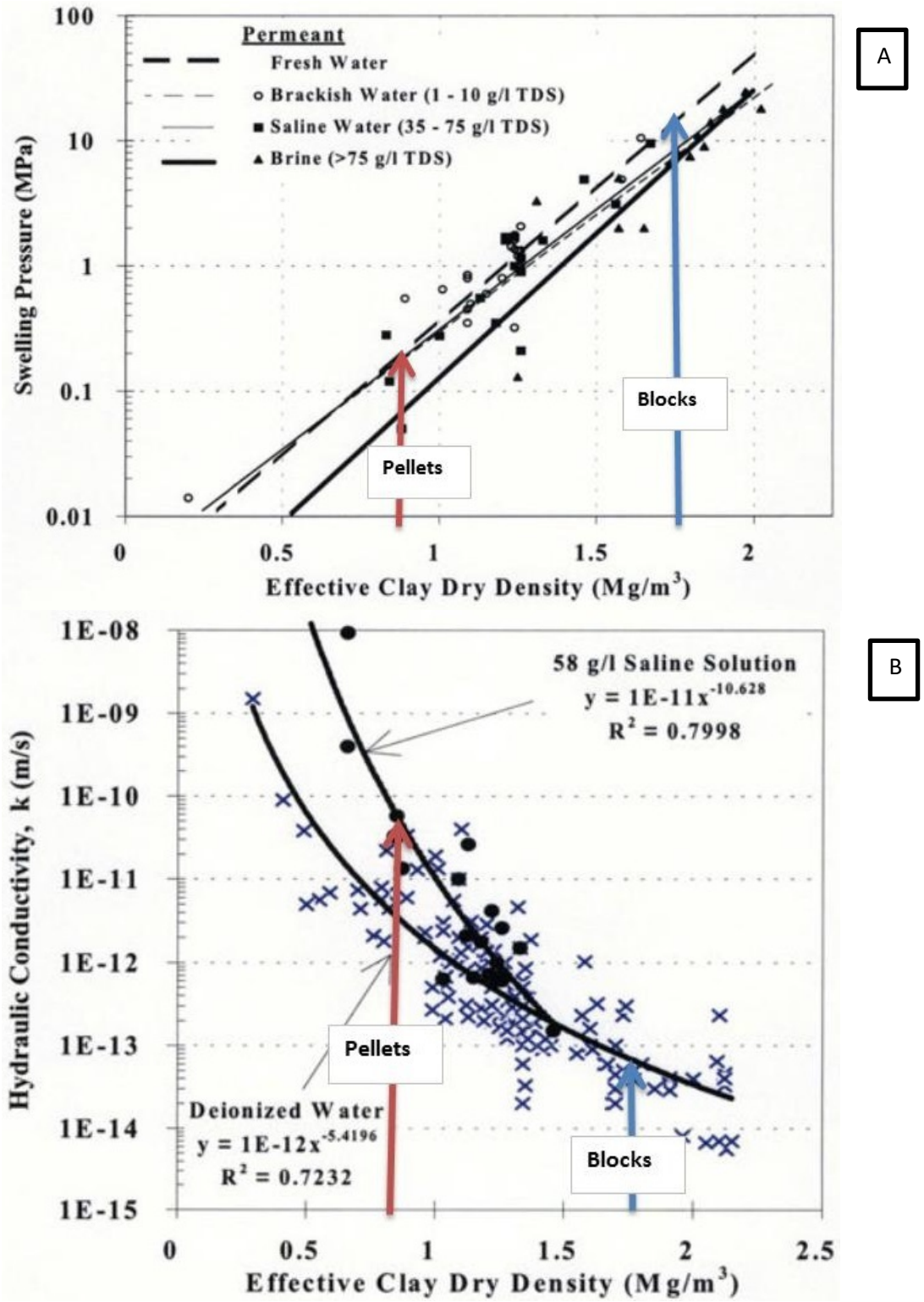

Figure 5-18. *Effect of salinity on swelling pressure (A) and hydraulic conductivity (B), Dixon (2000).*

Table 5-4. *Relationships between effective clay dry density (ECDD) and swelling pressure at various groundwater salinities and the expected bentonite pore water salinities in these bentonite-groundwater systems* (Dixon, 2000). *ECDD is defined as dry of mass clay / (volume occupied by clay + volume of voids).*

Ground water type	Groundwater TDS (g/L)	Estimated bentonite pore water TDS (g/L)	Swelling pressure equation	Correlation coefficient (R^2)
Fresh	<1	10-15	$P=0.0022e^{5.0331xECDD}$	0.7355
Brackish	1 – 10	10-25	$P=0.0065e^{4.22xECDD}$	0.8688
Saline	10 – 35	25-45	no data	no data
Saline	35 – 75	45-85	$P=0.0015e^{5.2044xECDD}$	0.7964
"Brine"	>75	>85	$P=0.0008e^{5.1503xECDD}$	0.7765

Table 5-5. *Hydro-mechanical parameters according to different rate of salinity.*

Material	Parameter	Fresh	3.5 g/L	70 g/L
MX-80	κ_{s0}	0.09	0.075	0.06
	k (m^2)	$5.6x10^{-21}$	$3.07x10^{-20}$	$5.6x10^{-20}$
Friedland clay	κ_{s0}	0.05	0.041	0.033
	k (m^2)	$7.6x10^{-20}$	$4.18x10^{-19}$	$7.6x10^{-19}$
Pillow pellets	κ_{micro}	0.09	0.075	0.06
	k (m^2)	$5x10^{-19}$	$2.75x10^{-18}$	$5x10^{-18}$
Rod pellets	κ_{micro}	0.09	0.075	0.06
	k (m^2)	$1.4x10^{-18}$	$7.7x10^{-18}$	$1.4x10^{-17}$
Granules	κ_{micro}	0.09	0.075	0.06
	k (m^2)	$1.5x10^{-19}$	$8.25x10^{-19}$	$1.5x10^{-18}$

In Case S1, materials have reached to full saturation slightly earlier compare to Base Case. There is an important difference between two cases in terms of stresses and vertical displacements at the buffer-backfill intersection. Generated stresses in buffer are depicted in *Figure 5-19*. It is clear that the increase of salinity of the inflow water reduces the swelling pressure of buffer and backfill considerably. In Case S1, it is seen a slight reduction in the displacements occurred at the buffer-backfill interface.

In Case S2, materials have reached the full saturation earlier because system components are more permeable. For example, the intrinsic permeability of buffer for three cases is showed in *Figure 5-19* together with the generated stresses. There is a considerable difference between the two cases in terms of stresses and vertical displacements at the buffer-backfill intersection. The model response of Case S3 is similar to Case S2 in general.

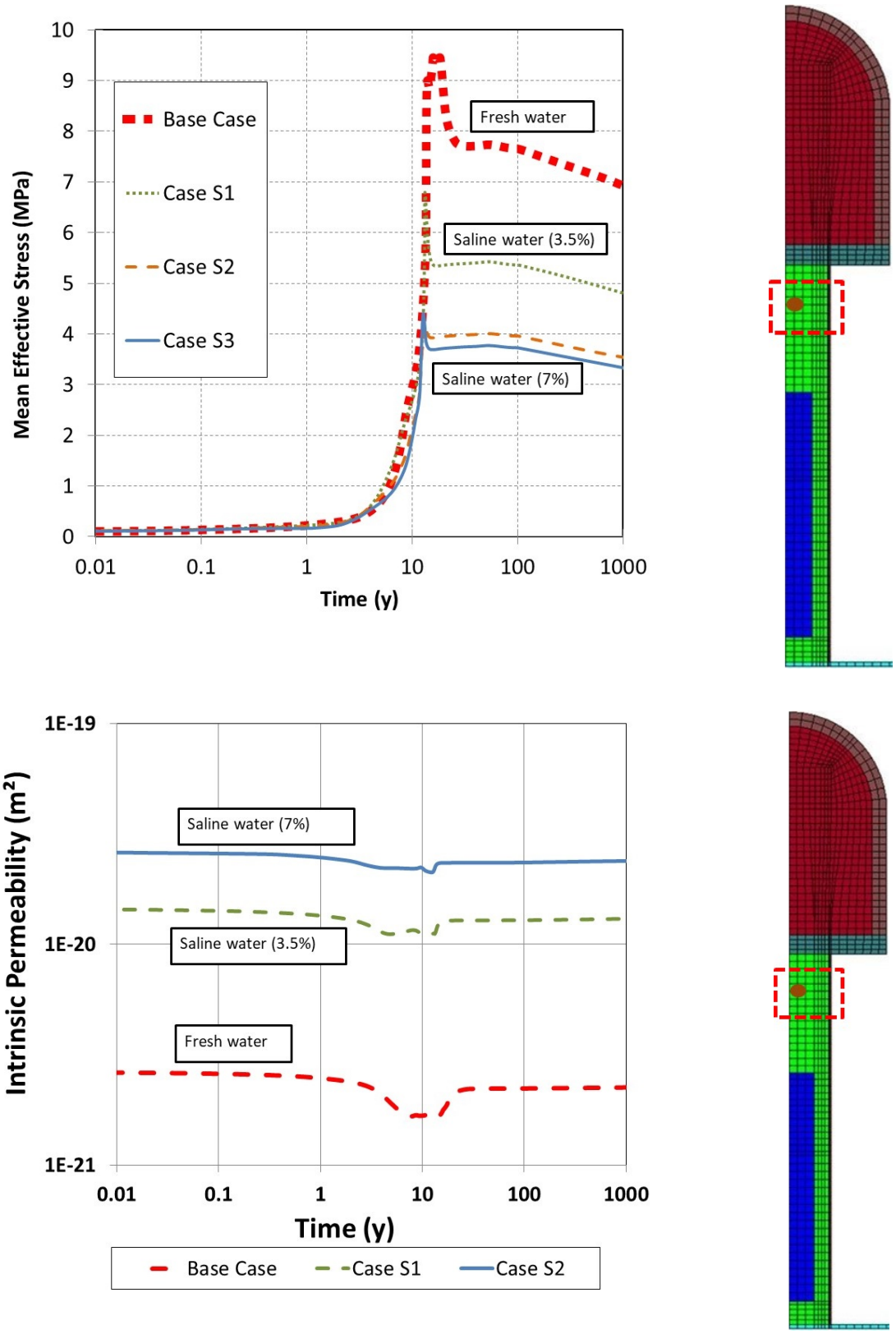

Figure 5-19. *Comparison of cases in terms of stresses and permeability.*

5.5 Effect of Initial Water Content

In this Chapter, the effect of the initial water content of buffer in model results has been investigated. Table 5-6 summarizes the differences between three cases. These cases are the following:

- Base case: Water content is 17%; initial suction for buffer is 35.2 MPa.
- Case W1: Water content is 11%; initial suction for buffer is 66 MPa.
- Case W2: Water content is 21.7%; initial suction for buffer is 11.7 MPa.

Table 5-6. *Comparison of cases according to the initial water content of the buffer.*

Results	Cases		
	Case W1 (w: 11%)	Base Case (w: 17%)	Case W2 (w: 21.7%)
T_{max} (°C) (air gap wall)	92.1	80.7	80.7
Time for S_r = 99 % (Buffer disc)	11.3	8.4	3.7
Time for S_r = 99 % (Backfill blocks)	7.1	6.7	6.1
Buffer Density (kg/m^3) (Disc)	1736	1729	1730
Backfill Density (kg/m^3) (Backfill blocks)	2027	2027	2026
Max. Effective Stress (MPa) (Buffer disc)	12	9.4	7
Displacements at buffer-backfill intersection (cm)	9.3	8.4	5.8
Time (years) for air gap closure	5.7	4.9	4.1

It has been observed that there is a significant difference in terms of maximum temperature, time to reach full saturation of buffer, generated vertical displacements and stresses in these three cases. In Case W1, due to delay of saturation, air gap closes later compare to other two cases. Hence, temperature reached in early times in Case W1 is greater than Base Case and Case W2. The time to reach full saturation and also the generated displacements at the buffer-backfill intersection decrease considerably in Case W2 comparing to the Base Case. It can be said that when the initial water content of buffer is lower, generated stresses and displacements are larger. The density of buffer disc is not affected significantly.

There is a significant difference in terms of desaturation of buffer ring (*Figure 5-20*) in three cases. The reason is a delay in saturation in Case W1. Stresses, vertical displacements at the buffer-backfill intersection and time to reach the gap closure are also larger in Case W1 compare to Base Case and Case W2.

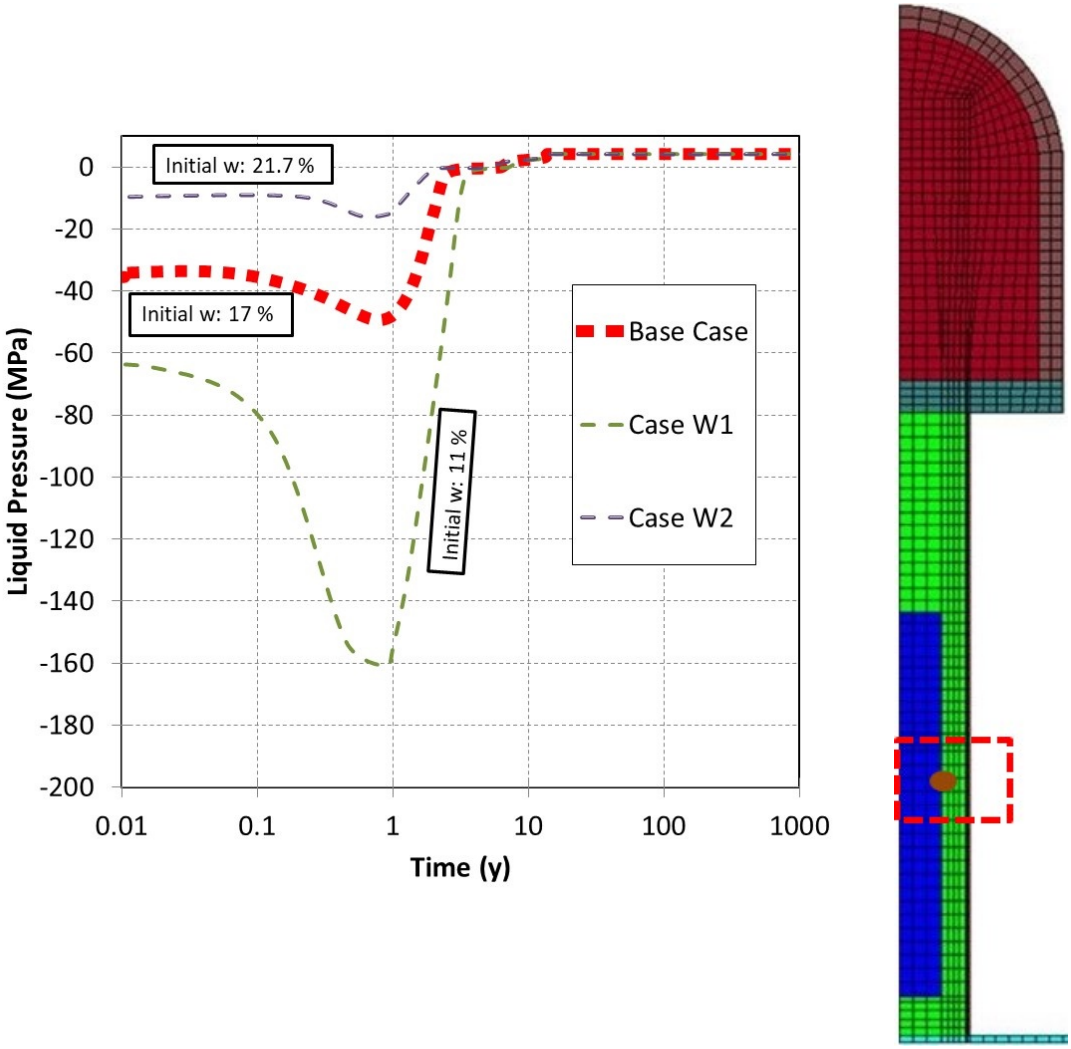

Figure 5-20. *Liquid pressure evolution in three cases.*

5.6 Effect of Buffer Density

In this Section, the effect of a higher buffer density is analysed. The density of the buffer rings was increased from 1752 kg/m^3 (Base Case) to 1840 kg/m^3 and the density of buffer discs was increased from 1700 kg/m^3 (Base Case) to 1788 kg/m^3. The average saturated density of the buffer in Base Case is 2000 kg/m^3 and in Case D1, 2100 kg/m^3.

To simulate Case D1, both swelling capacity and stiffness have been increased by 5% to account for the mechanical properties variation due to density increase. Change in the density implies that there are variations of porosity, permeability, retention curve and deformations.

As it is shown in *Figure 5-21*, there are some differences between two cases in terms of stress generation. Succeeded stresses and displacements at buffer backfill interface during wetting are higher in Case D1 which is consistent with a higher density. Time to reach full saturation is reduced which can be explained by the porosity and vapour diffusivity reduction in the buffer. Less drying implies less relative permeability reduction. Table 5-7 summarizes the differences between the two cases.

Table 5-7. *Comparison of cases according to density of buffer*

Results	Cases	
	Base Case (Average saturated density buffer 2000 kg/m^3)	Case D1 (Average saturated density buffer 2100 kg/m^3)
T_{max} (°C) (air gap wall)	80.7	80.7
Time for S_r = 99 % (Buffer disc)	8.4	6.4
Time for S_r = 99 % (Backfill blocks)	6.7	6.8
Buffer Density (kg/m^3) (Disc)	1729	1799
Backfill Density (kg/m^3) (Backfill blocks)	2027	2027
Max. Effective Stress (MPa) (Buffer disc)	9.4	10
Displacements at buffer-backfill intersection (cm)	8.4	10.2
Time (years) for air gap closure	4.9	3.9

Base Case
Saturated density of buffer 2000 kg/m^3

Case D1
Saturated density of buffer 2100 kg/m^3

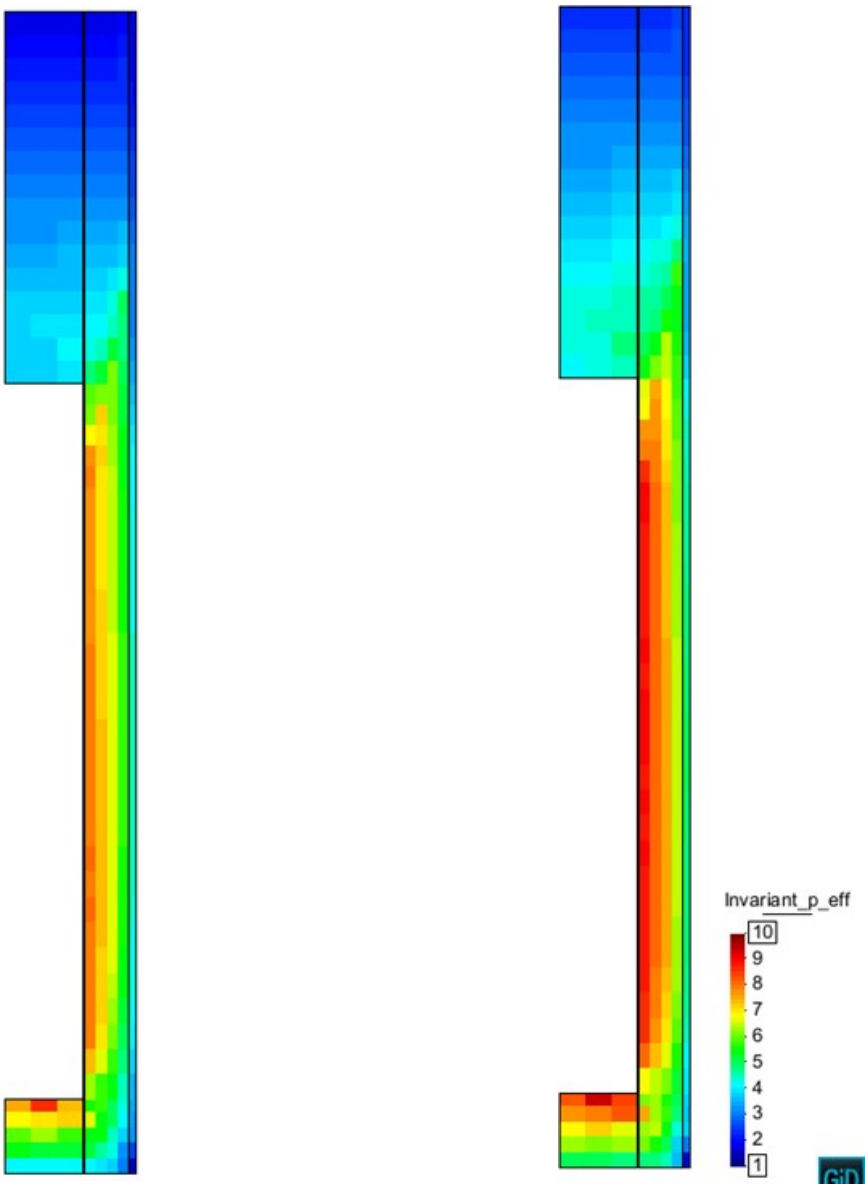

Figure 5-21. *Distribution of stresses in two cases after* 10 years.

5.7 Effect of Lagrangian method

In this Section, the differences between the Base Case and the Case L1 have been explained. In Case L1, Lagrangian method is considered.

Table 5-8 summarizes the differences between two cases.

Table 5-8. *Comparison of cases according to using of Lagrangian method.*

Results	Cases	
	Base Case (No lagrangian method)	Case L1 (Lagrangian method considered)
T_{max} (°C) (air gap wall)	80.7	80.2
Time for S_r = 99 % (Buffer disc)	8.4	8.8
Time for S_r = 99 % (Backfill blocks)	6.7	6.8
Buffer Density (kg/m^3) (Disc)	1729	1729
Backfill Density (kg/m^3) (Backfill blocks)	2027	2027
Max. Effective Stress (MPa) (Buffer disc)	9.4	9.4
Displacements at buffer-backfill intersection (cm)	8.4	8.4
Time (years) for air gap closure	4.9	2.5

In Case L1, temperature for air gap wall canister side and ring block side becomes a unique line in earlier years (*Figure 5-22*). The saturation of air gap wall ring block side is gradual in Base Case, while in Case L1 it saturates sharply. Some differences have been observed also in the gap closing process. In Case L1, the movement (closure) of air gap element can be seen clearly (deformed mesh - *Figure 5-22*). There are no significant differences observed in the rest of the results.

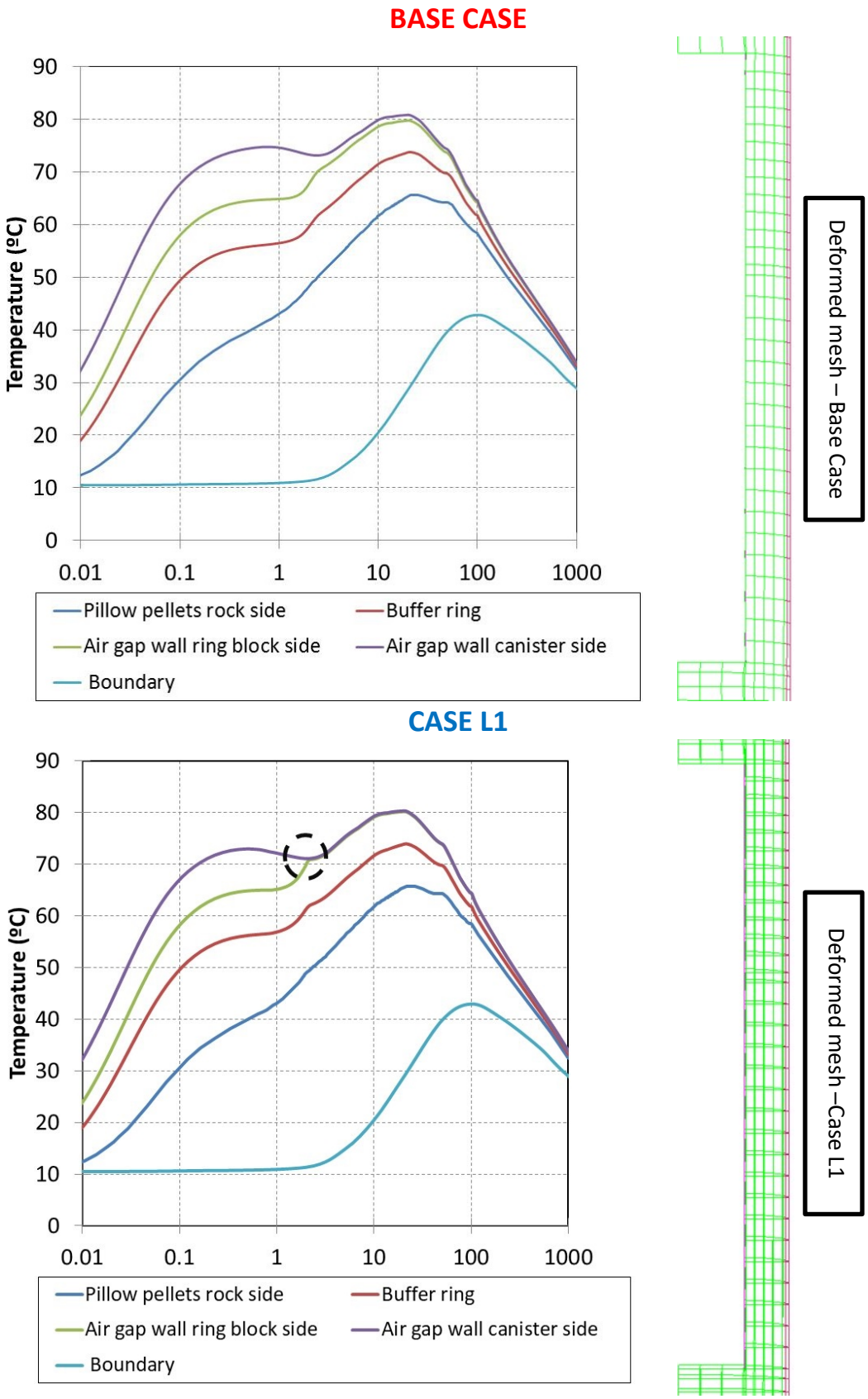

Figure 5-22. *Variation of temperature with time. Base case vs Case L1. Deformed mesh (factor 1) at the end of 1000 years.*

5.8 Effect of micro porosity of pillow pellets

In this Section, the differences between the Base Case and the Case M1 are explained. There are some slight differences between these two cases in terms of densities, effective stress, vertical displacements at the buffer-backfill intersection and gap closing process. Table 5-9 summarizes the differences between two cases.

Table 5-9. *Comparison of cases according to K^{Micro} for pellet-based materials.*

Results	Cases	
	Base Case (K^{Micro}=0.09)	Case M1 (K^{Micro}=0.135)
T_{max} (°C) (air gap wall)	80.7	80.7
Time for S_r = 99 % (Buffer disc)	8.4	7.9
Time for S_r = 99 % (Backfill blocks)	6.7	5.8
Buffer Density (kg/m^3) (Disc)	1729	1739
Backfill Density (kg/m^3) (Backfill blocks)	2027	2044
Max. Effective Stress (MPa) (Buffer disc)	9.4	9.8
Displacements at buffer-backfill intersection (cm)	8.4	7.8
Time (years) for air gap closure	4.9	4.8

The stresses generated in buffer blocks are slightly higher in Case M1. However, the displacements reached at the buffer-backfill intersection are slightly lower in Case M1. Micro porosity increases more in Case M1 (*Figure 5-23*) but it does not have a global effect on model results. There are no significant differences observed in the rest of the results.

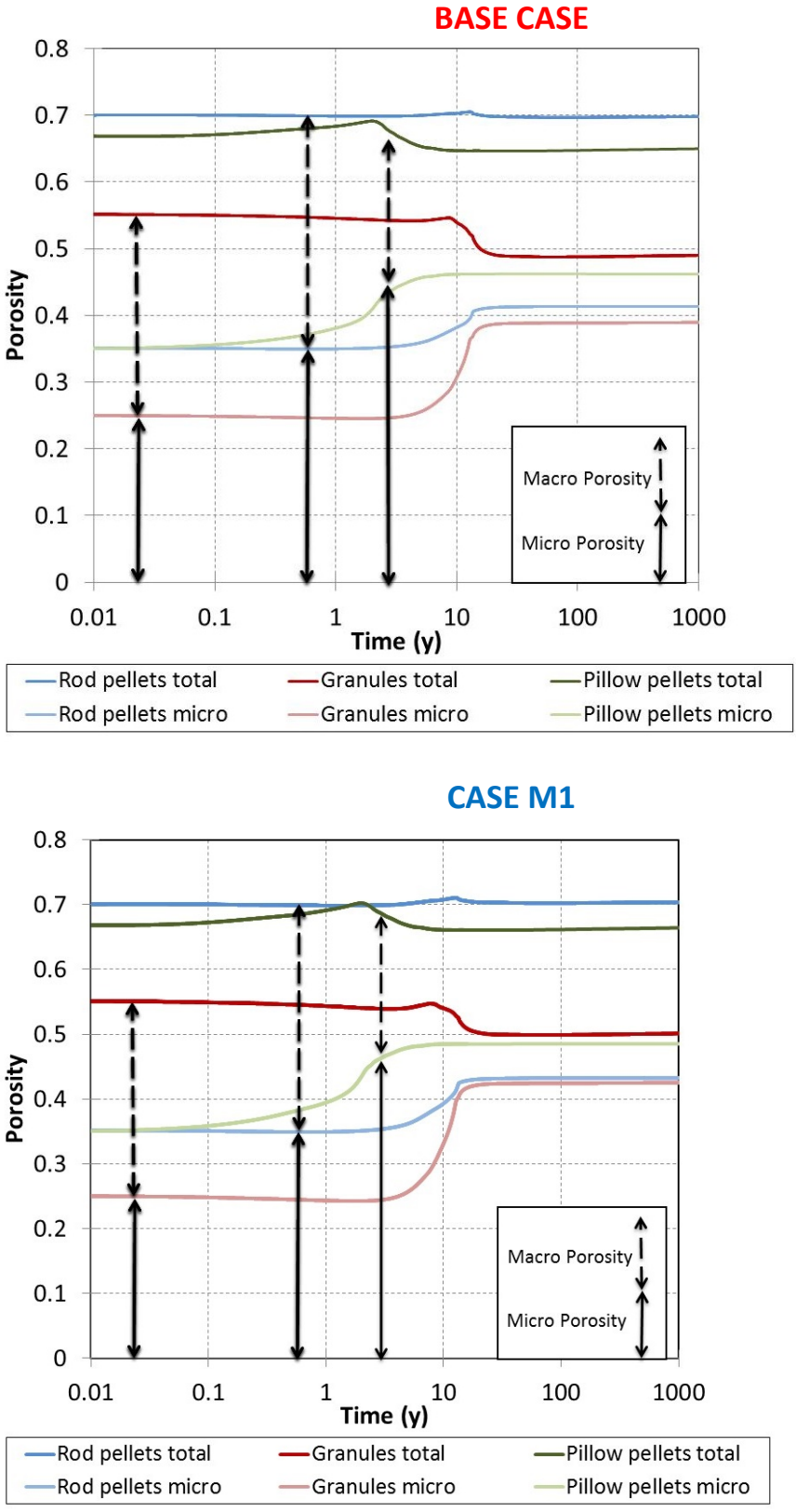

Figure 5-23. *Variation of porosity in pellets with time. Base case vs Case M1.*

5.9 Effect of filling material between buffer and rock

In this Section, the differences between the Base Case and the Case FM1 have been explained. Table 5-10 summarizes the differences between two cases. In Base Case, filling material (between rock and buffer) is pillow pellet. In Case FM1, slurry has been used as filling material. Slurry is also MX-80 bentonite and the material is initially almost saturated (initial Sr: 98%). The rest of the thermo-hydro-mechanical parameters are considered identical to the MX-80 parameters used for blocks.

Table 5-10. *Comparison of cases according to filling material.*

Results	Cases	
	Base Case (Filling material: pillow pellets)	Case FM1 (Filling material: Slurry)
T_{max} (°C) (air gap wall)	80.7	80
Time for S_r = 99 % (Buffer disc)	8.4	8.04
Time for S_r = 99 % (Backfill blocks)	6.7	8.04
Buffer Density (kg/m^3) (Disc)	1729	1729
Backfill Density (kg/m^3) (Backfill blocks)	2027	2027
Max. Effective Stress (MPa) (Buffer disc)	9.4	9.8
Displacements at buffer-backfill intersection (cm)	8.4	8.8
Time (years) for air gap closure	4.9	3.1

It is clear that air gap closes earlier in Case FM1. The slurry has been assumed to be almost saturated initially. This favours the water intake by the buffer as compared with the Base Case for which pellets were initially unsaturated. Comparison of two cases in terms of liquid pressure in earlier years (2.1 years after emplacement of the canister) is depicted in *Figure 5-24*. In Case FM1, the buffer swells faster than in the Base Case so that the gap between canister and buffer closes more rapidly.

The slurry is denser than pellets and with higher saturation and, therefore, it compresses less. This produces a higher stress development during swelling as compared with the Base Case.

In Case FM1, air gap closes earlier as indicated above and drying of buffer adjacent to the canister is not as stronger as Base Case. There are no significant differences observed in the rest of the results.

Base Case

Case FM1

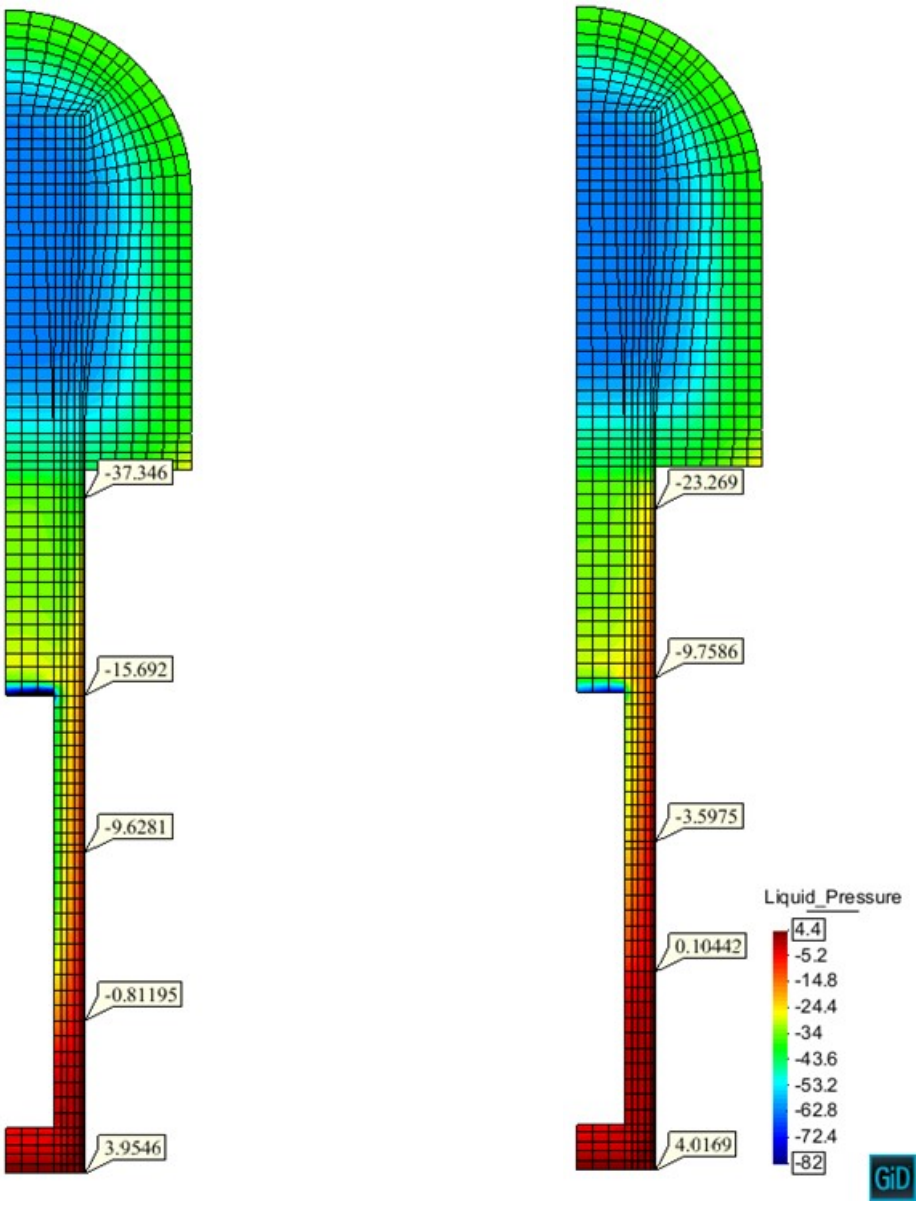

Figure 5-24 *Liquid pressure distribution in two cases at the end of* 2.3 years

5.10 Effect of rock hydraulic conductivity

In this Section, differences between the Base Case, Case R1, Case R2 and Case R3 have been explained. CODE_BRIGHT works with the intrinsic permeability (m^2), which is approximately seven orders of magnitude lower than the hydraulic conductivity (m/s) at ambient temperature. This relation changes when the temperature increases and water viscosity goes down, so the hydraulic conductivity increases (at 95°C could be 3 times higher than at 20°C due to change in water viscosity).

- Base Case: There is a rock fracture at the bottom of buffer. rock intrinsic permeability is$1.52x10^{-19}$ m^2
- Case R1: There is no fracture and rock intrinsic permeability is $1.52x10^{-19}$ m^2
- Case R2: There is no fracture and rock intrinsic permeability is $3x10^{-19}$ m^2
- Case R3: There is no fracture and rock intrinsic permeability is $3x10^{-21}$ m^2

Figure 5-25 shows the differences between cases and Table 5-11 summarizes the results of these cases. As can be seen in the table, rock intrinsic permeability has an important role to play in achieved results

Table 5-11. *Comparison of cases according to rock intrinsic permeability.*

Results	Cases			
	Base Case (fracture at the bottom of buffer; K_{rock}: $1.52x10^{-19}$ m^2)	Case R1 (No fracture, k_{rock}: $1.52x10^{-19}$ m^2)	Case R2 (No fracture; k_{rock}: $3x10^{-19}$ m^2)	Case R3 (No fracture; k_{rock}: $3x10^{-21}$ m^2)
T_{max} (°C) (air gap wall)	80.7	81.3	80.7	95.7
Time for S_r = 99 % (Buffer disc)	8.4	15	10	400
Time for S_r = 99 % (Backfill blocks)	6.7	9.3	5.7	260
Buffer Density (kg/m^3) (Disc)	1729	1729	1726	1696
Backfill Density (kg/m^3) (Backfill blocks)	2027	2027	2026	2028
Max. Effective Stress (MPa) (Buffer disc)	9.4	9.4	9.5	7.7
Displacements at buffer-backfill intersection (cm)	8.4	5.2	4.2	3.8
Time (years) for air gap closure	4.9	19.5	11	870

The time for gap closure is clearly dependent on the amount of water flowing to the buffer. The displacements at the buffer-backfill intersection are also clearly dependent on the amount of water flowing from the rock. The maximum effective stress seems to be relatively independent of the amount of water flowing from the rock and only when the hydraulic conductivity of the rock is very low, the main effective stress in buffer discs (swelling pressure) is reduced.

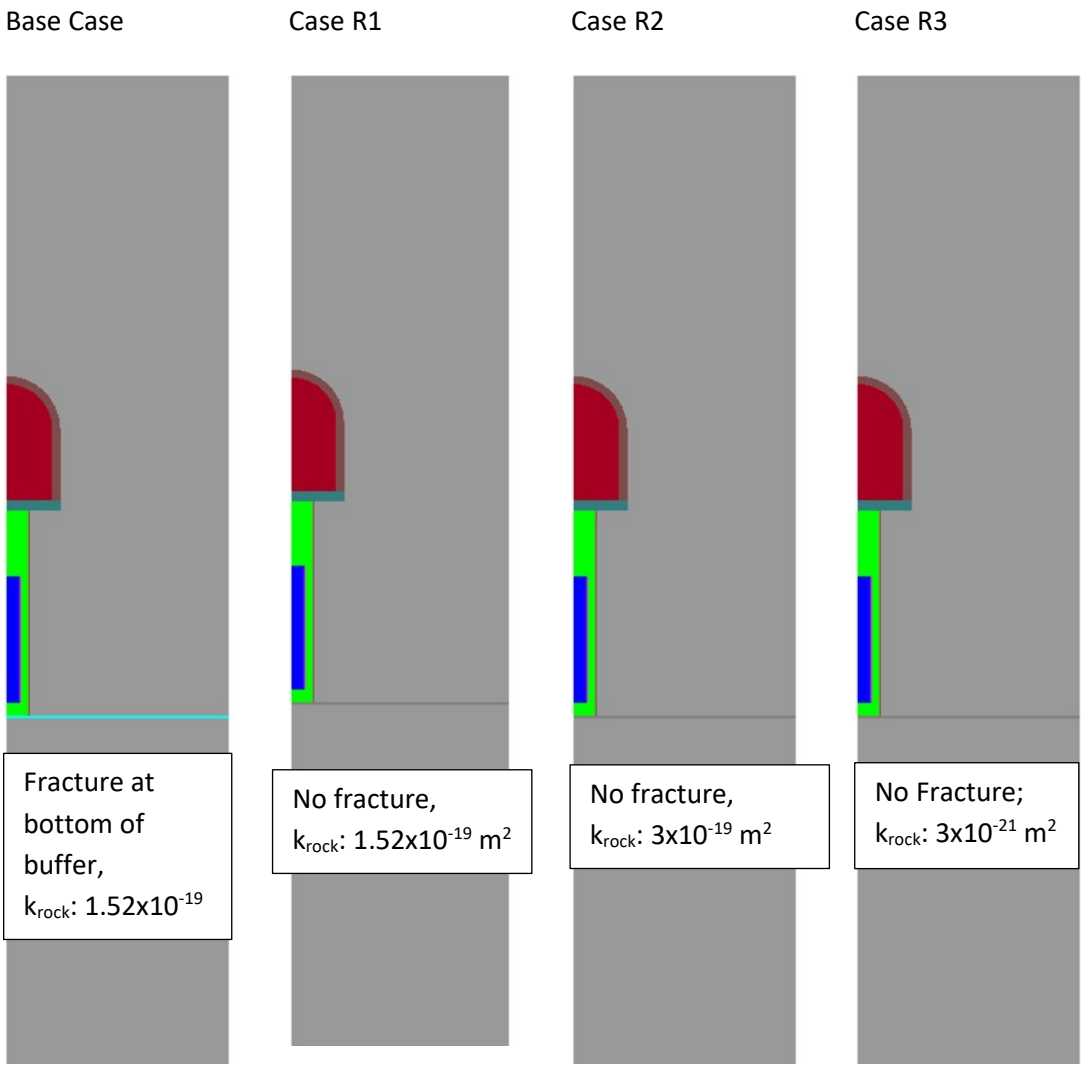

Figure 5-25. *Comparison of four cases*

As there is a delay on the air gap closure, the maximum temperature reached in earlier times on gap wall is higher in Case R1 compare to Base Case. The slow hydration in Case R1 leads a stronger drying process of buffer blocks (*Figure 5-26*) and fewer displacements at the intersection of buffer-backfill and finally longer gap closing process.

The reason for smaller displacements at the interface in the case R1 is explained in more detail in what follows. Displacements at the buffer-backfill contact depend on the velocity of hydration (therefore expansion) of the buffer and the backfill. Both, buffer and backfill hydrate but the

rates are different and depend on hydraulic conditions. Case R1, without any fracture, shows a slower hydration velocity of the buffer which implies slower expansion. If this happens, the backfill is able to sustain more stress (as it has expanded more) and therefore the interface will move upwards in a lesser magnitude. Due to model non-linearities, the final movement does not have to coincide.

In Base Case, air gap closes earlier and drying of buffer adjacent to the canister is not as stronger as Case R1 (*Figure 5-26*).

In Case R2, the rock is more permeable, however, there is no fracture. Hence, the hydration in backfill is faster than Base Case. The fracture has a more important impact on the buffer. Although the rock is slightly less permeable in Base Case, the hydration of buffer is slower in Case R2 as compared with the Base Case (Table 5-11). It is a clear effect of rock fracture. As there is a delay on the air gap closure, the maximum temperature reached in earlier times on gap wall is higher in Case R2. The slightly slower buffer hydration and faster backfill hydration in Case R2 lead less displacement at the intersection of buffer-backfill and finally longer gap closing (*Figure 5-26*).

In Case R3, the rock is less permeable and there is no fracture. Hence, the hydration is significantly slower than Base Case. As there is an important delay on the air gap closure in Case R3, the maximum temperature reached in earlier times on gap wall is higher. The desaturation of buffer due to canister heating is significantly high in Case R3 compare to Base Case (*Figure 5-26*). Extremely slow hydration of buffer in Case R3 leads fewer displacements at the intersection of buffer-backfill and even gap closure process (between canister and buffer) takes hundreds of years (*Figure 5-26*).

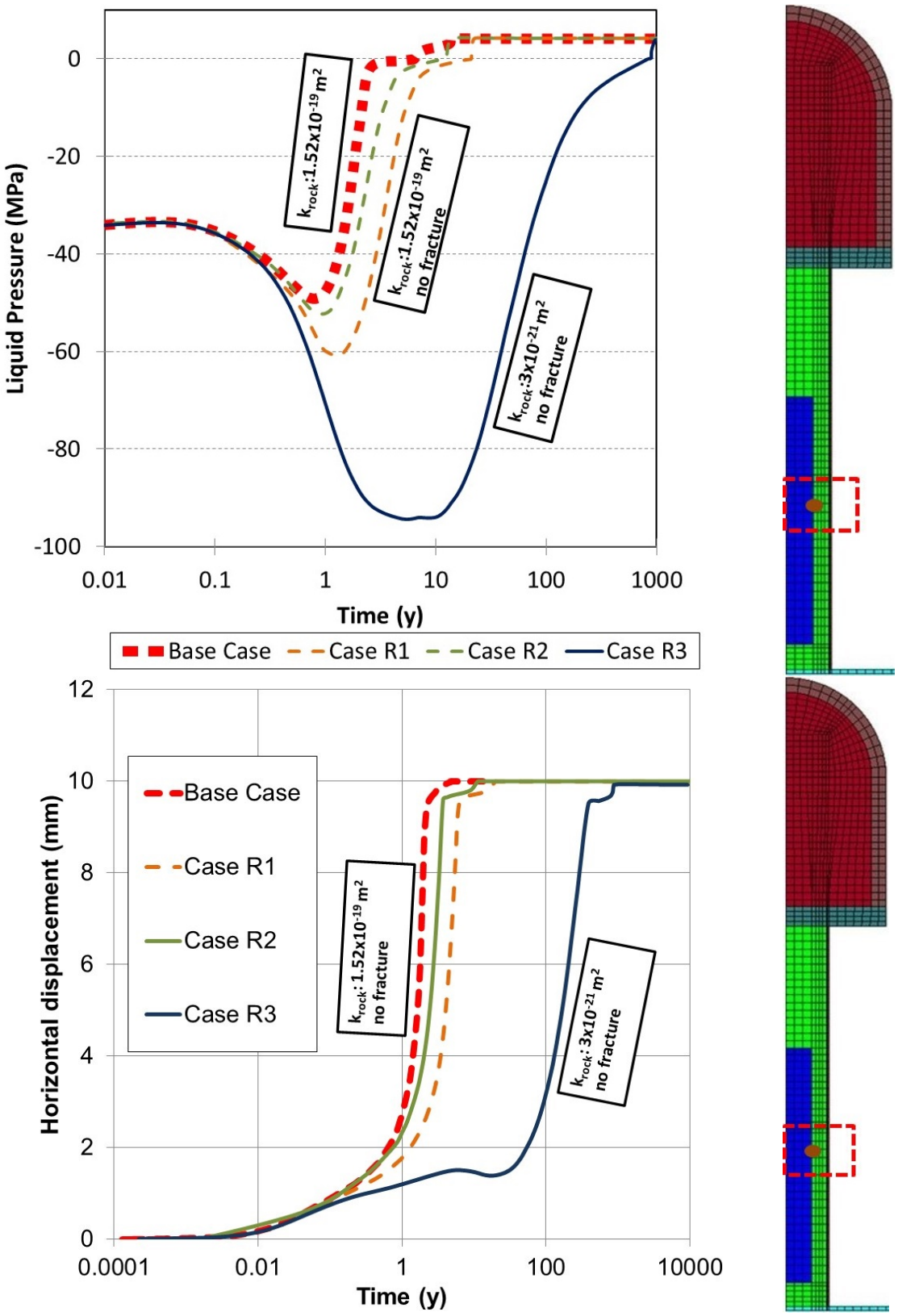

Figure 5-26. *Evolution of liquid pressure in buffer ring and closure of air gap element in four cases*

5.11 Effect of thermal expansion coefficient in buffer and backfill

In this Section, the differences between the Base Case and the Case TE1 have been explained. Table 5-12 summarizes the differences between two cases. In Base Case, linear thermal expansion coefficient α (ºC^{-1}) of buffer and backfill is 3x10^{-4} and in Case TE1 9x10^{-4}.

Table 5-12. *Comparison of cases according to thermal expansion coefficient*

Results	Cases	
	Base Case (α (ºC^{-1}) is 3x10^{-4})	Case TE1 (α (ºC^{-1}) is 9x10^{-4})
T_{max} (°C) (air gap wall)	80.7	80.7
Time for S_r = 99 % (Buffer disc)	8.4	8.9
Time for S_r = 99 % (Backfill blocks)	6.7	7
Buffer Density (kg/m^3) (Disc)	1729	1728
Backfill Density (kg/m^3) (Backfill blocks)	2027	2017
Max. Effective Stress (MPa) (Buffer disc)	9.4	10.3
Displacements at buffer-backfill intersection (cm)	8.4	9.8
Time (years) for air gap closure	4.9	5

As can be seen in the table there some slight differences between two cases.

In *Figure 5-29*, the evolution of mean effective stress for two cases is depicted. As it has been discussed in Chapter 5.1, the first reduction in mean effective stress is due to positive pore pressure and the second drop is caused by ambient conditions (cooling). In Case TE1, as the thermal expansive value is greater the secondary reduction in effective stresses is significant compare to Base Case.

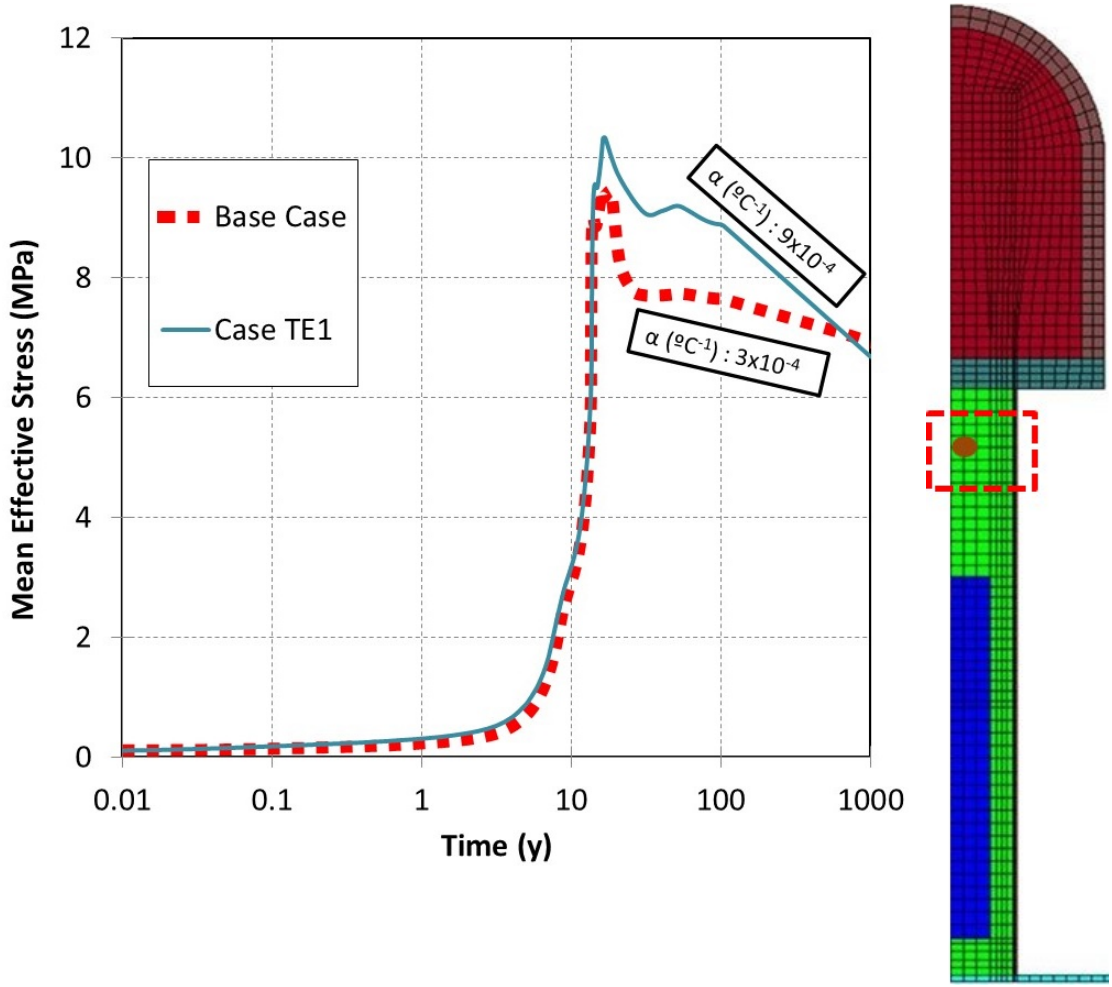

Figure 5-27. *Evolution of effective stress in buffer disc for two cases.*

5.12 Effect of thermal conductivity

In this Section, the differences between the Base Case and the Case TC1 have been explained. The thermal conductivity of buffer can decrease if the hydraulic conductivity of rock is very low and so that the buffer remains unsaturated. Another situation can make the thermal conductivity reduce is the drying of buffer adjacent to the canister. Hence, this sensitivity analysis on thermal conductivity of buffer has been carried out.

Table 5-13 summarizes the differences between two cases. In Base Case, the thermal conductivity of the water saturated medium λ_{sat} (W/ (m·K)) of buffer is 1.4 and in Case TC1; λ_{sat} is equal to 1.

Table 5-13. *Comparison of cases according to thermal conductivity*

Results	Cases	
	Base Case (λ_{sat} is 1.4 W/(m·K))	Case TC1 (λ_{sat} is 1 W/(m·K))
T_{max} (°C) (air gap wall)	80.7	86.4
Time for S_r = 99 % (Buffer disc)	8.4	8.4
Time for S_r = 99 % (Backfill blocks)	6.7	6.7
Buffer Density (kg/m^3) (Disc)	1729	1729
Backfill Density (kg/m^3) (Backfill blocks)	2027	2027
Max. Effective Stress (MPa) (Buffer disc)	9.4	9.4
Displacements at buffer-backfill intersection (cm)	8.4	8.5
Time (years) for air gap closure	4.9	4.9

As it can be seen above table there are not big differences between two cases under hydraulic and mechanical point of view. Only the maximum temperature in Case TC1 is greater than the Base Case. *Figure 5-28* shows the differences in the models.

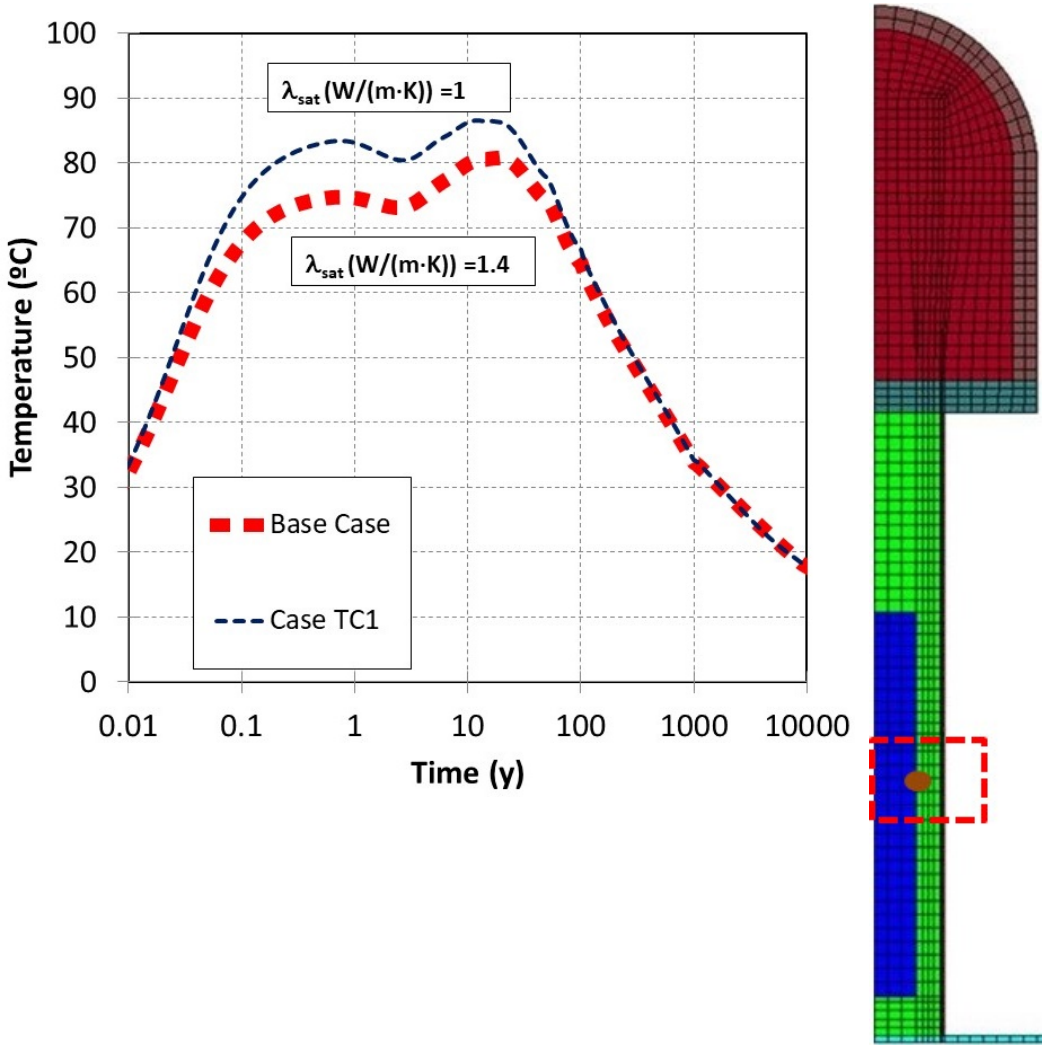

Figure 5-28. *Evolution of temperature in two cases at canister wall*

5.13 Effect of artificial wetting of pillow pellets

In this Section, the differences between the Base Case and the Case PW1 have been explained. Table 5-14 summarizes the differences between two cases. In Base Case, pellets are initially unsaturated. In the case of PW1, pellets have been considered almost saturated. It should be pointed out that this case does not reproduce the artificial wetting of pellets. The Barcelona Expansive Model implemented in CODE_BRIGHT assumes equilibrium between the suction of macro (s_M) and suction of micro (s_m). When there is artificial wetting of pellets, the water fills the large voids (macro voids) between the pellets almost instantaneously and the pellets start swelling, increasing the meso and micro porosity. Water mass exchange between macropores and micropores (aggregates) can be seen in Alonso and Navarro (2005) and Navarro et al. 2014 for MX-80 bentonite.

Table 5-14. *Comparison of cases according to initial conditions of pellets.*

Results	Cases	
	Base Case (Initial S_r for pellets: 25%)	Case PW1 (Initial S_r for pellets: 80%)
T_{max} (°C) (air gap wall)	80.7	80.7
Time for S_r = 99 % (Buffer disc)	8.4	8.7
Time for S_r = 99 % (Backfill blocks)	6.7	6.2
Buffer Density (kg/m^3) (Disc)	1729	1705
Backfill Density (kg/m^3) (Backfill blocks)	2027	2026
Max. Effective Stress (MPa) (Buffer disc)	9.4	8.8
Displacements at buffer-backfill intersection (cm)	8.4	6.5
Time (years) for air gap closure	4.9	2.58

As it can be seen in the Table, initial conditions of pillow pellets have a role to play in model results. In Case PW1; there is a reduction in buffer density, effective stresses and generated displacements at the intersection of buffer-backfill compare to Base Case. The gap closes earlier in Case PW1. One of the most important differences between the two models is the hydration process of the pillow pellets. Due to the fast saturation of pillow pellets in Case PW1, micro porosity does not increase as strong as in the Base Case. There is also less swelling pressure and accordingly, fewer displacements (*Figure 5-29*) in Case PW1. The total permeability of pillow pellets has a larger initial value in Case PW1. The reason is that total permeability mainly depends on saturation degree. Although the total permeability has a different trend in Case PW1, the reached final value is same as Base Case.

Base Case

Initial S_r for pellets: 25%

Case PW1

Initial S_r for pellets: 80%

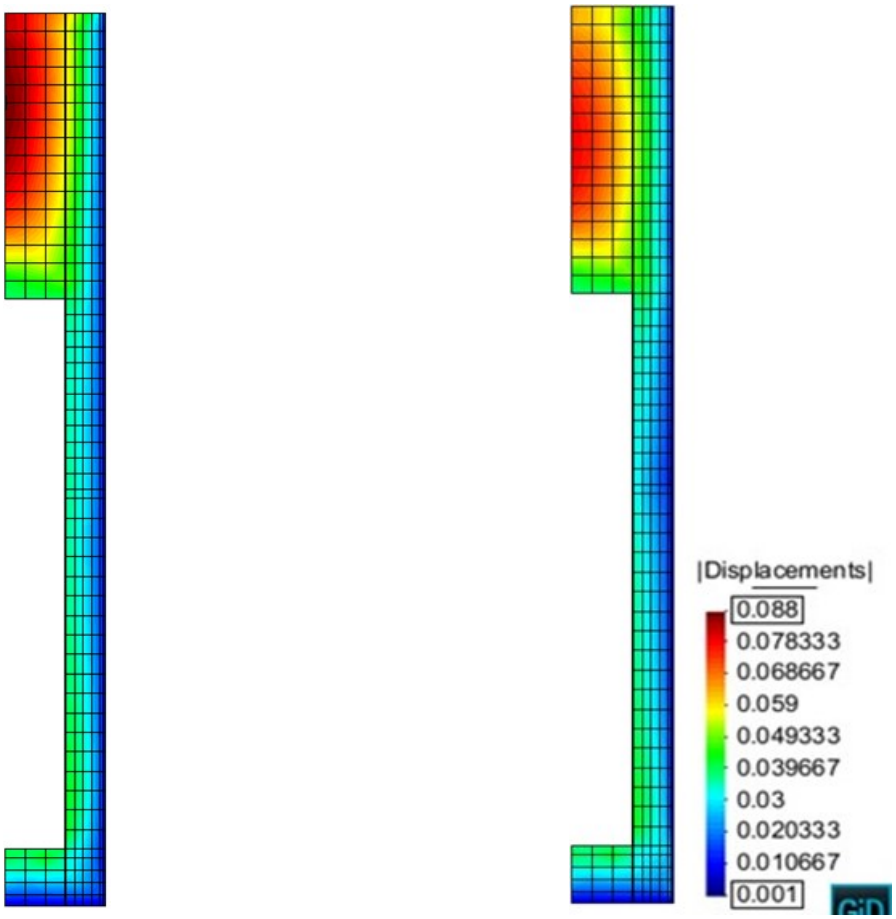

Figure 5-29. *Distribution of displacement in two cases at the end of* 30 years

5.14 Calculation under FISST Gaps Geometry

In Base Case, the gap between canister and buffer blocks has 10 mm width. A new design has been proposed with a gap of 35 mm width filled with pellets. Moreover, between rock and buffer has two levels of thickness of pillow pellets, which are 50 mm and 67.5 mm (***Figure 5-30***). In Base Case, pillow pellets gap has a unique thickness of 50 mm along the buffer boundary. In FISST gaps (it refers to the geometry of a full-scale test planned by Posiva Oy to be performed in Onkalo) geometry, pillow pellets have more volume compared to Base Case.

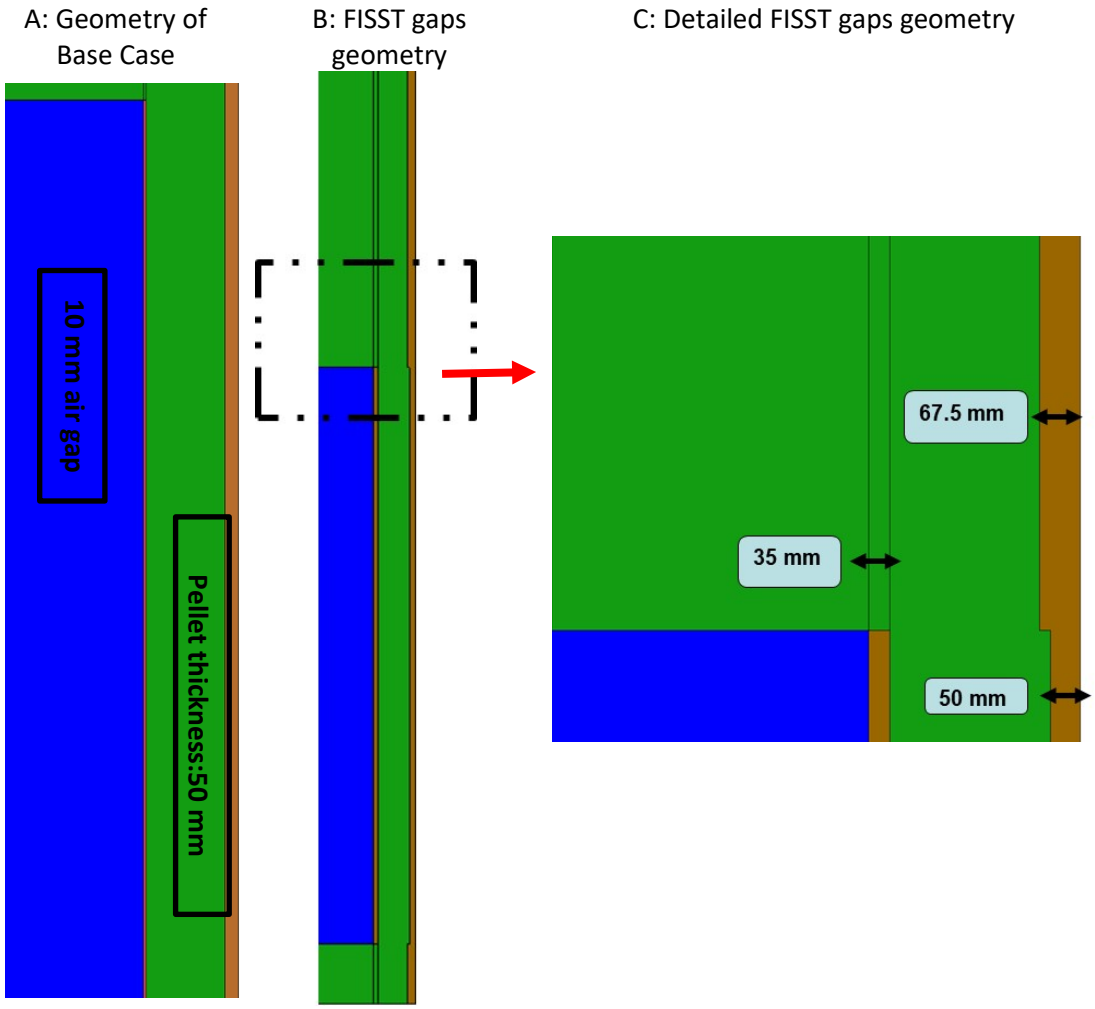

Figure 5-30. *Cross-section of canister area for the geometry of Base Case and current geometry.*

a) Effect of gap thickness and filling material

In this Section, four cases are compared according to geometrical differences and filling material between canister and buffer. *Figure 5-31* shows differences between four cases. FISST gaps geometry has been considered for Case GP1, Case GP2 and GP3.

Table 5-15 summarizes the model results of four cases. The maximum temperature reached in Case GP1 is higher than Base Case in some degrees (*Figure 5-32*). In Case GP1, the first peak of maximum temperature on gap wall is considerably higher than Base Case. However, desaturation at outer gap wall is not stronger as Base Case. The reason is the gap between canister and buffer has a big volume in Case GP1.

Table 5-15. *Comparison of cases according to filling material and thickness of filling material between canister and buffer*

Results	Cases			
	Base Case (10 mm air gap)	Case GP1 (FISST gaps geometry) (35 mm air gap)	Case GP2 (FISST gaps geometry) (35 mm pellet gap)	Case GP3 (FISST gaps geometry, 35 mm gap filled with MX-80)
T_{max} (°C) (air gap wall)	80.7	84.2	82.2	80.2
Time for S_r = 99 % (Buffer disc)	8.4	9	8.4	8.4
Time for S_r = 99 % (Backfill blocks)	6.7	6.6	6.7	6.5
Buffer Density (kg/m^3) (Disc)	1729	1724	1727	1725
Backfill Density (kg/m^3) (Backfill blocks)	2027	2027	2027	2027
Max. Effective Stress (MPa) (Buffer disc)	9.4	9.2	9.3	9.2
Displacements at buffer-backfill intersection (cm)	8.4	7.8	8.3	8.4
Time (years) for air gap closure	4.9	3.5	-	-

In Case GP2, pillow pellets have been considered as filling material for the gap between the canister and buffer blocks. The maximum temperature reached on inner gap wall (*Figure 5-32*) is higher than Base Case but desaturation at outer gap wall is not as stronger as Base Case.

Base Case 10 mm air gap	Case GP1 FISST gaps geometry; 35 mm air gap	Case GP2 FISST gaps geometry; 35 mm gap filled with MX-80	Case GP3 FISST gaps geometry, 35 mm gap filled with MX-80

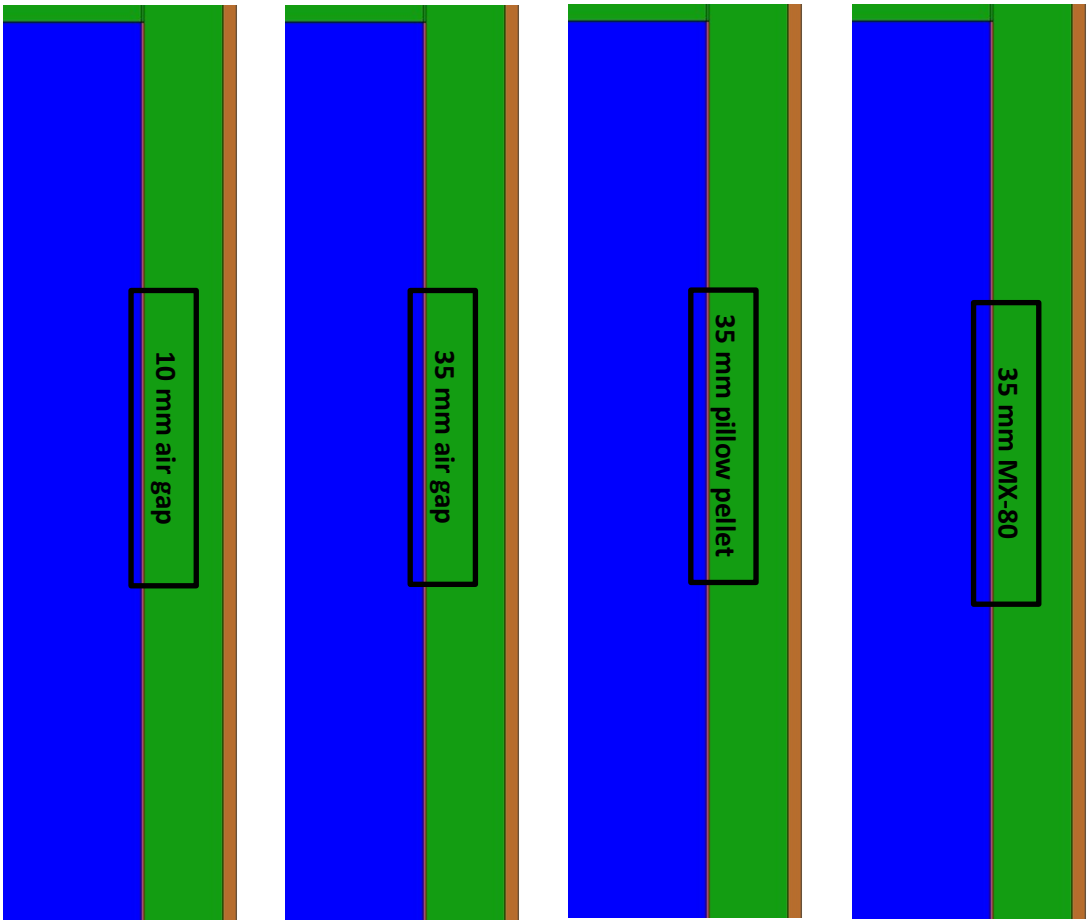

Figure 5-31. *Comparison of four cases*

In Case GP3, there is no gap. MX-80 has been considered as filling material surrounding the canister. As there is no air gap, there is not a peak in temperature in earlier years at the canister wall (*Figure 5-32*).

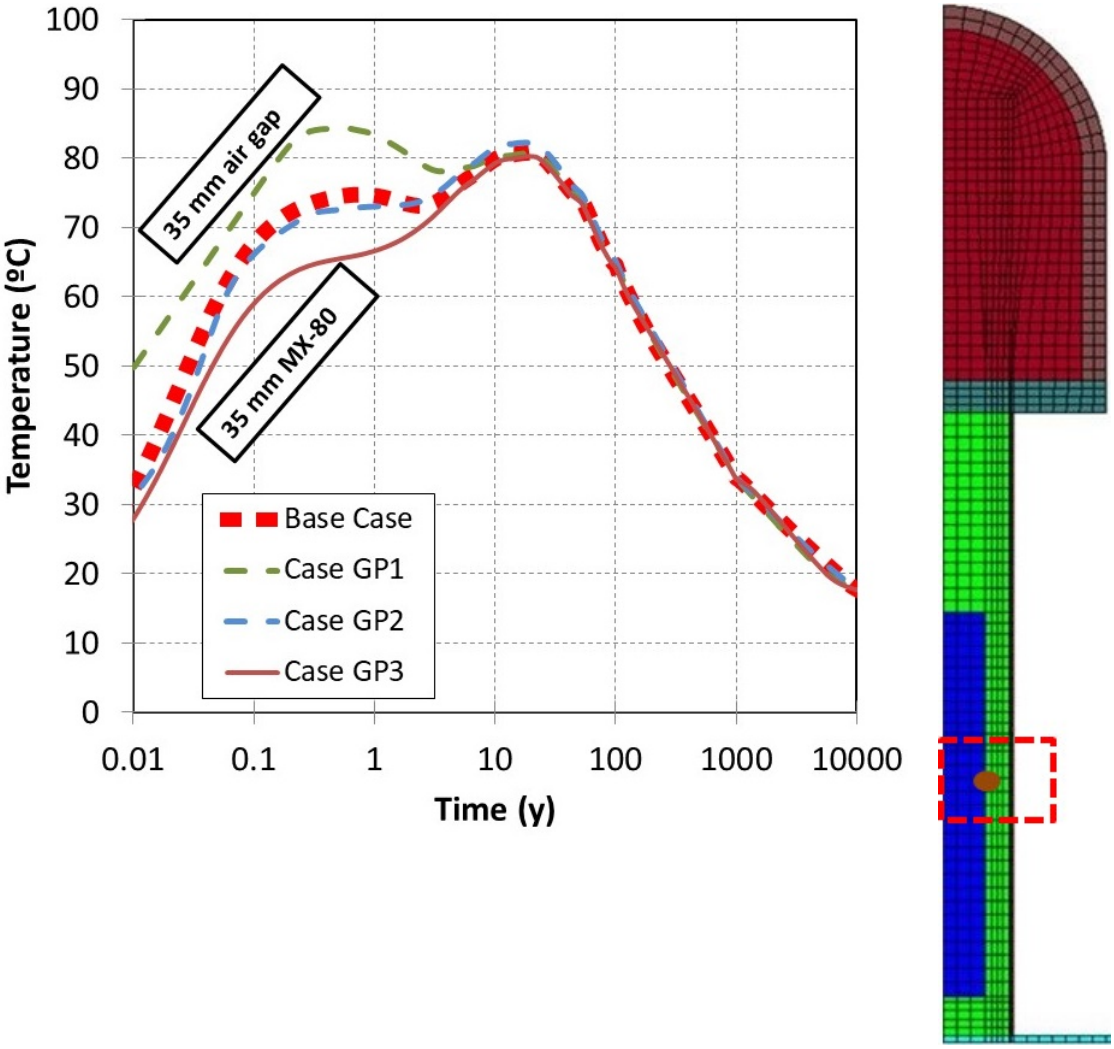

Figure 5-32. *Temperature evolution in four cases at canister wall*

b) Effect of water injection to pellets in FISST gaps geometry

In this Section, the differences between the Base Case and the Case PW2 are explained. Table 5-16 summarizes the model results for two cases. Case PW2 has Fisst gaps geometry. The gap between buffer and canister is filled with pillow pellets. Moreover, pillow pellets between rock and buffer have been considered as initially saturated.

Table 5-16. *Comparison of cases according to initial conditions of pillow pellets*

Results	Cases	
	Base Case (10 mm air gap)	Case PW2 (35 mm pellet gap) Initially saturated (96%) pellets
T_{max} (°C) (air gap wall)	80.7	82.2
Time for S_r = 99 % (Buffer disc)	8.4	7
Time for S_r = 99 % (Backfill blocks)	6.7	6
Buffer Density (kg/m^3) (Disc)	1729	1715
Backfill Density (kg/m^3) (Backfill blocks)	2027	2027
Max. Effective Stress (MPa) (Buffer disc)	9.4	9.2
Displacements at buffer-backfill intersection (cm)	8.4	7.7
Time (years) for air gap closure	4.9	-

According to above Table, there are some differences between two cases. In Case PW2, the hydration process for buffer and backfill is slightly faster than the Base Case. The generated stresses in buffer disc and displacements occurred at buffer backfill intersection in Case PW2, are somewhat less than Base Case. As there is no air gap in Case PW2, no gap closure observed.

There is no first peak in temperature evolution due to gap closure in Case PW2. In Case PW2, there is no strong desaturation at outer gap wall because it is initially saturated (*Figure 5-33*). Total permeability of pillow pellets decrease in Case PW2 instead of increasing due to its initial saturated conditions (*Figure 5-33*).

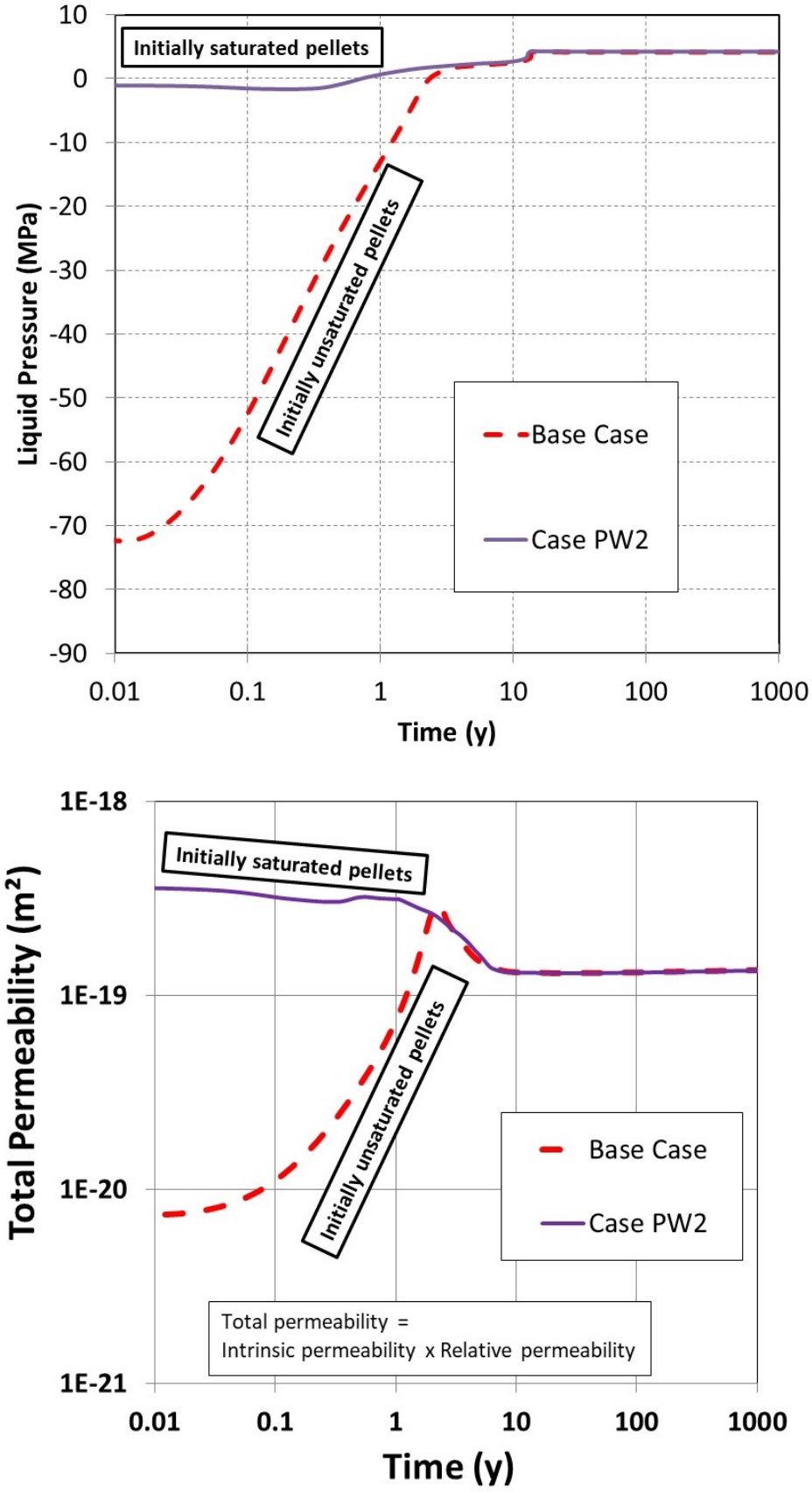

Figure 5-33. *Evolution of liquid pressure and total permeability in Base Case and Case PW2*

c) Effect of water content in FISST gaps geometry

In this Section, the differences between the Base Case and the Case W3 are explained. The results obtained from two cases has been compared in *Table 5-17*. In Base Case, the gap between canister and buffer blocks is 10 mm and initial humidity (w) for buffer is 17%. In Case W3, the gap between canister and buffer has a width of 35 mm and initial humidity (w) for buffer is 11%. In Chapter 5.5, the effect of humidity (11% and 21.7% respectively) has also been detailed. In this Chapter, the effect of lower humidity (11%) has been one more time analysed for the FISST gap geometry.

Table 5-17. *Comparison of cases according to initial humidity of buffer.*

Results	Cases	
	Base Case (10 mm air gap, w=17% for buffer)	Case W3 (35 mm air gap, w=11% for buffer)
T_{max} (°C) (air gap wall)	80.7	104
Time for S_r = 99 % (Buffer disc)	8.4	12.6
Time for S_r = 99 % (Backfill blocks)	6.7	9.1
Buffer Density (kg/m^3) (Disc)	1729	1703
Backfill Density (kg/m^3) (Backfill blocks)	2027	2005
Max. Effective Stress (MPa) (Buffer disc)	9.4	9.7
Displacements at buffer-backfill intersection (cm)	8.4	8.7
Time (years) for air gap closure	4.9	11.5

According to above Table, there are some important differences between the two cases. In Case W3, the achieved temperature on air gap wall (canister surface) is greater than 100 °C (*Figure 5-34*). The reason is to combine effect of the thicker air gap and the slow hydration. Temperature on canister wall increases dramatically due to slow closure of gap in Case W3. The lower humidity the buffer has, the higher initial suction, so it saturates slower in Case W3. Some slight differences related to density-porosity changes also have been observed.

There is strong desaturation at buffer adjacent to canister surface in Case W3 (*Figure 5-34*). Full saturation of buffer and backfill has a delay in Case W3 because of initial conditions. Density of buffer ring drops in Case W3. There are no important differences in terms of stresses and displacements.

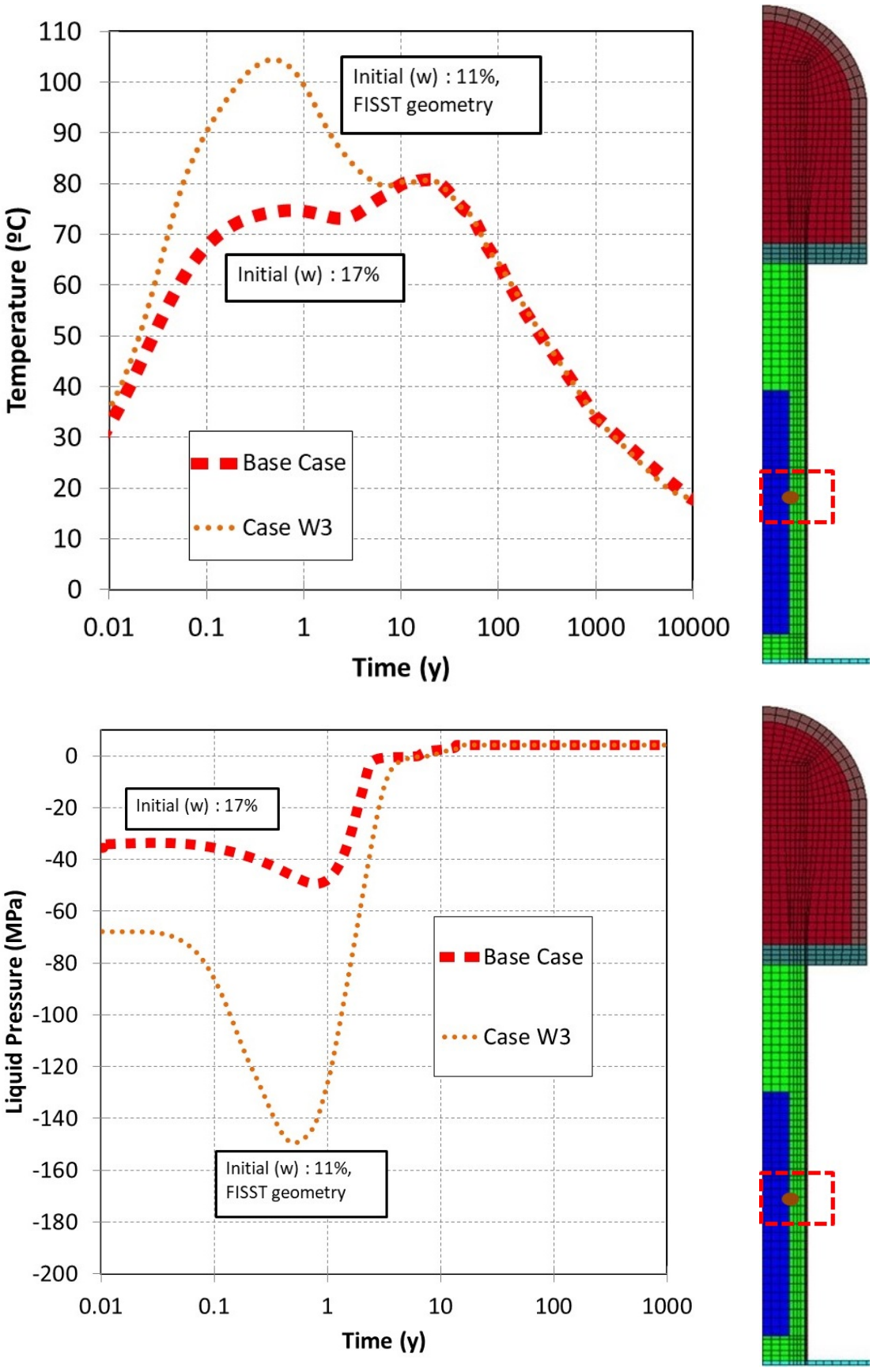

Figure 5-34. *Evolution of temperature at the canister wall and liquid pressure in buffer ring adjacent to canister for two cases.*

5.15 Effect of backfill tunnel volume

In this Section, the differences between the Base Case and the Case GM1 are explained. Table 5-18 summarizes the differences between the two cases. Figure 5-35 shows the 2D-axisymmetrical geometry of Base Case. As it is also demonstrated in Figure 5-35, backfill tunnel has more volume in 3D geometry. To have the same volume of backfill tunnel as in 3D geometry, the width of backfill tunnel has been increased.

Table 5-18. *Comparison of cases according to backfill tunnel volume.*

Results	Cases	
	Base Case (Tunnel width 2.05 m)	Case GM1 (Tunnel width 2.92 m)
T_{max} (°C) (air gap wall)	80.7	80.9
Time for S_r = 99 % (Buffer disc)	8.4	11.5
Time for S_r = 99 % (Backfill blocks)	6.7	9.5
Buffer Density (kg/m^3) (Disc)	1729	1721
Backfill Density (kg/m^3) (Backfill blocks)	2027	2016
Max. Effective Stress (MPa) (Buffer disc)	9.4	9.4
Displacements at buffer-backfill intersection (cm)	8.4	8.7
Time (years) for air gap closure	4.9	6

As can be seen in the previous Table, backfill tunnel volume has a role to play in achieved model results. In Model GM1, hydration time is larger comparing to Base Case.

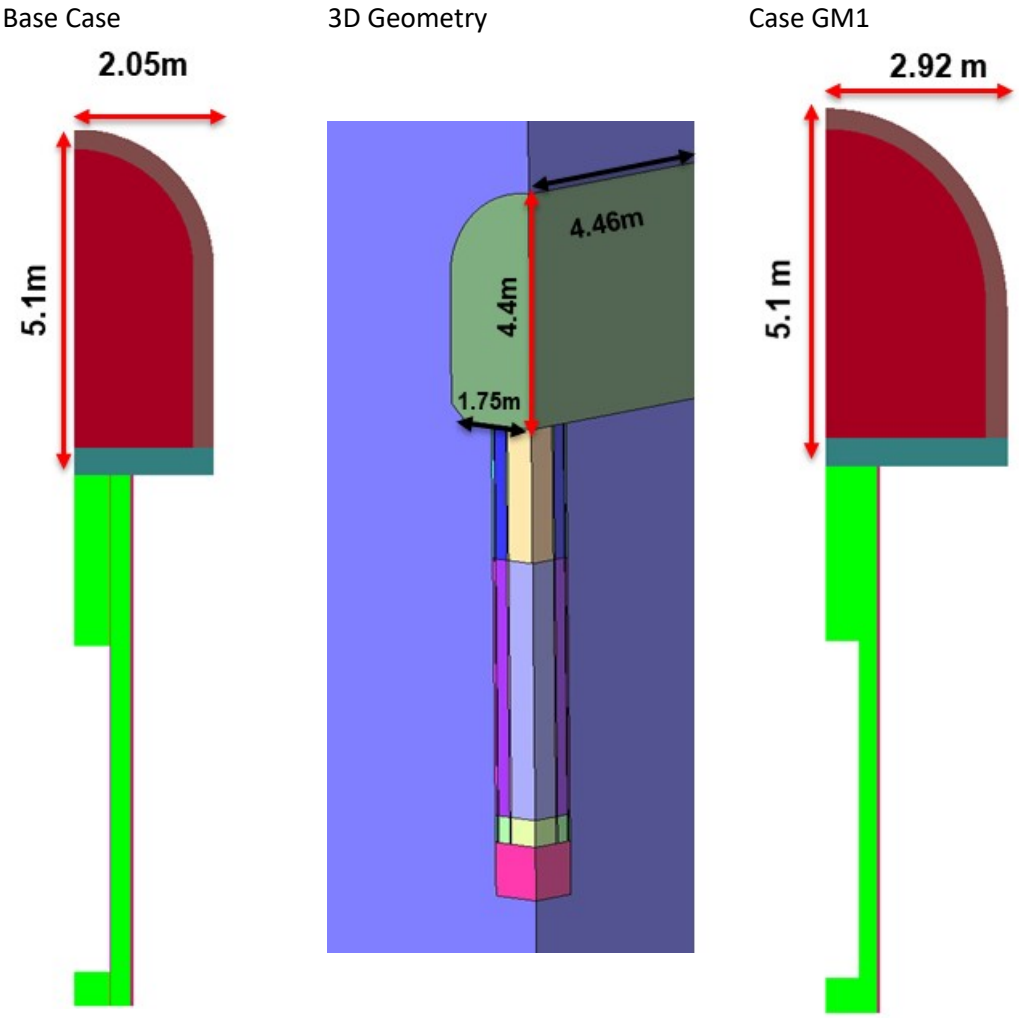

Figure 5-35. *Difference between Base Case and Case GM1.*

As it is shown in *Figure 5-36*, time needed for full saturation of buffer and backfill is greater in Case GM1. Bigger backfill volume causes a delay in full saturation. The rest of the results are similar.

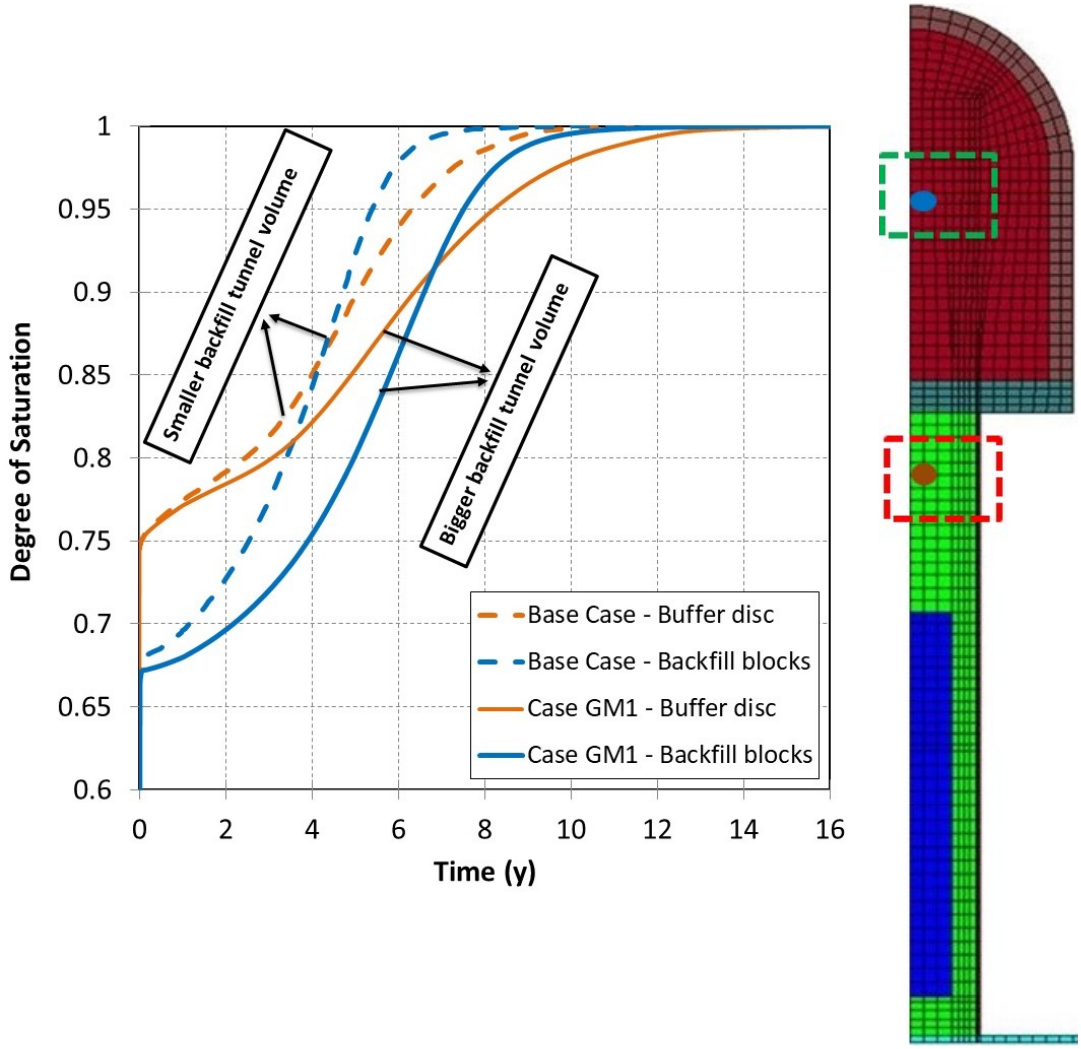

Figure 5-36. *Evolution of degree of saturation in buffer disc and central backfill for two cases*

5.16 Effect of Buffer Material (FEBEX Bentonite)

In this Section, the differences between the Base Case, Case BM1 and the Case FE are explained. Table 5-19 summarizes the achieved model results for these cases and differences between them.

Table 5-19. *Comparison of cases according to buffer material.*

	Cases		
	Base Case (Buffer:MX-80; w_{buffer}: 17%, ρ_d: 1700 kg/m^3)	Case BM1 (Buffer:MX-80; w_{buffer}: 14%, initial ρ_d: 1600 kg/m^3)	Case FE (Buffer: FEBEX; w_{buffer}: 14%, initial ρ_d: 1600 kg/m^3)
T_{max} (°C) (air gap wall)	80.7	95	90.2
Time for S_r = 99 % (Buffer disc)	8.4	12.6	18
Time for S_r = 99 % (Backfill blocks)	6.7	7.2	8
Buffer Density (kg/m^3) (Disc)	1729	1644	1626
Backfill Density (kg/m^3) (Backfill blocks)	2027	2026	2018
Max. Effective Stress (MPa) (Buffer disc)	9.4	9.4	7
Displacements at buffer-backfill intersection (cm)	8.4	6.3	5
Time (years) for air gap closure	4.9	5.8	6

An initial water content of 14% and an average dry density of 1600 kg/m^3 have been assumed for the clay barrier (FEBEX bentonite) in this simulation. These values correspond to a global degree of saturation of 0.55 and a value of suction of 135 MPa (Gens et al., 2009). In the Base Case, initial water content of buffer (MX-80) is 17% and average dry density is 1600 kg/m^3. Case BM1 has been prepared in order to have same initial conditions (water content and dry density) as Case FE. So that, Case BM1 has an initial water content of 14% and an average dry density of 1600 kg/m^3.

The comparison of THM parameters between MX-80 (in Case BM1) and FEBEX (Case FE) are given in Table 5-20, Table 5-21 and Table 5-22.

As it can be seen from Table 5-19, there are some important differences between three cases. Since the saturation delays in the Case BM1 and Case FE, the maximum temperature reached on canister wall is higher than in Base Case.

When buffer material is MX-80 bentonite (Case BM1), the maximum temperature reached on canister wall is higher in some degrees. However, desaturation of buffer is much stronger in Case FE1 as it is shown in *Figure 5-37*. Due to the strong heating by the canister, adjacent buffer dries and causes desaturation.

As the thermo-hydraulic parameters for MX-80 and FEBEX are different, there is a delay in the saturation of discs and rings in the Case FE compare to Case BM1. In Case BM1, buffer has a bigger swelling capacity so that pillow pellets compress a little bit and accordingly, total porosity of pillow pellets decreases. In Case FE1, total porosity remains constant. However, in both cases due to the saturation process, micro pores invade macro pores. Hence, micro porosity increases in both cases but in Case FE1 this increment is not as strong as in Case BM1 (*Figure 5-37*). As swelling capacity of MX-80 is stronger than FEBEX, achieved stresses and displacements are higher in Case BM1 compare to Case FE.

THM parameters for FEBEX bentonite were adopted from Gens et. al (2009). As distinct from the MX-80, FEBEX bentonite was simulated with coupling terms (α_s,α_{sp}). FEBEX bentonite has a greater pre-consolidation mean stress. The retention curve used in the simulation for FEBEX bentonite was a modification of Van Genuchten model. Water retention curve is given in Chapter 4.2. For thermal conductivity relationship, a different law is considered for FEBEX which is given in Chapter 4.2.

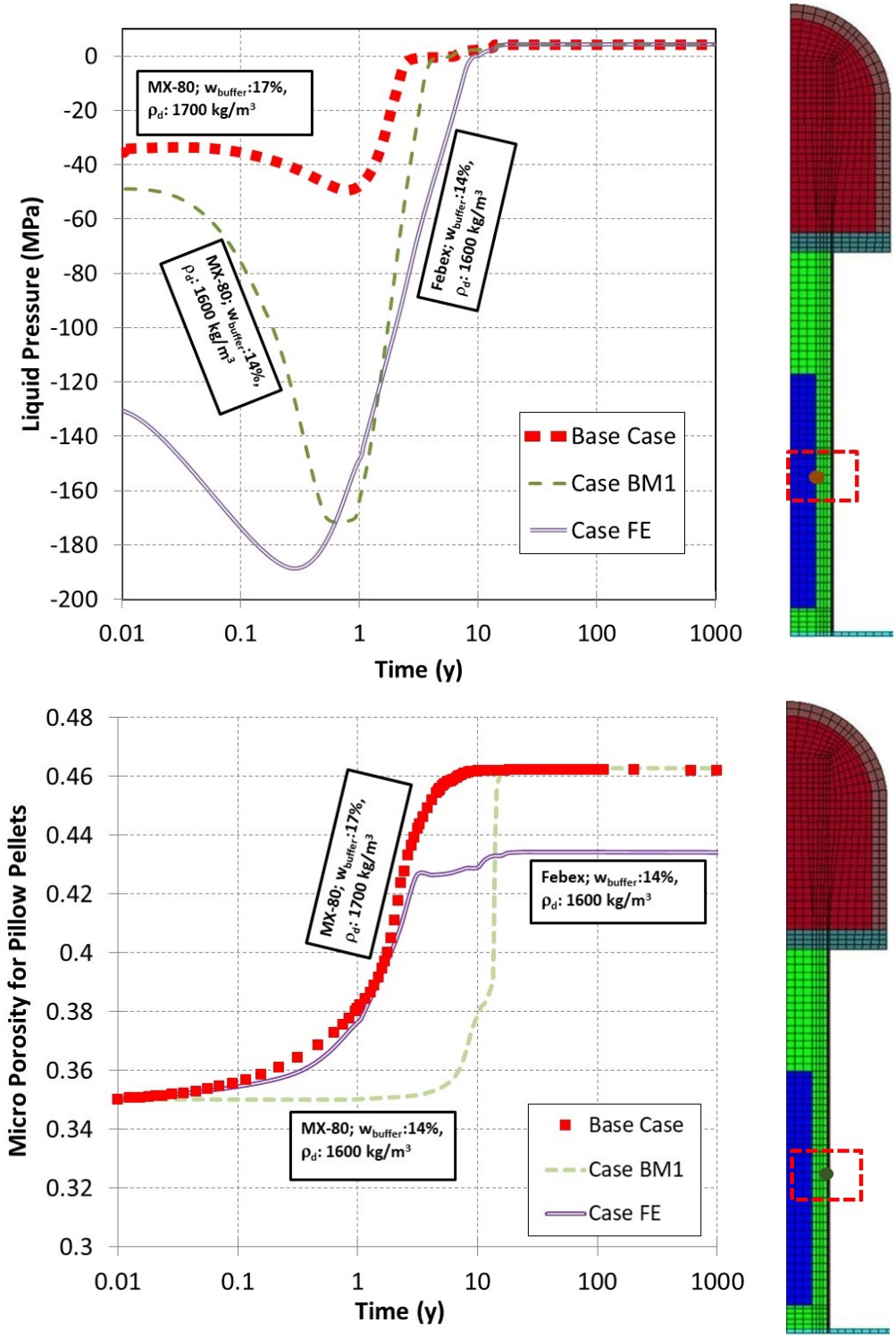

Figure 5-37. *Liquid pressure evolution in buffer adjacent to canister for three cases*

Table 5-20. *Mechanical parameters for MX-80 and FEBEX bentonite.*

Parameter	Symbol	MX-80	FEBEX(*)
Poisson ratio (-)	ν	0.3	0.4
Minimum bulk module (MPa)	K_{min}	10	-
Reference mean stress (MPa)	p_{ref}	0.01	0.01
Parameters for elastic volumetric compressibility against mean net stress change (-)	κ_{i0}	0.098	0.05
Parameters for elastic volumetric compressibility against suction change (-)	κ_{s0}	0.082	0.25
Coupling parameter (MPa)	α_s	-	-0.003
Coupling parameter	α_{sp}	-	-0.161
Slope of void ratio – mean net stress curve at zero suction	$\lambda(0)$	0.25	0.15
Parameters for the slope void ratio – mean net stress at variable suction (-,MPa^{-1})	r	0.8	0.925
	β	0.02	0.1
Reference pressure for the P_0 function (MPa)	p^c	0.1	0.5
Pre-consolidation mean stress for saturated soil (MPa)	P_o*	2	12
Critical state line (-)	M	1.07	1

(*) Gens et al., 2009

FEBEX model for retention curve is defined as below (it has been used to model FEBEX bentonite in Case FE1:

$$\widetilde{S_l}(p_l) = \left(1 + \left(\frac{p_g - p_l}{P}\right)^{\frac{1}{1-\lambda}}\right)^{-\lambda} \widetilde{f_d}(p_l) \quad (5.16\text{-}1)$$

$$P = P_0 \frac{\sigma}{\sigma_0} \quad (5.16\text{-}2)$$

$$\widetilde{f_d}(p_l) = \left(1 - \frac{p_g - p_l}{P_d}\right)^{\lambda_d} \quad (5.16\text{-}3)$$

Table 5-21. *Thermal parameters for MX-80 and FEBEX bentonite*

Parameter	MX-80	FEBEX(*)
ρ_s (kg/m^3)	2780	2773
c_s (J/kgK)	830	1091
λ_{dry} (W/mK)	0.2	0.47
λ_{sat} (W/mK)	1.4	1.15
b in $\lambda(S)$	-0.15	-
S_r* in $\lambda(S)$	0.5	-
$\phi_{initial}$	0.42	0.42

(*) $\lambda=\lambda_{sat}^{Sl}\cdot\lambda_{dry}^{(1-Sl)}$, Gens et al., 2009

Table 5-22. *Hydraulic parameters for MX-80 and FEBEX bentonite.*

Equation	Parameter	MX-80	FEBEX
Van Genuchten retention curve(*)	P (MPa)	27	7
	λ (-)	0.45	0.1
	a (-) in $P(\phi)$	11	-
	b (-)in $\lambda(\phi)$	4	-
	ϕ_0	0.4245	-
	λ_d	-	2.1
	P_d (MPa)	-	1100
Darcy flux(**)	k (m^2)	5.6x10^{-21}	1.9 x 10^{-21}
	b (-) in $k(\phi)$	15	-
	ϕ_0	0.438	0.4
	m (-)	3	3
Diffusive flux	τ (-)	0.4	0.8

(*) Modified Van Genuchten water retention curve in FEBEX bentonite defined in Gens et al., 2009

(**) Kozeny law in FEBEX bentonite (Gens et al., 2009)

5.17 Effect of filling material (water gap between buffer and rock)

In principle, it is foreseen to fill in the gap between rock and buffer with pillow pellets. However, there is also a possibility to use slurry instead of pellets, as it has been discussed in Chapter 5.9.

Yet, another alternative is considered which consist in not doing any filling of the buffer-rock space. In this Section, it is considered that the gap between buffer and rock is not backfilled with pellets or other materials. It will be referred to as an "empty-gap". Of course, it will contain air at the beginning and water later on after inflow of water from the rock. To investigate this case a simple configuration has been used (Toprak, et al. 2017). This configuration assumes homogeneous drift backfill materials. Figure 5-38 shows thermal and mechanical response of the corresponding models.

For the rock-buffer gap, the effect of filling or not with pellets is significant. Pellet-gap has lower hydraulic conductivity than if the gap is empty (air at the beginning and water later on). Empty gap permits faster saturation of the buffer as compared with the case of pellet-filled-gap.

The case (Case FM2) with empty-gap (air at the beginning and water later on) leads to earlier closure of the inner gap (i.e. the gap between canister and buffer), thus producing a decrease of temperature before 1 year.

Figure 5-38 (C and D) shows also the vertical displacement evolution at the buffer backfill interface (design variable). When the gap is empty (air at the beginning and water later on) (Figure 5-38-D), buffer blocks swell considerably. The generated displacements due to swelling of buffer are two times higher than in the case of pellet-filled gap.

It should be pointed out that the buffer-rock gap, if empty, it will be filled with bentonite with low density relatively at early times (a few weeks maximum). This fast filling process has been measured in different laboratory tests. Tests performed in cells where the bentonite fills a gap (Pintado et al., 2013, Dueck et al., 2016) indicated that the gap was filled in a few days (the sensors starts to read pressure quite soon). Other tests related with KBS-3H where a water filled gap was present indicated a relatively fast filling, in some cases, a couple of weeks (Perforated hole tests, Asensio, 2013) and in another case, the time estimated was around two months (Big Bertha tests Sandén et al., 2008 and Kristensson et al., 2017).

It should be taken into account that CODE_BRIGHT is a computer code for studying porous materials. The gap has a porosity of 1, so it cannot be considered as porous materials. Water is filling the gap uniformly, so there is not effect of water falling to the bottom.

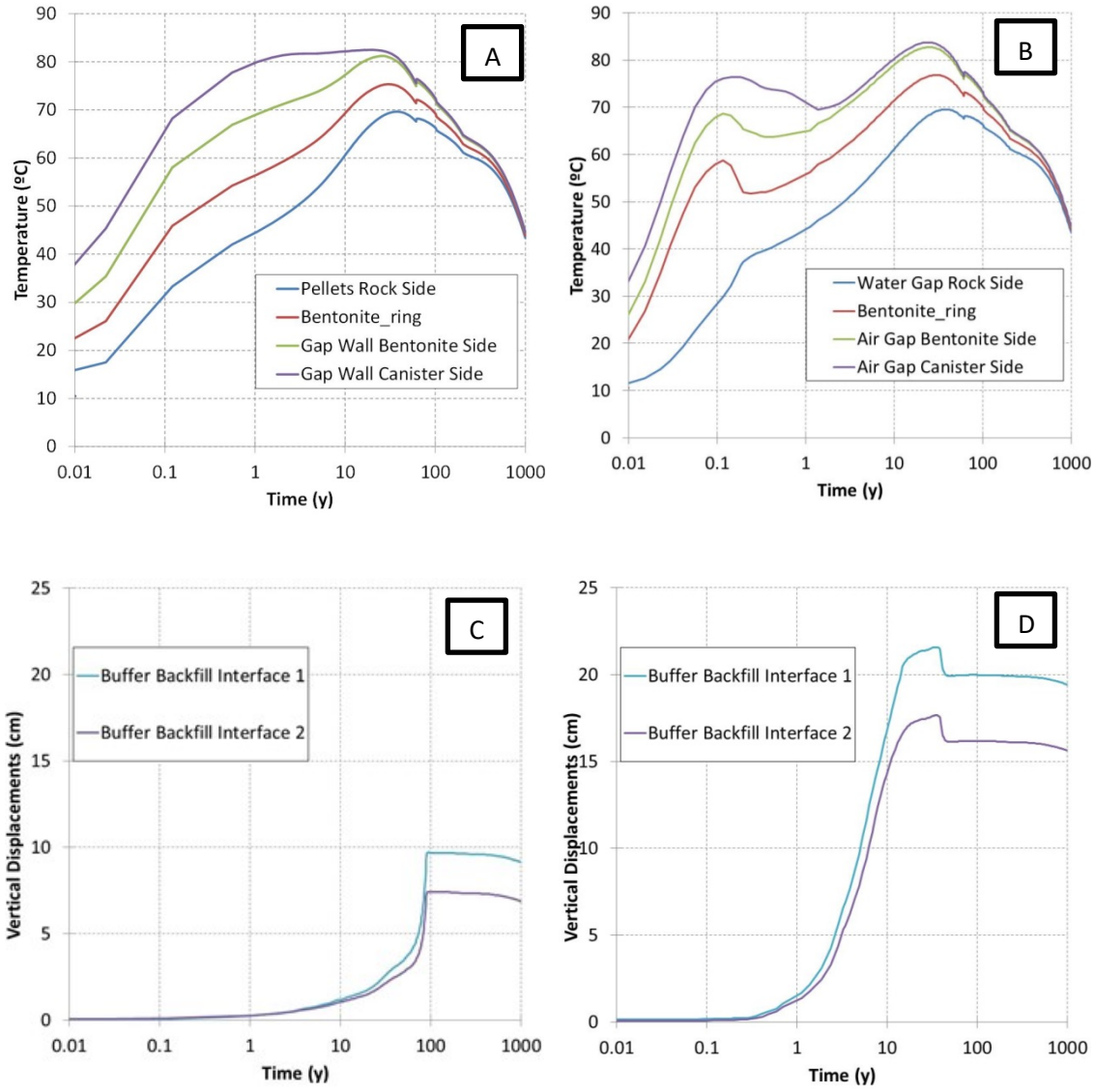

Figure 5-38. *Evolution of temperature (A: pellet filling, B: water filling (Case FM2) and vertical displacements in both models (C: pellet filling, D: water filling (Case FM2)*

5.18 Effect of rock dilation coefficient

In this Section, the differences between the Base Case and the Case RTE1 have been explained. Table 5-23 summarizes the differences between two cases. In Base Case, linear thermal expansion coefficient α (ºC^{-1}) of rock is 8x10^{-6} and in Case RTE1 8x10^{-7}. ***Figure 5-39*** depicts differences between two cases. The value of the dilatation coefficient has been analysed because this coefficient varies in a range of 7x10^{-6} ^{o}C^{-1} to 10x10^{-6} ^{o}C^{-1} (Posiva 2009). The value used by Gens et al. (2009) for the granite in Grimsel (7.8x10^{-6} ^{o}C^{-1}) in FEBEX "in situ" test analysis falls in this range.

Table 5-23. *Comparison of cases according to thermal expansion coefficient*

Results	Cases	
	Base Case α_{rock} (^{o}C^{-1}): 8x10^{-6}	Case RTE1 α_{rock} (^{o}C^{-1}): 8x10^{-7}
T_{max} (°C) (air gap wall)	80.7	80.8
Time for S_r = 99 % (Buffer disc)	8.4	8.6
Time for S_r = 99 % (Backfill blocks)	6.7	6.9
Buffer Density (kg/m^3) (Disc)	1729	1729
Backfill Density (kg/m^3) (Backfill blocks)	2027	2027
Max. Effective Stress (MPa) (Buffer disc)	9.4	9.4
Displacements at buffer-backfill intersection (cm)	8.4	7.5
Time (years) for air gap closure	4.9	5

As it can be seen above table, there are no significant differences between two cases in terms of THM behaviour of buffer and backfill. However, the generated stresses in two cases are significantly different as it has been shown in *Figure 5-39* and Figure 5-40. The mean effective stresses in three different points of the rock have been compared. The mean stresses reduce when the rock linear coefficient of dilatation reduces as well as it was expected. If it is reduced in one order of magnitude (Figure 5-39-A and Figure 5-40-B), the difference between generated stresses in two cases is still important.

At the end of the 10 years, developed stresses in Base Case are considerably higher than Case RTE1 (*Figure 5-39*-A). Representative points for rock have been depicted in *Figure 5-39*-B. There is no difference in terms of temperature of rock (Figure 5-40-A). As it has been demonstrated in Figure 5-40-B, stresses have reached up to 30 MPa while in Case RTE1 stresses are almost constant and around 10 MPa.

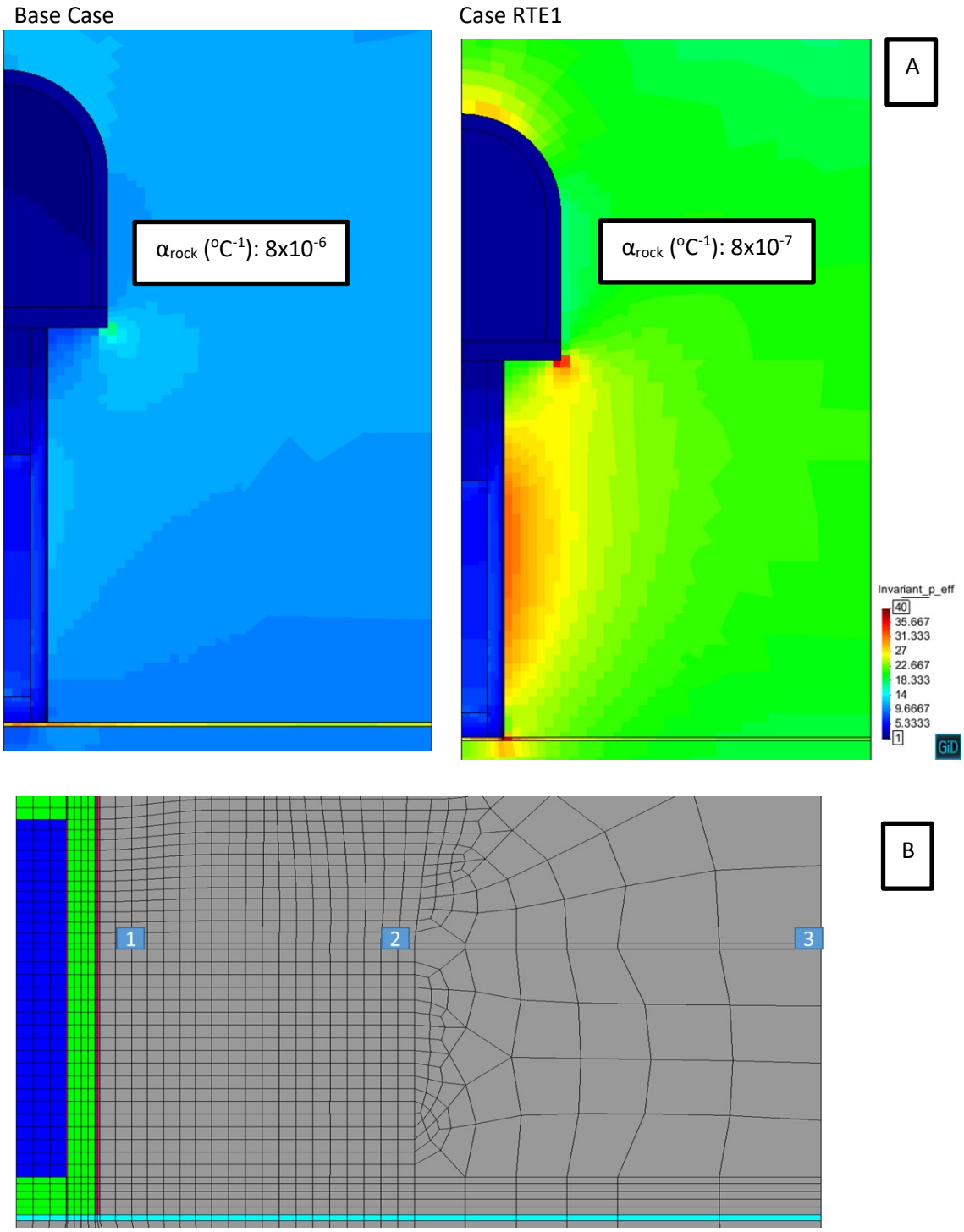

Figure 5-39. *Difference between Base Case and Case RTE1 in terms of mean effective stresses at the end of 10 years (A). Representative points for rock (B)*

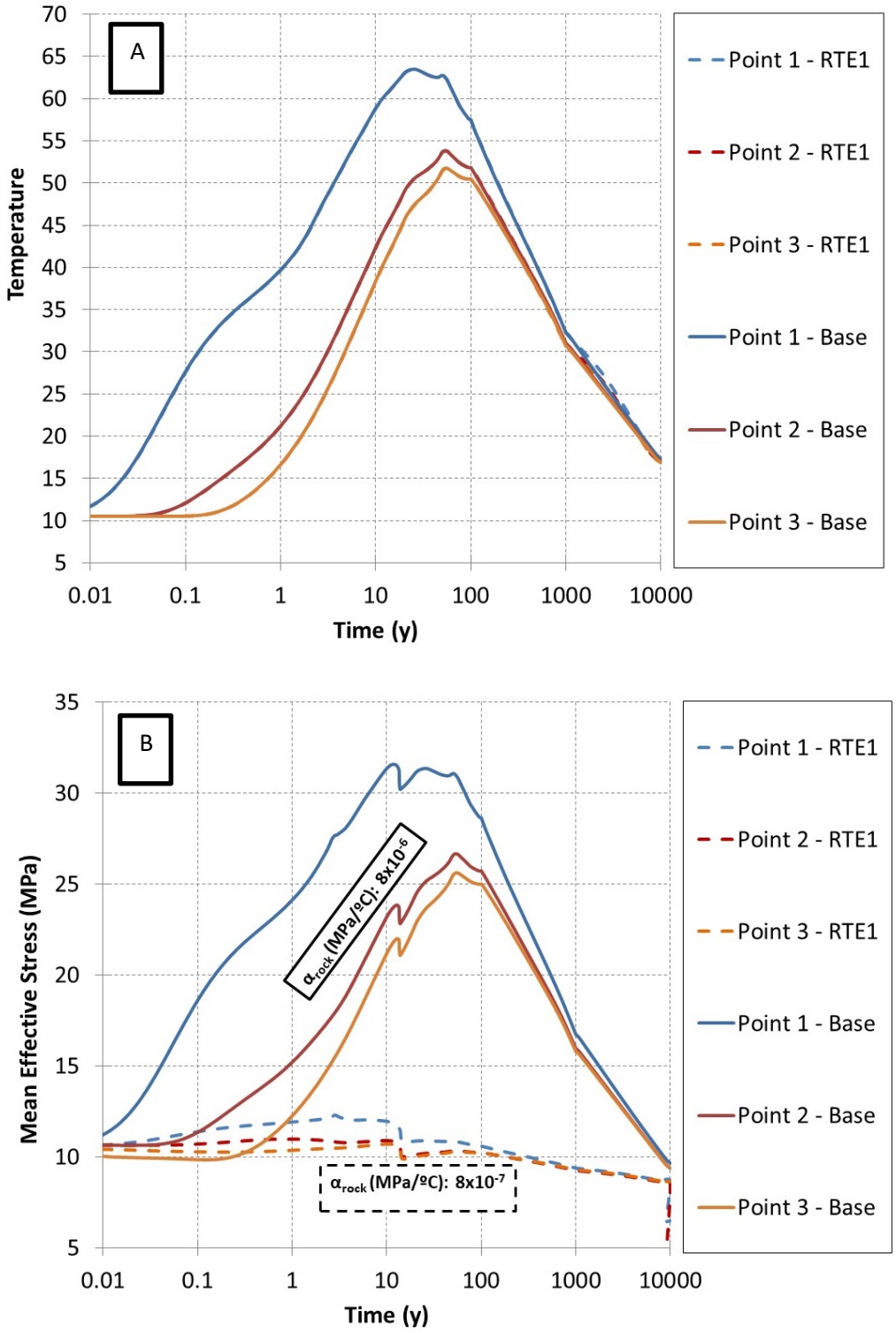

Figure 5-40. *Temperature (A) and mean effective stress evolution in two cases (B).*

5.19 Effect of fracture permeability

In this Section, the differences between the Base Case and the Case FP1 are explained. Table 5-24 summarizes the differences between two cases. In Base Case, intrinsic permeability of fracture has been considered as 1.52×10^{-16} m^2. In Case FP1, fracture has one order larger intrinsic permeability, which is 1.52×10^{-15} m^2.

Table 5-24. *Comparison of cases according to fracture permeability*

Results	Cases	
	Base Case $k_{rock\text{-}fracture}$ (m^2): $1.52x10^{-16}$	Case FP1 $k_{rock\text{-}fracture}$ (m^2): $1.52x10^{-15}$
T_{max} (°C) (air gap wall)	80.7	80.4
Time for S_r = 99 % (Buffer disc)	8.4	8.3
Time for S_r = 99 % (Backfill blocks)	6.7	6.7
Buffer Density (kg/m^3) (Disc)	1729	1730
Backfill Density (kg/m^3) (Backfill blocks)	2027	2027
Max. Effective Stress (MPa) (Buffer disc)	9.4	9.4
Displacements at buffer-backfill intersection (cm)	8.4	8.6
Time (years) for air gap closure	4.9	4.8

As it can be seen at the previous Table, there are no significant differences between the two cases in terms of THM behaviour of buffer and backfill. However, there are some local differences. For example, in earlier years buffer closer to fracture has a stronger desaturation in Base Case comparing to Case FP1, due to the fracture is less permeable. At the end of the two years, the suction under canister in Base Case is 13.5 MPa whereas in Case FP1 it is 7.7 MPa (*Figure 5-41*). This local effect of fracture can also be seen in Figure 5-42. There is a small difference in terms of drying of buffer. As long as the considered area is far away from the fracture, this difference disappears.

Base Case
$k_{rock\text{-}fracture}$ (m^2): $1.52x10^{-16}$

Case FP1
$k_{rock\text{-}fracture}$ (m^2): $1.52x10^{-15}$

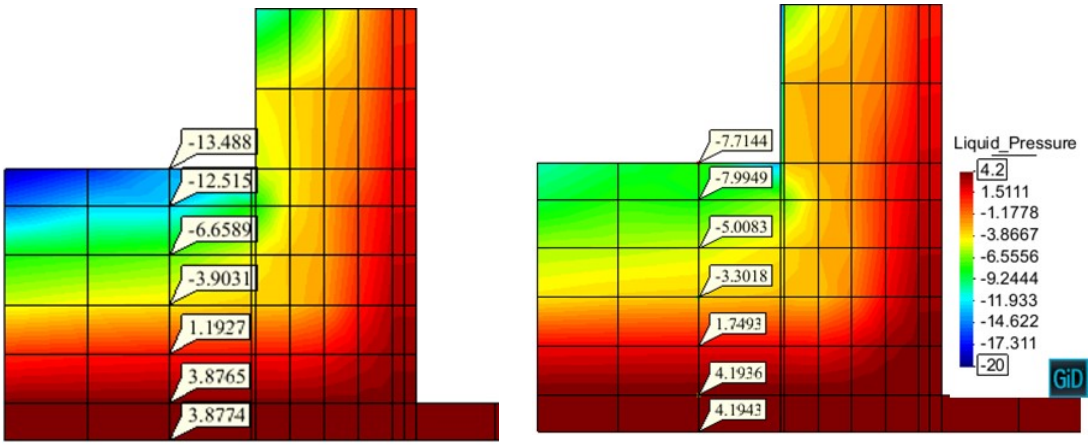

Figure 5-41. *Difference between Base Case and Case FP1 in terms of liquid pressure at the end of two years.*

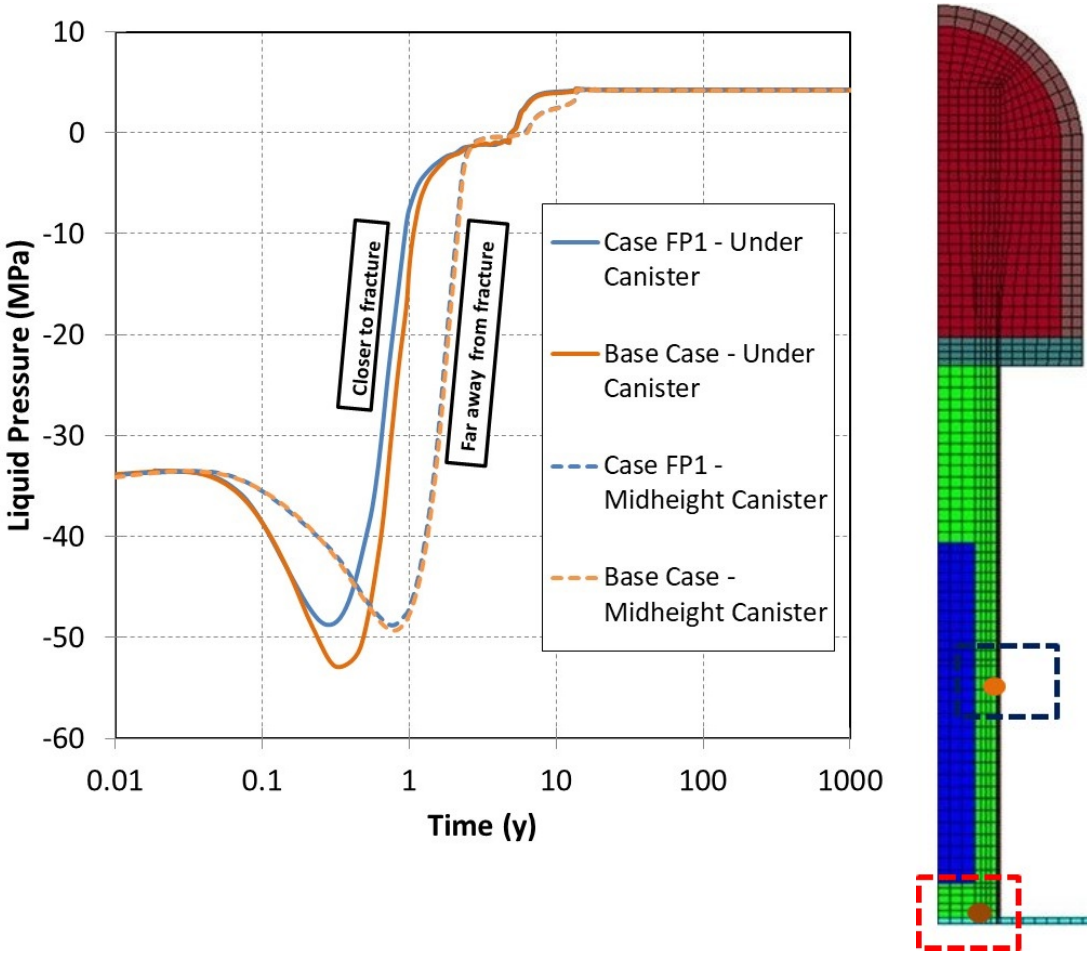

Figure 5-42. *Liquid pressure evolution in two cases according to distance to fracture.*

5.20 Effect of radiation - 3D TH Modelling

In this Section, the differences between the Base Case, Case RD1 and the Case 3D1 have been explained. Table 5-25 summarizes the differences between the three cases. In Base Case and Case RD1, 2D axisymmetric geometry has been considered. To evaluate the impact of third dimension over model results, a 3D model has been developed. However, only TH calculations have been performed in 3D model. Both 2D models (Base case and Case RD1) have been exposed to THM calculations. The results have been summarised in Table 5-25.

In Case RD1 and Case 3D1, the thermal conductivity of the gap under dry conditions has been modified by incorporating the radiation effect. This is done in the following simple way taking into account the equation given above. In this case the gap is considered with a high porosity and the thermal conductivity in its dry state is calculated as:

$$\lambda_{dry} = \frac{e_1 e_2}{e_1 + e_2 - e_1 e_2} 4\sigma(T + 273.15)^3 \Delta l + \lambda_{gas} \tag{5.20-1}$$

$$= 0.27 \times 4 \times 5.66 \times 10^{-8} \times (50 + 273)^3 \times 0.01 + 0.045$$

$$= 0.066 \text{ W/m/k}$$

The Base Case does not include radiation parameters. Therefore, when the gap is full of gas, a thermal conductivity of 0.045 W/ (m·K) (gas mixture of air and vapour) is considered, while when it is saturated, a value of 0.6 W/ (m·K) (water thermal conductivity) is considered (Toprak et al. 2013). The gap closure and how to deal with the available numerical tools is still an open issue which is being investigated.

Figure 5-43 shows materials (A), initial suction (B), initial porosity (C) and boundary conditions (D) for 3D model. The backfill in the 3D modelling has been considered as a homogenous material. There are neither rod pellets nor granules. The THM parameters for the materials (rock, pillow pellets, MX-80 and Friedland clay) are identical with Base Case model parameters.

Table 5-25. *Comparison of cases according to geometry.*

Results	Cases		
	Base Case (2D –THM; no radiation parameters for gap)	Case RD1 (2D –THM; gap has radiation parameters)	Case 3D1 (3D-TH; gap has radiation parameters)
T_{max} (°C) (air gap wall)	80.7	80.7	79
Time for S_r = 99 % (Buffer disc)	8.4	8.7	10
Time for S_r = 99 % (Backfill blocks)	6.7	6.7	9

As it can be seen in the previous Table, there are some differences between the three cases. Due to the consideration of the radiation, the maximum temperature in Case 3D1 is lower than in the Base Case. The hydration process is slower in Case 3D1 because of bigger volume of backfill tunnel. Figure 5-44 demonstrates the distribution of temperature, liquid pressure and degree of saturation respectively. Figure 5-45 shows temperature evolution on canister wall in three cases (A) and liquid pressure evolution in two cases (B). The temperature and desaturation in Case 3D1 is slightly lower than Base Case.

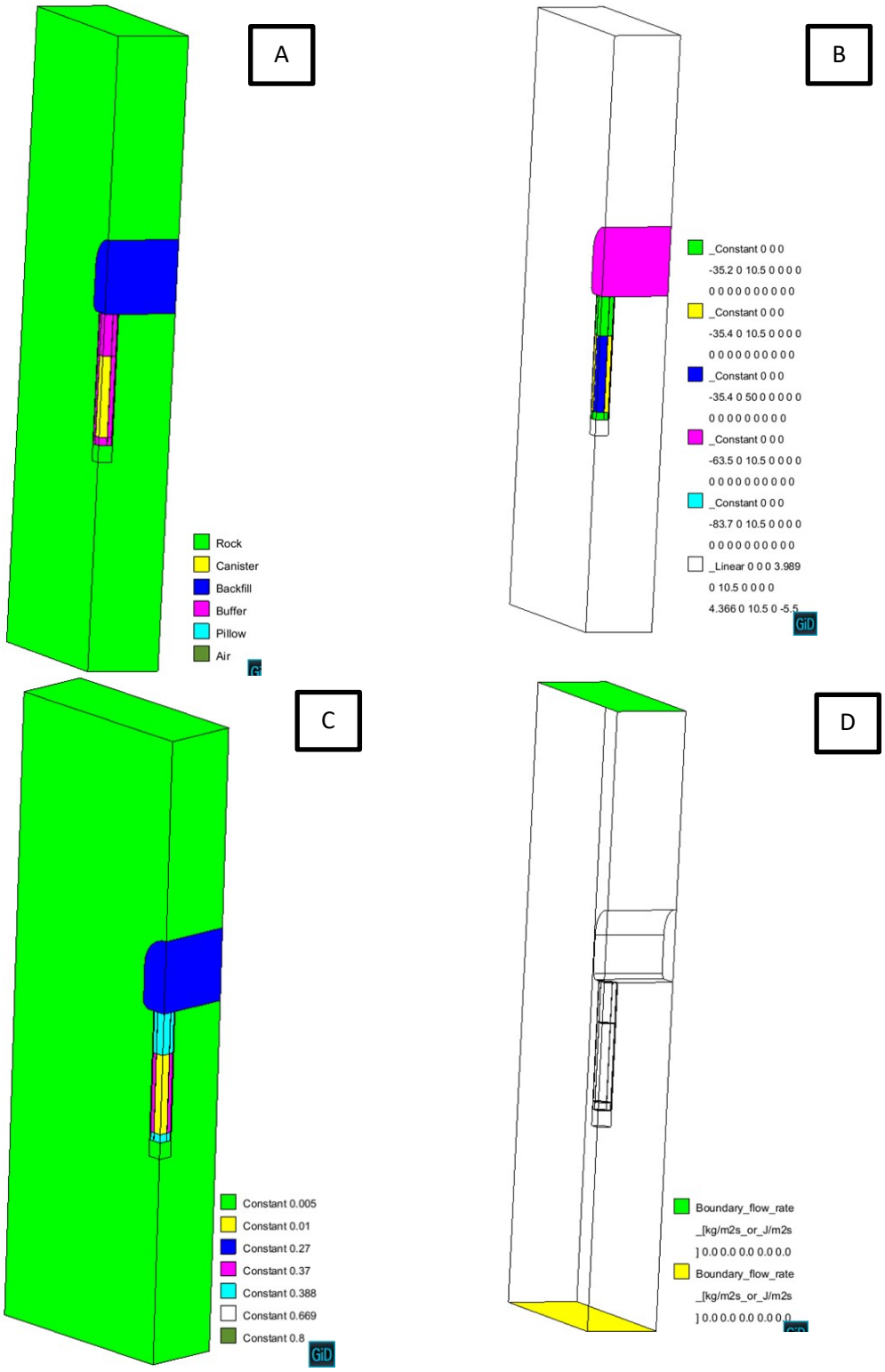

Figure 5-43. *Materials (A), initial suction (B), initial porosity (C) and boundary conditions (D) for 3D model.*

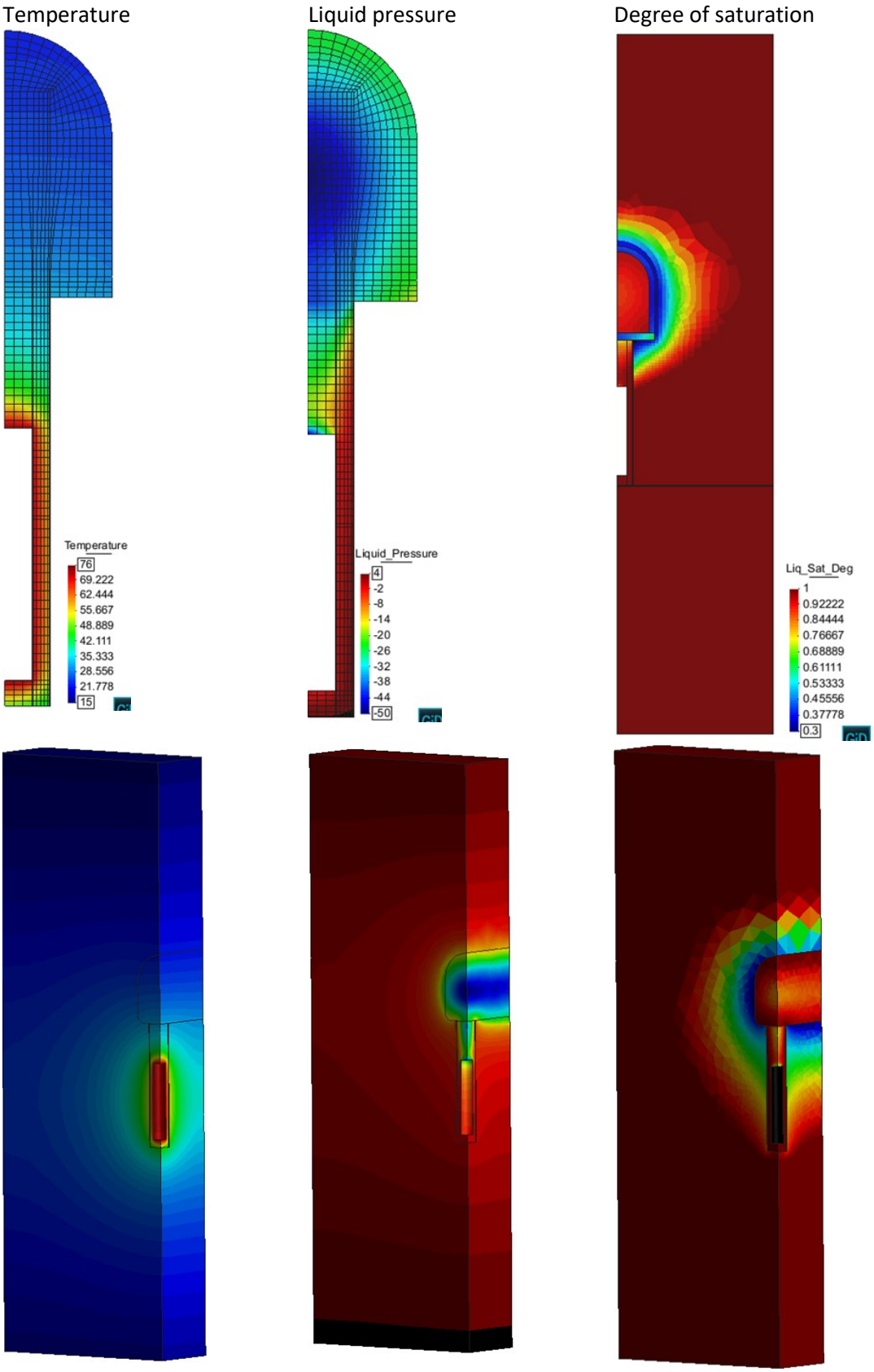

Figure 5-44 Comparison of Case RD1 and 3D1 (4.5 years after canister emplacement).

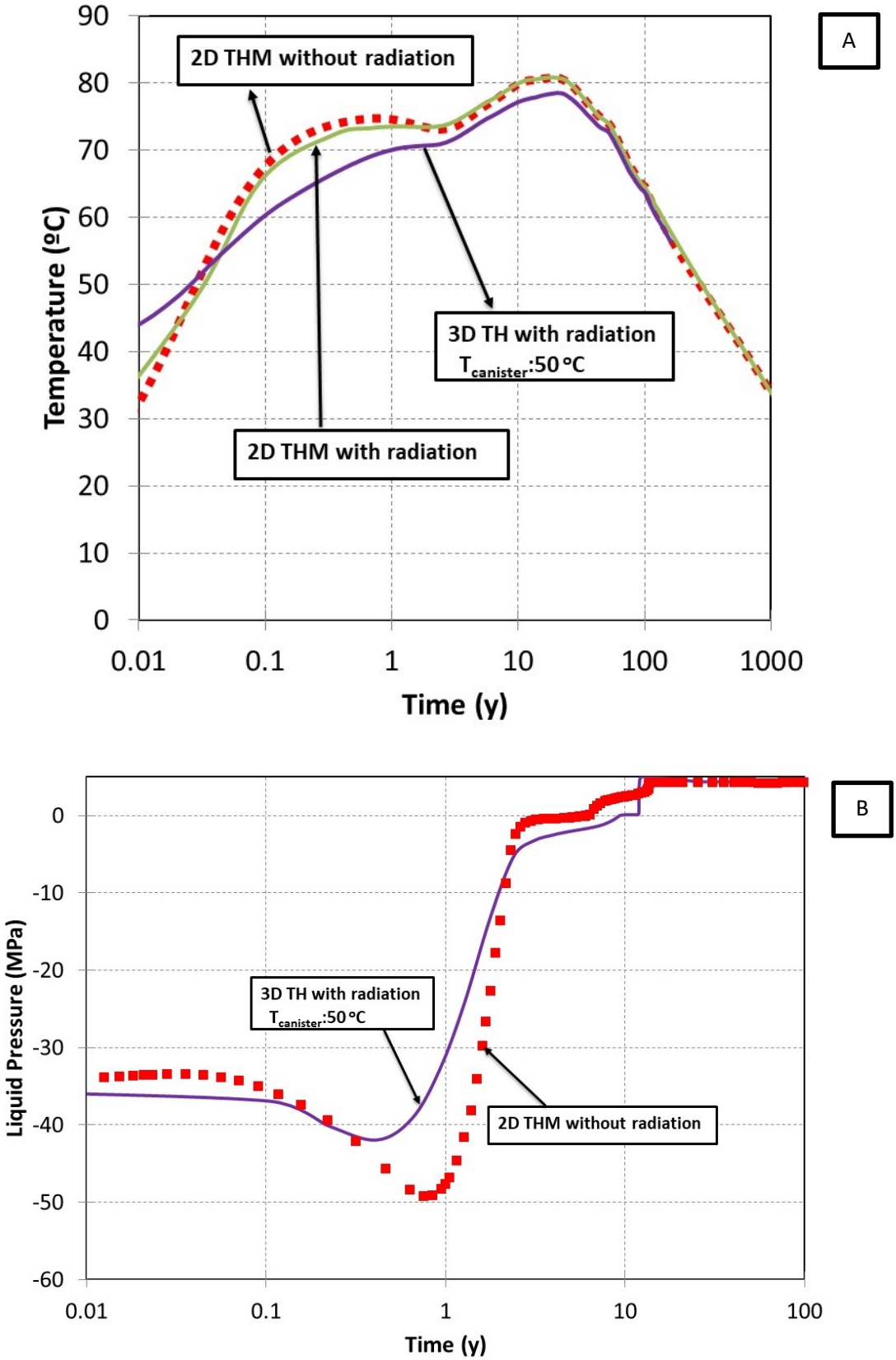

Figure 5-45 *Evolution of temperature in three cases (A) and liquid pressure in two cases (B)*

5.21 Concluding Remarks for 2D Analysis

Throughout Chapter 5, the THM response of deposition tunnel is investigated. The system components are: MX-80 and Friedland clay blocks, pillow pellets, rod pellets, granules, air gap, canister and rock. After obtaining THM parameters for all materials via laboratory and in-situ tests, sensitivity analyses have been performed to evaluate the buffer and backfill response under different conditions. The sensitivity analyses consist of:

- The effect of fracture position
- Different thickness of the space backfilled with pillow pellets
- Salinity of the inflow water
- Initial water content of buffer
- Buffer density
- Effect of Lagrangian method
- Swelling parameters of pellet
- Filling material between buffer and rock
- Rock hydraulic conductivity
- Thermal expansion coefficient for buffer
- Thermal conductivity of buffer
- Water injection to pillow pellets
- Geometry differences (more volume of pillow pellets or more volume of backfill tunnel, 3D modelling)
- Buffer material
- Rock dilation coefficient
- Fracture permeability

Comparison with a base case is carried out to investigate the effect of each variable on the results obtained. Depending on the case, different saturation times have been calculated, different stress developments have been achieved, and different displacements at the buffer-backfill interface calculated and different temperature evolutions have been obtained. These are summarized in a table for each section. The comparative figures and table are given in the following pages.

Complementary studies for the thesis can be considered as:

- Modelling of damage around excavated openings due to excavation or the heat produced by the spent nuclear fuel.

- Modelling of loss of material. Before full saturation, some buffer and backfill material may be lost through piping and erosion.
- Chemical analyses such as corrosion of canister.
- Gas generation due to corrosion of the canister, linking with the previous point.
- Reactive transport modelling.

Comparative results

Main safety requirements for THM calculations can be listed as:

- Maximum temperature in buffer should be less than 100 °C (Posiva, 2012).
- Developed swelling pressure should be less than 15 MPa (Raiko, 2013).
- Density of backfill should be larger than 1950 kg/m^3 (Posiva, 2012).
- Buffer saturated density > 1950 kg/m^3 and < 2050 kg/m^3 (Posiva, 2012).

Maximum temperature reached on canister wall, the time needed to reach full saturation of buffer, mean effective stresses developed in buffer blocks and vertical displacements at the buffer backfill intersection for all cases have been summarized in Table 5-26.

Temperature, liquid pressure, mean effective stresses and displacements on the representative points for all cases have been depicted from *Figure 5-46* to Figure 5-55.

Distribution of temperature, liquid pressure, mean effective stresses and displacements on the domain of deposition hole in 10.5 years (when the majority of the cases reach full saturation) for all cases is shown in various plots from Figure 5-58 to Figure 5-65.

The maximum temperature reached at the canister wall for all cases has been depicted in ***Figure 5-46***. Detailed evolution of temperature is compiled in Figure 5-47 and Figure 5-48. Case W3 (current geometry and w_{buffer} is 11%) marks the maximum temperature because of initial highly unsaturated conditions and the presence of a wider air gap element. Case R3 (No fracture; k_{rock}:$3x10^{-21}$ m^2) has one of the highest value for temperature from among all the cases. The rock has been considered less permeable and without fracture in Case R3. Therefore, hydration takes place very slowly. The air gap does not close in this case. As has been discussed in previous chapters, the air gap has a role to play in the isolation of heat. The temperature distribution in earlier period (10.5 years after the installation of components) for deposition tunnel is shown in Figure 5-58 and Figure 5-59. In Case TC1 (λ_{sat} for buffer is 1.0 W/(m·K)), thermal conductivity of the buffer is higher than the Base Case. As a result, the maximum temperature reached is greater in Case TC1. The air gap in the 3D model considers the radiation effect. Therefore, the maximum

temperature reached at the canister wall is lower. Although as mentioned above, the gap closure process and it influences on temperature is something to be studied in the near future.

The desaturation of the buffer due to strong heating of the canister is shown in Figure 5-49. Detailed evolution of liquid pressure is depicted in Figure 5-50 and Figure 5-51. In Case FE (buffer material is FEBEX), the initial suction has been assigned as 135 MPa. Therefore, there is a big difference in Case FE compared to the other cases. As the hydration is slower in Case R3 (no fracture; k_{rock}: $3x10^{-21}$ m^2), the desaturation of the buffer is also stronger than in the other cases. The liquid pressure distribution in earlier times (10.5 years after installation of components) for deposition tunnel is shown in Figure 5-60 and Figure 5-61. It can be seen that Case F3 (fracture at the upper part of canister), Case GM1 (bigger backfill tunnel) and Case FE (buffer material is FEBEX) have different trends as compared to other cases. In Case F3 (Fracture at the upper part of canister), hydration is faster because of the location of the fracture. The system saturates faster. In contrast, saturation takes place slowly in Case GM1 (bigger backfill tunnel). The backfill tunnel has a bigger volume in Case GM1 and as a result, there is a delay in saturation. The initial higher suction in Case FE (buffer material is FEBEX) also delays the saturation.

The developed effective stresses in the buffer are shown in Figure 5-52. Detailed linear evolution of liquid pressure is shown in Figure 5-53 and Figure 5-54. It can be seen that saline water has an important role to play in the generated swelling pressures. The rate of salinity is 7% in Case S2 (salinity 7%; w_{buffer}: 17%) and S3 (salinity 7%; w_{buffer}: 19.7%). The obtained stresses in these two cases are considerably lower as compared to the other cases. The mean effective stress distribution in earlier period (10.5 years after installation of components) for deposition tunnel is shown in Figure 5-62 and Figure 5-63. In Case F3 (fracture at upper part of canister), stress development takes place faster because of fast saturation. The slow saturation due to low permeability of rock and no presence of fracture in Case R3 (no fracture; k_{rock}: $3x10^{-21}$ m^2), causes a delay in stress development.

Figure 5-55 shows vertical displacements occurred at the buffer-backfill intersection for all cases. Detailed evolution in a linear time scale of liquid pressure is depicted in Figure 5-56 and Figure 5-57. Case F3 (fracture at the upper part of the canister) and Case FM2 (the gap between the rock and buffer is filled with water) undergo the maximum value for displacements. The fast saturation of the buffer in these two cases results in greater displacements. The displacement distribution in earlier period (10.5 years after installation of components) for deposition tunnel is shown in Figure 5-64 and Figure 5-65. As depicted throughout these figures, Case F2 (fracture at mid-height of the canister), Case F3 (fracture at the upper part of the canister) and Case FM2

(the gap between the rock and buffer is filled with water) cause the larger displacements. In Case R2 (no fracture; k_{rock}:$3x10^{-19}$ m^2) and R3 (no fracture; k_{rock}:$3x10^{-21}$ m^2), due to slow saturation and swelling process, the developed displacements at the buffer and backfill intersection are considerably lower compared to other cases.

Table 5-26. *Comparison of all cases.*

Cases	T (°C) [1]	t_{Sat} (y) [2]	P_{eff} (MPa) [3]	d (cm) [4]	Observation
1. Base	80.7	8.4	9.4	8.4	-
2. F1	80.7	8.2	9.4	8.7	Fracture at bottom of canister
3. F2	80.6	6	9.5	10.2	Fracture at mid-height of canister
4. F3	80.5	4	8.8	16.4	Fracture at upper of canister
5. P1	80	8	10.7	10	Pellet thickness: 35 mm
6. P2	81	9	9.3	8.4	Pellet thickness: 60 mm
7. S1	80.7	6.8	6.7	7.3	Salinity: 3.5%
8. S2	80.7	6.3	4.1	5.5	Salinity:7 %
9. S3	80.7	6.3	4.3	3.8	Salinity 7%; w_{buffer}: 19.7%
10. W1	92.1	11.3	11.98	9.3	w_{buffer}:11%
11. W2	80.7	3.7	7	5.8	w_{buffer}:21.7%
12. D1	80.7	6.4	10	10.4	Initial density buffer 2100 kg/m^3
13. L1	80.4	8.8	9.4	8.4	Lagrangian method
14. M1	80.7	7.9	9.8	7.8	K^{Micro} for pellets is 0.145
15. FM1	80	8.04	9.8	8.8	Between rock and buffer: slurry
16. R1	81.3	15	9.4	5.2	No fracture, k_{rock}:1.52x10^{-19} m^2
17. R2	80.7	10	9.5	4.2	No fracture; k_{rock}:3x10^{-19} m^2
18. R3	95.7	400	7.7	3.8	No fracture; k_{rock}:3x10^{-21} m^2
19. TE1	80.7	8.9	10.3	9.8	α_{buffer} (ºC^{-1}) is 9x10^{-4}
20. TC1	86.4	8.4	9.4	8.5	λ_{sat} for buffer is 1.0 W/(m·K)
21. PW1	80.7	8.7	8.8	6.5	Initial Sr for pellets: 80%; water injection to pellets
22. GP1	84.2	9	9.2	7.8	Current geometry, air gap between canister and buffer
23. GP2	82.2	8.4	9.3	8.3	Current geometry, pellets between canister and buffer
24. GP3	80.2	8.4	9.2	8.4	Current geometry, MX-80 between canister and buffer
25. PW2	82.2	7	9.2	7.7	Current geometry; initially saturated (96%) pellets
26. GM1	80.9	11.5	9.4	8.7	Bigger backfill tunnel
27. 3D1	79	10	-	-	3D TH calculations
28. FE	90.2	18	7	5	Buffer material is FEBEX
29. FM2	83	7.6	4.4	18	Between rock and buffer is water gap
30. W3	104	12.6	9.7	8.7	Current geometry, w_{buffer}:11%
31. RD1	80.7	8.7	9.4	8.5	Gap has radiation parameters
32. BM1	95	12.6	9.4	6.3	w_{buffer}:14%, ρ_d: 1600 kg/m^3
33. RTE1	80.8	8.6	9.4	7.5	α_{rock} (ºC^{-1}) is 8x10^{-6}
34. FP1	80.4	8.3	9.4	8.6	$k_{rock\text{-}fracture}$ is 1.52x10^{-15} m^2

Notation for Table 5-26:

(1) Maximum temperature at gap wall canister side (°C)

(2) Time needed to reach full saturation (99%) at the buffer (year)

(3) Maximum effective stress developed in the buffer (MPa)

(4) Displacements at intersection buffer-backfill (cm)

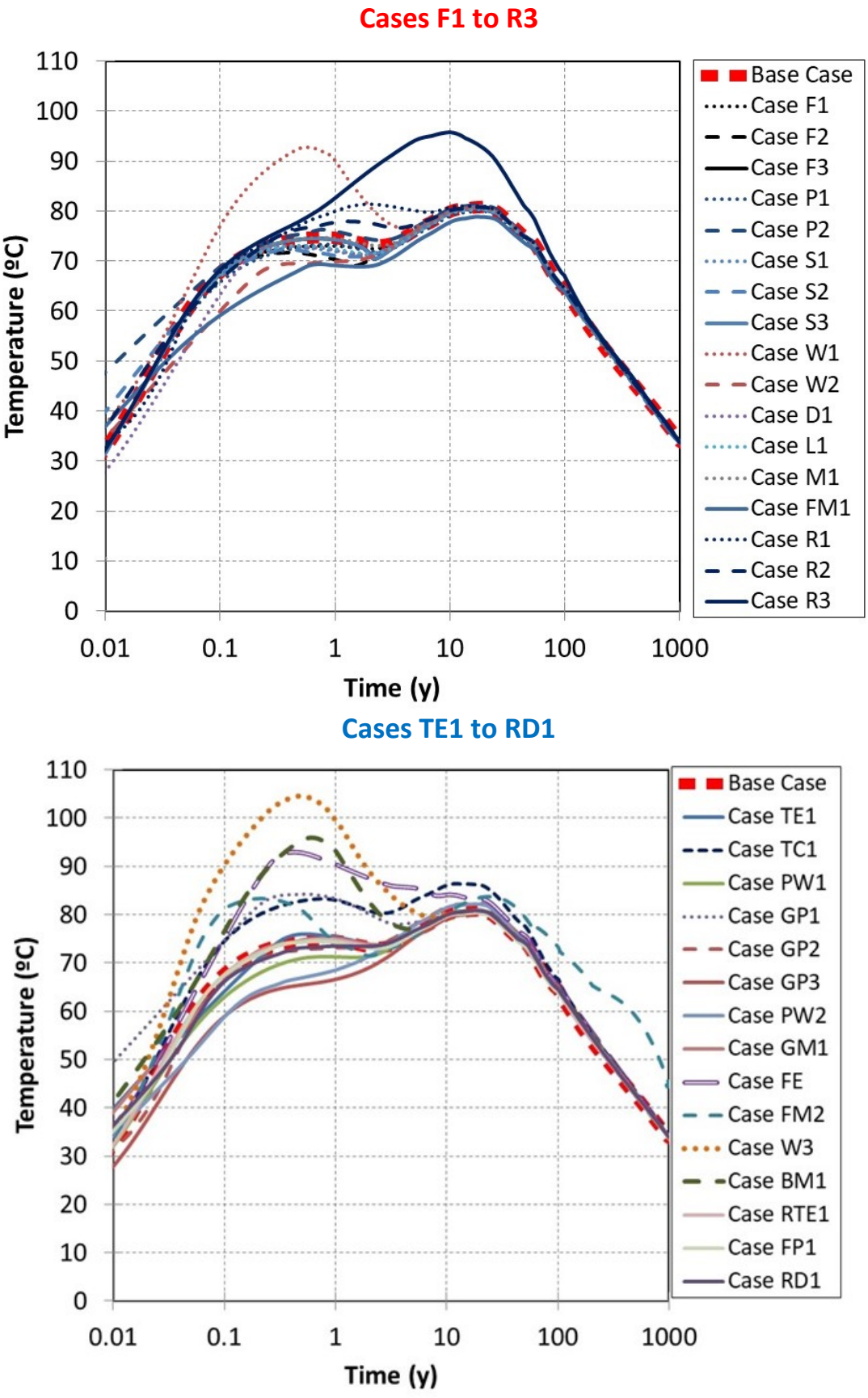

Figure 5-46. *Evolution of temperature with time. All Cases*

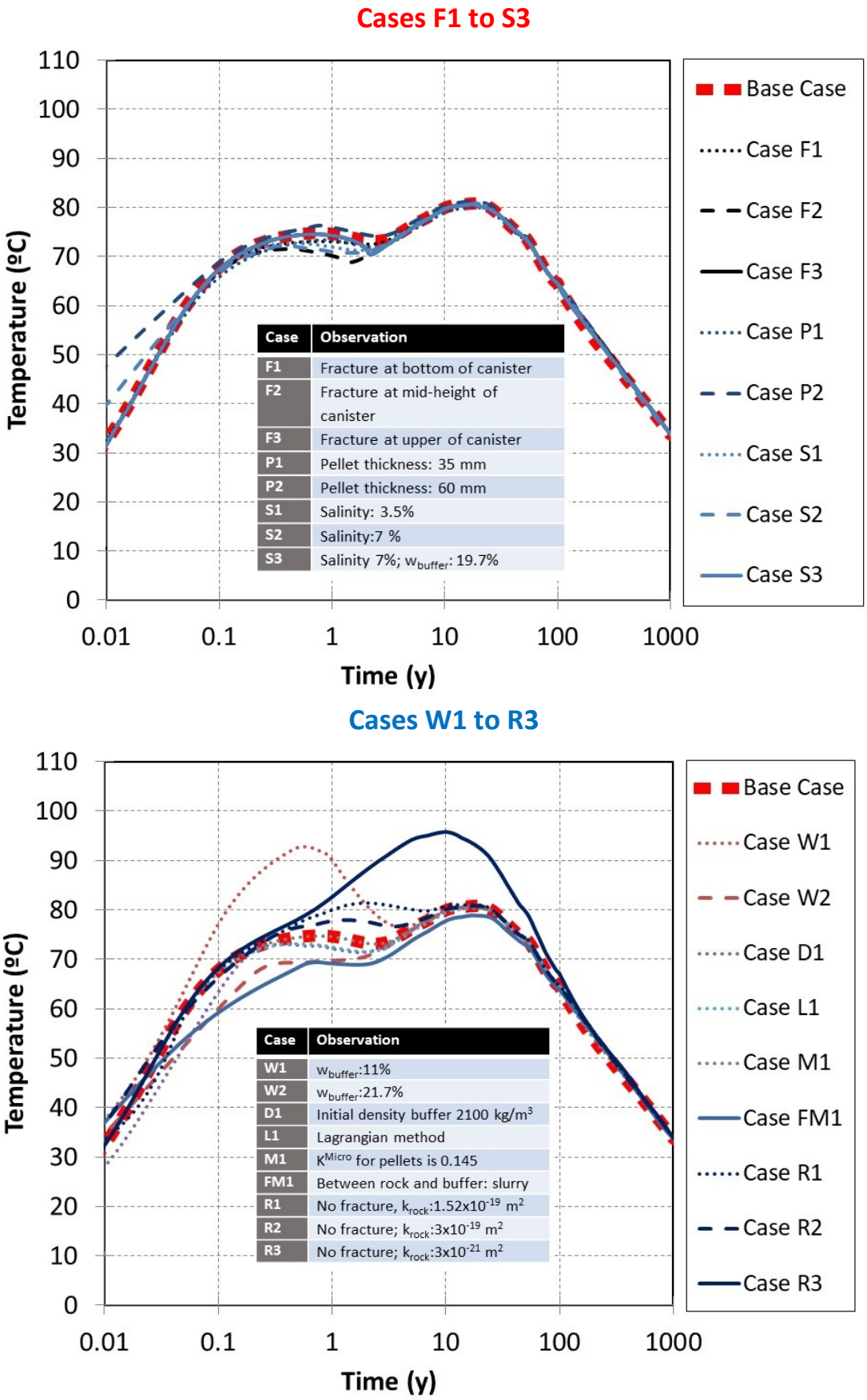

Figure 5-47. *Evolution of temperature with time. Cases F1 to S3 and Cases W1 to R3.*

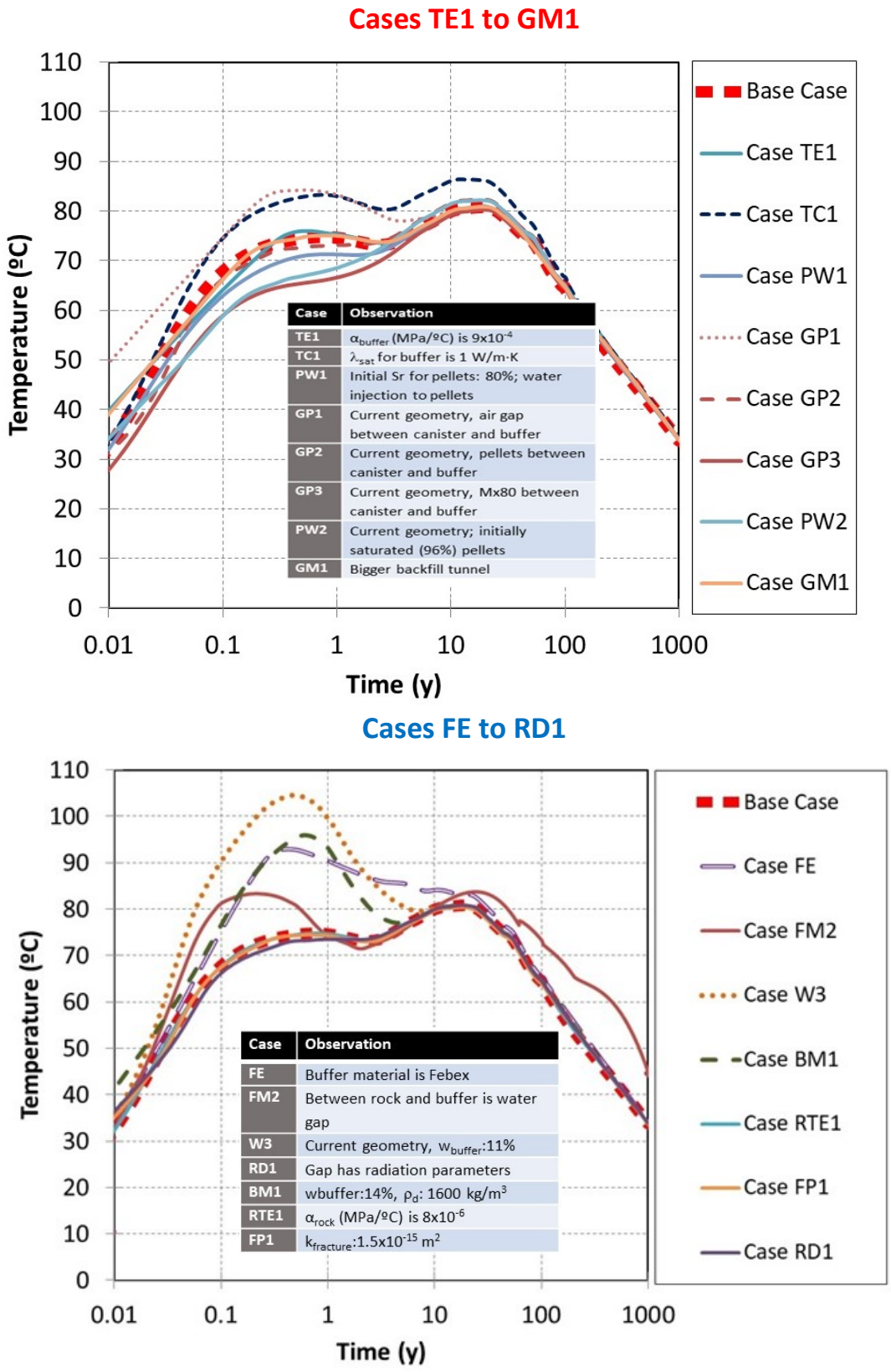

Figure 5-48. *Evolution of temperature with time. Cases TE1 to GM1 and Cases FE to 3D1.*

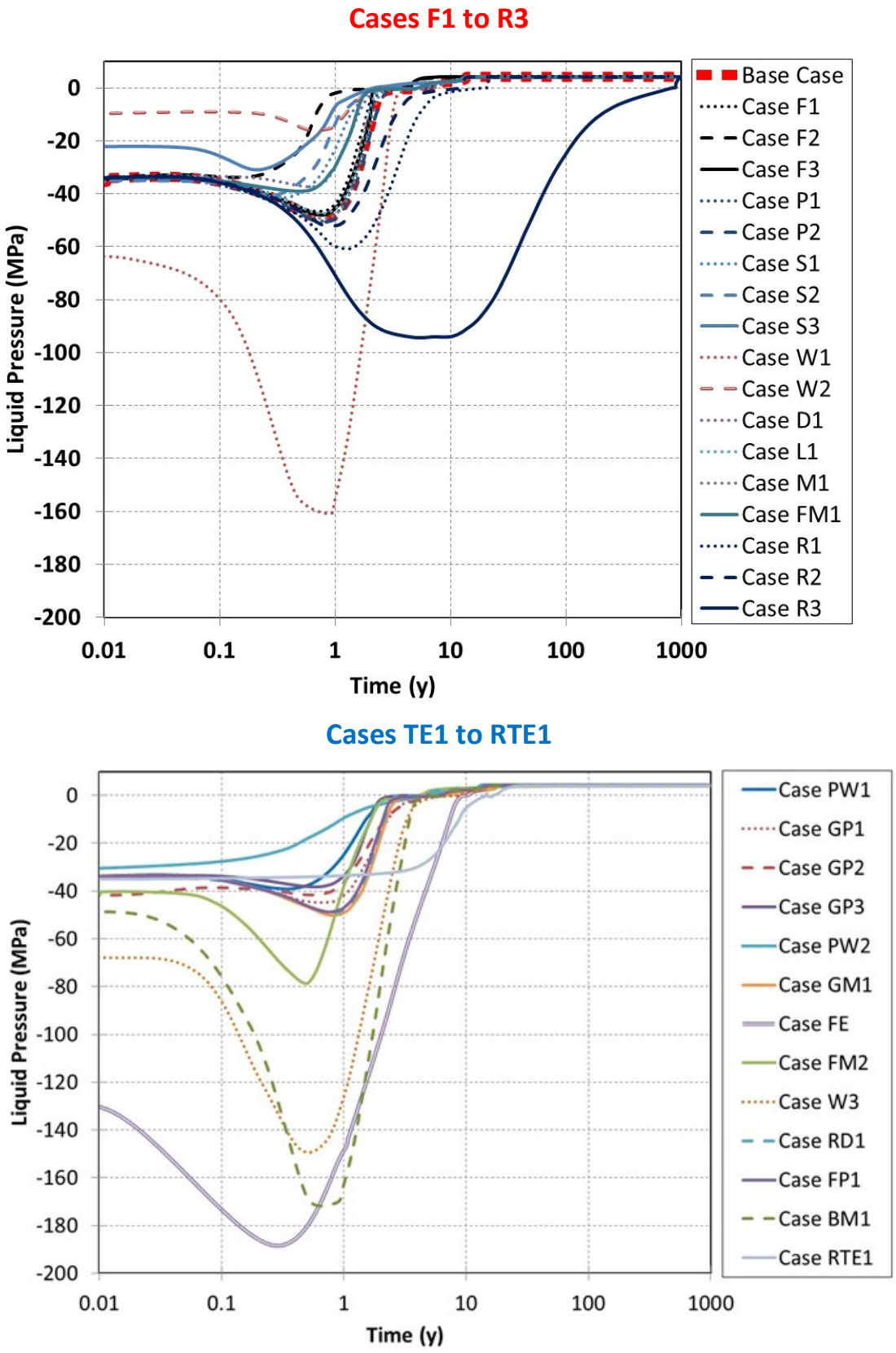

Figure 5-49. *Evolution of liquid pressure with time. All Cases.*

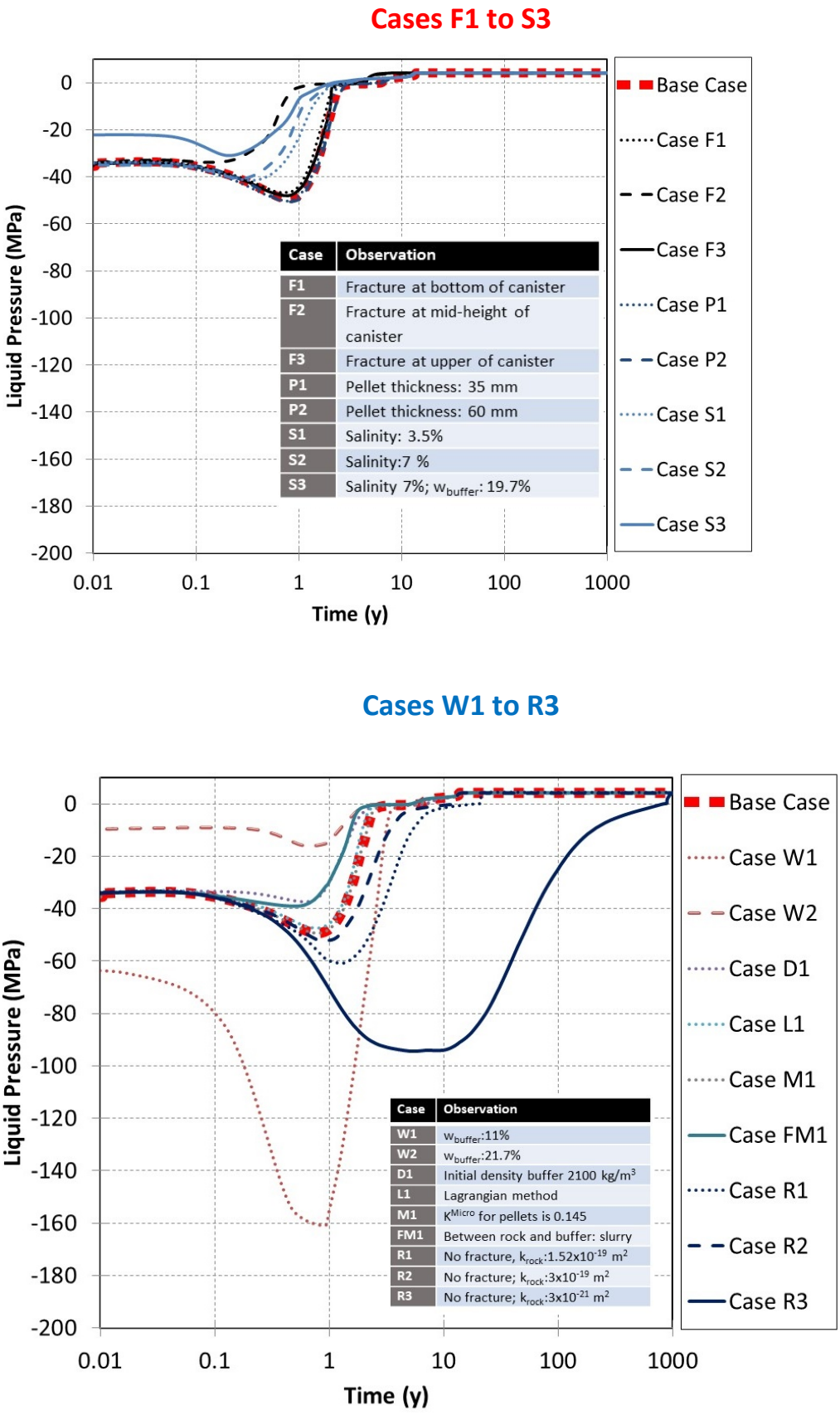

Figure 5-50. *Evolution of liquid pressure with time. Cases F1 to S3 and Cases W1 to R3.*

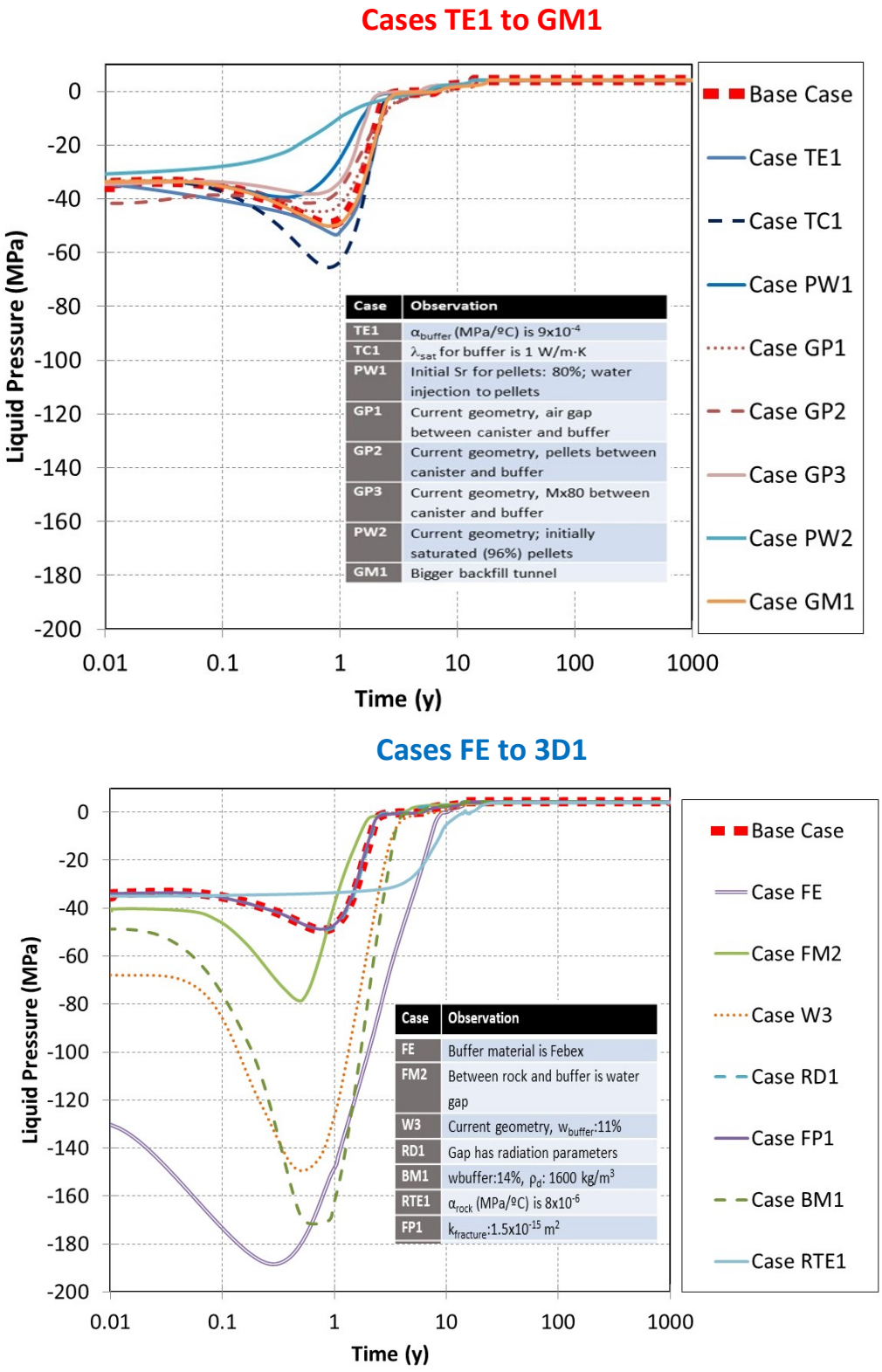

Figure 5-51. *Evolution of liquid pressure with time. Cases TE1 to GM1 and Cases FE to 3D1.*

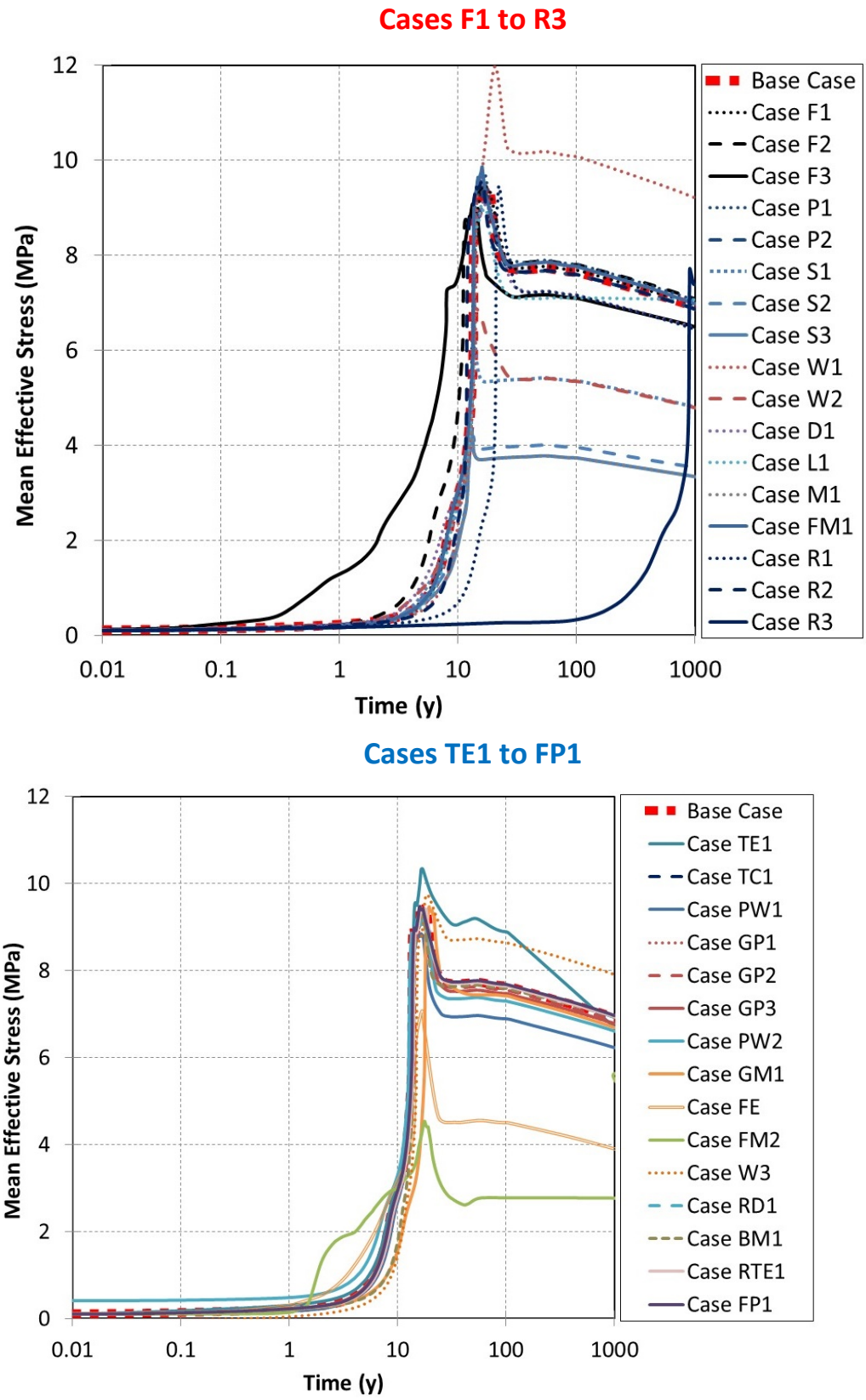

Figure 5-52. *Evolution of mean effective stresses with time. All Cases.*

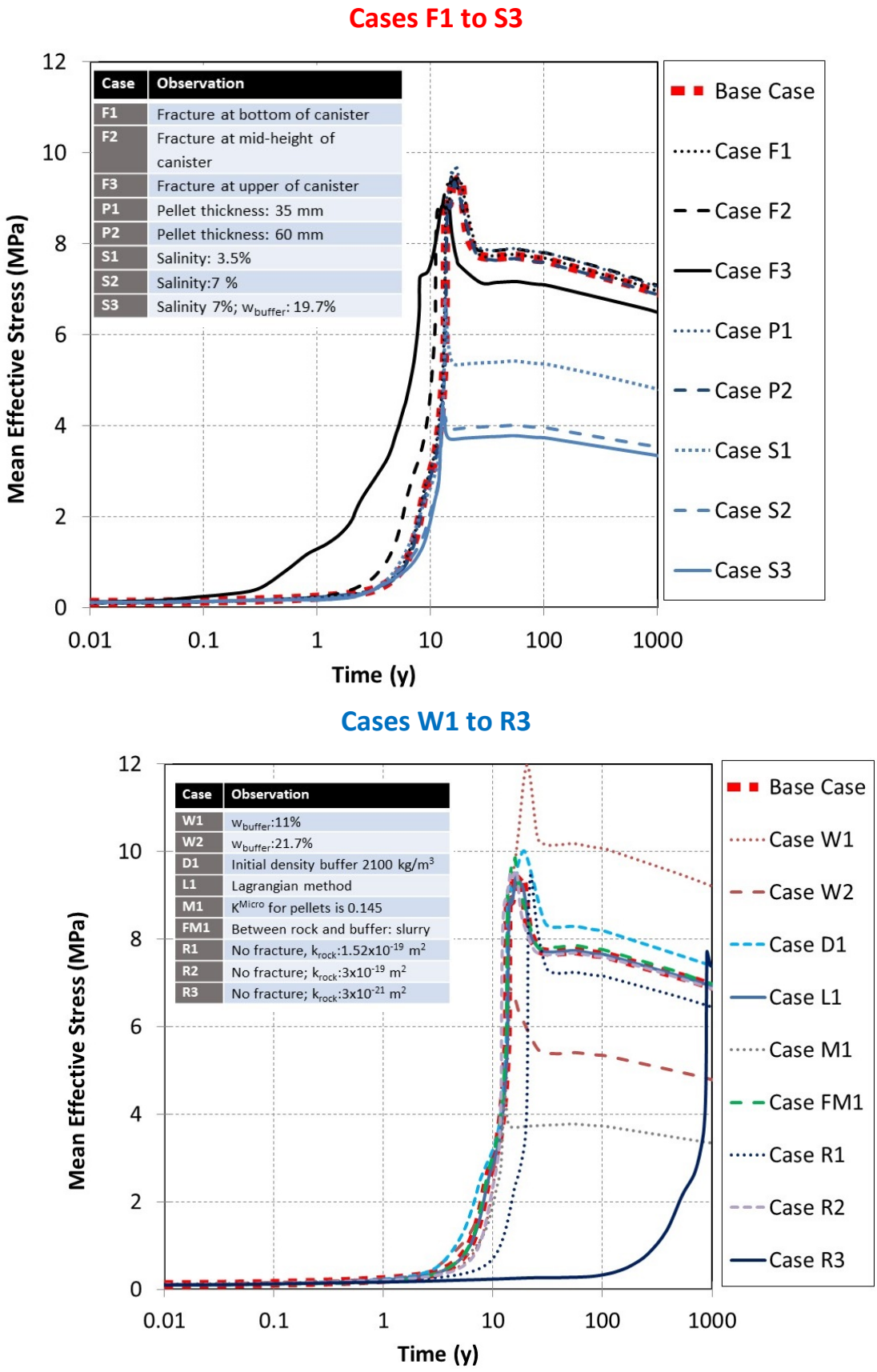

Figure 5-53. *Linear evolution of mean effective stresses with time. Cases F1 to S3 and Cases W1 to R3.*

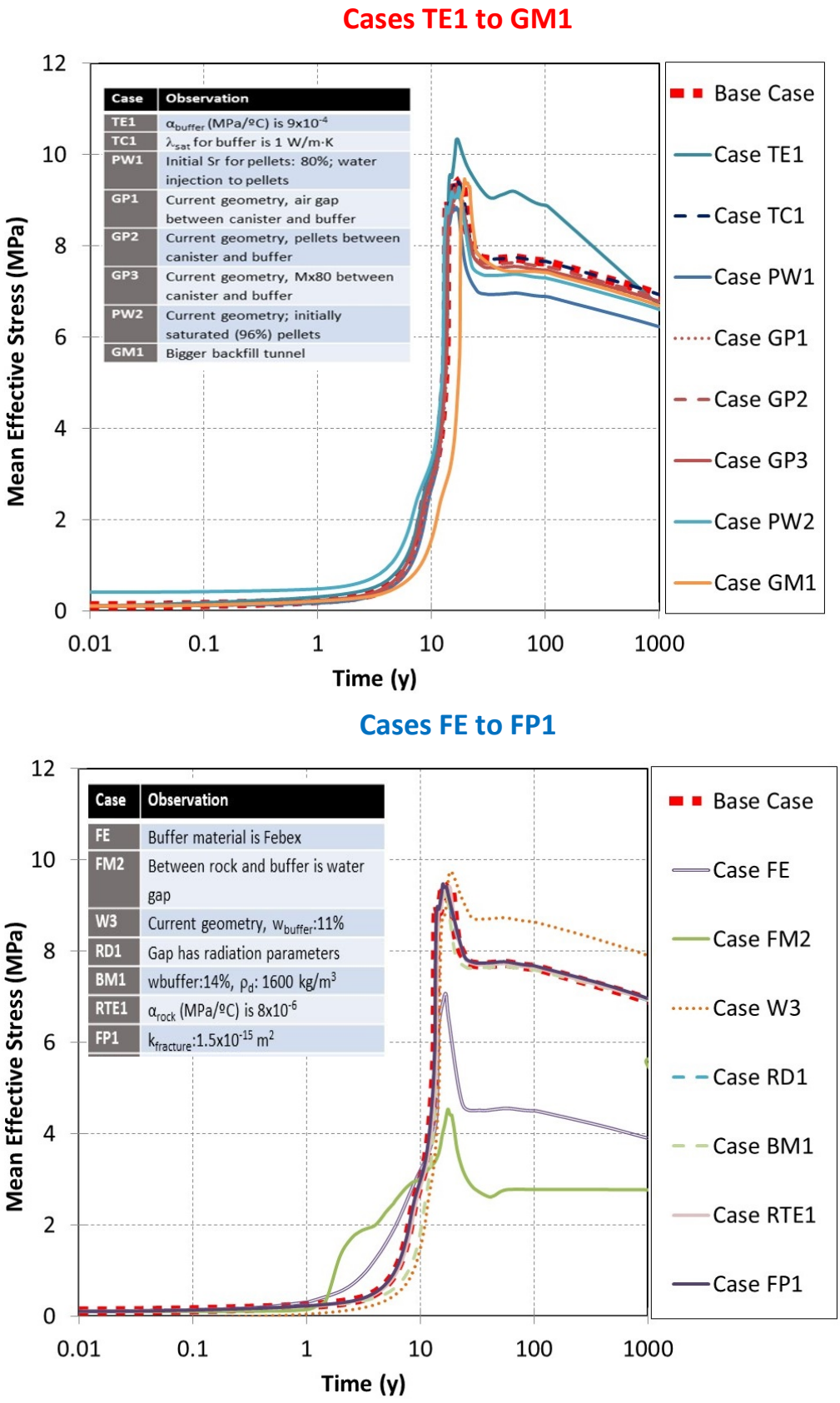

Figure 5-54. *Linear evolution of mean effective stresses with time. Cases TE1 to GM1 and Cases FE to FP1.*

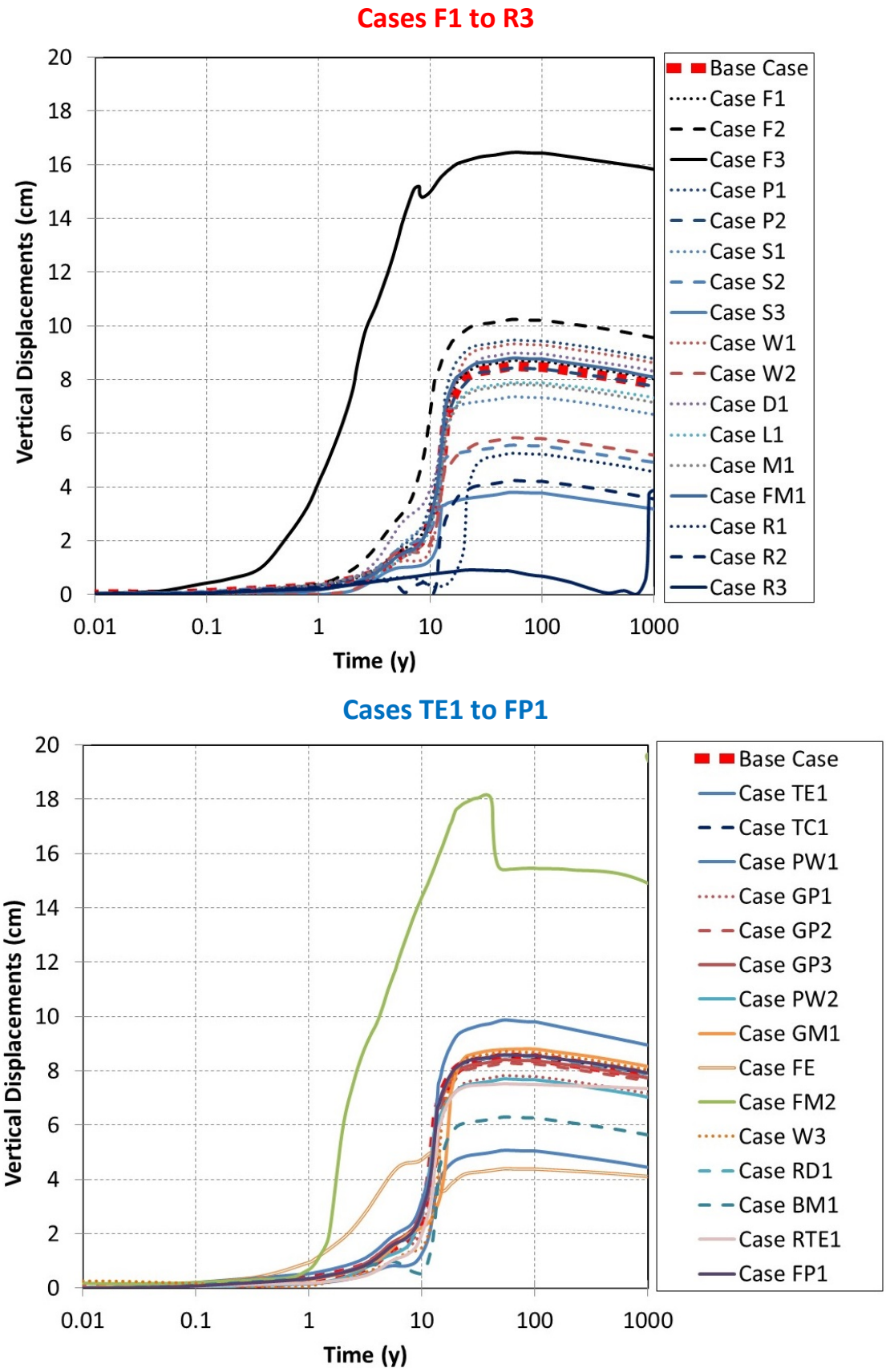

***Figure 5-55**. Evolution of vertical displacements at the buffer backfill intersection with time. All Cases.*

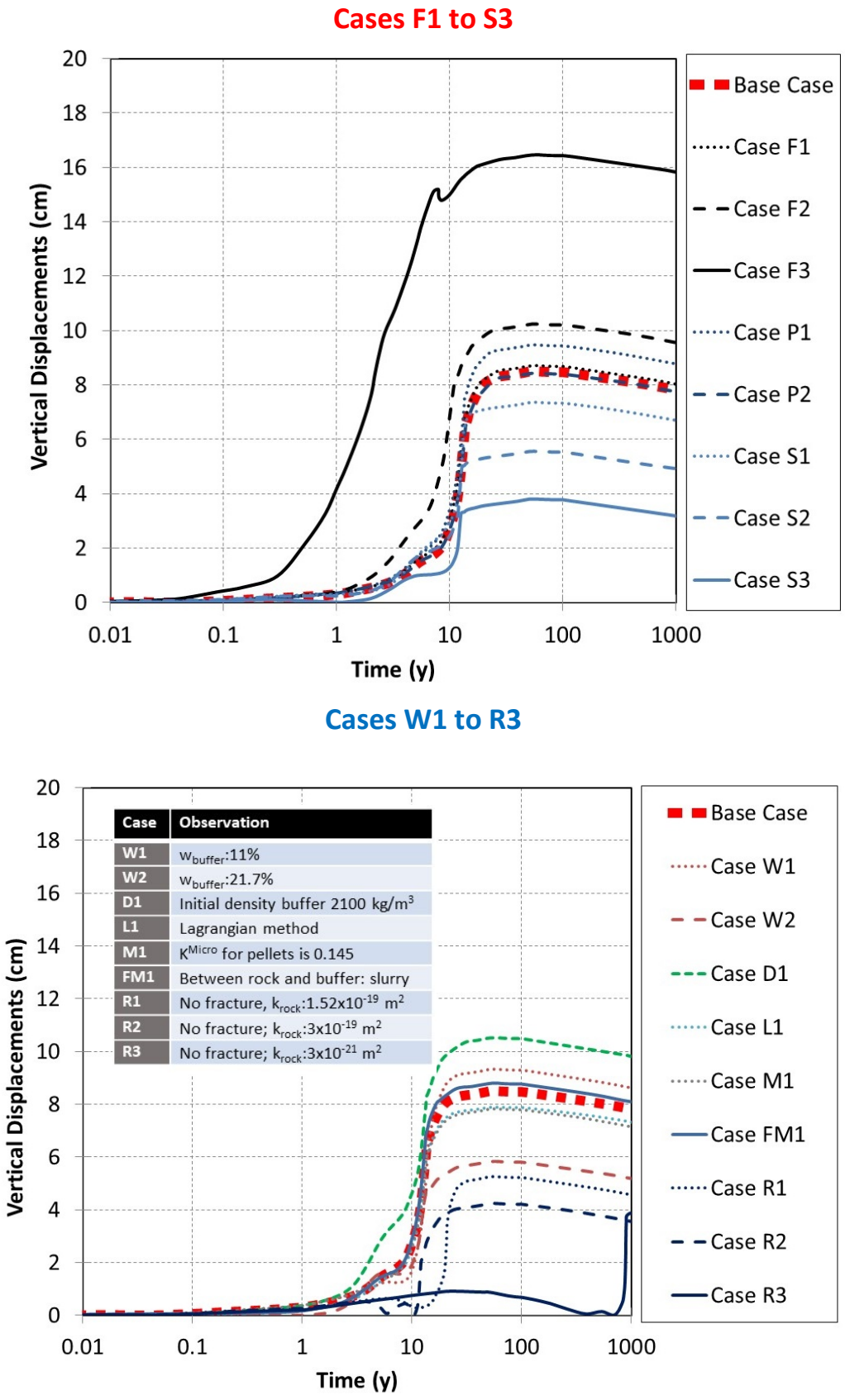

Figure 5-56. *Linear evolution of vertical displacements at the buffer backfill interface with time Cases F1 to S3 and Cases W1 to R3.*

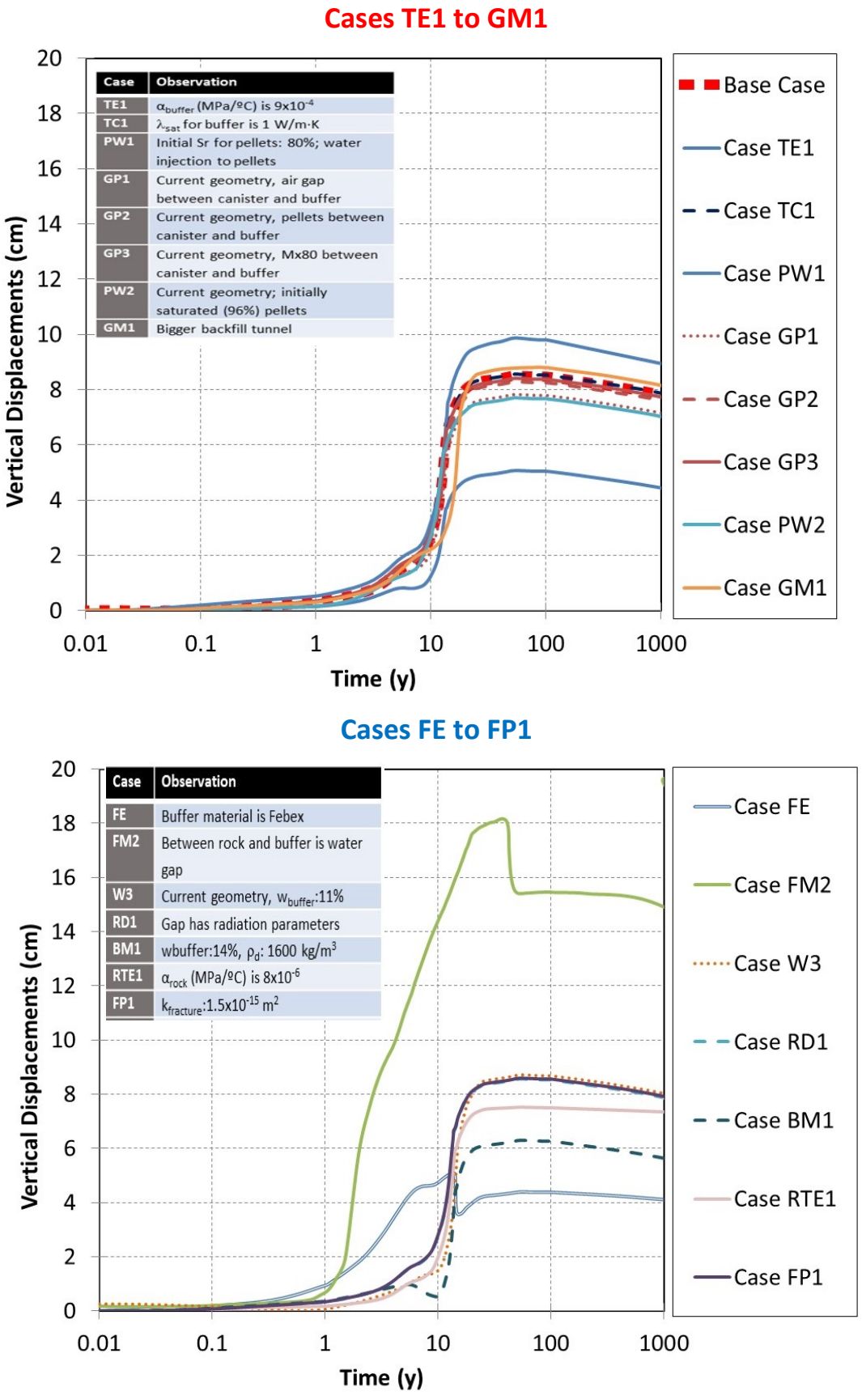

Figure 5-57. *Linear evolution of vertical displacements at the buffer backfill interface with time. Cases TE1 to GM1 and Cases FE to FP1.*

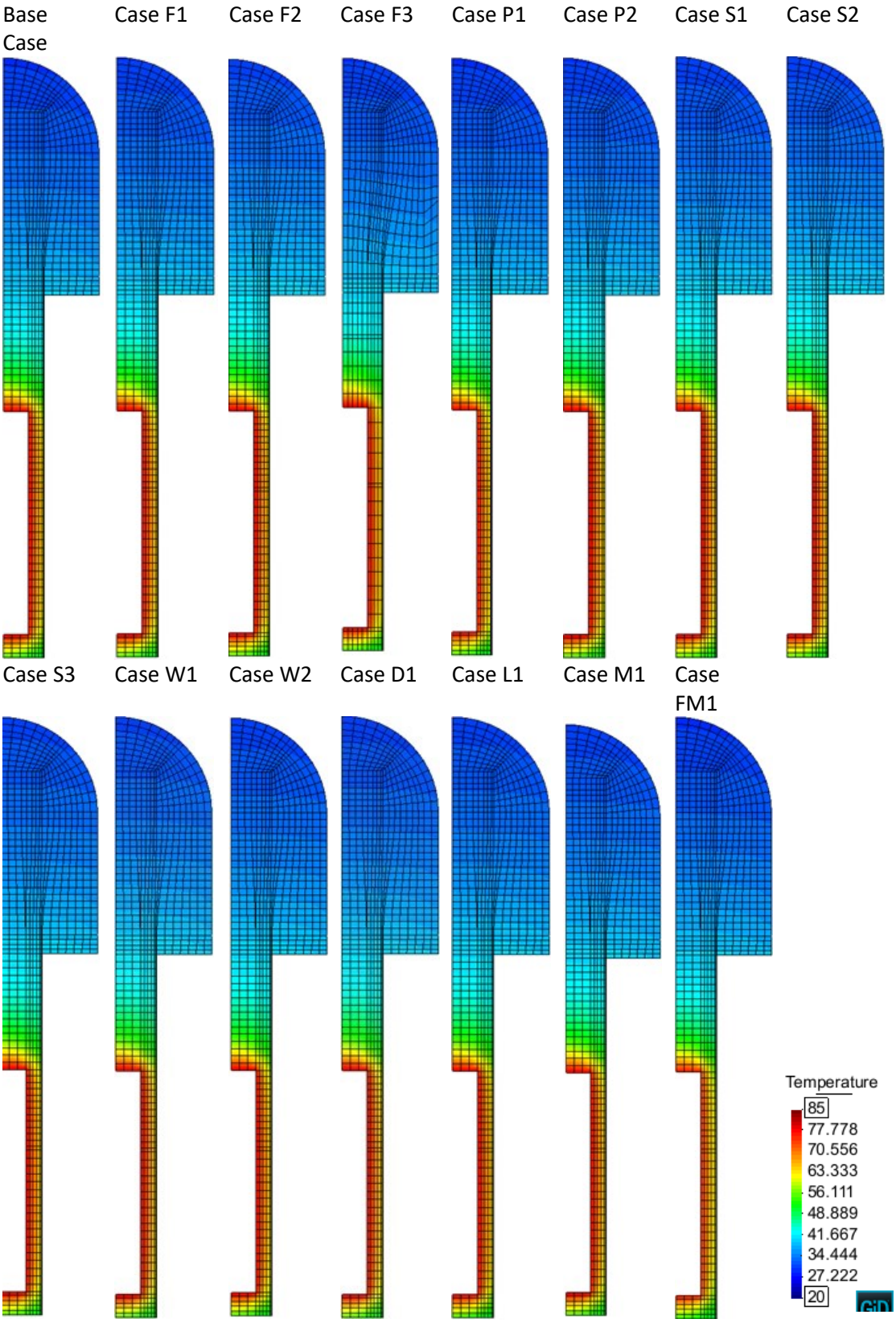

Figure 5-58. *Temperature distribution for cases (Base Case to Case FM1), 10.5 years after deposition.*

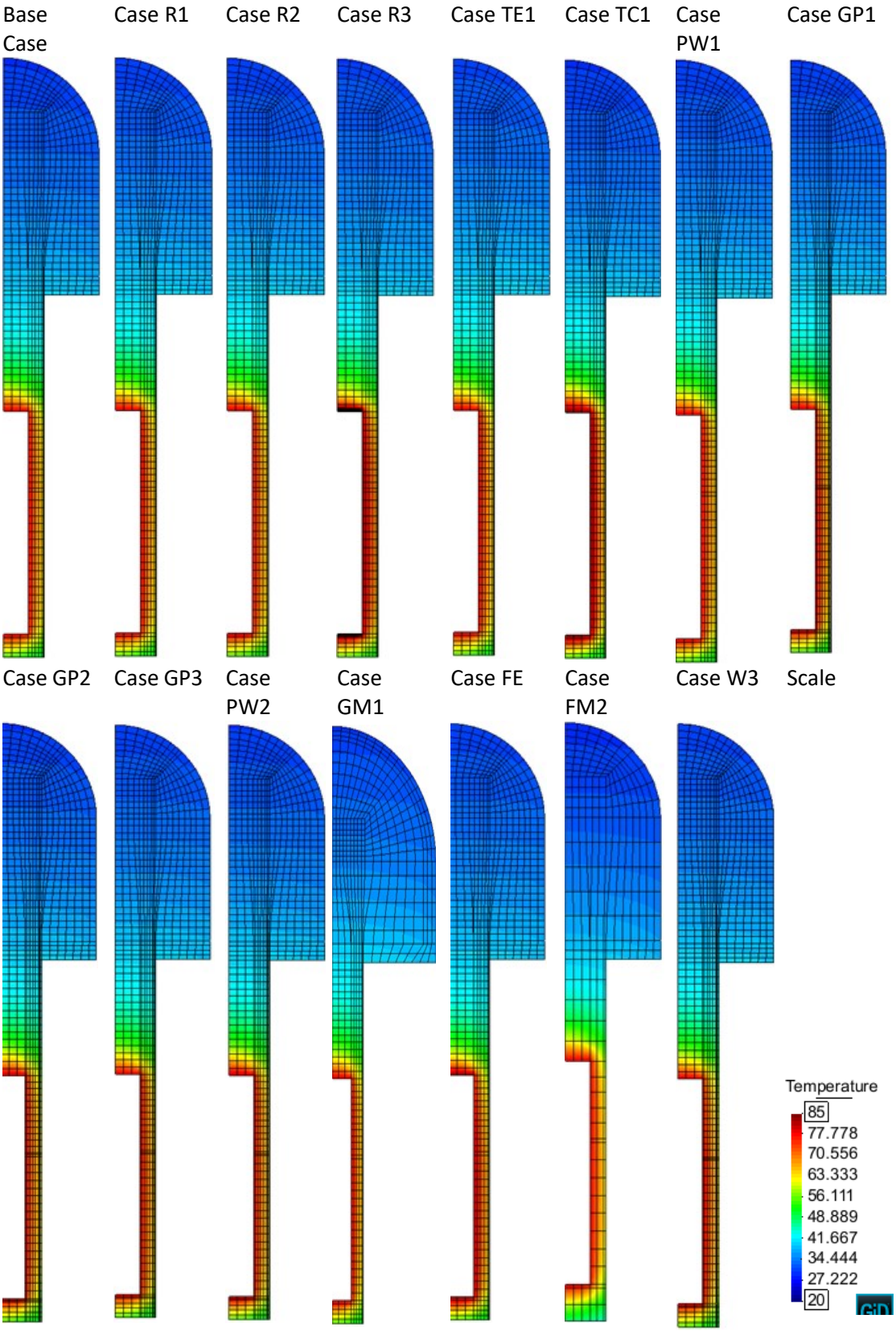

Figure 5-59. *Temperature distribution for cases (Base Case to Case W3), 10.5 years after deposition.*

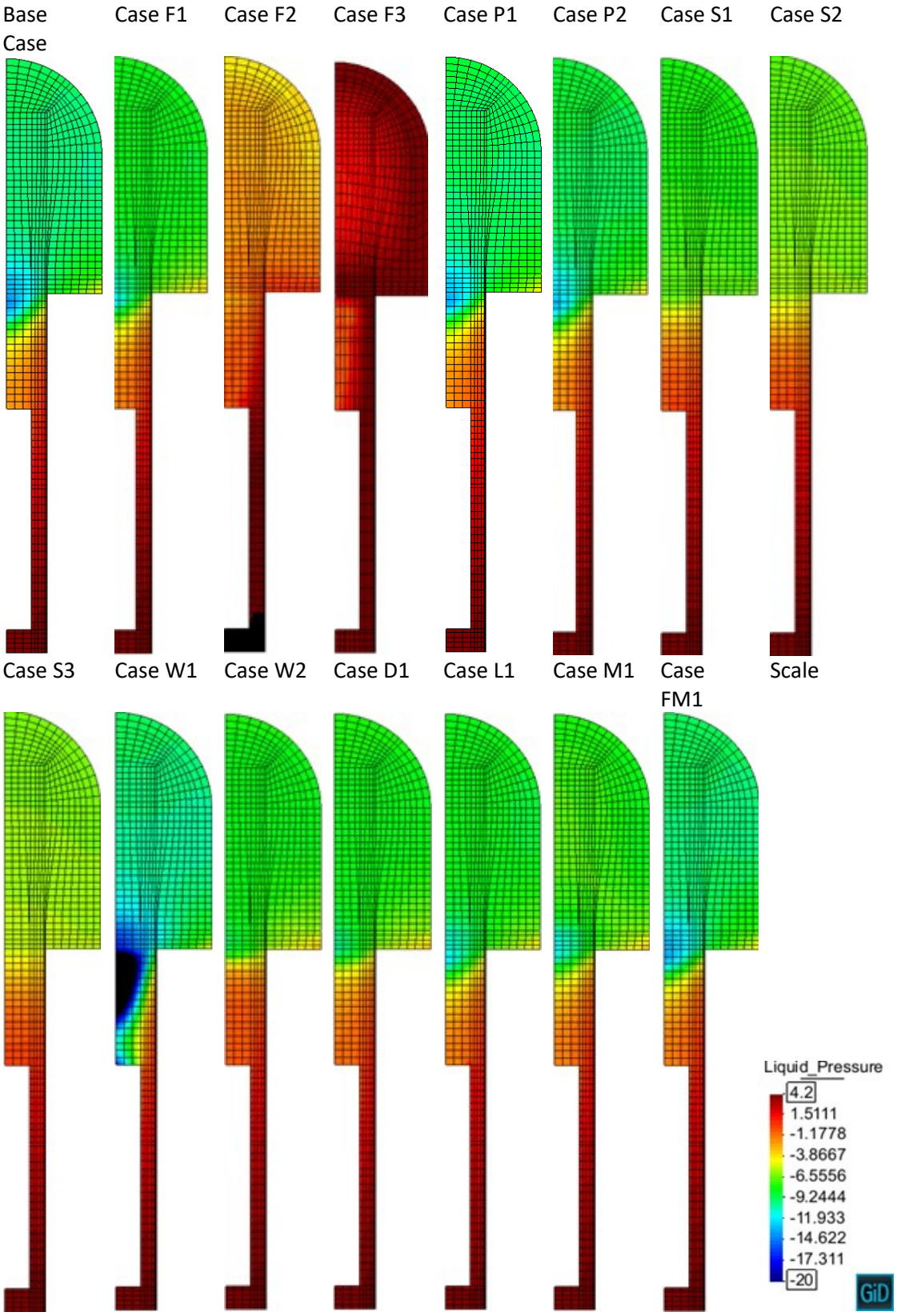

Figure 5-60. *Liquid pressure distribution for cases (Base Case to Case FM1), 10.5 years after deposition.*

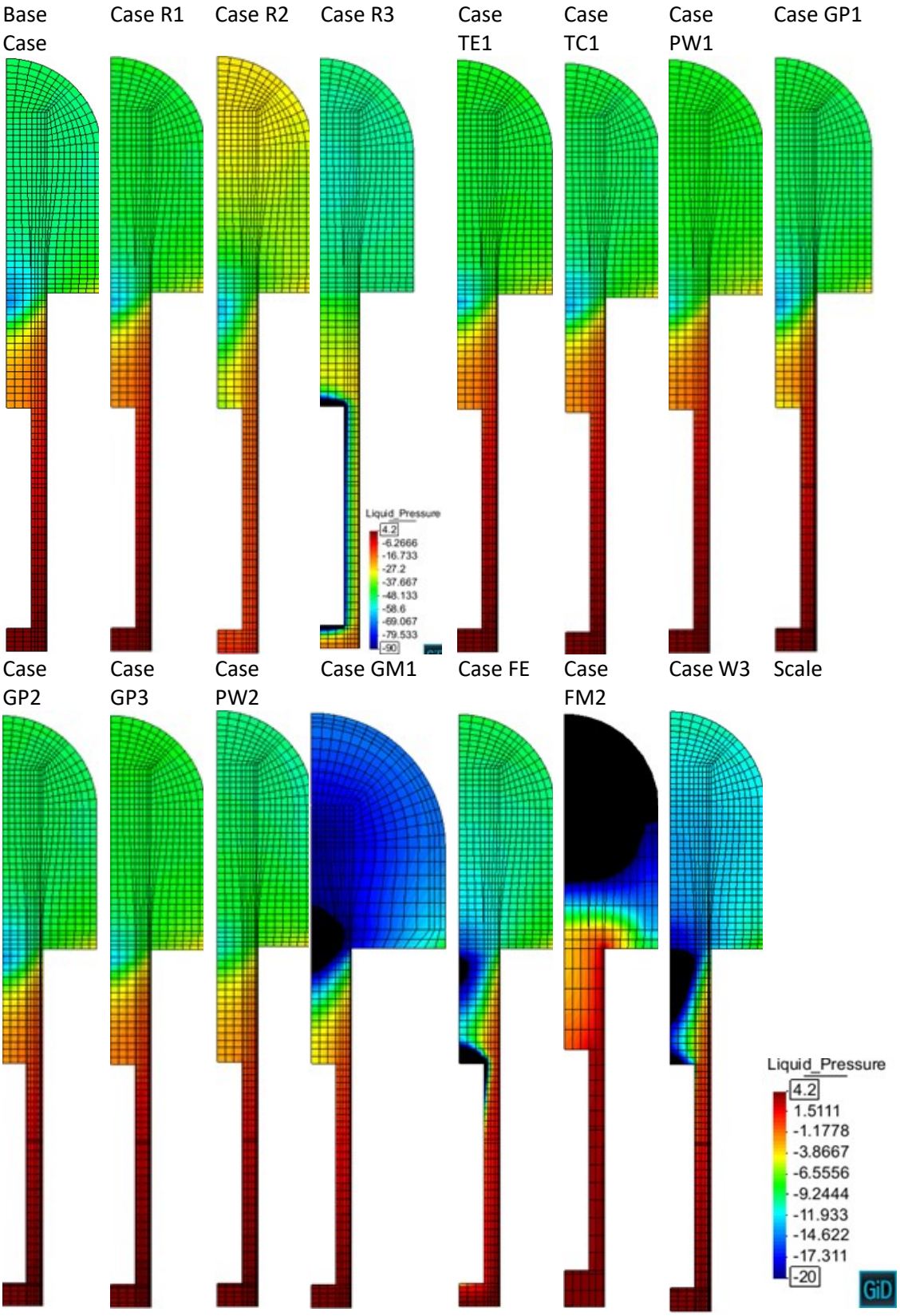

Figure 5-61. *Liquid pressure distribution for cases (Base Case to Case W3), 10.5 years after deposition.*

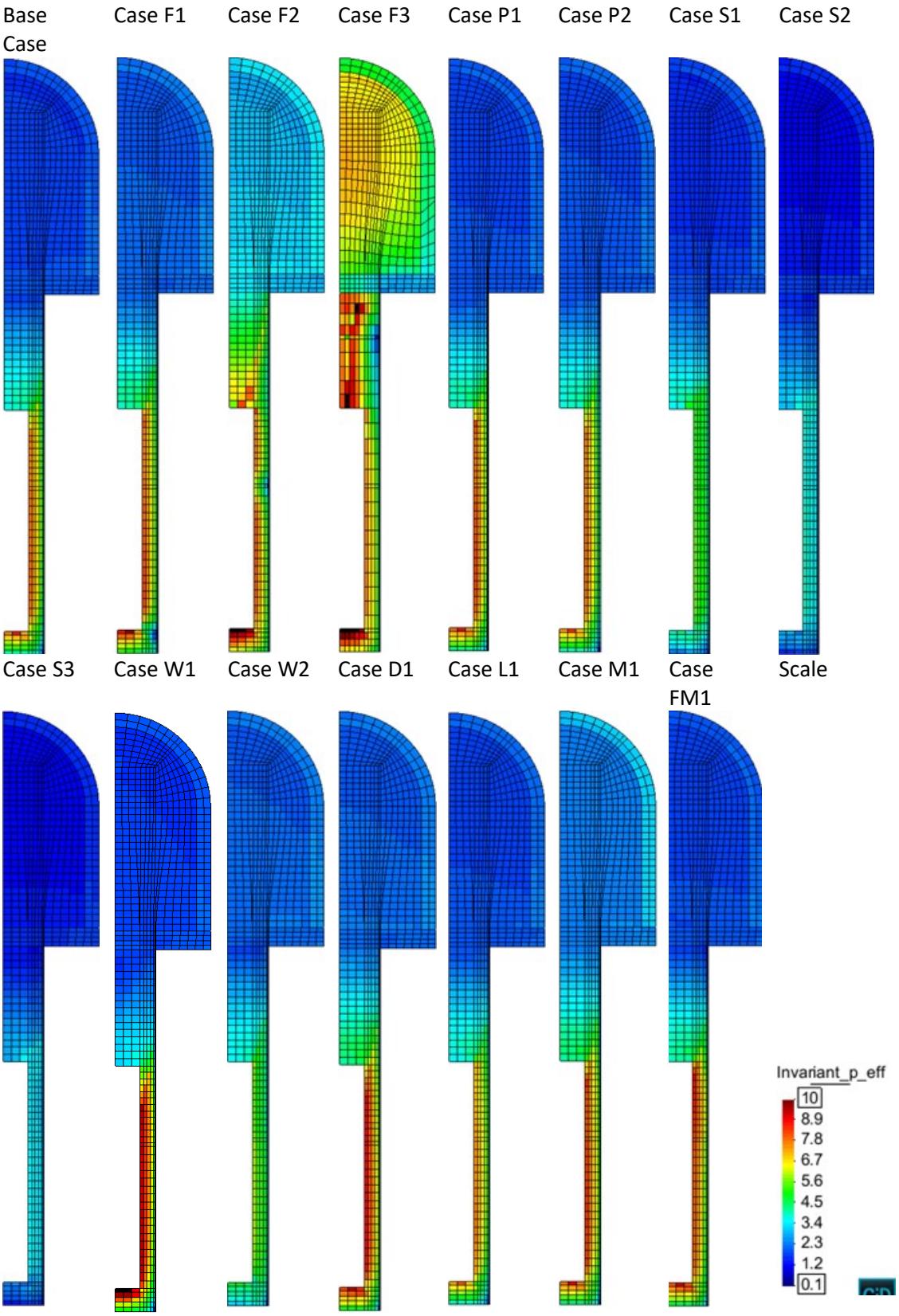

Figure 5-62. *Effective stress distribution for cases (Base Case to Case FM1), 10.5 years after deposition.*

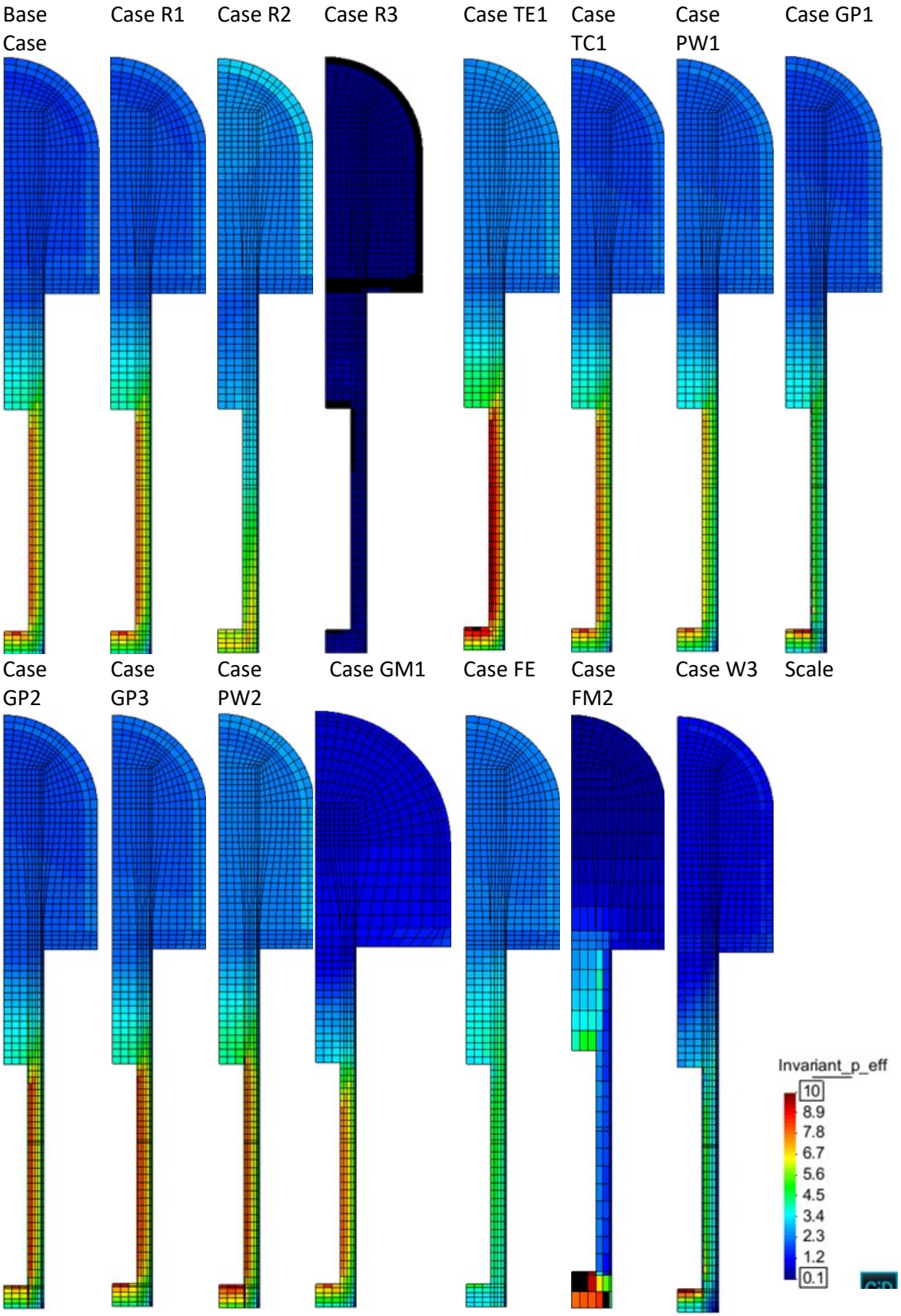

Figure 5-63. *Effective stress distribution for cases (Base Case to Case W3), 10.5 years after deposition.*

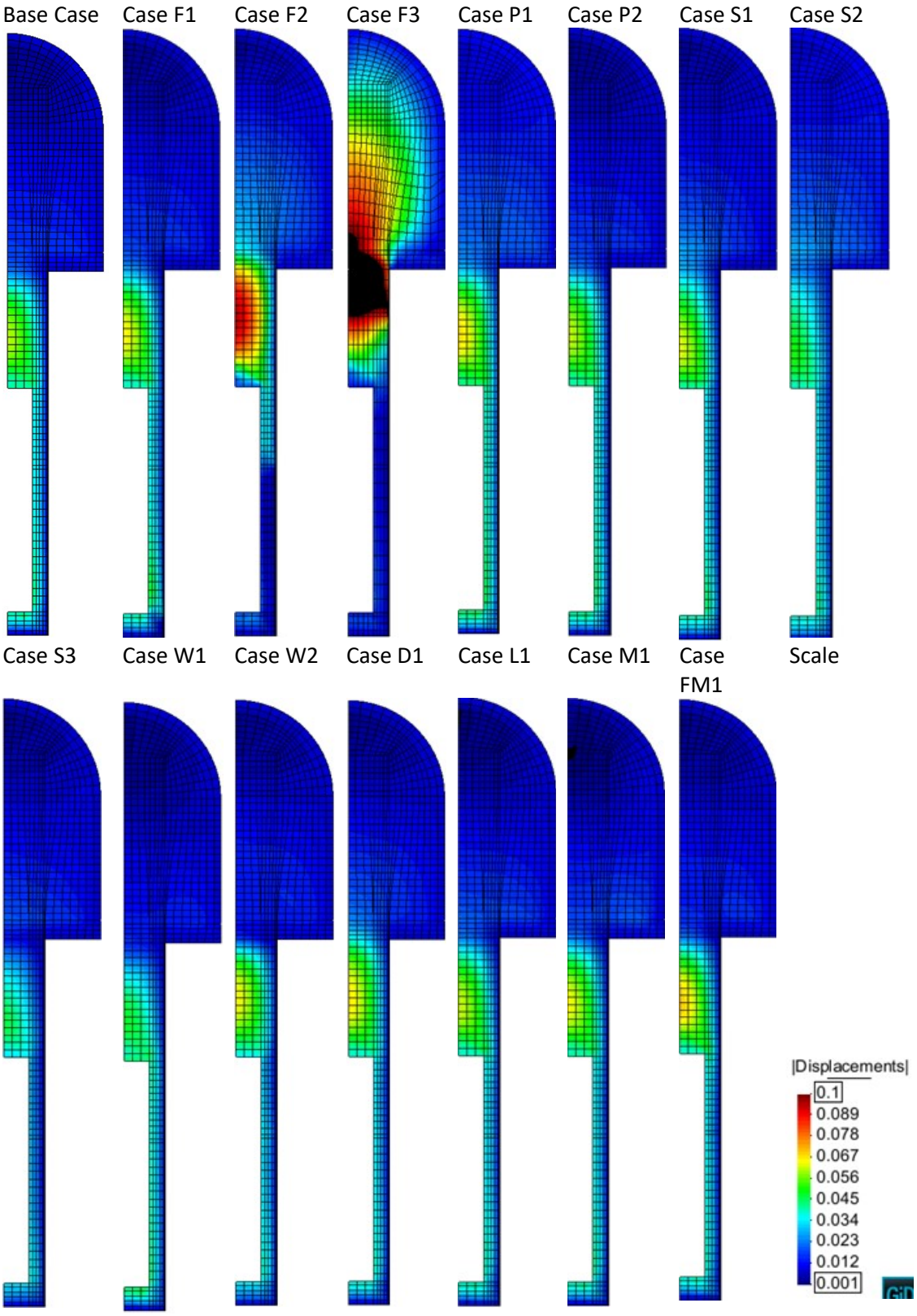

Figure 5-64. *Displacement distribution for cases (Base Case to Case FM1), 10.5 years after deposition.*

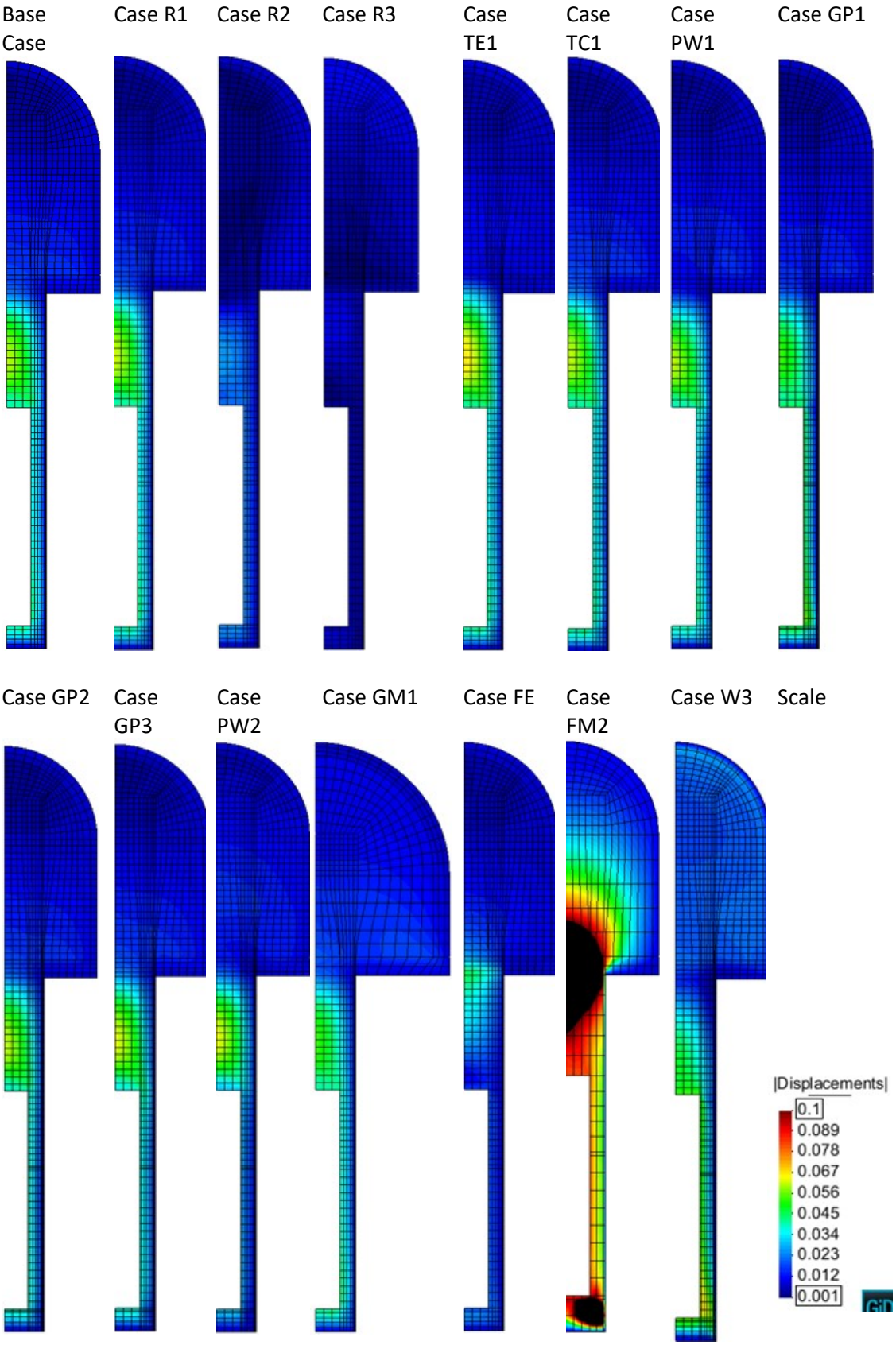

Figure 5-65. *Displacement distribution for cases (Base Case to Case W3), 10.5 years after deposition.*

6 3D THM ANALISIS

In this Chapter, a sensitivity analysis has been performed in order to investigate the effect of variable gas pressure on the thermo-hydro-mechanical (THM) results for the engineered barrier system (EBS) in spent nuclear fuel disposal facility of Posiva Oy. A simplified 3D geometry has been adopted for THM calculations. Buffer and backfill have been considered homogenous materials (neither pellets filling the gaps nor bottom layer in backfill are considered). The influence of variable gas pressure on maximum temperature, the time needed to reach full saturation, swelling pressure and vertical displacements generated at the buffer-backfill interface has been analysed. This case considers that the gas filling the voids does not keep its pressure constant, it is not a case where gas is generated due to corrosion.

6.1 Geometry and initial conditions

Figure 6-1 - A shows the geometry of the model (dimensions are 11 m x 12.5 m x 35 m) and the materials considered (rock, canister, backfill and buffer). This corresponds to 11 m of deposition hole spacing along the tunnel, and 25 m of spacing between parallel drifts keeping the maximum temperature calculated on canisters surface in 90°C at least (Ikonen, 2003). Note that half of the volume associated with a deposition hole is considered. The distance between deposition holes finally applied was 9.0 m because the allowed maximum temperature calculated in canisters surface was increased to 95°C (Ikonen and Raiko, 2012). The maximum temperature allowed is 100°C (Posiva, 2012) and the difference between this temperature and the maximum temperature calculated is a safety margin.

Although the buffer and backfill consist of different components i.e. a foundation bed (only in backfill), blocks, air gaps (only in buffer) and pellets, both components have been treated as a single material. The initial porosity considered in both components was 0.368, close to initial porosity of buffer blocks (Table 1-1, Juvankoski et al. 2013).

Hydraulic parameters used are listed in Table 6-1. Thermo-mechanical parameters are similar to the Base Case in 2D calculations and listed in Chapter 4.4. The exceptions are that dilation is not considered for materials, the water retention curve and the hydraulic conductivity do not depend on porosity, initial porosity was considered identical for backfill and buffer (ϕ=0.368).

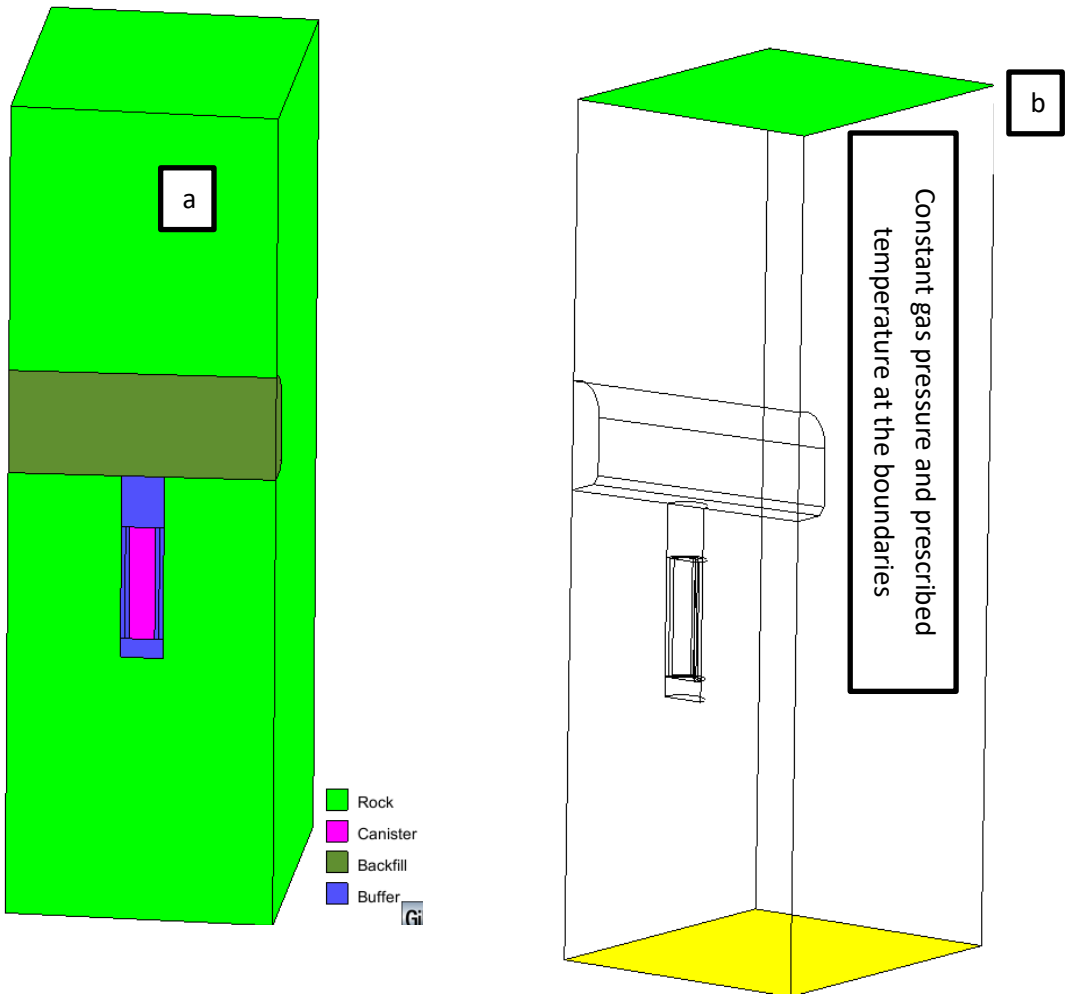

Figure 6-1. Materials and boundary conditions

Table 6-1 Hydraulic parameters for Rock, Friedland Clay and MX-80.

Parameters	Materials		
	Rock	Friedland-clay	MX-80
P (MPa)	1.5	25	31.25
λ (-)	0.3	0.4	0.5
k (m^2)	$3.52x10^{-20}$	$1.6x10^{-20}$	$5.6x10^{-20}$
m (-)	3	3	3
τ (-)	0.4	0.4	0.4

The initial water pressure for all materials in the deposition hole is -41 MPa. The initial temperature is 10.5ºC throughout the model domain. The rock has hydrostatic water pressure (with P_l = 4.37 MPa at z = 437 m and P_l = 4 MPa at z = 400 m) which is maintained with the corresponding boundary conditions (Figure 6-1 - B).

The boundary condition for gas is the pressure of gas P_g = 0.1 MPa. This means the gas dissolved at the boundaries is the value that corresponds to this pressure (according to Henry's law: 1.5×10^{-5} kg/kg). Some studies about dissolved gas in groundwater at Olkiluoto have been done (Pitkänen and Partamies, 2007) and they indicate a gas content of 200-300 mL/L measured at NTP (normal conditions of temperature and pressure). Assuming the density of the gas in Olkiluoto equal to density of air in NTP (1.2 kg/m^3), the mass fraction of gas (understanding the gas as a component, not as a phase) in groundwater is 2.4×10^{-4} kg/kg, so the air will need more time for scaping from the EBS voids than if it is assumed absence of gas dissolved in groundwater. In any case, it is not expected that the presence of gas in groundwater affects the gas migration process from the EBS.

An initial confining stress of 8 MPa has been considered for the host rock. The lateral and bottom boundaries have normal displacements prescribed to zero.

During the excavation of the deposition tunnel (assumed duration is 1 year), a prescribed liquid pressure (-5 MPa) is applied on the excavation surface to represent the process of ventilation. This boundary condition is removed when the buffer and backfill materials are emplaced. During the simulated time, the hydrostatic liquid pressure is imposed on the top and bottom boundaries.

The temperature on the boundaries of model evolves with time. This temperature can be calculated from an analytical solution which takes into account the presence of all canisters (Ikonen, 2003). Thermal boundary conditions are identical to 2D calculations. Regarding the power evolution of canister, there are two main parameters playing a fundamental role: the residual power at the time of deposition and the decay rate. The work of Hökmark et al. (2003) is considered as a reference for the calculation of the power and the decay heat rate in this study. The power when the canister is emplaced in deposition hole is 1700 W, so a 1700 W of canister power, 25 m of tunnel spacing, 11 m of canister spacing and variable temperature on the boundaries are used to perform THM calculations (Toprak et al., 2013, for detailed information about thermal calculations under 2D - axisymmetric conditions).

The air transport will be mainly by diffusion through the liquid phase (non-advective flow). Air is dissolved in liquid following Henry's law:

$$\omega_l^a = \frac{P_a}{H}\frac{M_a}{M_\omega} \quad \textbf{(6.1-1)}$$

Where ω_l^a is the mass fraction of air in liquid, P_a is the partial pressure of air in gas (gas filling the voids is a mixture of dry air and vapour), M_a and M_w are the molecular mass of air and water (0.02895 and 0.018 kg/mol) and H is the Henry's constant (10000 MPa). Once the air is dissolved in liquid (water), the air will flow by diffusion following the Fick's law:

$$\mathbf{i}_l^a = -\left(\tau\phi\rho_l S_l D_m^i \mathbf{I}\right)\nabla\omega_l^a \quad \textbf{(6.1-2)}$$

where τ is the tortuosity, ϕ the porosity, S_l the degree of saturation and $D_m^i$the diffusion coefficient ($3.32\text{x}10^{-9}$ m^2/s at 10.5°C). The main diffusion will be molecular diffusion. Mechanical dispersion, associated to non-advective flow as well, will not be important due to the low velocity of the liquid phase. Air will flow to the boundaries where the air dissolved concentration is assumed to be the value corresponding to atmospheric pressure (0.1 MPa).

Air dissolved will flow to the deposition hole by advection. The water will flow to the deposition hole till the liquid pressures reached the steady state conditions.

Gas will flow following Darcy's law in the unsaturated region due to gradients of gas pressure and following the Fick's law due to differences in air concentration. The value of the gas permeability in unsaturated bentonites can be found in Villar and Lloret (2001).

Darcy's law is defined as:

$$\mathbf{q}_\alpha = -\frac{\mathbf{k}k_{r\alpha}}{\mu_\alpha}(\nabla P_\alpha - \rho_\alpha \mathbf{g}) \quad \textbf{(6.1-3)}$$

Where α is the phase. In principle, k (the intrinsic permeability) is independent of the fluid which flows through the porous media but in bentonites, the intrinsic permeability changes some orders of magnitude (Villar and Lloret, 2001). This is due to the size of the pores, which is lower when the bentonite is wet than when it is dry (Seiphoori et al. 2014; Villar et al. 2012), so the permeability changes.

6.2 Results of comparative study

A comparative study has been performed to study the impact of considering variable gas pressure on long-term THM results. A model has been chosen with relatively standard properties. One characteristic of the model is that the permeability of backfill and host rock is in the low-level range. This is an adequate assumption to study the influence of variable gas pressure because the lower the permeability is, the more difficult the scape of gas. Larger permeabilities would tend to induce lower gas pressures.

The only difference between the two models presented in this thesis is the inclusion or exclusion of the air balance equation. Most of THM calculations do not take into account the air conservation. Instead, gas pressure is considered to be constant. With the constant gas pressure, it is still possible to consider vapour at low concentrations, i.e. at low partial pressure. In short, one model has variable gas pressure while the other has constant gas pressure. The used THM parameters for materials and the rest of the boundary conditions were considered to be identical. Obviously, when the air conservation is considered, specific boundary conditions are required. The additional boundary condition is only constant gas pressure on top and bottom of the model.

Figure 6-2 shows temperature distribution 70 years after the emplacement of canister. The distribution of temperature is practically identical in constant and variable air pressures.

Figure 6-3 shows the temperature evolution at different representative points. The behaviour of the components and the reached maximum temperature are the same in both constant and variable gas pressures.

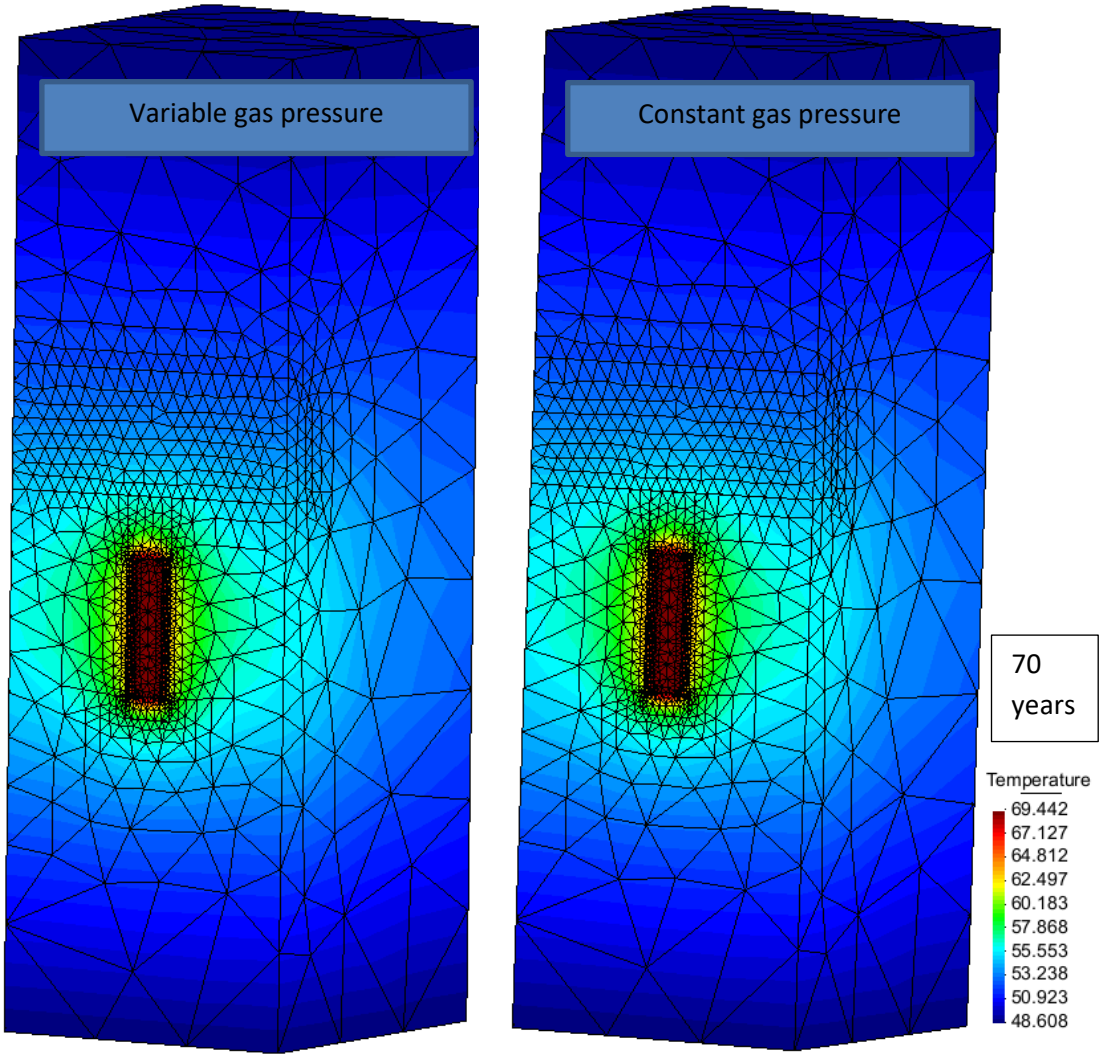

Figure 6-2. Distribution of temperature in canister, bentonite, backfill and host rock 70 years after canister emplacement.

Figure 6-4 shows the distribution of liquid pressure and saturation degree 70 years after the emplacement of the system components. It can be seen that the whole system is nearly saturated in 70 years. However, there is a slight difference in the distribution of liquid pressure, particularly in the domain of backfill. When the gas pressure is variable, the rock around backfill is slightly less saturated compared to the case with constant gas pressure.

Figure 6-5 demonstrates the evolution of liquid pressure for representative points in the two models. The results obtained in two cases are similar. However, there is a slight difference in time needed to reach full saturation. When the gas pressure is variable, the system components reach full saturation a few years later than in case of constant gas pressure model. In other words, variable gas pressure delays the saturation.

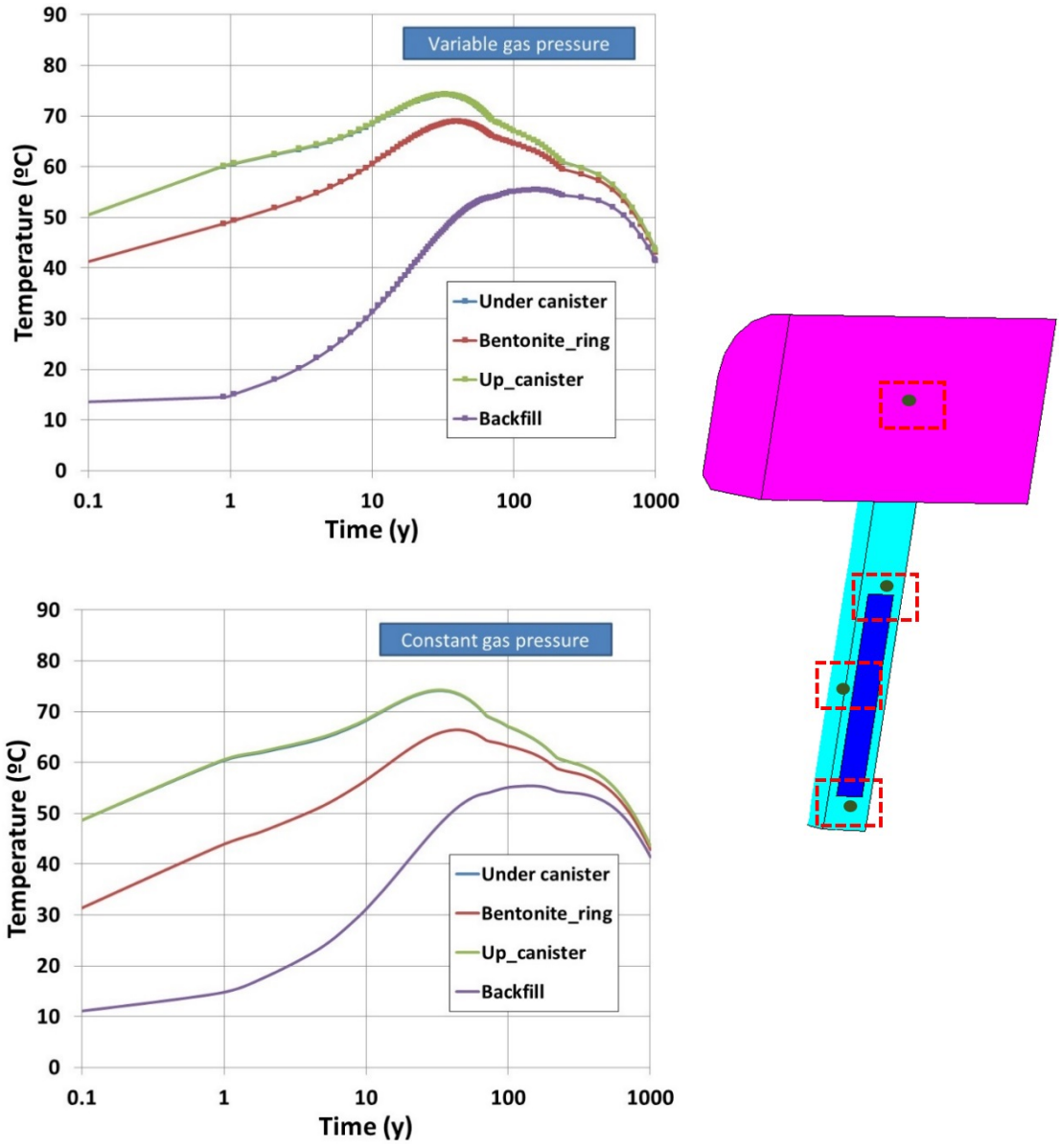

Figure 6-3. Temperature evolution at selected points.

Saturation of a porous material implies that the mass of air and water vapor in the gas phase should "disappear". In the case of vapor, a progressive condensation of vapor takes place and the final conditions of pressure and temperature imply that vapor transforms completely to liquid. In the case of air, there are two possibilities, flow towards other regions (through the model boundaries) or dissolution and diffusion/dispersion/advection.

In the case analysed here, air is evacuated by dissolution and molecular diffusion. As the dissolved gas reaches the boundary it escapes from the model domain as the top and bottom boundaries have constant gas pressure imposed. Gas pressure builds up and a gradient of gas pressure or concentration of dissolved air is generated.

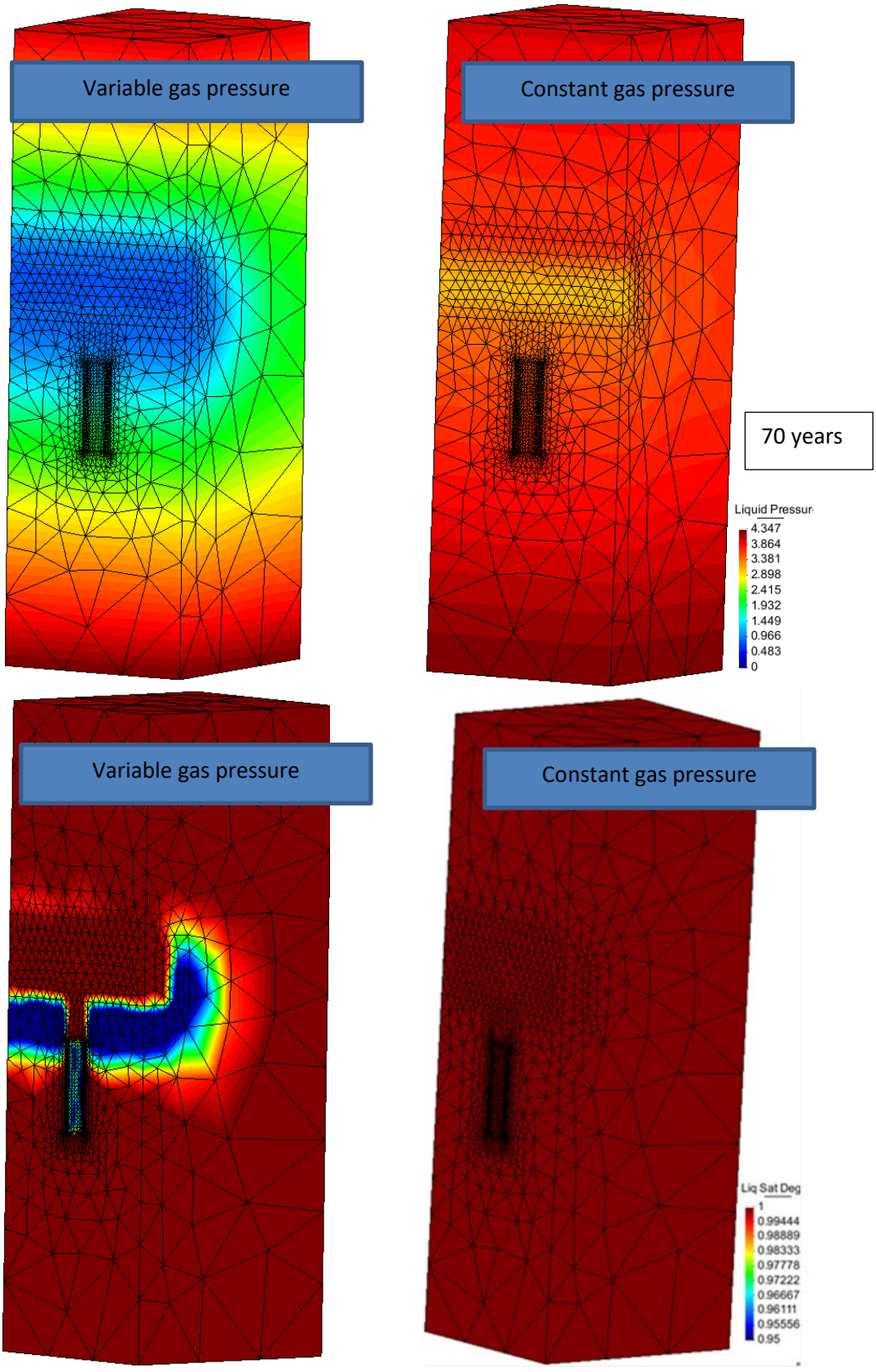

Figure 6-4 Distribution of liquid pressure (above) and saturation degree (below).

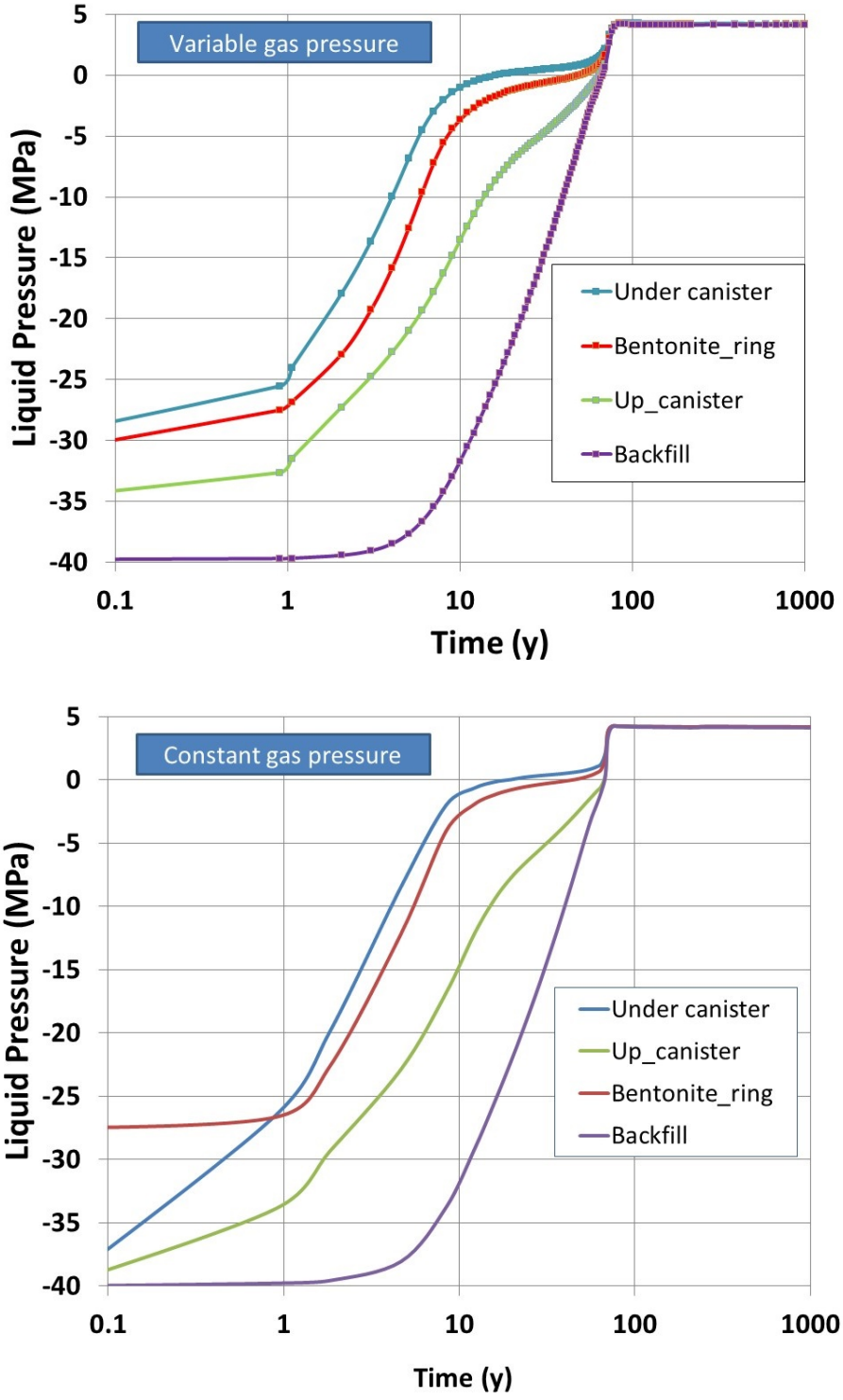

Figure 6-5 Comparison of liquid pressure

Figure 6-6 shows distribution of gas pressure, concentration of dissolved air 70 years after canister emplacement and the evolution of gas pressure. It can be seen that the contour plot of gas pressure and concentration of dissolved air are quite identical which is not surprising as the concentration of the dissolved air is calculated as a linear function of air pressure. Gas pressure is dominated by air pressure. It can be seen that the concentration is denser around the deposition hole.

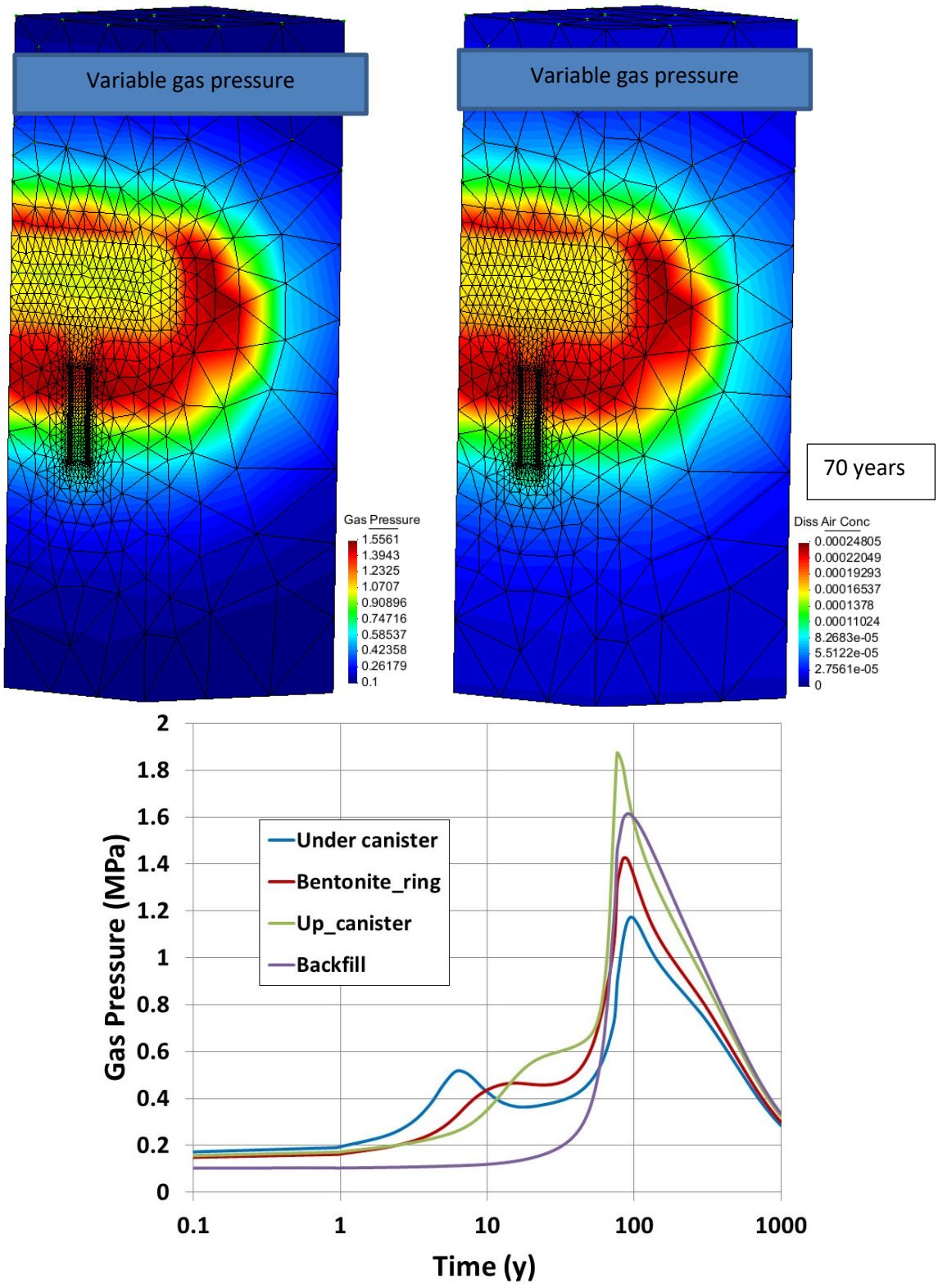

Figure 6-6. Distribution of gas pressure, concentration of dissolved air, and evolution of gas pressure at selected points.

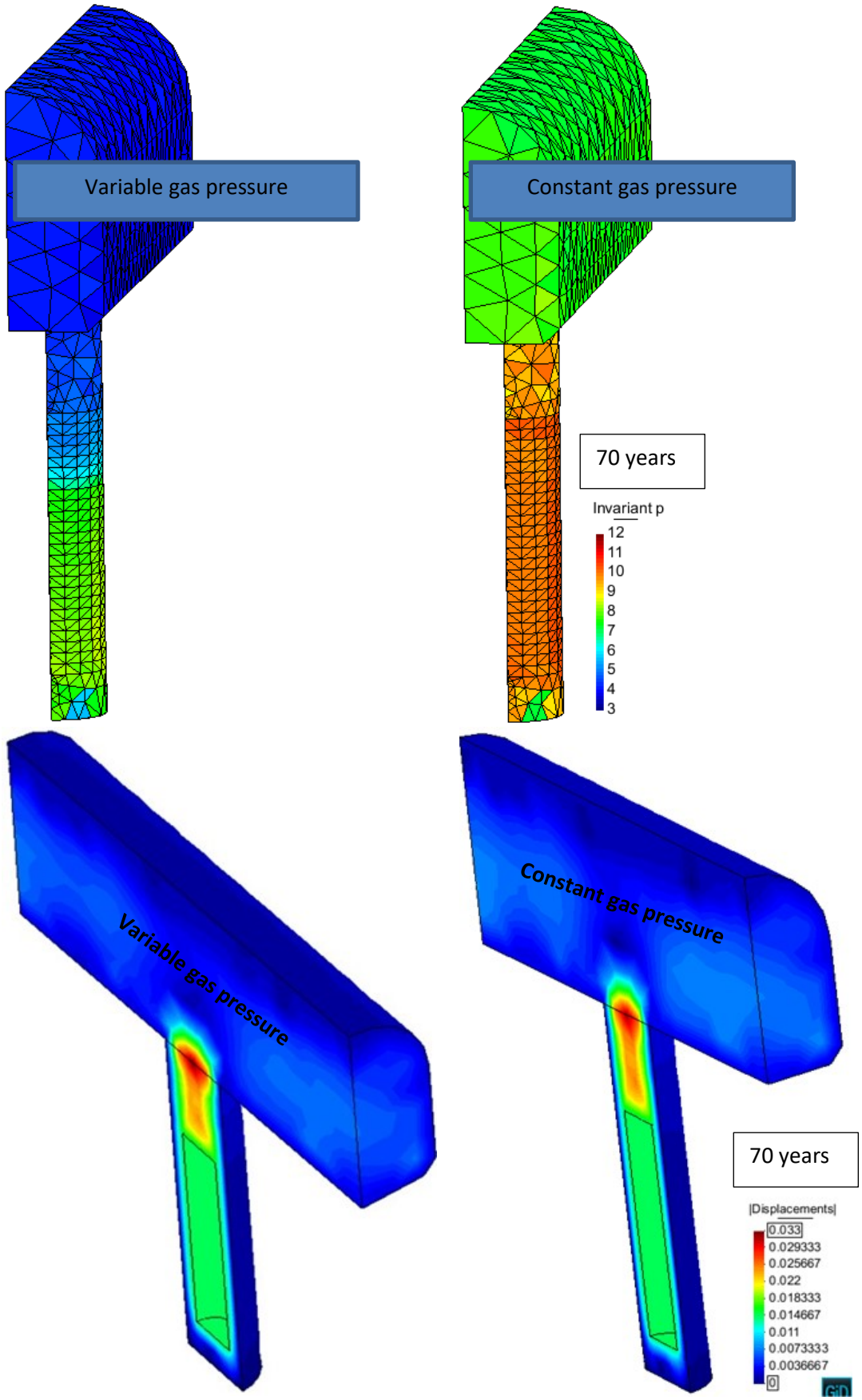

Figure 6-7. Distribution of mean stresses (above) and vertical displacements (below).

Gas migration from buffer to rock and backfill can be observed in the model (*Figure 6-6*). On top of the canister, gas pressure calculated 100 years after canister emplacement reaches a value around 1.9 MPa. Afterwards, gas pressure starts to decrease and progressively reaches steady state conditions. This is a slow process governed by molecular diffusion.

Figure 6-7 shows distribution of mean total stresses and vertical displacements 70 years after canister emplacement. The distribution of mean total stresses is slightly different. It is important to notice that 70 years is a critical point of time: full saturation is taking place. The long-term results are the same. Vertical displacements distribution is a little bit different between these cases. The maximum displacements are observed on the buffer-backfill interface.

Figure 6-8 shows mean total stress evolution in two cases. General trend and achieved stresses are almost same.

Figure 6-9 compares generated vertical displacements at the bottom part of the canister and in the buffer-backfill interface. The vertical displacements occurred on the buffer-backfill interface are smaller than 4 cm in both cases.

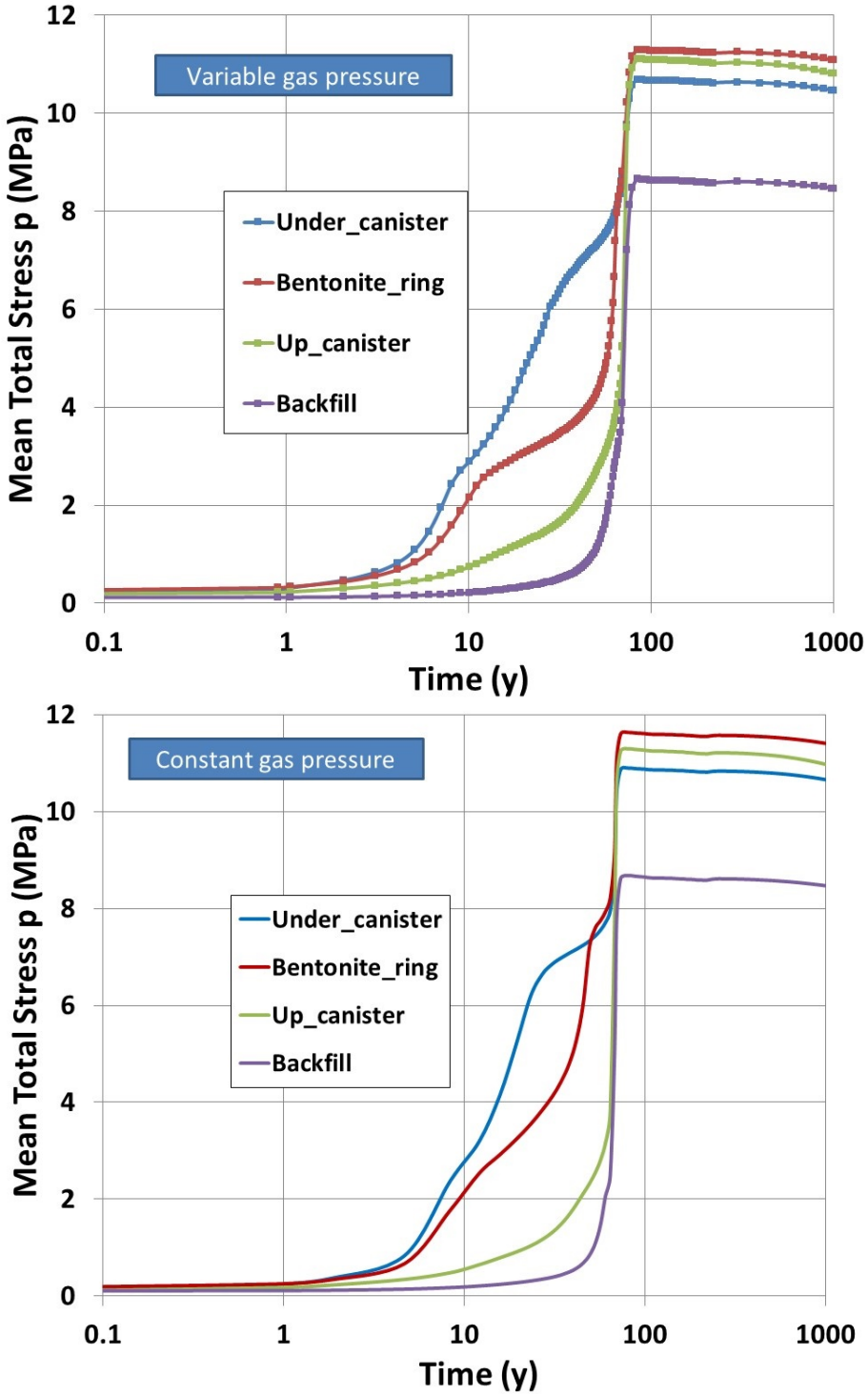

Figure 6-8. Comparison of mean total stresses

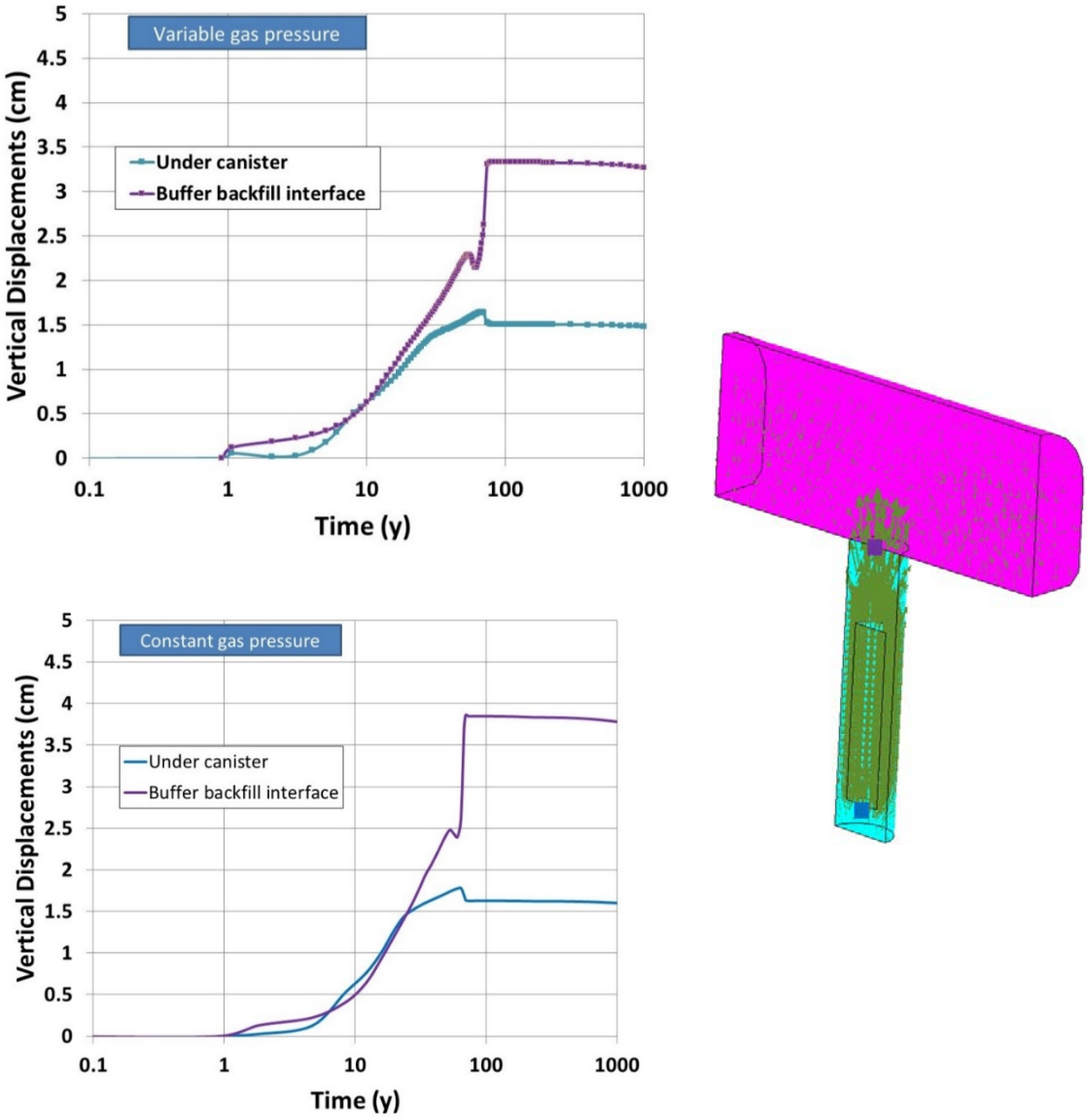

Figure 6-9. Comparison of vertical displacements

6.3 Conclusions for 3D sensitivity analysis

To investigate the effect of variable gas pressure on the THM results, a sensitivity study has been performed. The calculations have considered a simplified axisymmetric 3D domain. There are some local differences observed in the THM results obtained. However, there are no fundamental discrepancies among the compared models in terms of maximum temperature, stresses, degree of saturation and displacements. ***Table 6*** lists some of the vital results.

Table 6-2. Comparison of the two cases in terms of representative variables

Processes analysed	Units	Variable gas pressure	Constant gas pressure
Max. temperature at buffer ring	^{o}C	74.2	74.2
Time to full saturation of buffer discs – central	Year	65	60
Time to full saturation of backfill – central zone	Year	70	68
Swelling pressure of buffer discs under canister	MPa	10.6	10.6
Swelling pressure of backfill – central	MPa	8.6	8.6
Displacements at the buffer-backfill interface	cm	3.3	3.8
Buffer dry density (Disc)	kg/m^3	1723	1695

The time needed to reach full saturation is greater when gas pressure is variable. The delay varies depending on the point considered but it is in the range of 2-5 years for the model presented in this thesis. So the consideration of the air mass balance or, in other words, considering a variable gas pressure, delays full saturation slightly. Liquid pressure will reach steady state conditions before the air concentration reaches the steady-state conditions in liquid. The gas pressure drops once the liquid pressure becomes positive. Stress development due to swelling is practically not affected. However, vertical displacements generated at the buffer-backfill interface are slightly different. Displacements at that point are larger when gas pressure is constant compared to the case of variable gas pressure. It should be noted that this model is a simplification, so the values could change but the tendencies will not. The conclusion to this sensitivity analysis in 3D domain is that gas pressure does not play a significant role in either the saturation process or in the development of swelling pressure. The influence of gas pressure in temperature evolution is non-existent. It should be noted that the conditions in this study are quite extreme for gas migration. Gas can only escape by diffusion through the groundwater. It is expected that part of the gas will also escape through the backfill tunnel and access tunnels during saturation of the engineered barriers, which has not been taken into account here.

7. GENERAL CONCLUSIONS and COMMENTS

In this chapter, conclusions for each section in the thesis have been reviewed. Data uncertainties, limitations of numerical models used to simulate materials also future work are discussed.

General conclusions

The main objective of this thesis is to achieve an improved understanding of the thermo-hydro-mechanical processes and material properties that affect how the components of the radioactive spent fuel disposal system (buffer, backfill, pellets, rock, gaps and canister) behave during and after installation in the repository.

The generated models and methodologies developed in this thesis have provided a deeper understanding of the THM processes taking place in a radioactive spent fuel disposal system and offered strategies for design improvement, material choice and optimization.

The Thesis focuses on:

- material characterization (laboratory testing and numerical simulations of these tests),
- thermal dimensioning of repository (fixing canister and tunnel spacing, defining a power decay function for canister, adopting thermal boundary conditions),
- 2D sensitivity analyses (developing a better understanding of the modelled system, several cases have been studied throughout the thesis),
- 3D modelling (investigating the effect of variable gas pressure on the thermo-hydro-mechanical results).

One of the main contributions of the thesis is to combine comprehensive and complex models to perform the calculations of a single deposition scheme:

- BBM (Barcelona Basic Model) to represent clay buffer, BExM (Barcelona Expansive Model) to represent pellet-based components, combined with elasticity to represent rock and canister,
- Porosity-dependent permeability and water retention curve (macro-porosity dependent in case of pellets using BExM). Thermal conductivity depending of degree of saturation,
- Gap-specific THM modelling under simplifying assumptions but capturing effects like thermal conductivity which may produce an early peak of temperature, or specific

retention curve which produces extreme drying near the canister and gap closure which affects swelling pressure development.

- Full scale 3D THM modelling with elasto-plastic parameters (BBM) is also an important contribution.

Material characterization and calibration of model parameters

The characterization for the system components (MX-80, Friedland clay, granules, pillow and rod pellets) has been performed through laboratory tests designed for model parameter determination. Each system component has been characterized by means of laboratory tests (conducted at Saanio&Riekkola Oy laboratory and in some cases at UPC laboratory).

The laboratory tests conducted for characterization of materials include:

- water retention curve tests,
- thermal conductivity tests,
- infiltration tests,
- oedometer tests,
- tortuosity tests.

2D numerical simulation of laboratory tests demonstrate a globally good agreement with test results as shown in Chapter 4. Additional calibrations have been carried out following the same methodology and model adjustments with satisfactory results. In general, satisfactory agreement between numerical and measured results is achieved. Therefore, the code used in the thesis can be a useful analysis and design tool for modelling nuclear spent fuel repository. However, lessons learned in the thesis indicate that numerical models can have limitations.

No laboratory testing programme has been pursued for the adoption of parameter values for the rock and canister listed in the thesis, as this is beyond of the scope of the thesis. However, certain properties of rock including hydraulic conductivity and thermal expansion have been exposed to sensitivity analyses.

One of the biggest challenges was to adopt and calibrate THM parameters for gap element. Simulation of a full-scale swelling test (Toprak and Pintado, 2013) was performed to understand closure of gap element. The gap element has a complex THM behaviour because of closure during buffer swelling. Obviously, this produces local changes of hydraulic and thermal properties which affect temperature and liquid pressure at early times i.e. before gap closure.

The BBM (Barcelona Basic Model) has been considered to model the mechanical behaviour of unsaturated clays (MX-80 and Friedland Clay), while the BExM (Barcelona Expansive Model) has

been used to model the assumed double structure pellet-based materials (rod pellets, pillow pellets and granules). A bi-elastic model has been used to model gap elements (air or water gap) and elastic model for rock and canister.

The water rention curve, thermal conductivity and permeability of the materials have also been defined according to material behaviour. For example, in pellet-based materials, permeability depends on macro porosity while in clay based materials it depends on total porosity. FEBEX material has a specific water retention curve. Thermal conductivity parameters of the materials have been calibrated in a most suitable way to create as realistic as possible simulations.

Thermal calculations and boundary conditions

The maximum temperature at the surfaces of the spent nuclear fuel canisters in the repository must not exceed 100°C. This also applies to the KBS-3V concept. However, there are several material data uncertainties. For example, some variability in the values for bentonite thermal conductivity, rock heat capacity and rock thermal conductivity. Therefore, there is a 5°C safety margin that has been introduced to account for parameter uncertainty. Consequently, the permitted maximum temperature on canister surface is limited to 95°C (Ikonen and Raiko, 2015).This is a design criterion, which determines the thermal dimensioning of the deep repository. The power of the canisters at the time of deposition, the power decay function, the thermal properties of the engineered barrier, the occurrence of gaps and their properties, the orientation of the canisters and the rock thermal properties are the main factors that control the temperature on the canister surfaces.

The thermal calculations included in this thesis are an extension of the modelling task reported in Toprak et al., 2013 where the following aspects were investigated:

- Influence of canister and tunnel spacing,
- calibration of canister power function,
- numerical solution for thermal boundary conditions,
- effect of gap between canister and bentonite on canister temperature.

In this thesis, further contributions have been made to thermal calculations:

- radiation effect of the gap element,
- effect of gap thickness between buffer and canister,
- defining thermal conductivity of pellet based materials,
- effect of thermal conductivity of buffer,
- effect of thermal expansion of buffer and rock,

- analytical solution (Ikonen and Raiko, 2015) for thermal boundary conditions.

Full-scale 2D numerical analyses

Sensitivity analyses represent alternative models or alternative data corresponding to a Base Case. Sensitivity cases illustrate the effect of model and data uncertainties.

Comparison with a base case is carried out to investigate the effect of each variable on the results obtained:

- Thermal process: checking maximum temperature on canister wall,
- Hydraulic process: time needed to full saturation of system components, drying of buffer adjacent to canister,
- Mechanic process: developed stresses, displacements, gap closure.

The sensitivity analyses consist of (the order in the thesis):

1. The effect of fracture position
2. Different thickness of the space backfilled with pillow pellets
3. Salinity of the inflow water
4. Initial water content of buffer
5. Buffer density
6. Effect of Lagrangian method (mesh updating)
7. Swelling parameters of pellet
8. Filling material between buffer and rock
9. Rock hydraulic conductivity
10. Thermal expansion coefficient of buffer
11. Thermal conductivity of buffer
12. Artificial wetting of pillow pellets
13. Geometry differences: larger thickness for pillow pellets, bigger backfill tunnel, 3D TH modelling
14. Buffer material (calcium or sodium bentonite)
15. Thermal expansion coefficient of rock
16. Fracture permeability
17. Effect of radiation in gap element.

The sensitivity analyses can be grouped as:

- Buffer and backfill design option (2,4,5,8,12,13,14)
- Geological conditions (1, 3,9,16)
- Numerical simulation parameters (6,7,10,11,15,17)

As summarized in Table 5-26, some cases where initial water content relatively is low do not fulfil safety requirement for temperature, exceeding 95 ^{o}C. However, the majority of cases show a behaviour in safety margins in terms of temperature, density and stresses.

Full-scale 3D numerical analyses

A simplified 3D geometry has been adopted for THM calculations to check effect of third dimension. Full 3D calculations have been performed, aiming to realistic estimation of results. In 2D axisymmetric geometry, the volume of the backfill tunnel is underestimated which causes faster saturation of the backfill.

Globally, 3D THM analyses showed a good response of the buffer-backfill system and meet safety requirements such as:

- The maximum temperature does not exceed 95 ^{o}C (Ikonen and Raiko, 2015).
- Saturated density of buffer material does not drop below the threshold value of 1950 kg/m^3, which is necessary to ensure the effectiveness and durability of the buffer (Hansen et al. 2009).
- Swelling pressure does not exceed 15 MPa in order to avoid excessive isotropic stresses on the canister (Raiko, 2013).

3D calculations also include a sensitivity analysis. It has been shown that the full saturation of system components is delayed slightly when the air mass balance equation is considered, in other words, a variable gas pressure is taken into account.

Limitations of calculations

- Thermal: The ranges of possible errors in canister power and in the initial undisturbed rock temperature are difficult to estimate. In principle, it should be possible to assume that there will be no error of any significance in the determination of these parameters (Hökmark et al., 2003).
- 2D sensitivity analyses have limitations due to axisymmetric conditions. Backfill tunnel volume is under-estimated. However, a 2D geometry with a more realistic backfill volume and also 3D domain have been subjected to THM calculations.
- The model used to simulate numerical behaviour of pellets has limitations. In addition, there was not enough experimental data to capture the interaction functions of the Barcelona Expansive Model parameters. However, the set of parameters used to simulate pellet-based materials have reasonably captured from oedometer and infiltration tests results. It has been identified that pellets have triple structure

(Hoffman, 2005) but the Barcelona Expansive Model is based on double structure. Development of a new model to simulate hydro-mechanical behaviour of pellet-based materials seems important to have realistic approach.

- Due to lack of experimental data, granules have been simulated only considering the infiltration test results. There was no oedometer test simulation for them.
- Friedland clay has been considered as backfill material. However, it is not the final decision of Posiva Oy. There are other clays that are candidates for backfilling material.
- System details such as geometry and selected materials can also be updated by Posiva Oy. Therefore, these calculations should be validated once the final decision taken for the final geometry and backfilling material.
- In these calculations, long-term chemical influences on the mechanical properties of the materials (for example; chemical erosion of bentonite colloids) have not been studied specifically. Chemical processes may affect the homogenization and the stiffness of the bentonite in long term. However, in the thesis several sensitivity analyses on bentonite properties have been performed to handle the uncertainties.
- The parameters used to model materials need to be validated by modelling both small scale tests and large scale tests which is considered as future work.
- The 3D modelling included here is illustrative and not comprehensive. Therefore it is difficult to compare in detail the 3D model results and 2D axisymmetric ones. Actually there are several differences which include not only geometry, but for instance the absence of gaps and pellets; and a not correspondent set of parameters.

Future work

To validate, optimize and have better understanding the models and parameters used in the thesis, there is some future work suggested:

- Improving model for pellets, which considers its complex structure with three levels of porosity,
- Simulation of erosion, expanding THM calculations to THMC by adding chemical effects.
- 3D THM simulations of full scale FISST test (a real scale in situ test will be performed in Onkalo research facility) (Posiva Oy, 2018)

REFERENCES

Åkesson, M., Börgesson, L. and Kristensson, O. 2010. THM modelling of buffer, backfill and other system components. Stockholm, Sweden : Clay Technology AB, 2010. SR-Site Data report TR-10-44.

Åkesson, M., Jacinto, A-C and Gatabin, C., Sánchez, M., Ledesma, A. 2009. Bentonite THM behaviour at high temperatures: experimental and numerical analysis'. Geotechnique, 2009.s.l. : Volume 59 Issue 4, pp. 307-318.

Alcoverro, J., Alonso, E. 2001. Scientific bases of CODE_BRIGHT. Barcelona. Spain:s.n., 2001Informe técnico 70-UPC-L-1-001.

Alonso, E. and Navarro, V. 2005. Microstructural model for delayed deformation of clay: loading history effects. Canadian Geotechnical Journal 42: 381-392, 2005.

Alonso, E.E and Vaunat, J., Gens, A. 1999. Modelling the mechanical behaviour of expanive soils. Engineering Geology 54 (1999) 173–1831999.

Alonso, E.E. and Romero, E., Hoffmann, C. 2011. Hydromechanical behaviour of compacted granular expansive mixtures: experimental and constitutive study. Géotechnique, 2011 s.l. : Volume 61 Issue 4, April 2011, pp. 329-344.

Alonso, E.E., Gens, A. and Josa, A. 1990. A constitutive model for partially saturated soils. Géotechnique 40(3): 405-430. 1990. pp. 405-430.

Asensio, L. 2013. Hydro-mechanical elastoplastic model of expansive bentonite behaviour in free swelling conditions. Universidad de Castilla-La Mancha. Ciudad Real. Spain. PhD dissertation.

Börgesson, L., Hernelind, J. 2006. Canister displacement in KBS-3V. A theoretical study. tockholm, Sweden. SKB technical report TR-06-04.

Börgesson, L. and Sandén, T., Åkesson, M., Nilsson, U., Jensen, V. 2015. Transition zone homogenization test: KBS-3H laboratory test. SKB, Publication pending.

Börgesson, Lennart and Hernelind, Jan. 2014. Modelling of the mechanical interaction between the buffer and the backfill in a KBS-3V repository. Updated design of backfill and deposition hole. SKB, 2014. R-14-21.

Bossart, P. and Jaeggi, D., Nussbaum, Ch. 2017. Experiments on thermo-hydro-mechanical behavior of Opalinus clay at Mont Terri rock laboratory, Switzerland. Journal of Rock Mechanics and Geotechnical Engineering 9: 502-510.

Brooks, R.H. and Corey, A.T. 1964. Hydraulic Properties of Porous Media. Colorado State University, Fort Collins, USA. Hydrologic Paper 3.

Brown, G. O. 2002. Henry Darcy and the making of a law. Water resources research. Ref: 10.1029/2001WR000727

Chen, G. J. and Ledesma, A. 2009. Coupled thermohydromechanical modeling of the full-scale in situ test “Prototype Repository”. s.l. : Journal of Geotechnical and Geoenvironmental Engineering, *135 121-132.*

Collins, K. 1984. Characterization of expansive soil microfabric. P. s.l. : Proceedings of the 5th International Conference on Expansive soils, Adelaide, pp. 37-43.

Collins, K. and Mcgown, A. 1974. The form and function of microfabric features in a variety of natural soils. s.l. : Géotechnique, Volume 24 Issue 2, June 1974, pp. 223-254.

DECA-UPC. 2017. CODE_BRIGHT User's guide. Barcelona, Spain : Departament of Civil and Environmental Engineering, Escola de Camins. Universitat Politècnica de Catalunya,

Delage, P. and Cui, Y.C., Tang, A. M. 2010. Clays in radioactive waste disposal. s.l. : Journal of rock mechanics and geotechnical engineering 2(2): 111-123

Dixon, D.A. 2000. Porewater salinity and the development of swelling pressure in bentonite-based buffer and backfill materials. Eurajoki, Finland. Posiva Report 2000-04.

Dueck, A. 2004. Hydro-mechanical properties of a water unsaturated sodium bentonite. Laboratory study and theoretical interpretation. Lund University. Sweden. Ph. D. Thesis

Dueck, A. and Nilsson, U. 2010. Thermo-hydro-mechanical properties of MX-80. Results from advanced laboratory tests. Stockholm, Sweden. SKB TR-10-55.

Dueck, A., Goudarzi, R. and Börgesson, L. 2016. Buffer homogenization, status report 3. .Stockholm, Sweden : SKB Technical report TR-16-04.

Edelfsen, N.E. and Anderson. 1943. Thermodynamics of soil moisture. s.l. : Hilgardia 15(2): 31-298.

Enresa. 2000. FEBEX Project. Full-scale engineered barriers experiment for a deep geological repository for high level radioactive waste in crystalline host rock. Enresa, Madrid, Spain. Final report, 1/2000.

Enresa. 2006. Full-scale engineered barriers experiment. Enresa. Madrid. Spain. Updated final report 1994-2004. Technical publication 05-0/2006.

Fransson, Å. and Åkesson, M., Andersson, L. 2011.Bentonite rock interaction experiment. Characterization of rock and installation, hydration and dismantling of bentonite parcels. Stockholm, Sweden. SKB report R-14-11.

Fritz, S.J. 1986. Ideality of clay membranes in osmotic processes: a review. Clays and clay minerals, 34(2): 214-223.

García-Siñeriz, J-L and Villar, M.V., Rey, M., Palacios, B. 2015. Engineered barrier of bentonite pellets and compacted blocks. Engineering Geology 192:33-45,

Gens, A. and Alonso, E.E. 1992. A framework for the behaviour of unsaturated expansive clays. Canadian Geotech, 1992. s.l. : 29(6): 1013-1032

Gens, A. and Sánchez, M., Guimaraes, L. do. N, Alonso, E.E., Lloret, A., Olivella, S., Villar, M.V., Huertas, F. 2009. A full-scale in situ heating test for high-level nuclear waste disposal: observations, analysis and interpretation. s.l. : Géotechnique, 59(4): 377-399, 2009. pp. 377-399.

Hagros A., Kari Aikas, Tim McEvven, Pekka Anttila. 2003. Host Rock Classification Phase 2: Influence of Host Rock Properties, s.l. : Posiva Working Report 2003-04.

Hansen J, Korkiala-Tanttu L, Keski-Kuha E, Keto P. 2010. Deposition tunnel backfill design for a KBS-3V repository. Posiva Working Report 2009-129.

Henry, W. 1803. Experiments on the quantity of gases absorbed by water, at different temperatures, and under different pressures. s.l. : Phil. Trans. R. Soc. Lond., 1803. 93 29-274.

Hjerne, C. and Komulainen, J., Aro, S., Winberg, A. 2016. Development of Test Strategies in Support of Acceptance Criteria for Deposition Hole Positions – Results of Hydraulic Injection Tests in ONKALO DT2 Pilot Holes for Experimental Deposition Holes. Eurajoki. Finland. Posiva working Report 2016-06.

Hoffmann, C. 2005. Caracterización hidromecánica de mezclas de pellets de bentonite. Estudio experimental y constitutivo. Barcelona : Technical University of Catalonia, 2005. PhD dissertation.

Hoffmann, C., Alonso, E.E. and Romero, E. 2007. Hydro-mechanical behaviour of bentonite pellet mixtures. s.l. : Physics and Chemistry of the Earth, 32: 832-849.

Hökmark H, Fälth B. 2003. Thermal dimensioning of the deep repository. SKB-TR-03-09.

Holt, E., Löija, M., Fortino, S. & Marjavaara, P. 2014. Experimental studies of buffer gap design with artificial wetting. Eurajoki, Finland : Posiva Working Report 2013-52, 2014.

Ikonen, K. 2003. Thermal Analyses of Spent Nuclear Fuel Repository. Eurajoki, Finland. Posiva Report 2003-04.

Ikonen, K., Raiko, H. 2012. Thermal dimensioning of Olkiluoto repository for spent fuel. Posiva working report 2012-56.

Ikonen, K.; Raiko, H. 2015. Thermal analysis of KBS-3H repository. Eurajoki, Finland. Posiva working report 2015-01, 2015.

Johannesson, L-E. and Nilsson, U. 2006. Deep repository – engineered barrier systems. Geotechnical behaviour of candidate backfill materials. Laboratory tests and calculations for determining performance of the backfill. SKB-R-06-73, 2006.

Juvankoski, M. and N., Marcos. 2010. Design Basis for Buffer Components. Eurajoki, Finland. Posiva Working report 2009-132.

Juvankoski, M., Ikonen, K. and Jalonen, T. 2012. Buffer Production Line 2012. Design, Production and Initial State of the Buffer. Eurajoki,Finland. Posiva Report 2012-17.

Karnland, O., Olsson, S. and Nilsson, U. 2006. Mineralogy and sealing properties of various bentonites and smectite-rich clay materials. Stockholm, Sweden. Technical report SKB-TR-06-30.

Keto, P., et al. 2013. Backfill Production Line 2012. Design, Production and Initial State of the Deposition Tunnel Backfill and Plug. Eurajoki, Finland. Posiva Report 2012-18

Kivikoski, H. and Heimonen, I., Hyttinen, H. 2015. Bentonite Pellet Thermal Conductivity Techniques and Measurements. Eurajoki, Finland. Posiva working report 2015-09.

Kiviranta, L. and Kumpulainen, S. 2011. Quality Control and Characterization of Bentonite Materials. Eurajoki, Finland. Posiva Working report 2011-84, 2011.

Kiviranta, L., Kumpulainen, S, Pintado X., *Karttunen*, *P*. & Schatz, T. 2016. Characterization of bentonite and clay materials. Eurajoki, Finland. Posiva working report 2016-05.

Kristensson, O. and Börgesson, L. 2015. Canister retrieval test. Stockholm, Sweden. SKB technical report TR-14-19.

Kristensson, O. and Sandén, T., Börgesson, L. 2017. KBS-3H Summary report – Buffer laboratory test. Stockholm, Sweden. SKB report P-16-17.

Leoni, M. and Börgesson, L., Keto P. 2015. Numerical modelling of the buffer swelling test in Äspö HRL. Stockholm, Sweden. SKB technical report TR-17-03.

Lloret, A, et al. 2003. Mechanical behaviour of heavily compacted bentonite under high suction changes. s.l. : Géotechnique, 53, No. 1, 27–40.

Löfman, J., Poteri, A. and Pitkänen, P. 2010. Modelling of Salt Water Upconing in Olkiluoto. Eurajoki, Finland. Posiva Working report 2010-25.

Marjavaara, P. and Kivikoski, H. 2011. Filling the Gap Between Buffer and Rock in the Deposition Hole. Eurajoki, Finland. Posiva Working Report 2011-33.

Martikainen, J. and Schatz, T. 2011. Laboratory tests to determine the effect of Olkiluoto bonding brine water on buffer performance. Eurajoki, Finland. Posiva Working Report 2011-68.

Mayor, J.C. and Velasco, M., García-Siñeriz, J.L. 2007. Ventilation experiment in the Mont Terri underground laboratory. Physics and Chemistry of the Earth Parts A/B/C 32(8-14):616-628. DOI: 10.1016/j.pce.2006.04.030.

Miller, B and Marcos, N. (. 2007. Process report – FEPs and scenarios for a spent nuclear fuel repository at Olkiluoto. Eurajoki, Finland .Posiva report 2007-12.

Mills, A.E. 1999. Basic heat & mass transfer. 2nd edition, Prentince Hall, ISBN 0-13-096247-3.

Navarro, V. and Asensio, L., Alonso, J., Yustres, A., Pintado, X. 2014b. Multiphysics implementation of advanced soil mechanics models. s.l. : Computers and Geotechnics, 181:190-201.

Navarro, V. and Asensio, L., Yustres, A., Pintado, X., Alonso, J. 2014. An elastoplastic model of bentonite free swelling. Engineering Geology 181: 190-201.

Navarro, V. and Yustres, A., Asensio, L., De la Morena, G., González-Arteaga, J., Laurila, T., Pintado, X. 2017. Modelling of compacted bentonite swelling accounting for salinity effects. Enginering Geology 223: 48-58.

Navarro, V., Asensio, L., Yustres, Á., Pintado,. X. and Alonso, J. 2014a. An elastoplastic model of bentonite free swelling. Engineering Geology, doi: 10.1016/j.enggeo.2014.07.014.

Norrish, K. and Quirk, J.P. 1954. Crystalline swelling of montmorillonite: Use of Electrolytes to control swelling. Nature 173, 255–256.

Olivella, S, Carrera, J and Gens, A. & Alonso, E. E. 1994. Nonisothermal multiphase flow of brine and gas through saline media. Barcelona, Spain. Transport in Porous Media, 1994. 271–293.

Olivella, S. and Alonso, E.E. 2008. Gas flow through clay barriers. s.l. : Géotechnique 58(3): 157-176.

Olivella, S. and Gens, A. Vapour transport in low permeability unsaturated soils with capillary effects. Transport in Porous Media Volume 40, Issue 2, pp 219–241.

Olivella, S., A. Gens, J. Carrera, E.E. Alonso 1996. Numerical formulation for a simulator (CODE BRIGHT) for the coupled analysis of saline media. Engineering Computations 13, 1996. pp. 87–112.

Olsson, S., Karnland, O. 2013. Chemical and mineralogical characterization of the Indian tunnel backfill bentonite Asha NW BFL-L 2010. SKB R-13-48.

Pastina, B. and P., Hellä. 2010. Models and Data Report 2010. Eurajoki, Finland. Posiva report 2010-1.

Pekkanen, J. 2016. Flow measurements in Onkalo at Olkiluoto, investigation holes ONK-PP366, -PP368, -PP370, -PP372, -PP374, -PP376, -PP379-PP406, PP409-PP413, -KR16 and -PVA7. Eurajoki. Finland. Posiva working report 2016-07.

Pitkänen, P., Partamies, S. 2007. Origin and implications of dissolved gases in groundwater at Olkiluoto. Eurajoki. Finland. Posiva report 2007-04.

Pintado, X. and Adesola, F., Turtiainen, M. 2013. Downscaled tests on buffer behaviour. Eurajoki, Finland. : Posiva working report 2012-100.

Pintado, X. and Hassan, Md. M., Martikainen, J. 2013a. Thermo-hydro-mechanical tests of buffer material . Eurajoki, Finland : Posiva Report 2012-49.

Pintado, X. and Kristensson, O., Malmberg, D., Åkesson, M., Olivella, S., Puig, I. 2017. TH and THM modelling for a KBS-3H deposition drift. Eurajoki, Finland. Posiva working report 2016-25.

Pintado, X. and Rautioaho, E. 2013. Thermo-Hydraulic Modelling of Buffer and Backfill. Eurajoki. Finland. Posiva Report 2012-48.

Pintado, X., Ledesma, A. and Lloret, A. 2002. Backanalysis of thermohydraulic bentonite properties from laboratory tests. Engineering Geology 64: 91-115.

Pinyol, Nuria. and N-M, Alonso, E.E., Olivella, S. 2008. Rapid drawdown in slopes and embankments. s.l. : Water resources research 44, W00D03, doi: 10.1029/2007WR006525.

Pinyol, Nuria. 2014. Barcelona expansive model in coupled flow-deformation problems. Code bright short course. Barcelona, Spain.

Posiva. 2009. Olkiluoto site description 2008. . Eurajoki, Finland : Posiva Oy, 2009. Posiva Report 2009-01.

Posiva. 2012. Safety Case for the Disposal of Spent Nuclear Fuel at Olkiluoto – Performance Assessment 2012. Eurajoki, Finland. : Posiva Oy, 2012. Posiva Report 2012-04.

Posiva. 2018. Preparation of integrated systems test progresses to pilot hole drilling phase (http://www.posiva.fi/en/media/news/preparation_of_integrated_systems_test_progresses_to_pilot_hole_drilling_phase.3369.news#.WorQwudG2Uk)

Poteri, A. and Laitinen, M. 1997. Fracture network model of the groundwater flow in the Romuvaara site. Posiva report 96-26.

Pusch, R. 1987. Identification of Na-smectite hydration by use of “humid cell” high voltage microscopy. Applied Clay Science 2(4): 343-352.

Pusch, R. and Moreno, L. 2001. Saturation and permeation of buffer clay. Proceedings of the 6th International Workshop on Key Issues in Waste Isolation Research. s.l. : École Nationale des Ponts et Chaussées, Paris, pp.71-81.

Pusch, R.. 1982. Mineral-water interactions and their influence on the physical behavior of highly compacted Na bentonite. Canadian Geotechnical Journal 19(3): 381-387.

Raiko, H. 2013. Canister Design 2012. Eurajoki, Finland. Posiva working report 2012-13.

Raiko, H. and Pastina, B., Jalonen, T., Nolvi, L., Pitkänen, J., Salonen, T. 2012. Canister production line 2012. Eurajoki, Finland. Posiva report 2012-16.

Rautakorpi, J. and Johansson, E. & Tinucci. 2003. Effect of fracturing to tunnel orientation using block theory and 3DEC programs for repository of spent nuclear fuel in Olkiluoto. Eurajoki, Finland. Posiva working report 2003-09.

Rinta-Hiiro, V., Peura, J., Bohner, E., Holt, E., Heino, V. 2017. 1/6 scale laboratory experiment for bentonite buffer and backfill interaction in KBS-3V nuclear waste disposal concept. Tampere Univertsity of Techology, Finland. Master thesis of science.

Romero, E. and Gens, A., Lloret, A. 1999. Water permeability, water retention and microstructure of unsaturated compacted Boom clay. Engineering Geology 54 (1-2), 117-127.

Romero, E. and Simms, P.H. 2008. Microstructure investigation in unsaturated soils: a review with special attention to contribution of mercury intrusion porosimetry and environmental scanning electron microscopy. Geotechnical and Geological Engineering DOI 10.1007/s10706-008-9204-5.

Ruotsalainen, P., et al. 2000. Groundwater salinity at the Olkiluoto site. Posiva working report 2000-26.

Ryti, H. 1973. Heat and mass transfer. Technical handbook. K.J. Gummerus Osakeyhtiö (in Finnish). Vol. 1: 357-424.

Saanio, T. and Ikonen, A., Keto, P., Kirkkomäki, T., Kukkola, T., Nieminen, J., Raiko, H. 2012. Loppusijotuslaitoksen suunnitelma. Eurajoki. Finland. Posiva working report 2012-50

Sánchez, M. and Gens, A., Guimaraes, L., Olivella, S. 2005. A double structure generalized plasticity model for expansive soils. International Journal for Numerical and Analytical Methods in Geomechanics 10.1002/nag.434.

Sandén, T., et al. 2008. Deep repository - engineered barrier system. Erosion and sealing processes in tunnel backfill materials investigated in laboratory. Stockholm, Sweden. SKB R-08-135

Sandén, T., Nilsson, Ulf and Andersson, Linus. 2016. Investigation of parameters influencing bentonite block quality. Laboratory investigation. SKB Report: P-16-06.

Schatz, T. and Martikainen, J. 2012. Laboratory tests and analyses on potential Olkiluoto backfill materials. Posiva working report 2012-74.

Seiphoori, A. and Ferrari, A., Laloui, L. 2014. Water retention behaviour and microstructural evolution of MX-80 bentonite during wetting and drying cycles. Géotechnique Volume 64 Issue 9, July 2014, pp. 721-734, 2014.

Sinnathamby, G., Tanttu, L. and Fores, J. 2014. Interface shear behaviour of tunnel backfill materials in a deep-rock nuclear waste repository in Finland. Soils and Foundations. The Japanese Geotechnical Society. Volume 54, Issue 4, Pages 777-788.

SKB. 2010. Buffer, backfill and closure process report for the safety assessment SR-Site. SKB technical report TR-10-47.

Sun, Linlin. 2016. The effects of structural and environmental factors on the swelling behavior of montmorillonite beidellite Smectites : a molecular dynamics approach. University of Eastern Finland Faculty of Science and Forestry Department of Chemistry Dissertation. ISBN: 978-952-61-2045-4

Tang, A.-M. and Cui, Y.-J. 2005. Controlling suction by the vapour equilibrium technique at different temperatures and its application in determining the water retention properties of MX-80 clay. Canadian Geotechnical Journal NRC Research Press. 42 (1), pp.287-296., 2005.

Terzaghi, K. 1966. Soil mechanics. John Wiley and Sons. New York, USA.

Toprak, E. and Olivella, S. & Pintado, X. 2016. Coupled THM modelling of engineered barriers for the final disposal of spent nuclear fuel isolation. Geological Society, London, Special Publications, 443. doi:10.1144/SP443.19.

Toprak, E., et al. 2013. Thermo-Hydro-Mechanical Modelling of Buffer, Synthesis Report. Eurajoki, Finland. Posiva Report 2012-47.

Toprak E., X. Pintado (2013). Modelling of Big Bertha test. B+TECH (Interim Posiva report)

van Genuchten, R. 1980. A closed-form equation for predicting the hydraulic conductivity of unsaturated soils. Soil Science Society American Journal 44(5).

Vieno, T. 2000. Groundwater salinity at Olkiluoto and its effects on a spent fuel repository. Eurajoki, Finland. Posiva report 2000-11.

Vilarrasa, V. and Silva, O., Carrera, J., Olivella, S. 2013. Liquid CO2 injection for geological storage in deep saline aquifers. International Journal of Greenhouse Gas Control 14:84–96.

Villar, M.V, Lloret, A. (2001). Variation of the intrinsic permeability of expansive clays upon unsaturation. In Clay Science for Engineering. Edidted by K. Adachi and M. Fukue. Balkema, Rotterdam, the Netherlands. pp. 259-266.

Villar, M. 2002. Thermo-hydro-mechanical characterisation of a bentonite from Cabo de Gata. A study applied to the use of bentonite as sealing material in high level radioactive waste repositories. Madrid, Spain. ENRESA technical report 01/2002-258.

Villar, M.V. 2005. MX-80 bentonite, Thermo-hydro-mechanical characterization performed at CIEMAT in the context of the prototype project. Madrid, Spain. CIEMAT technical report CIEMAT/DIAE/54540/2/04.

Villar, M.V. and Lloret, A. 2007. Dismantling of the first section of the FEBEX in situ test: THM laboratory tests on the bentonite blocks retrieved. Physics and Chemistry of the Earth 32(8): 716-729.

Villar, M.V., Gómez-Espina, R., Campos, R., Barrios, I., Gutiérrez-Nebot, L. (2012). Porosity Changes Due To Hydration Of Compacted Bentonite. In: Mancuso, C.; Jommi, C. & D'Onza, F. (Eds.). Unsaturated Soils: Research and Applications, Volume 1, pp. 137-144. ISBN: 978-3-642-31115-4

Yustres, A. and Jenni, A., Asensio, L., Pintado, X., Koskinen, K., Navarro, V., Wersin, P. 2017. Comparison of the hydrogeochemical and mechanical behaviours of compacted bentonite using different conceptual approaches. s.l. : Applied Clay Science 141: 280-291.

Zandarín, MT. and Gens A, Olivella S, Alonso EE,. 2011. Thermo-hydro-mechanical model of the Canister Retrieval Test. Physics and Chemistry of the Earth 36(2011): 1806-1816.